JESSÉ JOABE VIEIRA CARNEIRO

CHARACTERIZATION AND BEHAVIOUR OF IRON ORE TAILINGS: THE EFFECT OF COMPACTION AND STRESSES

Dissertação apresentada à Universidade Federal de Viçosa, como parte das exigências do Programa de Pós-Graduação em Engenharia Civil, para obtenção do título de *Magister Scientiae*.

Orientador: Eduardo Antonio Gomes Marques

Coorientadores: António J. P. Viana da Fonseca
Roberto Lopes Ferraz

VIÇOSA – MINAS GERAIS
2021

Ficha catalográfica elaborada pela Biblioteca Central da Universidade Federal de Viçosa - Campus Viçosa

T
C289c
2021

Carneiro, Jessé Joabe Vieira, 1993-
Characterization and behaviour of iron ore tailings : the effect of compaction and stresses / Jessé Joabe Vieira Carneiro. – Viçosa, MG, 2021.
217 f. : il. (algumas color.) ; 29 cm.

Inclui apêndices.
Orientador: Eduardo Antonio Gomes Marques.
Dissertação (mestrado) - Universidade Federal de Viçosa.
Referências bibliográficas: f. 132-138.

1. Barragens de rejeito - Minas Gerais. 2. Solos - Permeabilidade. 3. Cisalhamento do solo - Resistência. 4. Mecânica dos solos. 5. Condutividade hidráulica. 6. Compactação. 7. Pressão do solo. I. Universidade Federal de Viçosa. Departamento de Engenharia Civil. Programa de Pós-Graduação em Engenharia Civil. II. Título.

CDD 22. ed. 622.130098151

Bibliotecário(a) responsável: Renata de Fatima Alves CRB6/2578

JESSÉ JOABE VIEIRA CARNEIRO

CHARACTERIZATION AND BEHAVIOUR OF IRON ORE TAILINGS: THE EFFECT OF COMPACTION AND STRESSES

Dissertação apresentada à Universidade Federal de Viçosa, como parte das exigências do Programa de Pós-Graduação em Engenharia Civil, para obtenção do título de *Magister Scientiae*.

APROVADA: 01 de julho de 2021

Assentimento:

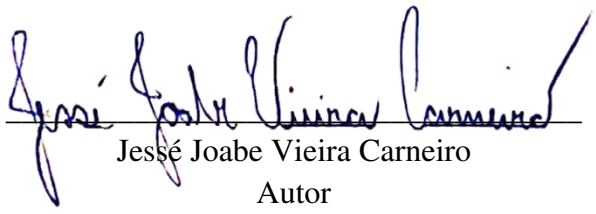

Jessé Joabe Vieira Carneiro
Autor

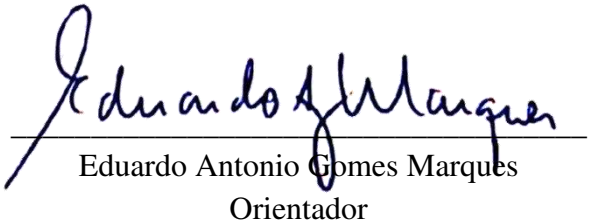

Eduardo Antonio Gomes Marques
Orientador

Dedico este trabalho aos meus pais, Suzete e Aparecido, e a minhas irmãs, Renata e Suzane, que não mediram esforços para que eu pudesse chegar até aqui.

ACKNOWLEDGEMENTS

A Deus pela vida e tudo de bom que vem junto com ela.

Aos meus pais por sempre colocarem a educação como prioridade dentro do nosso lar e às minhas irmãs por compartilharem desse princípio, sempre me motivando a seguir em frente.

À Bianca, por todo o suporte técnico e emocional concedido ao longo do mestrado, principalmente nesta reta final inacabável.

Ao professor Eduardo Marques, por ser orientador acadêmico e profissional, e estar sempre disposto a resolver qualquer problema antes mesmo dele acontecer.

Aos meus coorientadores António Viana da Fonseca e Roberto Ferraz por toda a gama de conhecimento compartilhada ao longo do mestrado e por estarem sempre dispostos a esclarecer qualquer dúvida.

Aos técnicos do LMS-UFV, em especial ao Anderson, Marcelo e Dedé, e à Daniela do LabGeo-FEUP, por conduzirem os ensaios mesmo com as dificuldades impostas pela pandemia e estarem sempre dispostos a fazer aquele ensaio a mais, ou a esclarecer qualquer dúvida sobre a montagem e execução dos ensaios.

Ao professor Igor Assis e seus orientados por todo o apoio na execução dos ensaios realizados no Laboratório de Física dos Solos da UFV e por serem sempre solícitos a esclarecer dúvidas.

À mineradora, não só por fornecer o material utilizado na pesquisa, mas também pelo engajamento no projeto. Aos meus colegas de projeto, Amadeu, Ângelo, Cassiano e Tadeu, pelas discussões técnicas e pelo apoio com os ensaios de laboratório e demandas do projeto.

Aos professores da Geotecnia do DEC/UFV por todo o conhecimento transmito dentro e fora de sala de aula e por serem sempre solícitos a nos ajudar.

À DF+ por me proporcionar desafios que me motivaram a desenvolver este trabalho, e aos meus colegas de trabalho por todo o conhecimento compartilhado. Em especial, ao Daniel, Henrique, e Ian pelas dúvidas esclarecidas e boas ideias sugeridas, e ao Lucas pelas caronas às 6 da manhã.

O presente trabalho foi realizado com apoio da Coordenação de Aperfeiçoamento de Pessoal de Nível Superior – Brasil (CAPES) – Código de Financiamento 001.

ABSTRACT

CARNEIRO, Jessé Joabe Vieira, M.Sc., Universidade Federal de Viçosa, July, 2021. **Characterization and behaviour of iron ore tailings: the effect of compaction and stresses.** Adviser: Eduardo Antônio Gomes Marques. Co-advisers: António Joaquim Pereira Viana Da Fonseca and Roberto Lopes Ferraz.

The massive yearly tonnage of tailings plus the demanding environmental legislation, after the catastrophic collapses of Fundão Dam (2015) and Feijão Dam I (2019), have been making the mining companies in Brazil to search for more sustainable and safer alternatives for tailings disposal. The dry stacking of filtered tailings, studied and gradually implemented by the major companies of the Brazilian mining industry, is consolidated in empirical-based knowledge for structures smaller than 100 m high (CRYSTAL et al., 2018). Nevertheless, to absorb the large tailings generation, the mining companies intend to develop great dry stacks that exceeds this limit. In this context, the main objective of this research was to characterize the intrinsic properties, geomechanical and hydraulic behavior of iron ore tailings from a mine located in the Quadrilátero Ferrífero, Brazil, which are being filtered. Initially, to characterize the material, index tests were conducted. Subsequently, Proctor compaction tests were run to define the maximum dry unit weight and optimum water content. Based on Proctor compaction test results, specimens were compacted to 93%, 95%, 97%, and 100% of Proctor maximum dry unit weight for oedometer tests, isotropic consolidation, and triaxial tests. For each degree of compaction, CID and CIU triaxial compression tests were conducted, and the hydraulic conductivity was defined for each confining pressure of the adopted range, 100 kPa, 200 kPa, 400 kPa, 800 kPa, 1600 kPa e 1900 kPa. The filtered tailings showed similar index properties to other iron ore tailings from the Quadrilátero Ferrífero. No significant particle crushing was identified with static compaction. Therefore, it was possible to define a unique semi-logarithmic critical state line. The increase of the degree of compaction resulted in less compressible denser specimens with dilatant behavior at low confining stresses. The material presented a tendency to pass from dilatant to contractile with the increase of confining pressure, also with the reduction of the degree of compaction. The parameters of dilatancy were out of the usual ranges, and the elastic moduli were relatively low. Even at 6,4 MPa of effective vertical stress, the one-dimensional compression curves did not converge to the normal consolidation line. And the hydraulic conductivity is shown to be proportional to the void ratio.

Keywords: Iron ore. Filtered tailings. Dry stacking. Quadrilátero Ferrífero. Index properties. Geomechanical behavior. Degree of compaction. Confining pressure. Critical state line. Dilatancy. Elastic moduli. Normal consolidation line. Hydraulic conductivity.

RESUMO

CARNEIRO, Jessé Joabe Vieira, M.Sc., Universidade Federal de Viçosa, julho de 2021. **Caracterização e comportamento de rejeitos de minério de ferro: efeitos da compactação e níveis de tensões.** Orientador: Eduardo Antonio Gomes Marques. Coorientadores: António Joaquim Pereira Viana Da Fonseca e Roberto Lopes Ferraz.

A grande tonelagem anual de rejeitos, somada à exigente legislação, após os rompimentos catastróficos das Barragens de Fundão (2015) e Feijão I (2019), têm feito as mineradoras brasileiras buscarem alternativas mais sustentáveis e seguras para a disposição de rejeitos. O empilhamento a seco de rejeitos filtrados, estudado e gradativamente implantado pelas principais mineradoras do Brasil, está consolidado em conhecimento de base empírica para estruturas com menos de 100 m de altura (CRYSTAL et al., 2018). Contudo, para absorver a enorme geração de rejeitos, as mineradoras pretendem desenvolver estruturas que excedem esse limite. Nesse contexto, esta pesquisa procurou caracterizar as propriedades intrínsecas e o comportamento geomecânico e hidráulico dos rejeitos de ferro de uma mina localizada no Quadrilátero Ferrífero, que estão sendo filtrados. Inicialmente, foi realizada a caracterização física do rejeito. Posteriormente, foram executados testes de compactação Proctor Normal e, a partir dos resultados, foram preparados corpos de prova com graus de compactação de 93%, 95%, 97% e 100% do Proctor Normal para execução de ensaios de adensamento edométrico e isotrópico, e ensaios triaxiais CID e CIU com tensões confinantes de 100 kPa, 200 kPa, 400 kPa, 800 kPa, 1600 kPa e 1900 kPa. A condutividade hidráulica foi definida para cada grau de compactação e tensões confinantes adotadas. Os rejeitos apresentaram características físicas semelhantes às de outros rejeitos do Quadrilátero Ferrífero. Não foi identificada quebra significativa de partículas com compactação estática, pelo que foi possível definir uma única linha semi-logarítmica de estado crítico. O aumento do grau de compactação resultou em um material menos compressível com comportamento dilatante em baixas tensões. O material demostrou tendência a passar de dilatante para levemente dilatante ou contrátil com o aumento da tensão confinante e, também, com a redução do grau de compactação. Os parâmetros de dilatância ficaram fora dos intervalos usuais e os módulos de elasticidade foram relativamente baixos. Mesmo sob tensão vertical de 6,4 MPa, as curvas de compressão unidimensional não convergiram para a linha de compressão normal. E a condutividade hidráulica se mostrou proporcional ao índice de vazios.

Palavras-chave: Minério de ferro. Rejeito filtrado. Empilhamento a seco. Quadrilátero Ferrífero. Características físicas. Comportamento geomecânico. Grau de compactação. Tensões confinantes. Linha de estado crítico. Dilatância. Módulos de elasticidade. Linha de compressão normal. Condutividade hidráulica.

LIST OF FIGURES

LIST OF TABLES

LIST OF SYMBOLS

B_q	Dynamic pore pressure ratio
C_c	One-dimensional compression index
C_r	One-dimensional recompression index
CSL	Critical state line
C_u	Coefficient of uniformity
C_v	Vertical coefficient of consolidation
C_z	Coefficient of curvature
c'_p	Dimensionless operational strength parameter (direct shear)
D	Dilatancy
D_{50}	Mean particle size
DC	Degree of compaction
D_{min}	Maximum dilatancy
D^P	Plastic component of dilatancy
$E_{50,D}$	Drained secant elastic modulus
$E_{50,U}$	Undrained secant elastic modulus
ESP	Effective stress path
e	Current void ratio
e_c	Critical void ratio
e_f	Final void ratio
e_i	Initial void ratio
e_{max}	Maximum void ratio
e_{min}	Minimum void ratio
F_r	Normalized frictional ratio
G_{max}	Elastic shear modulus
$G_{max\ @\ p0}$	Elastic shear modulus at the initial mean stress
G_{ref}	Shear modulus at the confining stress p'_{ref}
G_s	Specific gravity
g	Acceleration of gravity
H	Plastic modulus
H_0	Plastic modulus constant 1
H_ψ	Plastic modulus constant 2 (associated with the state parameter)
I_B	Brittleness index
IP	Plasticity index
K_0	Coefficient of earth pressure at rest
$K_{0,OC}$	Coefficient of earth pressure at rest of overconsolidated soils
K_c	Normalized cone resistance correction factor
k	Hydraulic conductivity
$\bar{k}$	Semi empirical parameter for estimating ψ

LEC	Linha do estado crítico
LCN	Linha de compressão normal
LL	Liquid limit
M	Critical friction ratio
M_{tc}	Critical friction ratio obtained through triaxial compression tests
$\bar{m}$	Semi empirical parameter for estimating ψ
m_v	Modulus of volume compressibility
N	Volumetric coupling coefficient
NCL	Normal compression line
n, $G_{\_exp}$	Stress component ($n \leq 1,0$)
OCR	Over consolidation ratio
p	Mean total stress
p_a	Atmospheric pressure
PL	Plastic limit
p'	Mean effective stress
p'_{max}	Ultimate mean effective stress
p'_{ref}	Mean effective stress of reference
Q_p	Tip resistance normalized by mean effective stress
$\overline{Q_p}$	Tip resistance normalized by mean effective stress and pore pressure
Q_t	Tip resistance normalized by vertical effective stress
Q_{tn}	Tip resistance normalized by vertical effective stress and soil type
$Q_{tn,cs}$	Clean sand equivalent normalized cone resistance
q	Deviatoric stress
q_t	Corrected tip resistance
S	Saturation
S_p	Specific surface
s_u	Undrained strength
$s_{u,p}$	Undrained strength at peak
$s_{u,c}$	Undrained strength at critical state
$s_{u,p}/p'_0$	Peak undrained strength ratio
$s_{u,c}/p'_0$	Critical undrained strength ratio
TSF	Tailings storage facility
TSP	Total stress path
t_{50}	Time for 50% dissipation
u	Porewater pressure
v	Specific volume
w	Water content
w_{opt}	Optimum water content
Γ	Specific volume/void ratio of the soil on the critical state line at p’ = 1,0 kPa
γ	Bulk unit weight
γ_d	Dry unit weight

$\gamma_{d,max}$	Maximum dry unit weight
$\gamma_{d,min}$	Minimum dry unit weight
γ_w	Unit weight of water (= 9,81 kN/m³)
ε_1	Axial strain
ε_q	Shear strain
$\dot{\varepsilon_q}$	Shear strain increment invariant
ε_v	Volumetric strain
$\dot{\varepsilon_v}$	Volumetric strain increment invariant
η	Stress ratio
κ	Slope of swelling and recompression line (isotropic recompression index)
λ	Slope of normal compression and critical state lines (isotropic compression index)
λ_{10}	Slope of normal compression and critical state lines on log base 10 (2,303 λ)
ν	Poisson's ratio
σ_1, σ_3	Principal normal stresses
σ'	Normal effective stress
σ_v	Total vertical stress
σ'_v	Effective vertical stress
σ'_{vc}	Past maximum effective vertical stress
$\sigma'_{v,ult.}$	Ultimate effective vertical stress
τ	Shear stress = q/2
φ'_c	Critical state frictional angle
φ'_p	Peak frictional angle
χ_{tc}	State-dilatancy coefficient obtained through triaxial compression tests
ψ	State parameter
ψ_D	Dilatancy angle
ψ_p	Peak dilatancy angle

TABLE OF CONTENTS

1 INTRODUCTION

1.1 PROBLEM AND RESEARCH JUSTIFICATION

The Brazilian iron ore reserves represent 19,8% of the worldwide reserves, with a mean iron content of 46,2%, as reported by Jesus and Joaquim (2018). In 2019, the metals' production was approximately 80% of the total value of the minerals produced in Brazil, from which the iron ore production represented 72,9% (BRAZIL, 2020).

In the mining industry, to turn the extracted ore into a marketable product, it must pass through beneficiation. In this process, the material is separated into the product (concentrate) with higher grades of mineral content, and the by-product (tailing). An average of 0,35 metric ton of tailings is generated in 1,0 metric ton of iron ore processing (LUZ e LINS, 2018).

The tailings represent an environmental liability to the mining industry and must be appropriately deposited in a tailings storage facility (TSF). Slurry disposal (in ponds or dams) is the conventional method of tailings deposition adopted since the early years of the mining industry. Because of the massive tonnage of iron ore production in Brazil, which leads to massive tonnage of tailings, large TSFs are required. Therefore, the storage in impoundments requires great containment embankments, that under extensive rainfall events and infrequent, but possible, cyclic loads, demand sophisticated and cautious designs to ensure safety.

The large tonnage of material plus the demanding legislation, especially after the catastrophic collapses of Fundão Dam (2015) – the largest environmental disaster of the country – and Feijão Dam I (2019) – that killed hundreds of people –, have been making mining companies in Brazil search for more sustainable and safer alternatives for tailings storage based on a dry iron ore processing production.

The dry stacking of filtered tailings has been studied and gradually implemented by the major companies of the Brazilian mining industry. However, it is worth mentioning that the dry stacking technique is consolidated in an empirically-based knowledge for structures smaller than 100 m high. Besides, to absorb the massive tailings generation, the mining companies intend to develop great dry stacks, which will exceed the limits of the current empirically-based knowledge about the stress states and strengths of this type of structure.

For large stacks, Davies (2011) emphasizes that geomechanical tests able to obtain strength and deformability parameters e.g., the triaxial compression tests, are essential. These tests allow the elaboration of constitutive models capable of analyzing the deformation of the dry stack and its foundation, which can also control the structural performance of the facility. Furthermore, Cristal et al. (2018) affirm that a critical state approach of soil mechanics is necessary to figure out the effect of the moisture content and density variation under higher loads; and comprehend the limitations for deposition rate, stacking heights, and the individual compaction layers thickness.

Thus, this research intends to answer questions about the intrinsic properties of tailings that are beginning to be stored in a dry stack in the Quadrilátero Ferrífero. It aims to understand the material's behavior in different states when changing the degree of compaction, confining pressures, and drainage conditions. It intends to evaluate the impact of the degree of compaction (DC), the confining stresses in the critical state line, and the effect of dilatancy in the soil behavior.

1.2 OBJECTIVES

1.2.1 GENERAL OBJECTIVE

Based on laboratory testing carried out on samples compacted to four different degrees of compaction – 93%, 95%, 97%, and 100% of Proctor maximum dry unit weight –, and consolidated under six different confining pressures – 100 kPa, 200 kPa, 400 kPa, 800 kPa, 1600 kPa, and 1900 kPa –, the main objective of this research is to characterize and evaluate the critical state intrinsic properties, also hydraulic and mechanical behavior of filtered iron ore tailings from a mine located in the Quadrilátero Ferrífero, Brazil.

1.2.2 SPECIFIC OBJECTIVES

The general objective can be broken down into the following specific objectives:

i) To determine the index properties of the studied tailings through particle size distribution tests, specific gravity test, plastic and liquid limit tests, and minimum and maximum void ratios tests.
ii) To identify possible particle crushing in static and dynamic compaction.
iii) To compare field compaction quality-control tests with laboratory tests.

iv) To evaluate the influence of the degree of compaction in the iron ore tailings hydraulic conductivity.

v) To evaluate the one-dimensional and isotropic consolidation behavior of the tailings under different degrees of compaction and confining stresses.

vi) To evaluate the effect of soil suction on the tailing's compressibility.

vii) To evaluate the influence of the compaction in the iron ore tailings behavior when sheared.

viii) To evaluate the influence of the confining pressure in the iron ore tailings behavior when sheared.

ix) To determine the critical state line (CSL) of the studied tailings and evaluate its evolution with the degree of compaction.

x) To determine the state conditions of the tailings in each degree of compaction.

xi) To compare the state parameters obtained in the triaxial tests with the state parameters obtained *in situ*.

xii) To determine the critical state intrinsic property parameters and behavior parameters of the iron ore tailings.

xiii) To determine the elastic and plastic moduli of the iron ore tailings.

2 LITERATURE REVIEW

2.1 AN OVERVIEW OF IRON ORE MINING AND PROCESSING IN BRAZIL

The iron ore reserves worldwide are estimated to be about 170 billion metric tons. The Brazilian iron ore reserves represent 19,8% of this total with a mean iron content of 46,2%, as reported by Jesus and Joaquim (2018).

As it is displayed in Figure 2.1, Brazilian iron ore production increases every year. Moreover, according to Brazil (2020), in 2019, metals' production was approximately 80% of the total value of minerals' production, from which the iron ore production represented 72,9%.

Figure 2.1 – Historical Brazilian and Global Iron Ore Production.

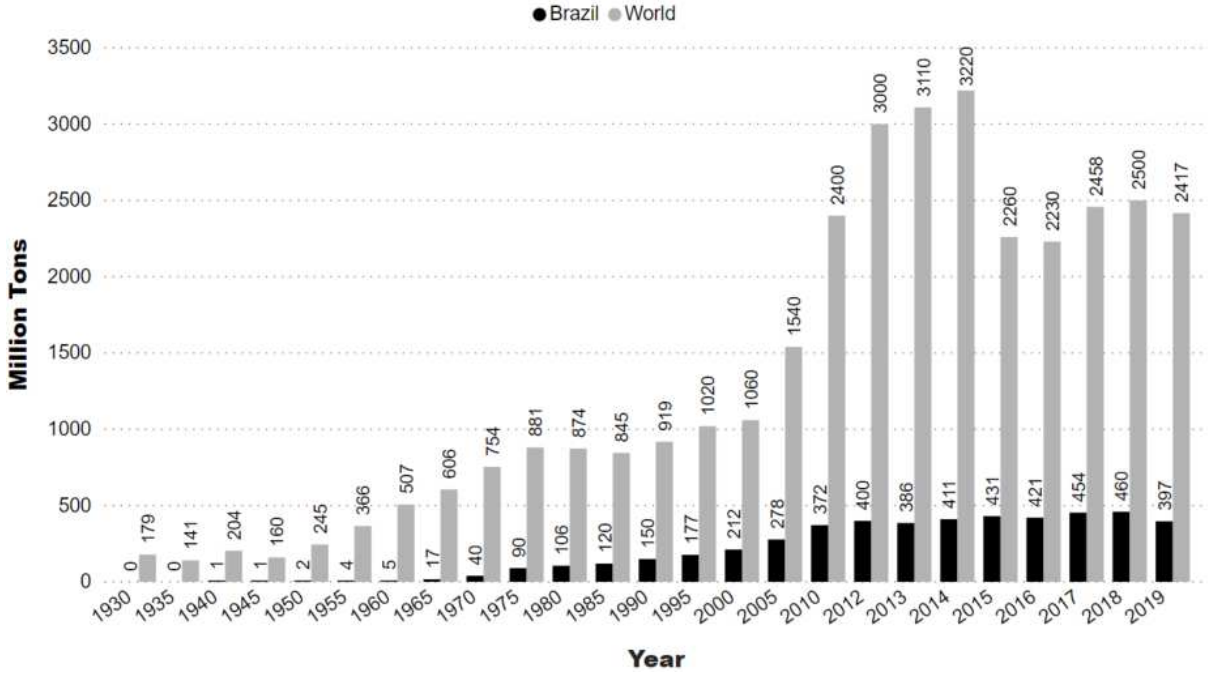

Source: adapted from Brazil, 2020.

Nowadays the Brazilian iron ore production is concentrated principally in the states of Pará (Carajás) and Minas Gerais (Quadrilátero Ferrífero). In 2019, the iron ore commercial production of the state of Pará was R$ 48,3 billion (51,5%), and the commercial production of the state of Minas Gerais was R$ 44,7 billion (47,7%), from a total national production of R$ 93,8 billion, as stated in the Brazilian Mineral Yearbook of 2020 (BRAZIL, 2020).

In the mining industry, the ore passes through beneficiation (or processing) to obtain higher-grade products and improve the economic value of extracted minerals.

The ore beneficiation, as stated in Luz and Lins (2018), consists of operations applied to the materials to modify its particle size distribution and mineral content without changing its physics and chemistry. Figure 2.2 presents the usual mining process flowchart with water recirculation.

Figure 2.2 – Usual mining process flowchart.

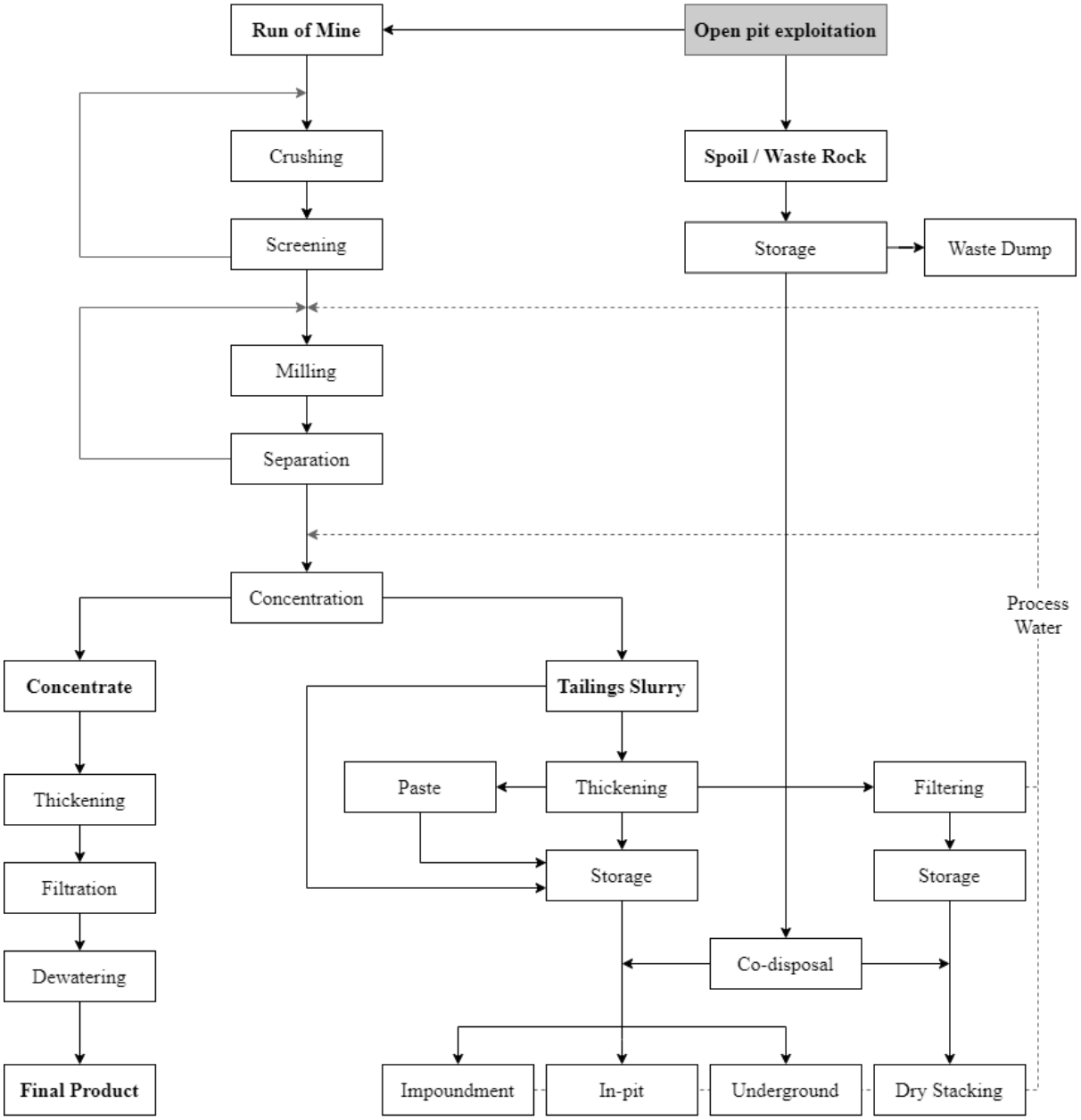

Source: adapted from Luz and Lins, 2018.

As shown in the flowchart, after the concentration process, the material is separated into the product (concentrate) and the by-product (tailing). In line with Luz and Lins (2018), an average of 0,35 metric ton of tailings is generated in 1,0 metric ton of iron ore processing. However, it

is noteworthy that the quantity of tailings generated in the ore processing varies from each beneficiation plant depending on the ore content of the extracted material.

Iron ore tailings usually are inert fine-grained silty-sandy materials composed mainly of quartz and iron minerals (hematite, goethite, and magnetite), as presented by Tolentino (2010), Huang et al. (2013), Dauce et al. (2018), Pires et al. (2019) and others.

Like any other kind of waste, tailings represent an environmental liability to the mining industry. Therefore, they must be appropriately deposited in a tailings storage facility (TSF). These TSFs are usually pounds and dams, decommissioned open pits, underground caves, or dry stacks. Moreover, the disposal methods include slurry disposal, thickened and paste disposal, filtered disposal (dry stacking), and co-disposal (Figure 2.2).

Slurry tailings are in a fluidized state and are a dissociating mass pumped to the TSF through pipelines, the conventional disposal system (DAVIES and RICE, 2001). The slurry can be discharged adopting subaqueous or subaerial methods and it may be from a single spigot or multiple points (DIXON-HARDY and ENGELS, 2007).

Thickened tailings are partially dewatered and have a higher solids content by weight than the slurry tailings but is still a pumpable semiliquid mixture. Chemical additives might be used to enhance the tailings thickening (DAVIES and RICE, 2001). As shown in Figure 2.2, the tailings thickening in the beneficiation plant enables the water process to be recycled, which reduces raw water demand and the amount of water discharged in the TSFs. Consequently, it lowers the water level of the impoundments decreasing seepage and evaporation losses; also, the risks of overtopping, piping, and liquefaction (AUSTRALIA, 2016).

In line with Davies and Rice (2001), paste tailings are thickened with some on-line chemical modifications, generally hydrating agents, that grant even further dewatering. Therefore, it results in little or no bleed water on displacement, and higher slope angle on discharge when compared with thickened tailings.

Davies et al. (2010) state that thickened and pastes tailings have mainly non-technical differences. These non-technical differences may include the type of dewatering facilities and process aids and the type of the tailings' transportation (positive displacement pumps, conveyors, or trucks).

Tailings can be filtered under vacuum or pressure (more common). After filtration, due to its reduced water content, the filter cake must be transported by conveyor or truck to the TSF, where it is placed, spread, and compacted to ideally form an unsaturated and stable dry stack (DAVIES, 2011).

As shown in the dewatering continuum presented in Figure 2.3, when tailings are dewatered, there is a decrease in the water content and an increase in the effective solids content that implies higher effective stresses, consequently higher internal resistance in the material. Figure 2.3 also shows the main changes in the beneficiation process and tailings disposal with the increase in dewatering efficiency.

Figure 2.3 – Tailings continuum.

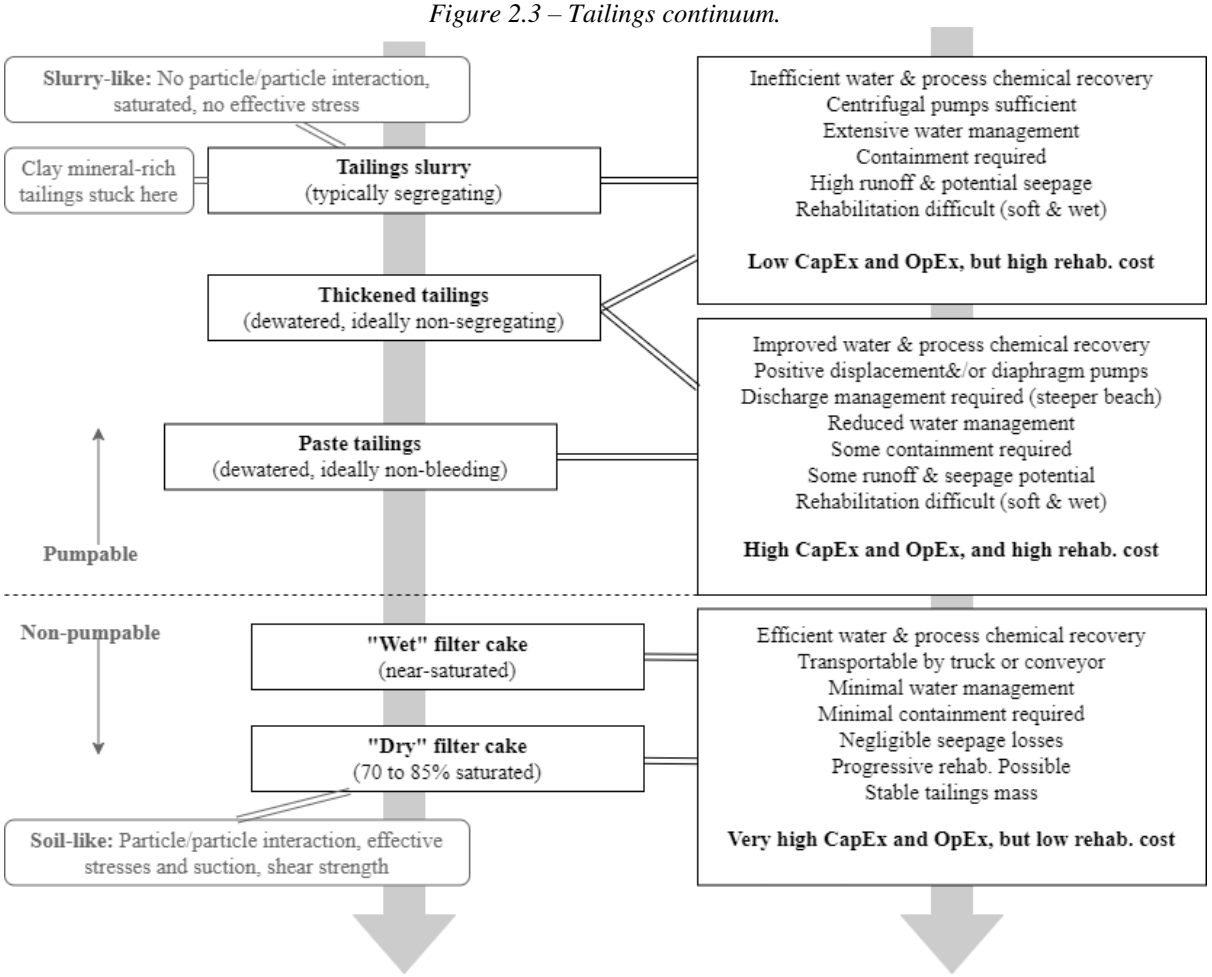

Source: adapted from Australia, 2016.

Co-disposal is the combined disposal of dewatered tailings (fine-grained mine waste) with coarser materials (spoil/waste rock). The mixture of the two materials results in more stable deposits since the fine-grained waste fills the void space between the coarse wastes. In addition, the mixed material requires lower disposal area than the separated disposal of the two waste

streams, which reduces its footprint. The major concern of the co-disposal is finding an economic, efficient and secure method of blending the materials (AUSTRALIA, 2016).

Slurry disposal is the conventional method adopted since the early years of the mining industry. From the methods displayed above, it is the only one that does not present a dewatering step in the tailings' generation process. Thus, as presented by Davies (2011), with the emergence of cheaper technologies for tailings dewatering, the major mining districts worldwide are changing their beneficiations for more water-efficient processes. It is happening for different reasons, but the fundamental objective is to diminish water losses/water consumption. Figure 2.4 presents the word's trend in using dewatering techniques that shows thickened disposal as the most adopted, followed by filtered disposal.

Figure 2.4 – Trends in use of dewatered tailings in mining.

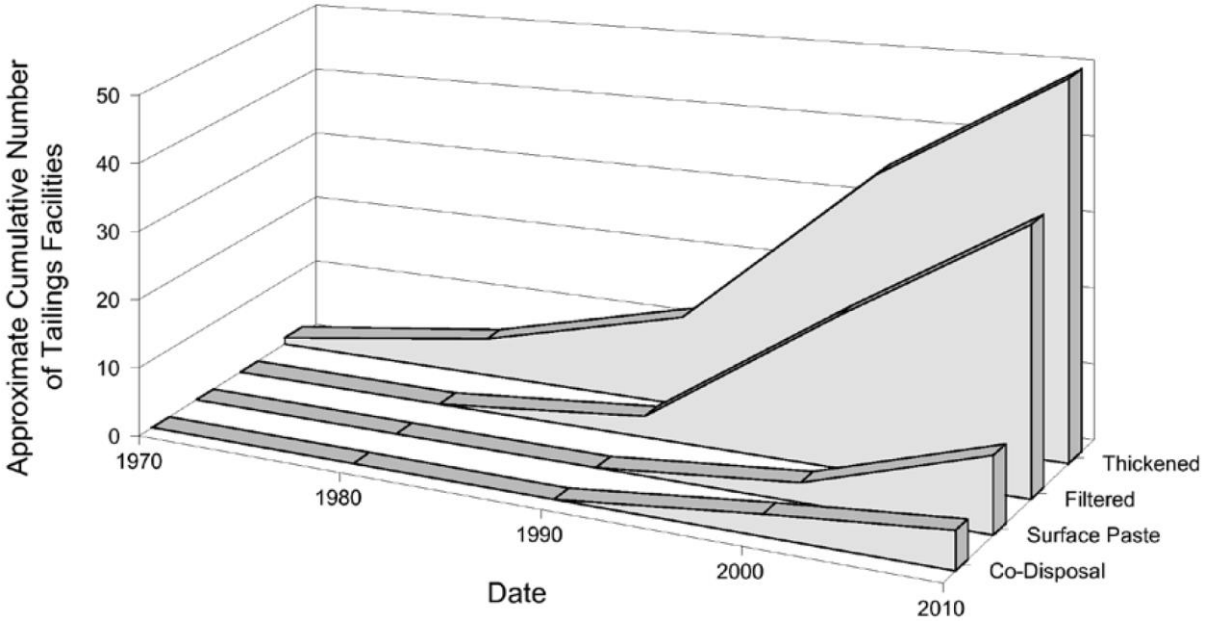

Source: DAVIES et al., 2010.

The massive tonnage of iron ore production in Brazil and, consequently, the large tonnage of tailings generated in the beneficiation, results in larger TSFs. Moreover, the deposition in impoundments requires larger containment embankments that, under extensive rainfall events and infrequent, but possible, cyclic loads, demand sophisticated and cautious designs to ensure safety.

This large tonnage of material plus the demanding legislation, especially after the catastrophic collapses of Fundão Dam (2015) – the largest environmental disaster of the country – and Feijão

Dam I (2019) – that killed hundreds of people –, have been making the mining companies in Brazil search ways of shifting their facilities for a dry iron ore processing production.

Vale S.A. represents 71,9% of all iron ore commercial production in Brazil (BRAZIL, 2020) and, according to Vale S.A. (2020), in the last ten years, they have invested about R$ 66 billion in the development of technologies and facilities for dry iron ore processing production. They intend to achieve the goal of 100% of the production of the state of Pará and 70% of their total iron ore production in Brazil through dry processing until 2024. Furthermore, since 2017, CSN, the second largest exporter of iron ore in Brazil, has been adapting its facilities to dry processing, and nowadays, using industrial filter presses, 100% of the tailings generated in their main mine, Casa de Pedra, are filtered (CSN, 2020).

2.2 FILTERED DRY STACKED TAILINGS

Dry stacking is a stable way of storing tailings in an unsaturated and dense solid state. As stated by Davies et al. (2010) and Davies (2011), this method of disposal is attractive in facilities where: economic recovery is enhanced by the method, water conservation is an important matter (arid regions), water treatment is difficult (cold regions); or high seismicity, topography and/or limited available deposition area makes the conventional impoundments unfeasible.

Notice that most parts of Brazil do not present any of the restrictions listed above, yet mine companies are investing in infiltration techniques. The explanation for this comes with the regulatory attraction associated with the smaller footprint of dry stacks compared with the conventional disposal methods, lower long-term liability concerning structural integrity, and its progressive closure and reclaim (DAVIES et al., 2010; HORE and LUPPNOW, 2014).

As stated by Davies (2011), it is essential to define the moisture retention, moisture-density relationship, geotechnical and hydraulic conductivity characteristics of the tailings for any tailings stack project. Therefore, tests may be run to verify the material's variability and determine the in-situ characteristics expected.

Davies (2011) presents a test program including tests to evaluate operational aspects such as the vendor engagements with filtration and transportation, and filters efficiency; also, material's properties, such as tailings gradation and mineralogy, moisture-density tests like the standard Proctor, geochemical tests, variable moisture tests, and field compaction trial.

For large stacks, Davies (2011) emphasizes that geomechanical tests, like the triaxial compression tests, are essential to obtain strength and deformability parameters. These tests allow the elaboration of constitutive models capable of analyzing the deformation of the dry stack and its foundation that can also control the structural performance of the facility. In addition, Lupo and Hall (2010) state that testing over a range of moisture contents and void ratios is necessary to evaluate the variability of the material that will be deposited in the dry stack.

Furthermore, Crystal et al. (2018) state that stacks higher than 100 m exceeds the limits of the empirically based knowledge currently existent about the stress states and strengths of this type of structure. Therefore, a critical state approach of soil mechanics is necessary to figure out the effect of the moisture content and density variation under higher loads, also comprehend the limitations for deposition rate, stacking heights, and the individual lift thickness.

As it will be explored in subchapter 2.3, loose materials contract and dense materials dilate under shear stresses, also loose materials tend to present excessive deformation and strength loss while dense materials tend to present resistance gain and higher yield stresses due to the interlocked grains. Thus, to avoid the contractive behavior, mechanical compaction of the individual rases is necessary. According to Crystal et al. (2018), the lift thickness must not exceed 0,2 m to 0,3 m, as in conventional compacted earthworks. In addition, Davies (2011) states that lifts must be compacted at Standard Proctor optimum moisture content (1 to 2% under, for wetter climates, and 1% over, for extremely dry climates) and for higher stacks, the Modified Proctor optimum moisture content may be more adequate.

Nevertheless, it is known that consolidated under high confining pressures, with effective stresses exceeding the pre-consolidation value, even soils in an initial dense condition tend to present contractive behavior. Moreover, under high confining pressures, the soil may lose cementation (if existent), particles breakage and polishing of particle surfaces in coarse materials and increase of face-to-face orientation of particles in fine materials may occur, resulting in a large tendency for volume decrease (TERZAGHI et al., 1996). Therefore, even with compaction control, it is necessary to identify the height limits through the geomechanical tests to avoid contractive behavior in the lower portions of the stack.

Only some unique tailings containing expressive amounts of process chemicals, like gypsum, are not filterable, so the main concern in tailings filtration is the efficiency to reach the desired

filter cake moisture content necessary to dry stacking (CRYSTAL et al., 2018). This efficiency depends on the filtering technology, the variability of the tailings' physical characteristics, and the daily production/filtration rate (DAVIES, 2011; CRYSTAL et al., 2018).

Thus, if not properly controlled with moisture measurements, the material can be deposited in a loose and high-moisture state. Moreover, as shown in Figure 2.5, increasing the compaction energy (e.g., Modified Proctor energy), consequently increasing the dry density of the material, the saturation ratio will also increase for the same target moisture content (TRINDADE et al. 2008). What draws the attention for the fact that, for high dry stacks, when increasing the energy of compaction, if it does not decrease the target moisture content of the filtration, the material will likely behave as saturated, and at high confining pressures, it may demonstrate contractive behavior.

Figure 2.5 – Dry density vs. saturation ratio for given moisture contents.

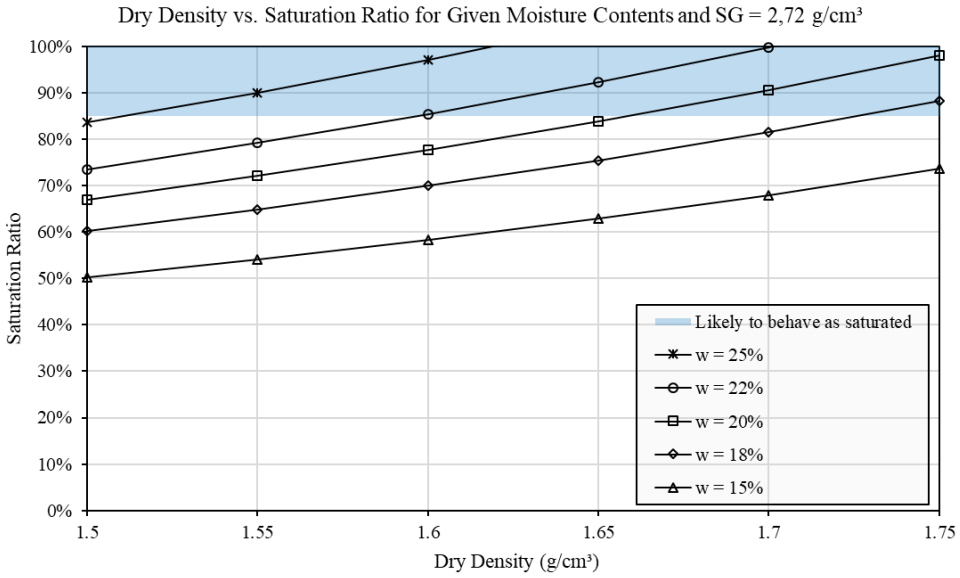

Source: adapted from Crystal et al., 2018.

Moreover, Lupo and Hall (2010) mention the importance of doing compressibility tests to investigate whether the tailings are highly compressible or not. With the stacking process, the material is gradually loaded and, if compressible, it may reduce its void ratio, increasing its dry density and saturation. The higher the stack is, the higher is the loading in the inferior layers, and more likely this process is to happen.

As stated by Lupo and Hall (2010), compacted tailings in a dry stack usually present low hydraulic conductivity. Therefore, portions of the stack becoming or standing saturated can result in porewater pressure increase and mobilization of only the undrained resistance of the

material, possibly combined with a strength reduction component likewise seismic and static liquefaction (CRYSTAL et al., 2018). This means that not only the moisture content of the material after filtration is a concern, but also the lifting rate and water infiltration.

The lifting rates must be slow enough to allow excessive pore pressures to dissipate and for drainage and consolidation to occur. Identifying zones with high moisture contents is essential to reduce the lifting rate to allow excessive pore pressures to dissipate. For this, it is fundamental to have adequate field instrumentation and monitoring system to certify the dissipation of pore pressures (CRYSTAL et al., 2018).

As mentioned above, after consecutive lifts, the basal zone of a stack may become saturated, especially if the structure is susceptible to water infiltration. Therefore, dry stacks must be placed in areas neither with a convergence of water runoff nor groundwater discharge, except if a well-designed underdrainage system is built (DAVIES, 2011). When placed out of natural water incidence, the biggest concern will be minimizing the effects of rainfall incidence and infiltration through adopting a proper superficial drainage system. Nevertheless, risks and uncertainties may be extenuated with instrumentation and monitoring for both infiltration and seepage (CRYSTAL et al., 2018).

2.3 CRITICAL STATE SOIL MECHANICS

2.3.1 ISOTROPIC COMPRESSION AND SWELLING

Any change in the effective stress state of soils results in rearrangement of grains and volume change that culminate in swelling or compression of the medium. As loose soils have more free space to the particles rearrange themselves, stiffness increases from the loose state to the dense state (ATKINSON, 2007).

Figure 2.6 illustrates the isotropic compression and unloading and reloading curves of a soil in (p', v) and (ln p', v) spaces. The first space shows the non-linearity of the bulk stiffness behavior for both first the loading curve (O, A, C, D), also called normal compression line (NCL), and the unloading and reloading (A, B, C) curves. The second space presents the linearization by the logarithmic scale of both the NCL and unloading and reloading curves, which are considered the same curve, called swelling line, even though they are not coincident.

The NCL and the swelling line are given by Equation 2.1 and Equation 2.2, respectively. Where λ is the gradient of NCL, κ is the gradient of the swelling line, N and v_κ are the specific volumes of each curve referent to $p' = 1\text{kPa}$, and λ, κ, and N are intrinsic parameters of the soil. Note that the swelling line presents a smaller gradient than the normal compression line. It happens because of the plastic strains, so irreversible strains, caused by the rearrangement of particles in the first loading.

Figure 2.6 – Isotropic consolidation and swelling lines.

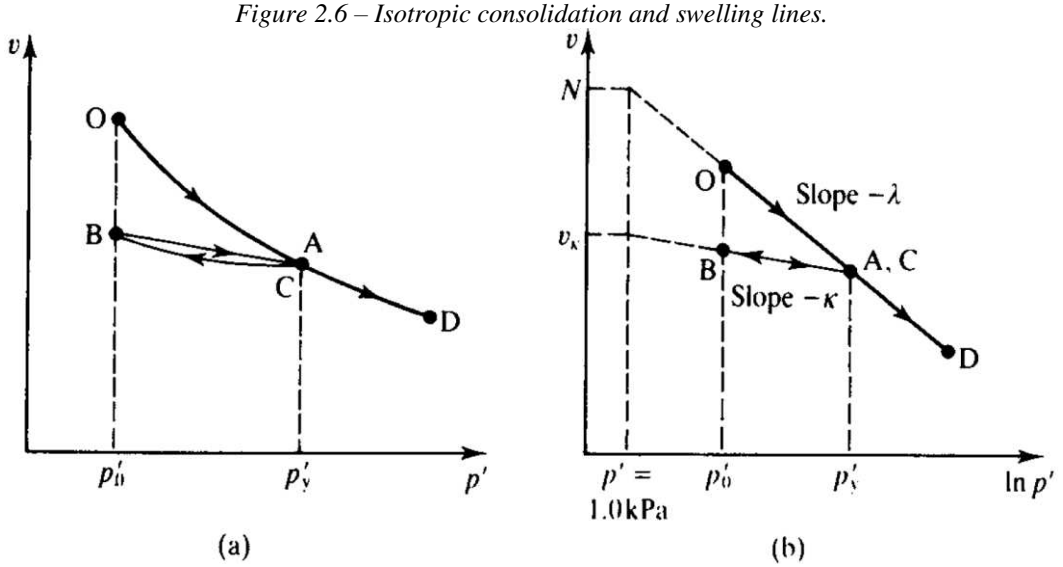

Source: Atkinson, 2007.

$$v = N - \lambda \cdot \ln p' \qquad \text{Equation 2.1}$$

$$v = v_\kappa - \kappa \cdot \ln p' \qquad \text{Equation 2.2}$$

Where,

$$v = 1 + e \qquad \text{Equation 2.3}$$

$$p' = \frac{\sigma_1' + 2\sigma_3'}{3} \qquad \text{Equation 2.4}$$

Fundamentally, the NCL is a frontier between possible and impossible states for isotropic compression since the soil can reach any point below the NCL, by unloading; but cannot reach the region above the NCL (ATKINSON, 2007). At any point below the normal compression line, the soil is overconsolidated, and the over consolidation ratio is given by Equation 2.5; where p'_m is the maximum stress state through which the soil has been, and p'_0 is the current stress state of the soil.

$$OCR = \frac{p'_m}{p'_0} \qquad \text{Equation 2.5}$$

Figure 2.7 illustrates two points, N_1 and R_2, that have the same stress state but will present different behaviors because R_2 is way stiffer than N_1. Nonetheless, R_1 and R_2, under different stress states, but with the same over consolidation ratio, are likely to behave in the same way. In addition, the line that passes through R1 and R2 contain all soils with the same OCR and it is parallel to the NCL.

Notice that the normal consolidation line is not unique, and its position might change due to soil structure, which is affected by layering, bonding, water salinity, oxidation, and other effects.

Figure 2.7 – Schematic representation of soils with same OCR.

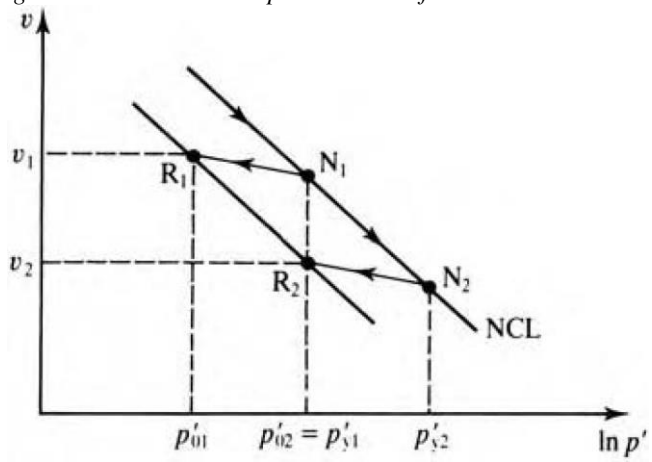

Source: Atkinson, 2007.

2.3.2 CRITICAL STATE

Starting from the words used by Casagrande (1938) and Taylor (1948) concerning drained and undrained tests, respectively, Roscoe et al. (1958) introduced the concepts of critical state and critical state line (CSL). According to them, the critical state would be an ultimate state where, under drained conditions, the material would have no change of void ratio with a further increment of shear stress; and under undrained conditions, so constant void ratio, the effective stress would change to bring the material to it.

Moreover, Roscoe et al. (1958) added that to reach the critical state, the soil should be submitted to high shearing strains (higher to 10%) until achieving the condition of keep distorting at constant stresses and void ratio. Additionally, in line with Schofield and Wroth (1968), in the

critical state, the soil would behave as a frictional fluid presenting only frictional resistance just like normally consolidated soils.

As shown in Figure 2.8, Roscoe et al. (1958) then defined the critical state line in the (p', q, v) space by Equation 2.6 and Equation 2.7, as a particular locus to which all loading paths assemble.

Figure 2.8 – Critical state line defined in the space p', q, v.

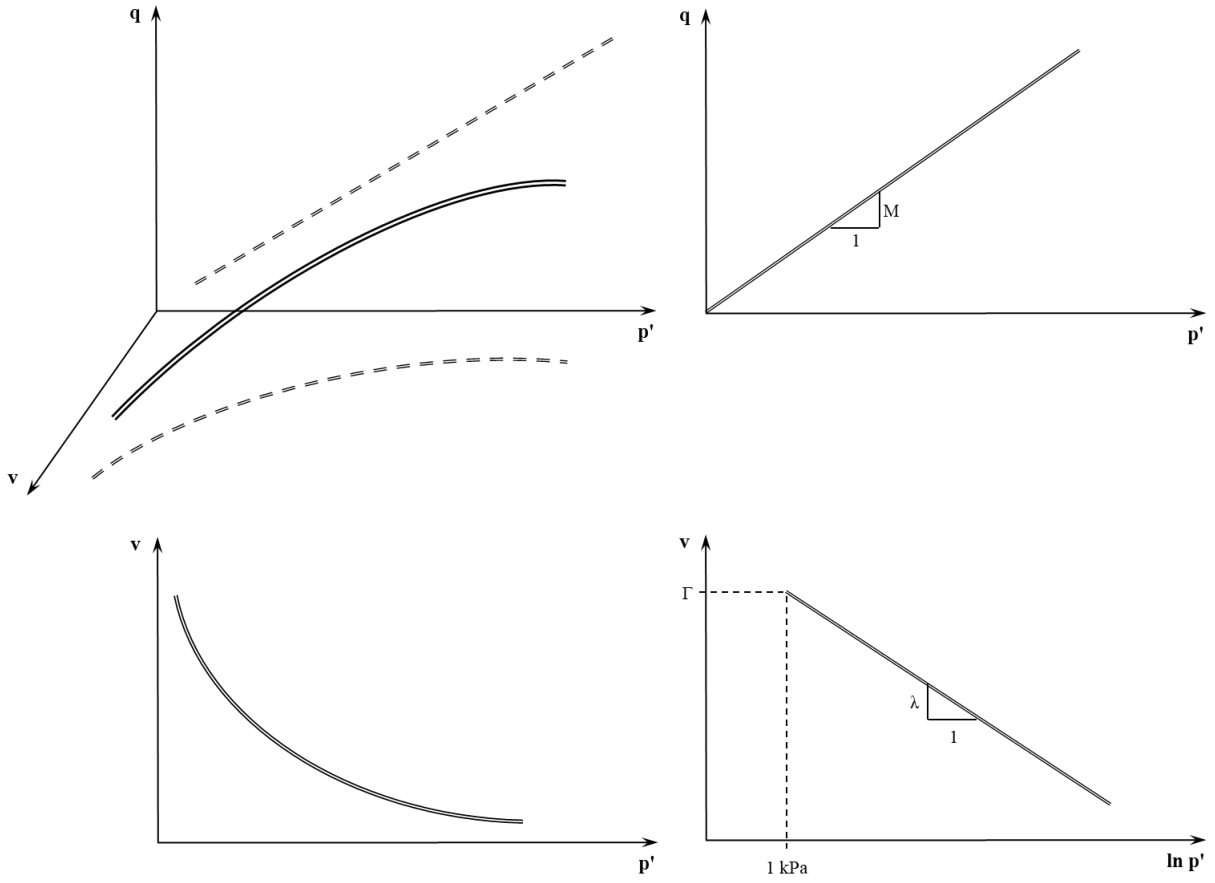

Source: elaborated by the author.

$$v = \Gamma - \lambda \cdot \ln p' \qquad \text{Equation 2.6}$$

$$q = M \cdot p' \qquad \text{Equation 2.7}$$

Where,

$$q = \sigma_1' - \sigma_3' \qquad \text{Equation 2.8}$$

According to Schofield and Wroth (1968), Equation 2.6 postulates that the specific volume decreases as the effective stresses increase, and Equation 2.7 determines the deviatoric stress

necessary to reach the critical state, which is a function of the critical friction angle (φ'_c) or the critical shear stress ratio (M). Thus, the critical state theory integrates volumetric change with shear strength (KNAPPETT and CRAIG, 2012).

The constants φ'_c, M, Γ, and λ are intrinsic soil properties regardless of initial stress-state conditions and soil structure. M can be correlated to the critical state frictional angle, as given by Equation 2.9 and Equation 2.10 for triaxial compression and triaxial extension, respectively. Moreover, Γ is correlated somewhat with the maximum void ratio (JEFFERIES and BEEN, 2015), and it is possible to affirm that the slope of the CSL (λ) is the same as the normal compression line (NCL), which means that both lines are parallel and in any point of the CSL the soil will have the same overconsolidation ratio.

$$M_{tc} = \frac{6 \cdot \sin \varphi'_c}{3 - \sin \varphi'_c} \qquad \text{Equation 2.9}$$

$$M_{te} = \frac{6 \cdot \sin \varphi'_c}{3 + \sin \varphi'_c} \qquad \text{Equation 2.10}$$

The critical state line or critical state locus is the relationship between the critical void ratio and the mean effective stress. It is singular and independent of test or field conditions; or stress paths followed to achieve the critical state. Thus, it can be used as a reference condition for soil behavior (Been, 1999).

It is worth mentioning that the correlation between the critical specific volume and critical mean effective stress is not necessarily a logarithm equation. A power law equation may also be used to better fit critical state lines with higher curvatures (see Equation 2.11). According to Been (1999), the critical state line suffers a significant impact of fines content. Soils with a significant amount of silt on their composition (silty sands, sandy silts, and silts) show high compressibility at low confining pressures. Consequently, the CSL of these types of soils tends to be steeper and have greater curvature than typical silica sands. The same behavior is verified on crushable sands.

$$v = A - B \cdot \left(\frac{p'}{p'_{ref}}\right)^C \qquad \text{Equation 2.11}$$

Where, A, B and C are constants.

Jefferies and Been (2015) state that the silts content alone is not a good indicator of the CSL's shape, since well-graded silty sands might behave just as clean silica sands. Furthermore, the increase in silts content increases the soil compressibility until a certain point. Soils with high silts content where the particles fulfill the interstitial space between sand grains also tend to behave as clean silica sands. Thus, besides the fines content, grain size distribution, mineralogy, grain shape, and surface roughness of the grains also affect CSL's shape.

As presented by Atkinson (2007), the critical state not only represents the ultimate state to which the soils under shear stress converge, but also is the locus that separates the heavily overconsolidated clays and dense sands (OCR > 3) from the normally consolidated or lightly overconsolidated clays and loose sands (OCR < 2).

The overconsolidated soils are located under the critical state line in the so-called *dry side* since overconsolidated soils tend to dilate under shearing stresses, absorbing water when drained and generating negative pore pressures when undrained. Meanwhile, lightly overconsolidated soils are comprehended between the critical state line and the normal compression line in the *wet side*, where soils tend to contract under shearing stresses, exuding water when drained and generating positive pore pressures when undrained (SCHOFIELD and WROTH, 1968).

Figure 2.9 – Soil behavior during shearing.

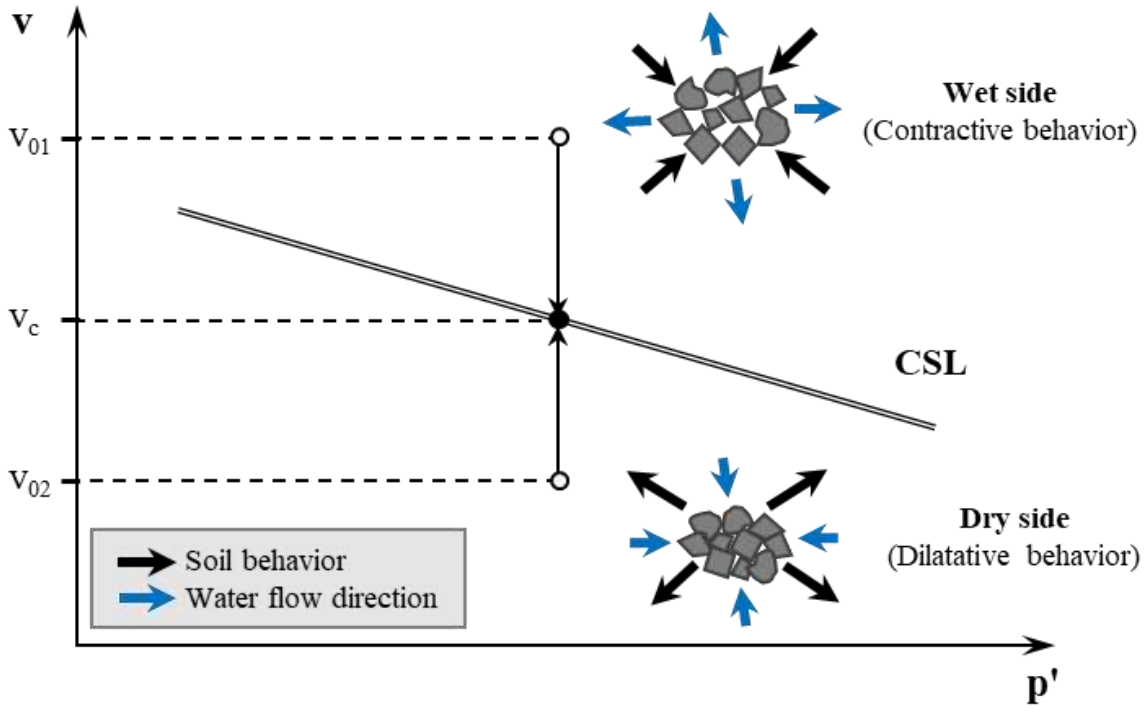

Source: elaborated by the author.

Independently whether the soil is in the wet side or the dry side, as presented in Figure 2.9, at the ultimate state it will converge to the same stress state and volume.

2.3.3 STATE PARAMETER

Although the critical state is independent of the initial stress state and volume conditions, the soil behavior under shearing is completely dependent on its initial position (state) relative to the critical state line. Successively, the initial position is dependent on the stress state and void ratio (Maranha das Neves, 2016). Thus, to identify this initial state and predict soil behavior until reaching the critical state, it was developed the concept of state parameter, which is the difference between the initial void ratio and the void ratio at the critical state (Been, 1999), as presented in Equation 2.12**.**

$$\psi = v - v_c = e - e_c \qquad \text{Equation 2.12}$$

From Equation 2.12, positive state parameters indicate materials with a contractive behavior while negative state parameters indicate materials with a dilatant behavior, as illustrated in Figure 2.10.

Figure 2.10 – Soil behavior and state parameter.

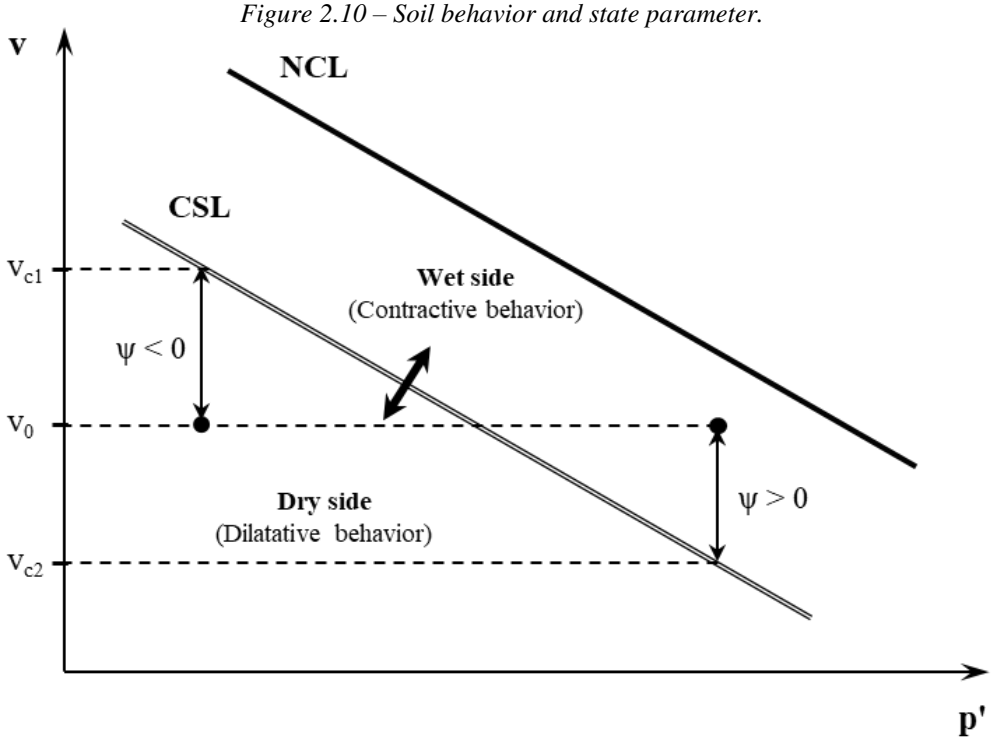

Source: elaborated by the author.

2.3.3.1 CPTu Test

According to Jefferies and Been (2015), when referring to granular soil sampling, there is no such thing as undisturbed samples. Even when adopting freezing techniques there is no guarantee that sampling will not generate minute strains, dilation, or contraction of the material. Moreover, reconstituted samples do not recreate the exact field state and fabric.

On the other hand, in-situ tests only measure the soil reaction to an applied disturbance, from which the soil properties are calculated. Field tests do not determine any parameter directly; thus, standards are necessary to assure the tests' accuracy. Laboratory tests must then be used to identify the intrinsic characteristics of the materials and to create the database for determining the in-situ state and properties through field tests (JEFFERIES and BEEN, 2015).

Therefore, the ideal campaign of investigation must be composed of field and laboratory tests wherein the soil intrinsic properties and behavior, such as the critical state parameters and soil indexes, should be determined by laboratory tests, while in-situ state and other parameters not measurable in the laboratory should be determined by field tests (JEFFERIES and BEEN, 2015).

Having three data channels: cone tip resistance, sleeve friction, and pore pressure, the CPTu test can identify the hydraulic and mechanical behavior of soil layers up to 5 cm tick. The continuous data recording gives considerable data density with exceptional repeatability and accuracy, penetration resistance accuracy better than 2% (JEFFERIES and BEEN, 2015), which provides the appropriate basis for the determination of state-parameter in-situ.

Jefferies and Been (2015) show that the cone resistance depends on the in-situ stress level, which in turn depends on the material density. In other words, cone resistance can be directly associated with the state parameter, and over the years a few methodologies have been developed to estimate the state parameter from the tip cone resistance.

Plewes et al. (1992) have presented a methodology to estimate the in-situ state parameter based on the CPTu test results that allows to calibrate the equations by inputting the critical state parameters obtained through laboratory tests.

$$\psi = -\frac{\ln\left(\frac{\overline{Q_p}}{\overline{k}}\right)}{\overline{m}} \qquad \text{Equation 2.13}$$

Where,

$$\overline{Q_p} = Q_p \cdot (1 - B_q) \quad \text{Equation 2.14}$$

$$\bar{k} = \left(3 + \frac{0,85}{\lambda_{10}}\right) \cdot M_{tc} \quad \text{Equation 2.15}$$

$$\bar{m} = 11,9 + 13,3\lambda_{10} \quad \text{Equation 2.16}$$

$$B_q = \frac{u - u_0}{q_t - \sigma'_{v_0}} \quad \text{Equation 2.17}$$

And,

$$Q_p = \frac{(q_t - p)}{p'} = \frac{3Q_t}{(1 + 2K_0)} \quad \text{Equation 2.18}$$

$$Q_t = \frac{(q_t - \sigma_v)}{\sigma'_v} \quad \text{Equation 2.19}$$

Robertson (2010) has also developed a methodology to estimate the in-situ state parameter based on the CPTu test results. In a simplified manner, the author correlated the state parameter with the clean sand equivalent normalized cone resistance ($Q_{tn,cs}$). This correlation is presented in Equation 2.20.

$$\psi = 0,56 - 0,33 \cdot \log(Q_{tn,cs}) \quad \text{Equation 2.20}$$

Where,

$$Q_{tn,cs} = K_c \cdot Q_{tn} \quad \text{Equation 2.21}$$

$$Q_{tn} = \left(\frac{q_t - \sigma_v}{p_a}\right) \cdot \left(\frac{p_a}{\sigma'_v}\right)^n \quad \text{Equation 2.22}$$

And,

$K_c = 1,0$; if $I_c \leq 1,64$ Equation 2.23

$K_c = 5,581\, I_c^3 - 0,403\, I_c^4 - 21,63\, I_c^2 + 33,75\, I_c - 17,88$; if $I_c > 1,64$ Equation 2.24

$$n = 0{,}381\ I_c + 0{,}05\left(\frac{\sigma'_{v_0}}{p_a}\right) - 0{,}15; \text{ and } n \leq 1{,}0 \qquad \text{Equation 2.25}$$

2.3.4 NORMALIZATION

Although the CSL is unique, the soil behavior before it reaches the critical state is highly dependent on different aspects. Among others, initial specific volume, confining pressures, load path, initial fabric, and strain rate (Been, 1999). Therefore, when analyzing the states before critical, as the peak state, it may be necessary to compare results of tests with different consolidation stresses and initial void ratio, and the normalization of void ratios and stresses becomes handy (ATKINSON, 2007).

Soil states with the same OCR can be normalized by the specific volume for 1 kPa, like points A and A' in Figure 2.11 that can be normalized by v_λ. Furthermore, different states can also be normalized by the referring stress for the same void ratio on the CSL or NCL, e.g., point A can be normalized by p'_c or p'_e in Figure 2.11. However, it is preferable to do the stress normalization using p'_c due to the uniqueness of the critical state line.

Figure 2.11 – Parameters for normalization.

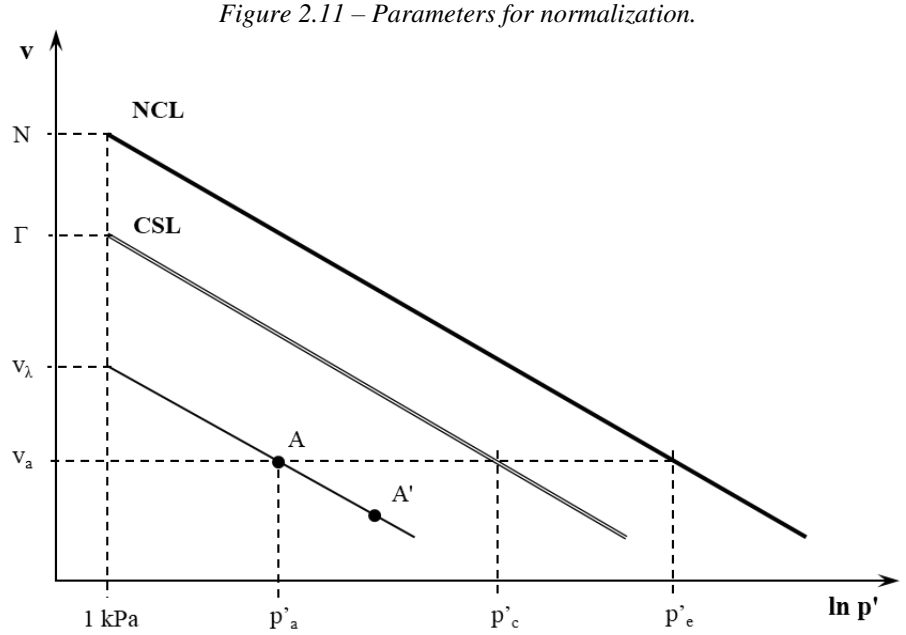

Source: adapted from Maranha das Neves, 2016.

After normalization, either by stress or specific volume, points with the same OCR tend to converge to the same point, as presented in Figure 2.12.

Figure 2.12 – Normalization of normal consolidation and critical state lines by a) stress (p'_c) and b) specific volume (v_λ).

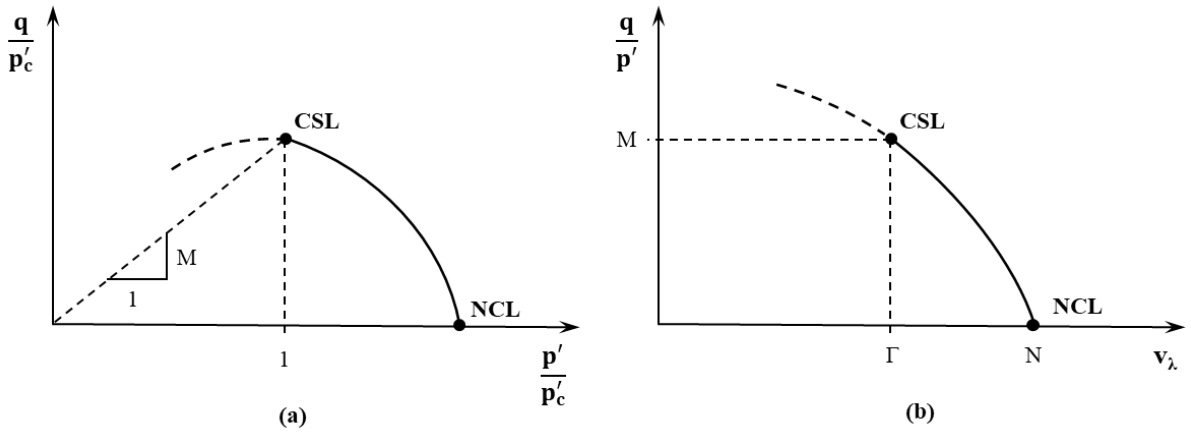

Source: adapted from Maranha das Neves, 2016.

2.3.5 PEAK STRENGTH AND DILATANCY

As presented in 2.3.2, soils located on the wet side of the CSL tend to contract, while soils on the dry side tend to dilate when they are sheared. This tendency to volumetric change during shearing is called dilatancy. According to Maranha das Neves (2016), the dilatancy phenomenon is inseparable from the Critical State Soil Mechanics, and it is fundamental to describe soil behavior.

Under shear stresses, the movement of the particles does not happen entirely in the main shear direction. When under low confining pressure, particles of a dense granular medium move up and over adjacent particles, pushing them away. It results in the expansion of the mass and resistance increment. As the initial void ratio increases, the particles have more free space to dislocate relatively to the others, and the contribution of dilation decreases (TERZAGHI et al., 1996).

Reynolds (1885) was the first to demonstrate that, for a granular medium, at equilibrium the particles are held by stresses transferred through the mass, and there is no change in the relative position of the grains without changing of bulk. Moreover, he has defined dilatancy as the permanent change in volume due to a permanent alteration in the distortional strains.

Taylor (1948) related dilatancy with the shearing strength of granular materials. According to him, the shearing strength was composed of two components: the frictional resistance between grains and the *interlocking*, as he called. Furthermore, the author presented that, in dense sands the interlocking was responsible for a considerable portion of the peak strength, and the

progressive loss of strength after reaching the peak point would be connected to the progressive reduction in interlocking (contribution of dilatancy) as a result of density declining.

From both concepts reviewed above, emerged two different definitions of dilatancy in general literature: the absolute dilatancy, which accounts for the change in volumetric strain acquired from the initial condition; and the rate definition, in which the dilatancy is the ratio of the increment of volume change with the increment of shear strain (JEFFERIES and BEEN, 2015). Figure 2.13 shows the difference between both definitions. Note that the rate definition is more widespread in the technical literature, and it is the basis for the development of the stress-dilatancy theory and the state-dilatancy law, as it follows.

Rowe (1962) formulated the *stress-dilatancy* theory, in which the author associated the mobilized stress ratio during shearing with the plastic strain rates. Equation 2.26 presents the stress-dilatancy theory, in which the stress invariant (η) is a correlation of the critical friction ratio (M_{tc}) with the dilatancy (D), which is described as (…) "the ratio between the two work conjugate strain increment invariants" (JEFFERIES and BEEN, 2015).

Figure 2.13 – Absolute and rate definitions of dilatancy.

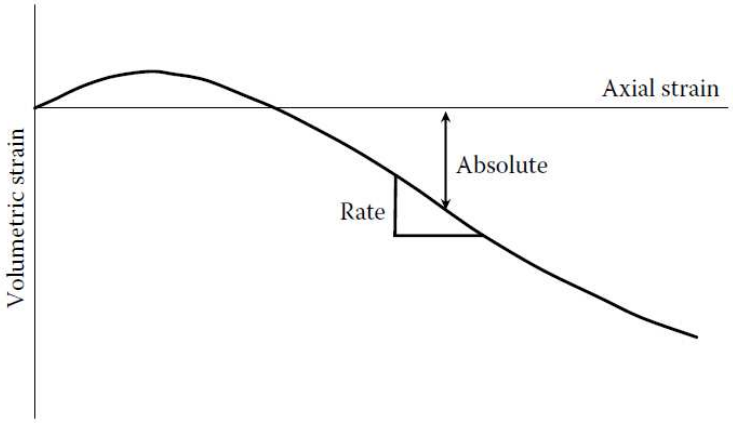

Source: Jefferies and Been (2015).

$$\eta = M_{tc} - D \qquad \text{Equation 2.26}$$

Where,

$$\eta = \frac{q}{p'} \qquad \text{Equation 2.27}$$

$$D = \frac{\dot{\varepsilon_v}}{\dot{\varepsilon_q}} = \frac{\varepsilon_{vn+2} - \varepsilon_{vn-2}}{\varepsilon_{qn+2} - \varepsilon_{qn-2}} \qquad \text{Equation 2.28}$$

And,

$$\varepsilon_v = \frac{\Delta e}{1 + e_i} \qquad \text{Equation 2.29}$$

$$\varepsilon_q = \varepsilon_1 - \frac{\varepsilon_v}{3} \qquad \text{Equation 2.30}$$

Meanwhile, the dilatancy in the critical state is null, the peak strength represented by the maximum shear invariant (η_{max}) is defined when the maximum dilatancy (D_{min}) is developed. It shows that dilatancy is important to identify soil behavior before shearing, mainly in the peak stress state. Note that only heavily overconsolidated soils show positive dilatancy before the critical state (MARANHA DAS NEVES, 2016). η_{max} and D_{min} of drained triaxial tests can be plotted in the stress-dilatancy space, from which it is possible to determine M_{tc} and the volumetric coupling between distortional and mean strain (N) as shown in Figure 2.14 (JEFFERIES and BEEN, 2015).

Figure 2.14 – Example of D_{min} vs. η_{max} plot.

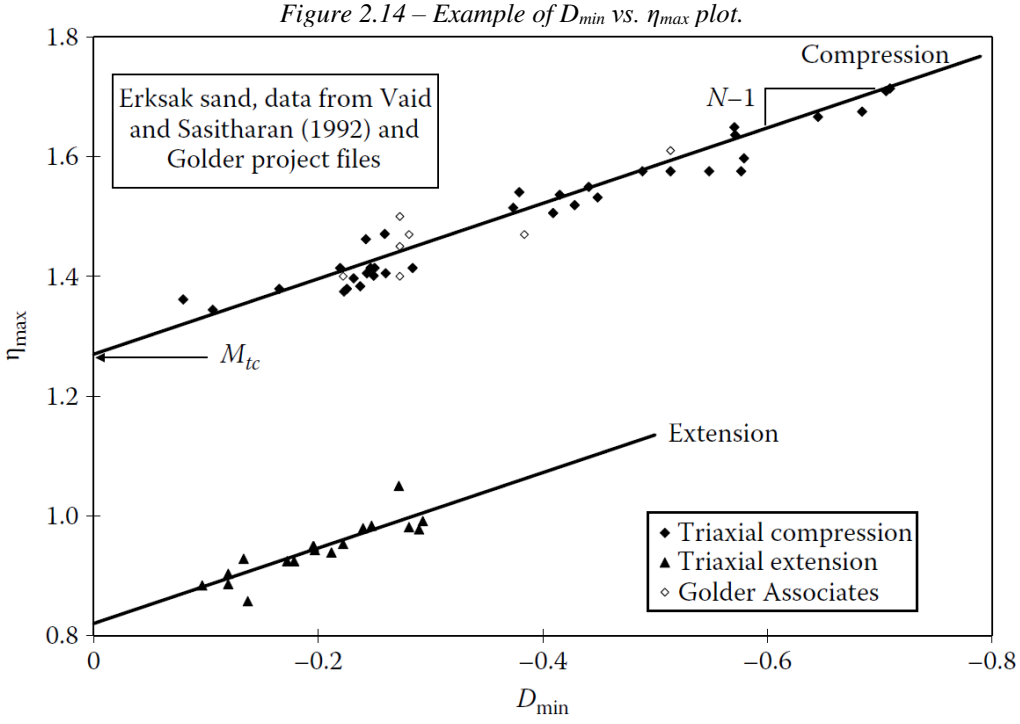

Source: Jefferies and Been (2015).

According to Maranha das Neves (2016), the stress-dilatancy theory describes the behavior of materials with the same OCR. Figure 2.15 demonstrates, based on generic results of a direct shear test, that two samples (B1 e C2) with the same OCR, but different void ratio and initial confining stresses, have their peak state defined by the stress-dilatancy equation (Equation 2.31,

which is analog to Equation 2.26, but defined for direct shear tests instead of triaxial tests) with the same dilatancy, represented in this case by the peak dilatancy angle (ψ_p).

$$\frac{\tau}{\sigma} = tg(\varphi'_c + \psi_D) \qquad \text{Equation 2.31}$$

Still based on Figure 2.15, Atkinson (2007) discusses the importance of contemplating the void ratios additionally to the effective stresses when studying the soil behavior. In line with the author, points B1 and B2, which are under the same normal stress, reach the same critical state (Bc) even though B2 presents a lower void ratio than B1; however, to it happens, B2 must dilate more than B1 because of its lower void ratio.

According to Jefferies and Been (2015), dilation is a kinematic result of the grains geometry and their capability of moving relative to each other. In addition, as presented above, Atkinson (2007) explains that the void ratio at the peak states directly affects the peak strength and maximum dilation. Therefore, to compute the effect of state using maximum dilatancy (D_{min}) and the state parameter (ψ) is more appropriate than using strength parameters, since the first one is associated with the void ratio change and the second one presents void ratio as its input.

Figure 2.15 – Representation of the peak strength of soils with different initial states.

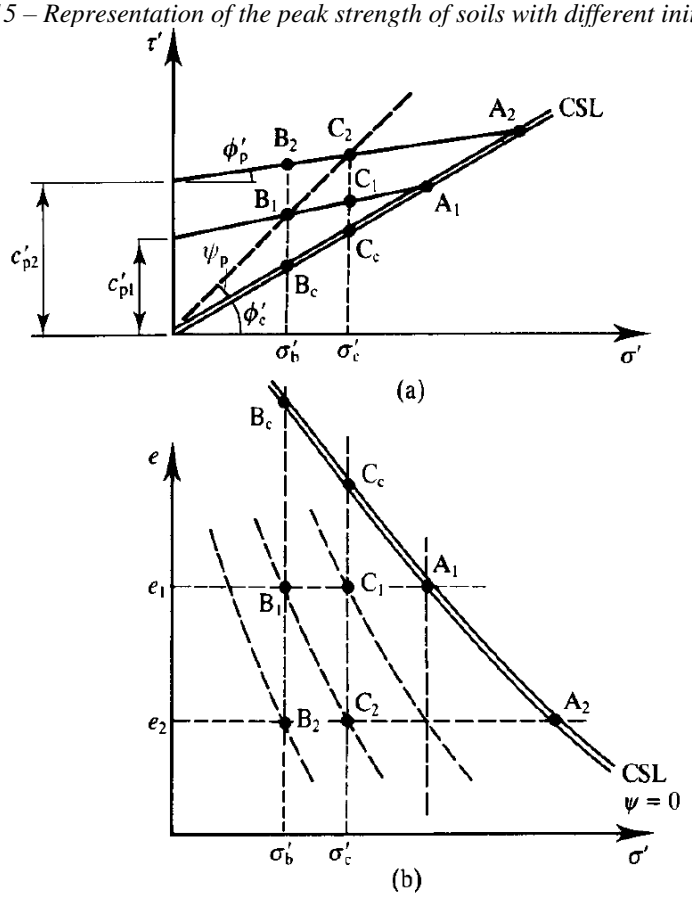

Source: Atkinson, 2007.

Jefferies and Been (2015) state that the maximum dilatancy and the state parameter can be related through a soil property, and it defines a *state-dilatancy* law presented on Equation 2.32, which expands the utility of the critical state soil mechanics.

$$D_{min} = \chi_{tc} \cdot \psi \qquad \text{Equation 2.32}$$

Notice that the maximum dilation is given when the material reaches peak strength, and in this state, there are no elastic strain rates ($D = D^P$). Furthermore, when the state parameter is zero, the maximum dilatancy will also be zero, which represents the critical state (JEFFERIES and BEEN, 2015). This correlation between dilatancy at peak strength (D_{min}) and state parameter (ψ) can be plotted in the space ψ x D_{min}, from which it is easy to obtain the state-dilatancy coefficient (χ_{tc}), as shown in Figure 2.16.

Figure 2.16 – Example of ψ at D_{min} vs. D_{min} plot.

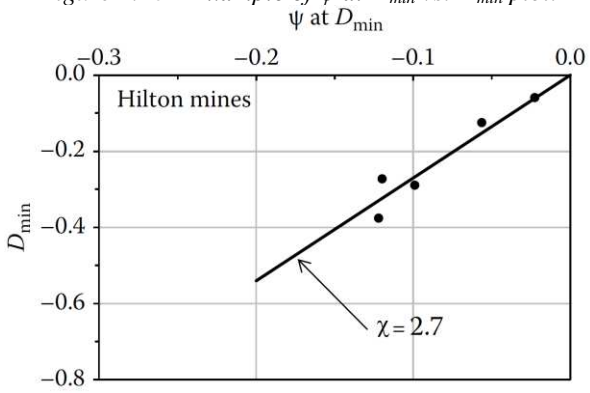

Source: Jefferies and Been (2015).

Nowadays it is known that other components may affect soil's peak strength besides dilatancy. Figure 2.17 presents a schematic representation of these components, in which φ'_p represents the peak frictional angle and φ'_c represents the critical state frictional angle.

Figure 2.17 – Components that affects the peak strength.

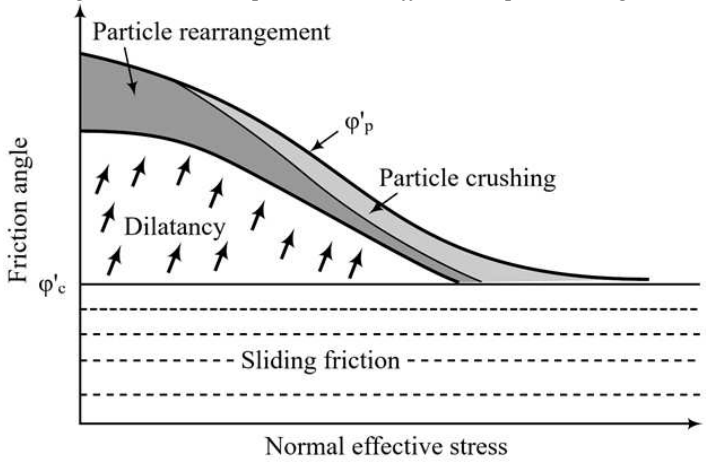

Source: adapted from Budhu (2011).

Notice that, at low effective stresses, the material strength is incremented by dilatancy and particle rearrangement. However, as the effective stresses increase, the contribution of dilatancy and particle rearrangement decreases, and particle crushing, and shattering may occur. Consequently, peak shear resistance may not develop.

Nevertheless, it is difficult to quantify the influence of particle rearrangement and particle crushing. Therefore, peak strength is commonly presented as a function of the interparticle sliding friction and the dilatancy, in which dilatancy represents a combination of all three components: particle rearrangement, particle crushing and dilatancy itself (BUDHU, 2011).

2.3.6 UNDRAINED STRENGTH

According to Maranha das Neves (2016), in the field, when the soil is saturated, it is hard to determine the effective strength of the material because it is difficult to define the pore pressures due to changes in the stress state. However, if it is an undrained condition, which is defined by the non-existence of water flow, so no change in the water content under loading, it is possible to determine the undrained shear strength (s_u) of the soil.

As presented by Equation 2.33, the undrained shear strength of a soil is described by the Tresca failure criterion using the total stress Mohr's circles (Figure 2.18.d). Moreover, as the saturation and water content are constant under the undrained condition, the void ratio also does not change ($e = w \cdot G_s/S$), and the undrained strength is only dependent on the initial void ratio (ATKINSON, 2007). It also means that the undrained strength is independent of the total stress path (TSP), and all total stress Mohr's circles, for the same void ratio, will have the same diameter of the effective stress circle, and the undrained frictional angle (φ_u) will always be equal to zero. Thus, the soil strength will always be governed by the frictional resistance, which in turn is controlled by the effective stresses (WROTH, 1984).

$$s_u = \frac{\sigma_1 - \sigma_3}{2} = \frac{q}{2} = \frac{M \cdot p'}{2} \qquad \text{Equation 2.33}$$

Just as for drained conditions, to study the undrained shear strength of samples in different initial void ratios, it may be helpful to turn the parameters dimensionless by normalizing them by the initial mean effective stress (p_0'). For the triaxial compression test, the s_u/p_0' ratio is given by equation Equation 2.34.

Figure 2.18 – Undrained strength of soil.

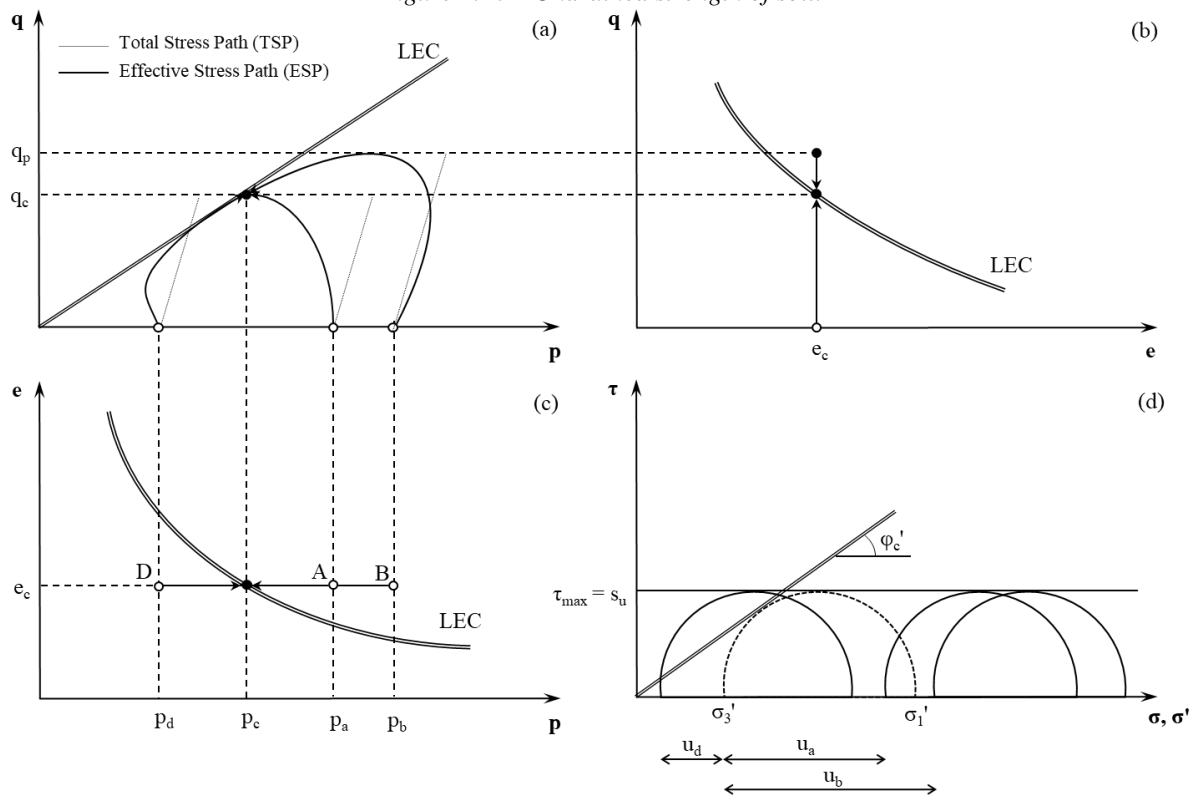

Source: elaborated by the author.

$$\frac{s_u}{p_0'} = \frac{\sigma_1 - \sigma_3}{2\sigma_3'} = \frac{(q/2)}{\sigma_3'} \qquad \text{Equation 2.34}$$

As presented by Jefferies and Been (2015), Figure 2.19 shows the relationship between the state parameter and the undrained strength ratio. Materials with the same state parameter tend to present approximately the same undrained strength ratio. Also, the undrained strength ratio increases as the soils get denser (lower state parameters).

Following the data presented in Figure 2.19, Figure 2.18.b illustrates that the higher the initial void ratio, the lower the undrained strength, which means that, differently of φ'_c, M, Γ, and λ, s_u is not an intrinsic property of the soil, but a state-dependent parameter, and any change in the initial void ratio affects the undrained shear strength. Furthermore, in line with Budhu (2010), the undrained shear strength can be defined for the peak load ($s_{u,p}$), or the load at critical state ($s_{u,c}$), and the relationship between these two parameters is determined by the soil's brittleness.

Figure 2.19 – Normalized undrained strength vs. state parameter

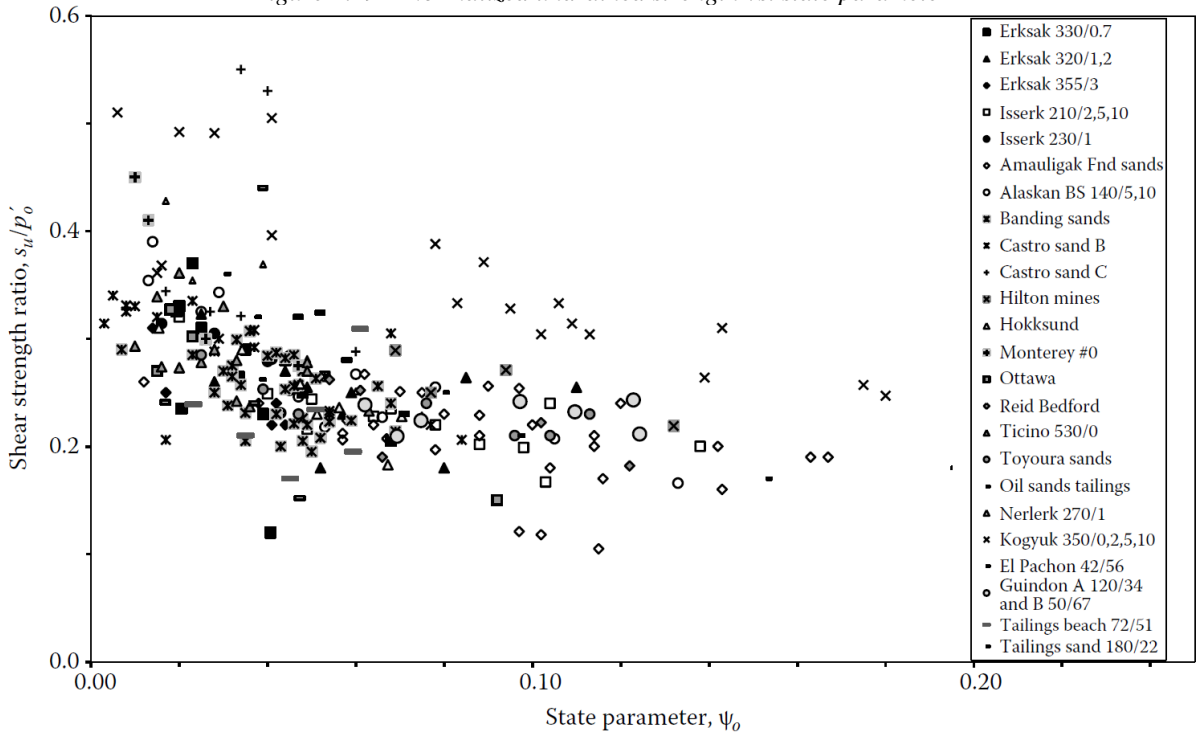

Source: Jefferies and Been, 2015.

Different from the drained peak shear strength, the peak undrained shear resistance is associated with very loose soils such as sensitive clays and liquefiable sands. As illustrated in Figure 2.18.a, by sample B, after reaching the peak state, the soil presents a collapsing behavior until reaching the critical state. The higher the soil's brittleness, the higher the difference between $s_{u,p}$, and $s_{u,c}$, which means that the higher is the tendency of the soil to lose resistance after reaching the peak load (JEFFERIES and BEEN, 2015). The brittleness index is given by Equation 2.35.

$$I_B = \frac{s_{u,p} - s_{u,c}}{s_{u,p}} \qquad \text{Equation 2.35}$$

2.4 CHARACTERIZATION OF THE IRON ORE TAILING

Mineralogical, physical, geotechnical, and hydraulic characteristics of tailings are mainly dependent on the matrix rock. As mentioned in 2.1, the iron ore tailings usually are inert fine-grained silty-sandy materials composed essentially of quartz and iron minerals. However, characteristics such as the minerals grade and grain size distribution – consequently, all the other aspects – vary from mine to mine depending on the particularities of the mining process and disposal methods.

Despite the singularities of the mining beneficiation of each company, as the major mines of the Quadrilátero Ferrífero are in the same geological formation – Cauê formation –, some similarities between tailings of the different facilities are expected. Thus, this section presents a bibliographic review on the database of tailings characteristics of iron ore mines located in the Quadrilátero Ferrífero, collected through the last two decades.

In this section, after comparing the characteristics of the different tailings generated in the Quadrilátero Ferrífero, it is expected to identify patterns and ranges of variation, which will later be used to analyze the tailings studied on this research.

2.4.1 PARTICLE SIZE DISTRIBUTION

The particle size analysis is essential to the characterization of any soil. According to Budhu (2011), the particle size distribution affects the flow of water through the medium and the material's response to loads. Moreover, Torrez-Cruz and Santamarina (2019) state that the shape of the grains and the particle size distribution also affect the index properties and critical state parameters.

A material's grade curve can be poorly graded when it is almost vertical, well-graded when flat, or gap-graded when some grain sizes are absent. The grain size distribution of the tailings will depend on the quartz and clay contents in the original ore, the particle breakdown generated during the mining process, and the disposal method (VICK, 1990).

This subsection presents all particle size distribution curves collected in the literature of iron ore tailings from the Quadrilatero Feríferro. Notice that many of the samples have been collected in TSFs adopting different sampling methodologies (some of them not specified), and not all authors have cited the depth of sampling and distance from the discharge point. Moreover, most of the authors have done conventional hydrometer testing following the ABNT standards.

The limits adopted to classify the particle size distributions were based on the limits adopted by Robertson et al. (2019). The authors subdivided the grading curves of the Feijão Dam I in coarse, fine tailings, and slimes. The coarse tailings were composed of a maximum fines content of 50%, the fine tailings were composed of 50% to 96% of fines, and the slimes had a fines content of approximately 100%. According to the authors, the main difference between the materials, besides the grain size distribution, was the material's response to CPTu loading.

Coarse tailing presented a drained behavior during CPTu; fine tailings, an undrained behavior with rapid pore pressure dissipation (t_{50} < 400 s); and the slimes, an undrained behavior with longer slow pore pressure dissipation (t_{50} > 1000 s).

As an initial reference, due to their significant database, the contours of the grain size distributions of the materials of Feijão Dam I and Fundão Dam were plotted as presented in Figure 2.20. The limits of coarse tailings and fine tailings defined by Robertson et al. (2019) after the historical data of Feijão Dam I were plotted in light yellow and light blue, respectively. The limits of the samples of coarse tailings, fine tailings, and slimes collected by the Robertson et al. (2019) were plotted in vivid yellow, vivid blue, and gray, respectively.

Figure 2.20 – Initial particle size distribution curves of references.

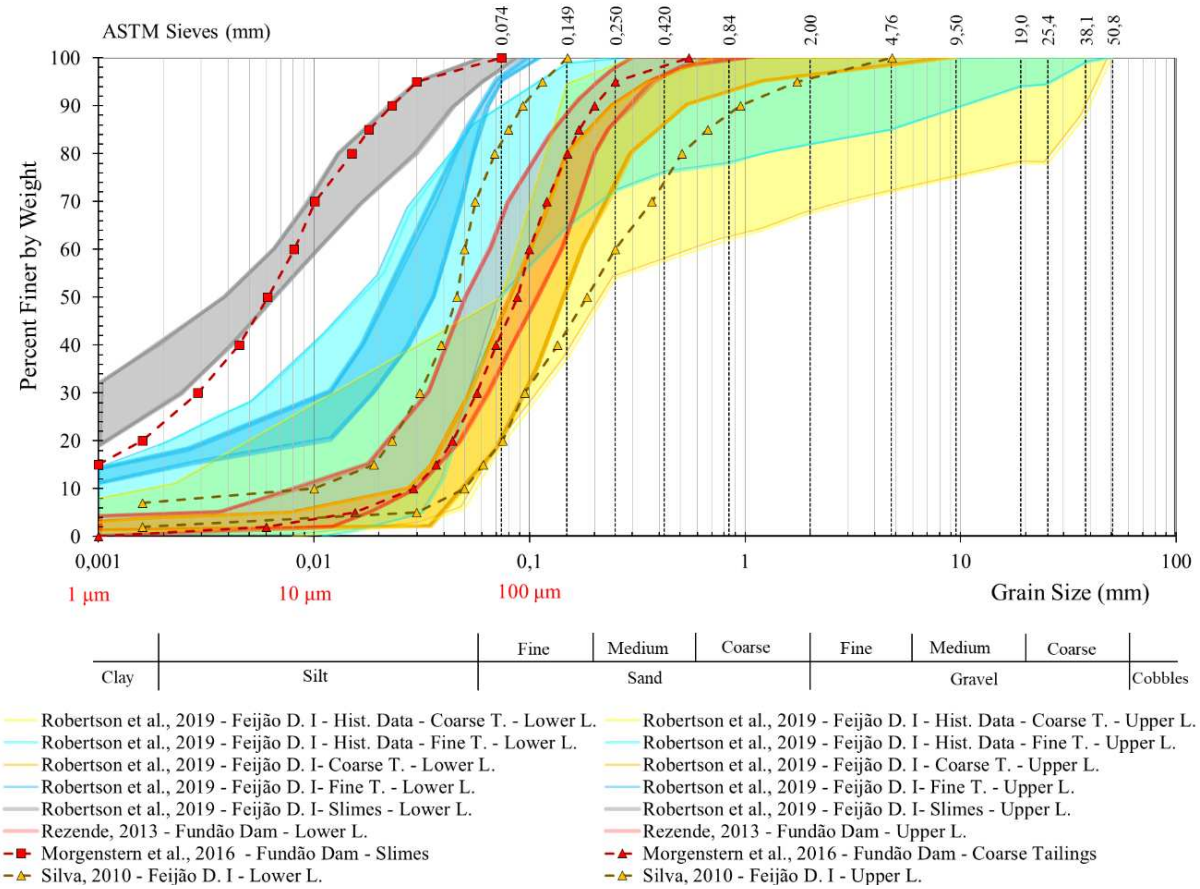

Source: elaborated by the author.

The limits determined by Silva (2010) based on samples also collected at Feijão Dam I are represented by the yellow dashed lines with yellow triangular markers. The limits of the coarse tailings of Fundão Dam analyzed by Rezende (2013), and adopted as an initial database by Morgenstern et al. (2016), were plotted in red. The coarse tailings and slime samples collected by Morgenstern et al. (2016) are illustrated with the red dashed lines with red triangular and

squared markers, respectively. Later, the reconstituted samples adopted by Robertson et al. (2019) for further studies were plotted in black dashed lines (see Figure 2.21).

There was significant convergence of the particle size distribution curves of slimes from both structures. Furthermore, although the fine tailings analyzed by Robertson et al. (2019) were a little shifted from Fundal Dam limits, the reconstituted sample of fine tailings adopted for further studies converged to the lower boundary of Fundão Dam's tailings, presented by Rezende (2013), and the lower boundary of Silva (2010). The coarse tailing samples analyzed by Robertson et al. (2019), as well as the reconstituted sample adopted by the authors for further studies, concentrated between the upper limits of the curves studied by Rezende (2013) and Silva (2010).

Figure 2.21 – Initial particle size distribution curves of references, and the particle size distributions curves of the reconstituted samples of Robertson et al. (2019).

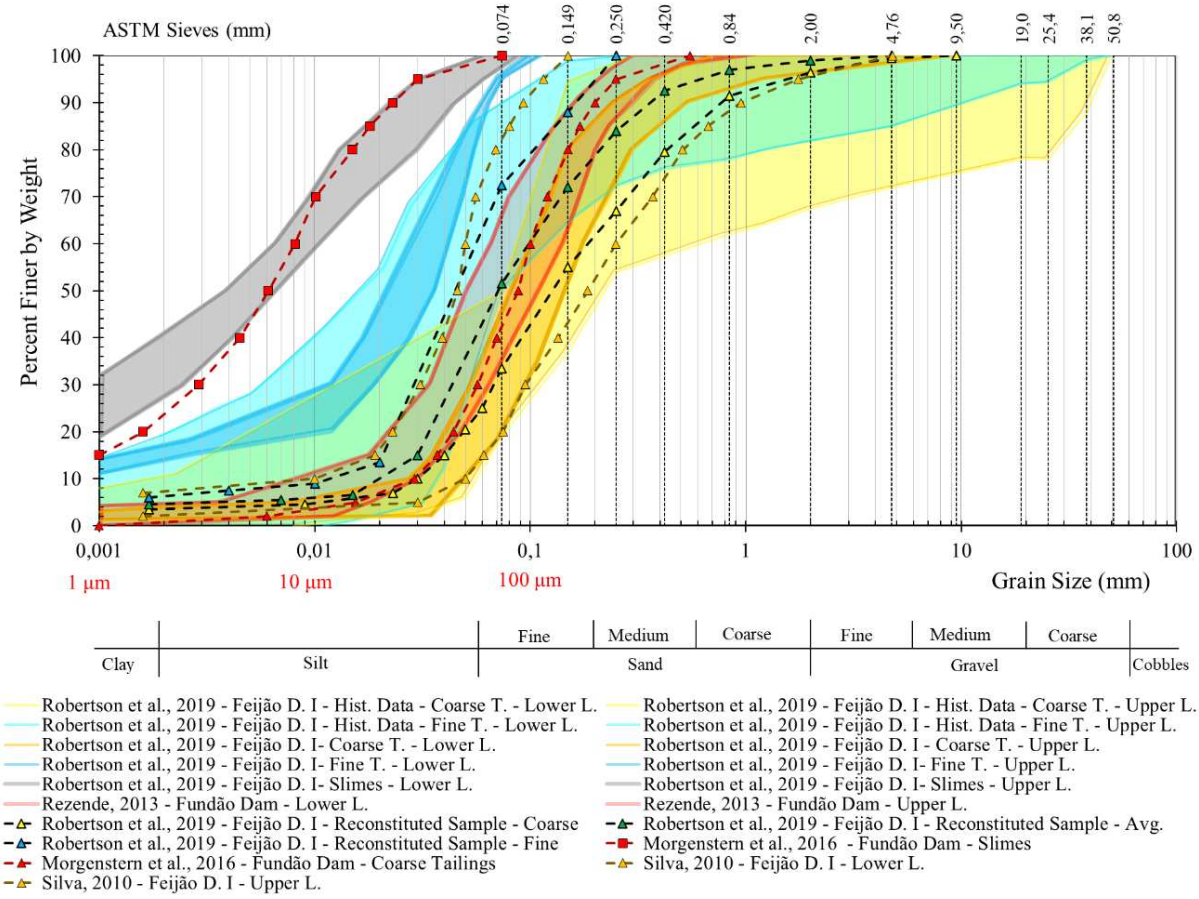

Source: elaborated by the author.

Pereira (2005), Silva et al. (2013), and Pires et al. (2019) worked with tailings' samples collected in different locations of the Quadrilátero Ferrífero. Gomes et al. (2016) presented a grain size distribution that, according to the authors, was representative of the slimes of the Quadrilátero Ferrífero. The limits presented by each author are illustrated in Figure 2.22. Notice

that the three pairs of limits, referent to the tailings, diverge a little from each other. Nevertheless, all of them are inside the contours presented by Robertson et al. (2019), the lower limits are in the fine tailings area of the chart, and the upper limits are in the coarse grain area of the chart. Moreover, the grading curve presented by Gomes et al. (2016) is very similar to the one presented by Morgenstern et al. (2016).

Figure 2.22 – Initial particle size distribution curves of references, and the particle size distributions curves of the Quadrilátero Ferrífero proposed by Pereira (2005), Silva et al. (2013), Gomes et al. (2016), and Pires et al. (2019).

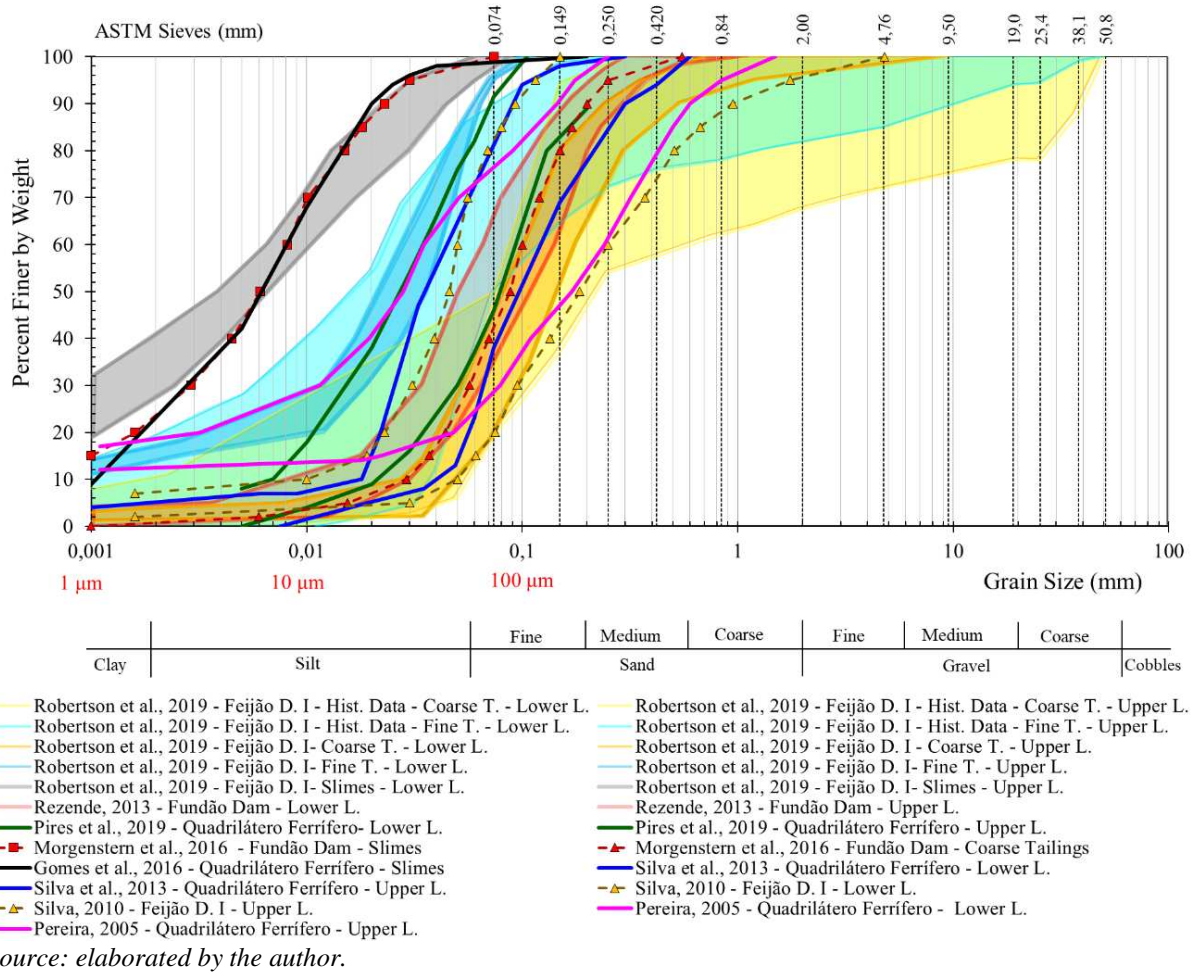

Source: elaborated by the author.

Finally, all the particle size distribution curves of tailings generated in facilities located in the Quadrilátero Ferrífero found in the literature were plotted in Figure 2.23. Table 2.1 presents the average, standard deviation, maximum and minimum values for all grading curves (general), coarse and fine tailings (tailings), coarse tailings, fine tailings, and slimes. These values were calculated using the lower and upper limits of each different sample analyzed by the authors – e.g., Pereira (2005) presented ten different particle size distributions curves, two from each studied structure; therefore, all the grading distributions were used in the statistics calculation, instead of only using the lower limit and upper limit defined after all ten curves.

From 72 grading curves, 65 were tailings (25 coarse tailings and 40 fine tailings). Based on the high values of C_u and C_z, the tailings would be classified as well-graded or gap-graded soils. However, most grade curves presented in Figure 2.23 are reasonably vertical followed by a tail of finer particles that confers the high values of C_u and C_z. The same characteristic was identified by Li et al. (2018) for gold tailings. According to the authors, these materials are relatively poorly graded instead of well graded.

Figure 2.23 – Particle size distribution curves of tailings generated in facilities of the Quadrilátero Ferrífero.

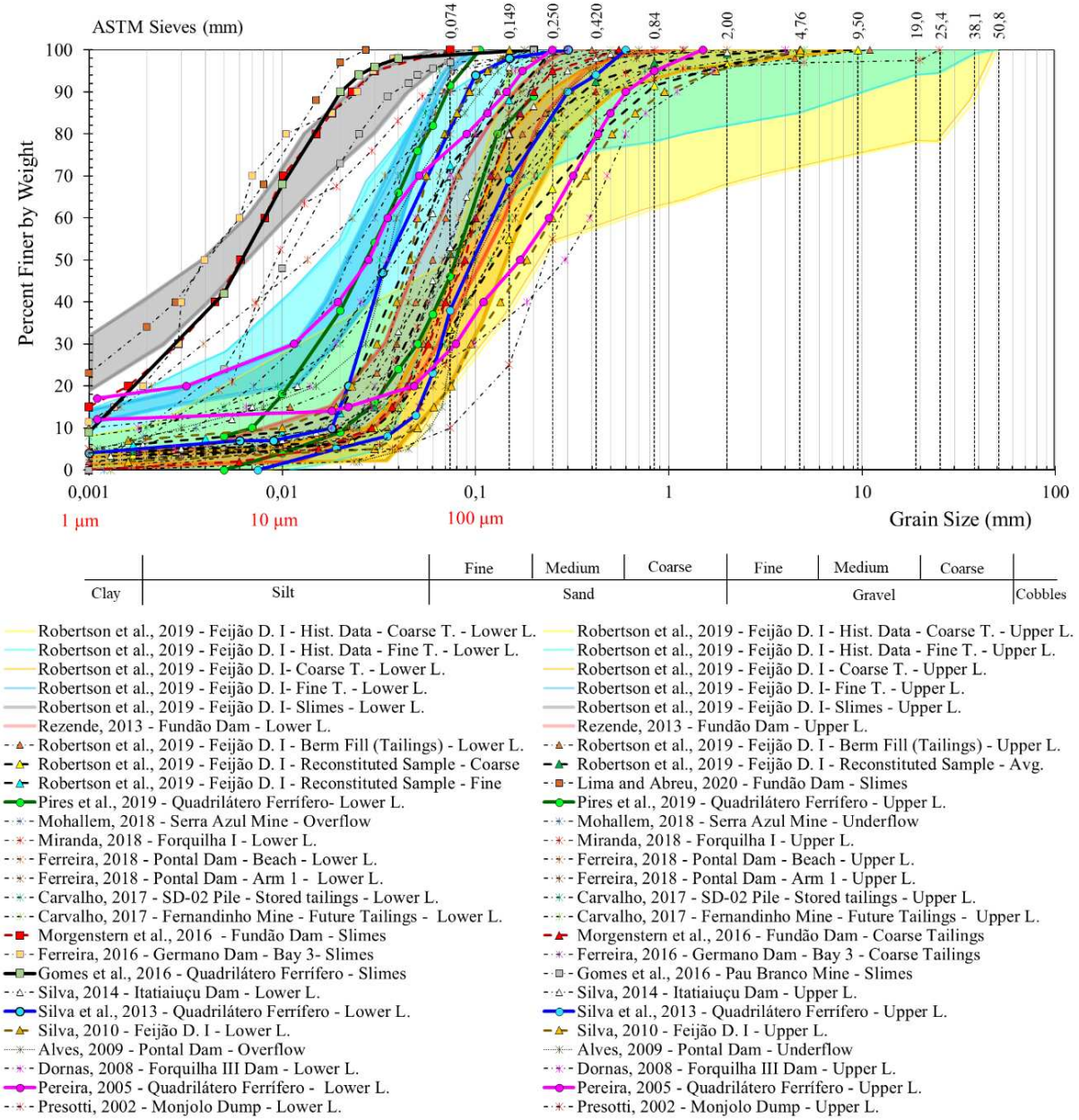

Source: elaborated by the author.

Table 2.1 – Statistic of the particle size distribution curves and percent of particle sizes.

						Percent ABNT - NBR 6502:1995					
								Sand			
Author	**Sample**	**D_{50} (mm)**	**C_U**	**Cz**	**Percent Fines < 0,075 mm**	**Clay < 0,002 mm**	**Silt 0,002 - 0,06 mm**	**Fine 0,06 - 0,2 mm**	**Medium 0,2 - 0,6 mm**	**Coarse 0,6 - 2,0 mm**	**Gravel > 2,0 mm**
General (72)	Average	0,07	23,0	4,6	62,2	7,8	45,0	35,8	8,6	1,7	1,0
	Standard Deviation	0,05	38,1	7,8	24,2	8,5	21,4	18,3	10,2	3,5	4,4
	Maximum	0,29	233,0	31,7	100	41	85,5	72	45	16	32
	Minimum	0,00	2,2	0,1	10	0	3	0	0	0	0
Tailings (65)	Average	0,08	23,5	5,0	58,3	5,9	42,1	39,5	9,5	1,9	1,1
	Standard Deviation	0,05	39,8	8,2	22,0	5,7	20,2	15,2	10,3	3,6	4,6
	Maximum	0,29	233,0	31,7	100	19,5	82	72	45	16	32
	Minimum	0,01	2,2	0,1	10	0	3	10	0	0	0
Coarse Tailings (25)	Average	0,12	24,6	4,1	35,9	3,6	23,3	49,9	17,3	4,0	1,9
	Standard Deviation	0,06	53,3	8,6	11,0	4,3	10,2	12,6	11,1	5,0	6,4
	Maximum	0,29	233,0	30,8	50	13,5	38,5	72	45	16	32
	Minimum	0,07	2,2	0,4	10	0	3	18,5	3	0	0
Fine Tailings (40)	Average	0,05	22,9	5,6	72,2	7,3	53,9	33,0	4,7	0,5	0,7
	Standard Deviation	0,02	29,1	7,9	14,2	6,0	15,5	13,0	5,9	1,3	2,9
	Maximum	0,12	106,0	31,7	100	19,5	82	55	23	5	18
	Minimum	0,01	2,3	0,1	50	0	23	10	0	0	0
Slimes (7)	Average	0,01	17,9	1,3	99,0	25,9	72,2	1,9	0,0	0,0	0,0
	Standard Deviation	0,00	14,2	0,3	1,2	9,9	8,9	2,2	0,0	0,0	0,0
	Maximum	0,01	46,4	1,6	100	41	85,5	5,5	0	0	0
	Minimum	0,00	6,7	0,7	97	10	59	0	0	0	0

Source: elaborated by the author.

Therefore, nearly all tailings presented poorly graded curves composed essentially of silt and fine sands. The average particle size distribution curve of the coarse tailings indicates a silty sand material with 49,9% of fine sand and 23,3% of silt, while the average particle size distribution curve of the fine tailings indicates a sandy silt material with 53,9% of silt and 33,0% of fine sand. The slimes showed more well-graded curves composed mainly of silt size material (average of 72,2%) and clay size material (average of 25,9%). Nonetheless, the high standard deviation of all categories indicates high variability of the tailings' grading curves.

Despite de outliers, most tailings grade curves are between the lower boundary of the fine tailings' samples of Robertson et al. (2019) and the upper boundary of the samples tested by Silva (2010). Figure 2.24 present the contours in which the particle size distribution curves of slimes (in red) and tailings (in navy blue) from the Quadrilátero Ferrífero are most likely to be. In white, it is also presented the average curve that separates the fine tailings from the coarse tailings.

Figure 2.24 – Contours in which the grain size distribution of the iron ore tailings of the Quadrilátero Ferrífero are most likely to be.

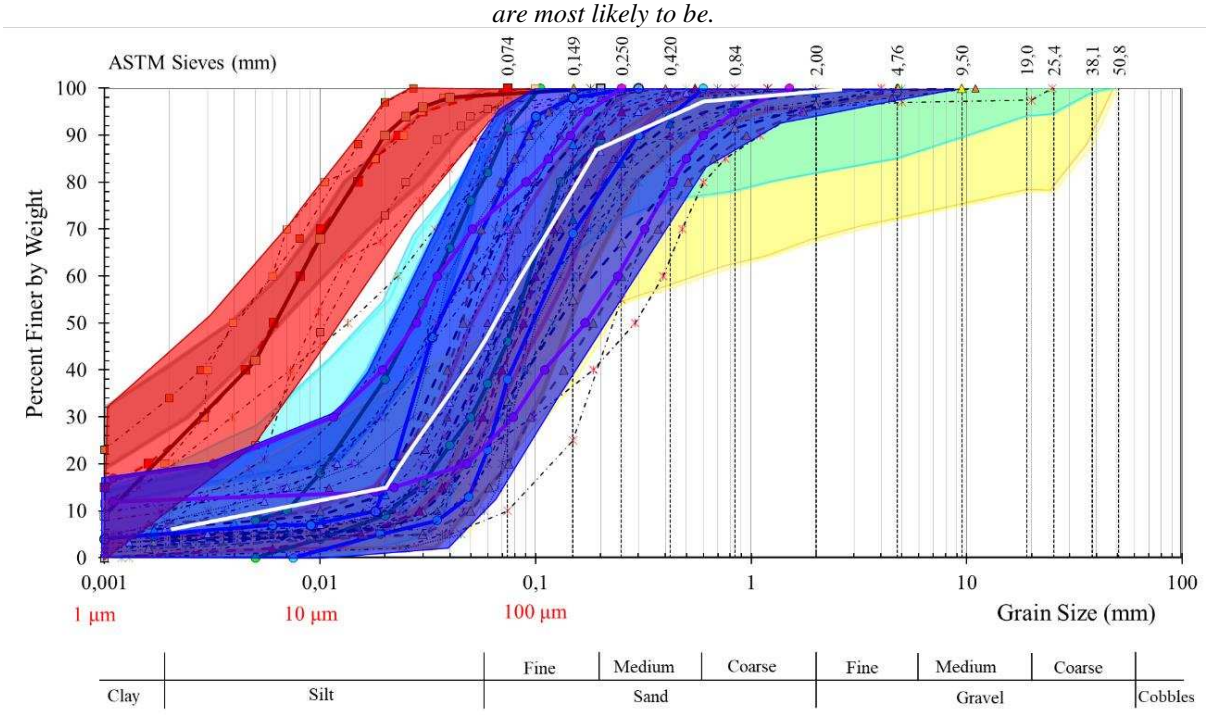

In red, the slimes contours, in navy blue the tailings, and in white the average curve that separates fine tailings from coarse tailings. Source: elaborated by the author.

It is worth mentioning that Fundão Dam and Feijão Dam I collapsed through flow liquefaction. As the defined contours are inside the particle size distribution range initially presented by Robertson et al. (2019) for Feijão Dam I, all the already studied tailings of the Quadrilátero

Ferrífero, which are located inside these contours, may be susceptible to liquefaction. The particle size distribution alone is not enough to dictates if the material is susceptible to liquefaction or not, but it may be used as a preliminary reference. Moreover, yet based on Robertson et al. (2019), the tailings below the average (with more than 50% of fines) are prone to have an undrained behavior under saturated conditions.

2.4.2 SPECIFIC GRAVITY

Specific gravity (G_s) of the tailings is dependent on the specific gravity and concentration of each constituent mineral. The iron ore tailings, as mentioned before, are composed basically of quartz (G_s = 2,65 g/cm^3), hematite (G_s = 5,30 g/cm^3), goethite (G_s = 4,27 g/cm^3), and magnetite (G_s = 5,15 g/cm^3)[1]. Table 2.2 and Table 2.3 present the mineral and the elemental composition of tailings from the Quadrilátero Ferrífero, respectively. When more than one sample was collected for the same material, it is shown the average value and the range of obtained values between parentheses.

From Table 2.2 and Table 2.3, it is notable the high variability of iron minerals and quartz contents from sample to sample. Some tailings are composed essentially of quartz, such as QF – AM01 (Pires et al., 2019), and others are composed mainly of iron minerals, such as Feijão D. I - Coarse Tailings (Robertson et al., 2019). The grades of hematite, magnetite, and goethite vary from each sample. Nevertheless, the concentration of hematite is usually the highest. Moreover, the slime samples present higher grades of iron minerals than the coarse and fine tailings. After iron ore beneficiation and slurry disposal, the quartz particles, which are larger than the iron minerals particles, tend to deposit close to the discharge point in the tailings' beach, while the small particles tend to deposit away from the discharge point generating the slimes' ponds.

The iron content is inversely proportional to the efficiency of iron ore processing. The more efficient the process is, the lower is the iron content of the tailings. Thus, it is expected old tailings deposits, as Feijão Dam I, to have higher iron content than the tailings generated nowadays, as the future tailings of Fernandinho Mine (Carvalho, 2017).

[1] Specific gravity from the Mineralogy Database available at http://webmineral.com/

Table 2.2 – Mineral composition of iron ore tailings from the Quadrilátero Ferrífero.

Author	Sample	Hematite (%)	Magnetite (%)	Goethite (%)	Quartz (%)
Tolentino, 2010	Germano Dam	< 20	-	< 5	> 80
Morgenstern et al., 2016	Fundão Dam - Slimes	42,9	0	30,9	19,2
Ferreira, 2018	Pontal Dam - Arm 1	45,3 (38,2-56,0)	0,4 (0,04-0,9)	4,4 (2,9-7,7)	45,5 (39,3-53,1)
Pires et al., 2019	QF - AM01	14,5	-	0,9	82,7
	QF - AM02	42,0	-	2,0	53,7
	QF - AM03	28,9	-	12,6	54,4
	QF - AM04	46,7	-	7,1	42,6
	QF - AM05	18,2	-	4,0	75,1
	QF - AM06	34,0	-	2,8	60,7
	QF - AM07	39,5	-	4,6	50,1
Robertson et al., 2019	Feijão D. I - Hist. Data - Tailings	77,1	8,6	7,1	2,6
	Feijão D. I - Coarse Tailings	87,3 (86,8-87,7)	7,1 (6,5-7,6)	3,2 (3-3,4)	6 (5,4-6,6)
	Feijão D. I - Fine Tailings	48,0 (43,1-54,1)	1,5 (1,3-1,9)	15,0 (10,2-20,7)	7,5 (1,5-14,9)
	Feijão D. I - Slimes	47,3 (44,4-50,1)	0,4 (0,4-0,4)	33,0 (32,0-34,0)	25,2 (21,8-28,5)
General	Average	42,3	3,0	9,5	43,2
	Standard Deviation	20,4	3,8	10,3	27,4
	Maximum	87,7	8,6	34,0	82,7
	Minimum	14,5	0,0	0,9	1,5
Tailings	Average	41,8	4,4	5,7	46,7
	Standard Deviation	22,1	4,0	4,2	28,1
	Maximum	87,7	8,6	20,7	82,7
	Minimum	14,5	0,0	0,9	1,5
Slimes	Average	45,1	0,2	32,0	22,2
	Standard Deviation	3,1	0,3	1,5	4,2
	Maximum	50,1	0,4	34,0	28,5
	Minimum	42,9	0,0	30,9	19,2

Tailings (coarse and fine) results are presented in the white lines and the slimes results are presented in the gray lines. Source: elaborated by the author.

Table 2.4 shows the specific gravity of the tailings generated in facilities located in the Quadrilátero Ferrífero found in the literature. The average values of all samples (general), tailings (coarse and fine), and slimes do not diverge much from each other. The small standard deviation shows considerable consistency of the values: 3,75 g/cm^3 for general, 3,71 g/cm^3 for tailings, and 3,97 g/cm^3 for slimes.

Table 2.3 – Elemental composition of iron ore tailings from the Quadrilátero Ferrífero.

Author	Sample	Iron (%)	Silica (%)
Presotti, 2002	Morro Agudo Mine	23	67
Pereira, 2005	Germano Dam	14,2	73
	Germano Pit	19,9 (17,6-22,2)	72,9 (69,2-76,7)
	Itabiruçu Dam	20,1 (19,2-21,0)	76,5 (72,1-80,9)
	Forquilha III Dam	34,5 (33,7-35,2)	44,8 (43,2-46,5)
	Forquilha II Dam	53,96	18,47
	Campo Grande Dam	42,45	37,71
	Córrego do Doutor Dam	22,2 (21,4-23,0)	68,6 (66,3-70,9)
Tolentino, 2010	Germano Dam	13,1	82,6
Carvalho, 2017	Fernandinho Mine - Fut. Tailings	20,8 (14,6-26,9)	67,1 (56,1-78,1)
Dauce et al., 2018	Serra Azul Mine	30,3	50,4
Ferreira, 2018	Pontal Dam, Arm 1	34,2 (29,9-38,8)	46,7 (40,5-54,9)
	Pontal Dam, Beach	30,4 (21,4-56,5)	55,1 (18,1-69,4)
Pires et al., 2018	QF - AM01	11,4	81,6
	QF - AM02	27,4	57,4
	QF - AM03	25,0	60,2
	QF - AM04	32,8	51,3
	QF - AM05	12,7	79,4
	QF - AM06	23,9	64,2
	QF - AM07	26,8	57,8
Lima and Abreu, 2020	Fundão Dam - Slimes	51,4	15,1
Robertson et al., 2019	Feijão D. I - Hist. Data - Tailings	66,6	2,4
General	Average	28,6	56,4
	Standard Deviation	14,1	22,2
	Maximum	66,6	82,6
	Minimum	11,4	2,4
Tailings	Average	26,7	58,1
	Standard Deviation	10,9	17,9
	Maximum	66,6	82,6
	Minimum	11,4	2,4

Tailings (coarse and fine) results are presented in the white lines and the slimes results are presented in the gray lines. Source: elaborated by the author.

It is interesting to notice that the average values of specific gravity are more consistent with the specific gravity of samples with approximately the same grades of iron minerals and quartz (e.g., Pontal Dam - Arm 1, Ferreira, 2018). While high values of specific gravity, as 5,22 g/cm^3, and low values as 2,38 g/cm^3 are punctual and they are associated with samples with high and low grades of iron minerals, respectively.

Table 2.4 – Specific gravity of iron ore tailings from the Quadrilátero Ferrífero.

Authors	Sample	G_s (g/cm³)
Presotti, 2002	Monjolo Dump (hydraulic fill)	3.38 (2,89-4,41)
Santos, 2004	Monjolo Dump (hydraulic fill)	3,08 (2,95-3,19)
Pereira, 2005	Germano Pit	3,33 (3,27-3,40)
	Itabiruçu Dam	3,37 (3,34-3,41)
	Forquilha III Dam	3,88 (3,81 -3,95)
	Forquilha II Dam	4,80
	Campo Grande Dam	4,15
	Córrego do Doutor Dam	3,38 (3,37-3,40)
Dornas, 2008	Forquilha III Dam	3,71 (3,27-4,52)
Alves, 2009	Pontal Dam	3,35 (3,32-3,41)
Silva, 2010	Feijão Dam I	4,49 (3,80-5,11)
Rezende, 2013	Fundão Dam	2,98 (2,77-3,41)
Silva, 2014	Itatiaiuçu Dam	3,70 (3,44-3,84)
Ferreira, 2016	Germano Dam, Bay 3 - Coarse Tailings	2,91
	Germano Dam, Bay 3 - Slimes	3,83
Morgenstern et al., 2016	Fundão Dam - Coarse Tailings	3,00 (2,38-4,34)
	Fundão Dam - Slimes	3,90 (3,69-3,99)
Carvalho, 2017	SD-02 Pile - Stored tailings	3,46 (2,55-4,10)
	Fernandinho Mine - Future tailings	3,11 (2,98-3,27)
Ferreira, 2018	Pontal Dam, Arm I	3,50 (3,23-3,99)
	Pontal Dam, Beach	3,34 (2,97-3,68)
Miranda, 2018	Forquilha I Dam	3,63 (2,74-4,29)
Mohallem, 2018	Serra Azul Mine	3,65 (3,41-3,84)
Lima and Abreu, 2020	Fundão Dam - Slimes	4,17
Robertson et al., 2019	Feijão Dam I - Historical Data - Coarse Tailings	4,60 (2,71-5,22)
	Feijão Dam I - Historical Data - Fine Tailings	4,21 (2,66-5,14)
	Feijão Dam I - Coarse Tailings	4,89 (4,64-4,99)
	Feijão Dam I - Fine Tailings	3,89 (3,87-3,90)
	Feijão Dam I - Slimes	3,97 (3,61-4,32)
	Feijão Dam I - Berm Fill (Tailings)	4,39 (4,10-4,93)
General	Average	3,75
	Standard Deviation	0,55
	Maximum	5,22
	Minimum	2,38
Tailings	Average	3,71
	Standard Deviation	0,58
	Maximum	5,22
	Minimum	2,38
Slimes	Average	3,97
	Standard Deviation	0,23
	Maximum	4,32
	Minimum	3,61

Tailings (coarse and fine) results are presented in the white lines and the slimes results are presented in the gray lines. Source: elaborated by the author.

2.4.3 ATTERBERG LIMITS

As by-products of the ore beneficiation, the tailings and even the slimes typically do not have considerable amounts of clay minerals and, consequently, present non to low plasticity. High-plastic iron ore tailings are uncommon and associated with high grades of clay minerals in the parent ore (Vick, 1990).

Table 2.5 presents the Atterberg limits of the tailings generated in facilities located in the Quadrilátero Ferrífero found in the literature. The table displays the values obtained by the authors for each different material studied by them. When more than one sample were collected for the same material, it is shown the average value, and the range of obtained values between parentheses. It also shows the number of samples of each material classified as plastic and non-plastic.

Most of the analyzed samples (68,8%) were non-plastic. When evaluating only the tailings (coarse and fine), this value is even greater (78,3%). All the analyzed slimes' samples were plastic. However, it is noteworthy mentioning that all average values of the plastic samples indicated low plasticity, even for the slimes. Based on the Casagrande plasticity chart, high-plastic materials (LL > 50%) were found by Ferreira (2018), Miranda (2018), and Robertson et al. (2019).

Table 2.5 – Atterberg limits of iron ore tailings from the Quadrilátero Ferrífero.

Author	Sample	Liquid Limit (LL)	Plastic Limit (PL)	Plasticity Index (PI)	Number of Samples	
					Non Plastic	Plastic
Silva, 2010	Feijão Dam I	NP/24 (18,2-33,3)	NP/17,9 (13,8-23,5)	NP/6,1 (4,3-9,8)	10	6
Silva, 2014	Itatiaiuçu Dam	NP	NP	NP	1	0
Ferreira, 2016	Germano Dam, Bay 3 - Coarse Tailings	NP	NP	NP	1	0
	Germano Dam, Bay 3 - Slimes	24,1	11,2	12,9	0	1
Morgenstern et al., 2016	Fundão Dam - Coarse Tailings	NP	NP	NP	1	0
	Fundão Dam - Slimes	27,1 (26,0-28,4)	17,4 (16,0-19,0)	9,7 (7,0-11,1)	0	3
Carvalho, 2017	Fernandinho Mine - Stored tailings	NP/16,7 (15,2-18,2)	NP/10,9 (9,3-12,4)	NP/5,9 (5,8-5,9)	13	2
	Fernandinho Mine - Future tailings	NP	NP	NP	6	0
Ferreira, 2018	Pontal Dam, Arm I	NP	NP	NP	0	14
	Portal Dam, Beach	NP/44,5 (21,0-62,0)	NP/22,5 (11,0-35,0)	NP/22,0 (10,0-31,0)	8	6
Miranda, 2018	Forquilha I Dam	NP/39,1 (24,5-53,7)	NP/25,2 (17,9-32,4)	NP/14,0 (6,6-21,3)	2	2
Mohallem, 2018	Serra Azul Mine	NP/20,0 (18,1-21,9)	NP/13,6 (12,3-14,9)	NP/6,4 (5,7-7,0)	2	2
Robertson et al., 2019	Feijão Dam I - Historical Data - Coarse Tailings	NP	NP	NP	15	0
	Feijão Dam I - Historical Data - Fine Tailings	NP/22,2 (18,0-30,0)	NP/16,8 (14,0-23,0)	NP/5,2 (4,0-7,0)	25	5
	Feijão Dam I - Coarse Tailings	NP	NP	NP	12	0
	Feijão Dam I - Fine Tailings	21,0 (19,0-22,0)	17,0 (16,0-18,0)	4,0 (3,0-4,0)	0	2
	Feijão Dam I - Slimes	43,0 (15,0-53,0)	25,4 (11,0-31,0)	17,7 (4,0-26,0)	0	15
	Feijão Dam I - Berm Fill (Tailings)	20,3 (16,0-29,0)	15,7 (14,0-18,0)	4,7 (1,0-11,0)	0	3
General	Average	27,9	18,1	9,8		
	Standard Deviation	9,6	5,1	5,8	108	49
	Maximum	62,0	35,0	31,0	(68,8%)	(31,2%)
	Minimum	15,0	9,3	1,0		
Tailings	Average	25,9	17,4	8,5		
	Standard Deviation	10,1	4,6	6,3	108	30
	Maximum	62,0	35,0	31,0	(78,3%)	(21,7%)
	Minimum	15,2	9,3	1,0		
Slimes	Average	31,4	18,0	13,4		
	Standard Deviation	10,2	7,1	4,0	0	19
	Maximum	53,0	31,0	26,0	(0%)	(100%)
	Minimum	15,0	11,0	4,0		

Tailings (coarse and fine) results are presented in the white lines and the slimes results are presented in the gray lines. Source: elaborated by the author.

2.4.4 MAXIMUM AND MINIMUM VOID RATIOS

According to the ASTM D4253:2016 and the ASTM D4254:2016, the maximum (e_{max}) and minimum (e_{min}) void ratios are only determined in soil mechanics for cohesionless free-draining materials with less than 15% of fines passing the nº 200 sieve. However, different authors in the literature have determined the maximum and minimum void ratios of tailings with fines content up to 40% to extend the use of relative density to tailings (VICK, 1990).

Torres-Cruz and Santamarina (2019) – following Lade et al. (1998), Carrera et al. (2011), Park and Santamarina (2017), Li and Coop (2018), and Torres-Cruz 2019 – extend the determination of e_{max} and e_{min} to characterize the behavior of non-plastic silts. According to the authors, there is some correlation between the state parameters and the extreme void ratios. Furthermore, the variability of e_{min} in a tailings deposit may correlate to the spatial variability of the state parameters. Therefore, the determination of the extreme void ratios could assist the elaboration of sampling programs.

Table 2.6 presents the maximum and minimum void ratios of the tailings generated in facilities located in the Quadrilátero Ferrífero found in the literature. The table displays the values obtained by the authors for each different material studied by them. When more than one sample was collected for the same material, it is shown the average value and the range of obtained values between parentheses.

The average value of the minimum void ratio (e_{min} = 0,66) is representative of the sampled data since there is little scatter (SD = 0,09). Because of the high outliers, the maximum void ratio showed higher dispersion (SD = 0,22), but the average value (e_{max} = 1,22) is still representative of the distribution.

It is noteworthy mentioning that the high outliers, like the ones presented by Ferreira (2018), are usually associated with materials with high contents of clay size particles. However, the values obtained by Ferreira (2018) have been associated with samples collected in the tailing's beach that presented no plasticity. It indicates some inconsistency in the data.

Table 2.6 – Maximum and minimum void ratios of iron ore tailings from the Quadrilátero Ferrífero.

Author	Sample	e_{min}	e_{max}
Presotti, 2002	Monjolo Dump (hydraulic fill)	0,65 (0,58-0,75)	0,95 (0,89-1,05)
Santos, 2004	Monjolo Dump (hydraulic fill)	0,57 (0,51-0,65)	0,95 (0,88-0,99)
Pereira, 2005	Germano Pit	0,62	1,29 (1,26-1,33)
	Itabiruçu Dam	0,67	1,38 (1,37-1,39)
	Forquilha III Dam	0,61 (0,57-0,64)	1,68 (1,59-1,77)
	Forquilha II Dam	0,74	1,63
	Campo Grande Dam	0,74	1,25
	Córrego do Doutor Dam	0,61 (0,60-0,61)	1,31 (1,25-1,37)
Dornas, 2008	Forquilha III Dam	0,54 (0,45-0,59)	1,11 (1,02-1,21)
Alves, 2009	Pontal Dam	0,68 (0,50-0,91)	1,26 (1,04-1,70)
Silva, 2010	Feijão Dam I	0,75 (0,57-0,80)	1,33 (1,14-1,48)
Rezende, 2013	Fundão Dam	0,55 (0,53-0,57)	1,04
Morgenstern et al., 2016	Fundão Dam	0,53 (0,47-0,58)	0,87
Carvalho, 2017	Fernandinho Mine - Future tailings	0,68 (0,63-0,72)	1,05 (1,02-1,08)
Ferreira, 2018	Pontal Dam, Arm I	0,64 (0,55-0,85)	1,16 (0,97-1,45)
	Pontal Dam, Beach	0,89 (0,46-1,69)	1,40 (0,90-2,28)
Miranda, 2018	Forquilha I Dam	0,67 (0,63-0,70)	1,28 (1,20-1,35)
Mohallem, 2018	Serra Azul Mine - Underflow	0,74 (0,71-0,77)	1,05 (1,01-1,09)
Tailings	Average	0,66	1,22
	Standard Deviation	0,09	0,22
	Maximum	1,69	2,28
	Minimum	0,45	0,87

Source: elaborated by the author.

2.4.5 MAXIMUM DRY UNIT WEIGHT AND OPTIMUM WATER CONTENT

Through the years, tailings have been used as material to construct the embankment rases of tailing dams, and today the tailings are deposited in stacks. Thus, knowing the maximum dry unit weight ($\gamma_{d,max}$) and optimum water content ($w_{opt.}$) just as the state of the material under different degrees of compaction is necessary.

Table 2.7 presents the maximum dry unit weight and the optimum water content of the tailings generated in facilities located in the Quadrilátero Ferrífero found in the literature. The table displays the values obtained by the authors for each different material studied by them. When more than one sample was collected for the same material, it is shown the average value and the range of obtained values between parentheses.

Most of the values of $w_{opt.}$ are between 10% and 17%, with an average value of 13% when considering only coarse and fine tailings samples. The most of $\gamma_{d,max}$ is between 17,7 kN/m^3 and 21,7 kN/m^3, with an average of 19,75 kN/m^3 when considering only coarse and fine tailings samples.

Notice that the maximum dry unit weight is directly proportional to the specific gravity of the material. Therefore, it is expected to have higher values of $\gamma_{d,max}$ for the samples with higher G_s

– Forquilha III Dam samples, Dornas (2008) – and lower values of $\gamma_{d,max}$ for samples with lower G_s – Germano Dam, Bay 3, coarse tailings samples, Ferreira (2016).

Table 2.7 – Maximum dry unit weight and optimum water content of iron ore tailings from the Quadrilátero Ferrífero.

Author	Sample	w_{opt} (%)	$\gamma_{d,max}$ (kN/m³)
Dornas, 2008	Forquilha III Dam	11,0 (9,3-12,1)	23,13 (20,47-25,56)
Silva, 2010	Feijão Dam I	18,1 (16,1-19,9)	22,19 (20,68-23,27)
Silva et. al 2013	Brucutu Mine - Flotation + Magnetic C.	10,8	18,95
	Timbopeba Mine - Flotation	11,3	18,75
	Conceição Mine - Flotation	13,8	17,75
	Vargem Grande Mine - Flotation	14,6	17,39
	Pico Mine - Flotation	12,5	18,50
	Fabrica Mine - Underflow	13,3	17,65
Silva, 2014	Itatiaiuçu Dam	12,4 (11,9-12,9)	21,83 (21,58-22,07)
Ferreira, 2016	Germano Dam, Bay 3 - Coarse Tailings	14,1	17,50
	Germano Dam, Bay 3 - Slimes	16,3	21,90
Morgenstern et al., 2016	Fundão Dam - Coarse T. - *Modified Proctor**	13,1	17,84
	Fundão Dam - Slimes	16,7	22,56
Carvalho, 2017	SD-02 Pile - Stored tailings	7,2 (6,2-9,2)	19,21 (17,71-20,79)
	Fernandinho Mine - Future tailings	21,2	19,57
Ferreira, 2018	Pontal Dam, Arm I	10,6 (9-12,4)	21,26 (18,56-22,81)
	Portal Dam, Beach	10,6 (5,3-14,7)	20,94 (19,91-22,17)
Mohallem, 2018	Serra Azul Mine - Overflow	12,8	21,66
General	Average	13,4	19,94
	Standard Deviation	3,3	1,98
	Maximum	21,2	25,56
	Minimum	5,3	17,39
Tailings	Average	13,0	19,75
	Standard Deviation	3,3	1,92
	Maximum	21,2	25,56
	Minimum	5,3	17,39

*Value not used to calculate the averages.
Tailings (coarse and fine) results are presented in the white lines and the slimes results are presented in the gray lines. Source: elaborated by the author.

2.4.6 HYDRAULIC CONDUCTIVITY

The hydraulic conductivity (k) is hard to generalize because it is affected by the fines content, plasticity, confining stresses, void ratio, stratigraphy, material structure, also sampling and testing procedures. According to Vick (1990), hydraulic conductivity can vary from 10^{-10} m/s in slimes to 10^{-4} m/s in coarse tailings.

Moreover, the hydraulic conductivity tends to decrease with the reduction of the void ratio. In coarse tailings, the permeability can reduce up to five times the initial value by reducing the void ratio, while this reduction can be about a factor of ten in slimes (VICK, 1990).

As stated in Chapuis and Aubertin (2003), with the right precautions, good laboratory tests may give k-values between one-third and three times the real (*in situ*) value of hydraulic conductivity. Thus, to ensure good results, during testing, complete saturation of the specimens is necessary, and the steady-state condition must be reached. According to the authors, the

inflow and outflow rates change with time, and if the test stops before stabilization, k may be underestimated. Moreover, the hydraulic gradient must be determined using lateral piezometers, and internal erosion must be prevented in coarse materials.

Wet samples compacted by impact may present either clogs or local internal erosion, which results in underestimation or overestimation of k-values. On the other hand, the compaction of dry tilled soils may result in micro-fissures that result in overestimated k-values (CHAPUIS and AUBERTIN, 2003).

The Kozeny-Carman (KC) equation is a well-known equation to estimate the permeability of natural homogeneous soils. Chapuis and Aubertin (2003) studied the applicability of this equation to mine tailings. According to the authors, tailings are usually composed of angular and acicular particles, which increase the tortuosity of the internal channels and affect the void spaces of the material. Thus, the KC equation may be used to predict the k-value of tailings if it accounts for the particle shape effect. The authors suggest Equation 2.36 to predict the k-value of mining tailings.

$$\log\frac{k}{1m/s} = 1{,}46 \cdot \left[0{,}5 + \frac{e^3}{G_s^2 S_p^2 (1+e)}\right] + 1{,}99 \qquad \text{Equation 2.36}$$

Where, k is given in m/s, G_s is the specific gravity of the tailings, and S_p is the specific surface (m^2/kg), which can be estimated from the complete gradation curve procedure presented by Chapuis and Légaré (1992).

According to Chapuis and Aubertin (2003), differences between the estimated value and the value measured in the laboratory may be associated with the imprecise determination of the specific surface (S), theoretical limitations of the equation, inadequate testing procedures, and homogeneity of the samples. The KC equation does not estimate the k-values of intact tailings samples due to their increased stratigraphy and high anisotropy.

Table 2.8 presents the hydraulic conductivity of tailings generated in facilities located in the Quadrilátero Ferrífero found in the literature. The table displays the values obtained by the authors for each different material studied by them. When more than one sample was collected for the same material, it is shown the average value and the range of obtained values between parentheses. When specified by the authors, it is presented the vertical stress and the void ratio associated with the hydraulic conductivities.

Table 2.8 – Hydraulic conductivity of iron ore tailings from the Quadrilátero Ferrífero.

Author	Sample	Test type	σ'_v (kPa)	e	k (m/s)
Santos, 2004	Monjolo Dump - Remolded S.	Rigid Wall Permeameter - Constant-Head Test	-	0,67-0,62	$4,77 \times 10^{-5}$ ($7,66 \times 10^{-5}$-$8,37 \times 10^{-6}$)*
			-	0,77-0,70	$8,94 \times 10^{-5}$ ($1,03 \times 10^{-4}$-$7,82 \times 10^{-5}$)*
			-	0,86-0,81	$9,45 \times 10^{-5}$ ($1,54 \times 10^{-4}$-$1,75 \times 10^{-5}$)
		Flow Pump - Constant-Head Test	-	0,98-0,91	$6,00 \times 10^{-5}$ ($9,90 \times 10^{-5}$-$2,09 \times 10^{-5}$)*
			-	0,67-0,62	$4,80 \times 10^{-5}$ ($7,63 \times 10^{-5}$-$9,66 \times 10^{-6}$)*
			-	0,77-0,70	$8,91 \times 10^{-5}$ ($1,02 \times 10^{-4}$-$7,85 \times 10^{-5}$)*
			-	0,86-0,81	$9,32 \times 10^{-5}$ ($1,50 \times 10^{-4}$-$1,67 \times 10^{-5}$)
			-	0,98-0,91	$6,23 \times 10^{-5}$ ($1,01 \times 10^{-4}$-$2,35 \times 10^{-5}$)*
	Monjolo Dum - Undisturbed S.	Flow Pump - Constant-Head Test	-	0,86-0,79	$8,86 \times 10^{-5}$ ($1,20 \times 10^{-4}$-$6,62 \times 10^{-5}$)*
	Monjolo Dump - *In Situ*	Borehole Constant-Head Test	-	0,86-0,79	$1,45 \times 10^{-4}$ ($2,01 \times 10^{-4}$-$1,16 \times 10^{-4}$)*
		Guelph Permeameter - Two-Ponded Heights	-	0,86-0,79	$1,17 \times 10^{-4}$ ($1,42 \times 10^{-4}$-$9,12 \times 10^{-5}$)*
		Guelph Permeameter - Two or More Ponded Heights	-	0,86-0,79	$7,16 \times 10^{-5}$ ($1,03 \times 10^{-4}$-$3,51 \times 10^{-5}$)*
		Guelph Permeameter - Philip's Method	-	0,86-0,79	$1,02 \times 10^{-4}$ ($1,18 \times 10^{-4}$-$9,69 \times 10^{-5}$)*
		Guelph Permeameter - One-Ponded Height	-	0,86-0,79	$8,94 \times 10^{-5}$ ($1,01 \times 10^{-4}$-$7,81 \times 10^{-5}$)*
Dornas, 2008	Forquilha III Dam - Remolded S.	Oedometer test	Unspecified	< 0,70	$4,58 \times 10^{-7}$ ($5,88 \times 10^{-7}$-$3,28 \times 10^{-7}$)
Alves, 2009	Pontal Dam - Overflow - Remolded S.	Flow Pump - Constant-Head Test	-	1,10-0,80	$3,35 \times 10^{-8}$ ($5,60 \times 10^{-8}$-$1,10 \times 10^{-8}$)
	Pontal Dam - Sump CB3 - Remolded S.		-	0,84-0,75	$1,50 \times 10^{-6}$ ($1,70 \times 10^{-6}$-$1,30 \times 10^{-6}$)
	Pontal Dam - Underflow -Remolded S.		-	0,86-0,80	$1,04 \times 10^{-5}$ ($1,10 \times 10^{-5}$-$9,80 \times 10^{-6}$)
Rezende, 2013	Fundão Dam - Undisturbed S.	Rigid Wall Permeameter - Constant-Head Test	-	Unspecified	$3,72 \times 10^{-6}$ ($9,00 \times 10^{-6}$-$1,10 \times 10^{-6}$)
		Oedometer Test	12,49 - 3196,47	0,76-0,45	$2,84 \times 10^{-6}$ ($3,65 \times 10^{-6}$-$1,37 \times 10^{-6}$)
			24,97-3196,47	1,33-0,79	$2,31 \times 10^{-6}$ ($3,90 \times 10^{-6}$-$1,85 \times 10^{-6}$)
			99,89-3196,47	0,65-0,52	$3,54 \times 10^{-6}$ ($5,25 \times 10^{-6}$-$2,50 \times 10^{-6}$)
		Flexible Wall Permeameter - Constant-Head Test	75-600	Unspecified	$1,02 \times 10^{-5}$ ($1,48 \times 10^{-5}$-$4,96 \times 10^{-6}$)
			75-600	Unspecified	$7,41 \times 10^{-6}$ ($8,96 \times 10^{-6}$-$3,80 \times 10^{-6}$)
			75-600	Unspecified	$3,04 \times 10^{-6}$ ($2,21 \times 10^{-6}$-$3,20 \times 10^{-6}$)

Author	Sample	Test type	σ'_v (kPa)	e	k (m/s)
Morgenstern et al., 2016	Fundão Dam - Coarse T. - Remolded S.	Oedometer Test	6,3-100	0,86-0,82	$1,32 \times 10^{-8}$ ($3,10 \times 10^{-8}$-$4,00 \times 10^{-9}$)
			25-300	0,82-0,79	$1,68 \times 10^{-9}$ ($9,10 \times 10^{-10}$-$1,10 \times 10^{-9}$)*
			50-600	0,79-0,77	$4,35 \times 10^{-10}$ ($1,80 \times 10^{-9}$-$9,90 \times 10^{-11}$)
			50-3200	0,77-0,70	$1,15 \times 10^{-10}$ ($3,20 \times 10^{-10}$-$9,50 \times 10^{-11}$)
	Fundão Dam - Slimes - Remolded S.	Oedometer Test	2-1024	1,05-0,73	$2,49 \times 10^{-9}$ ($2,60 \times 10^{-9}$-$8,40 \times 10^{-10}$)
		Large Strain Consolidation Test	0,4 - 1000	2,61-0,83	$2,26 \times 10^{-8}$ ($7,84 \times 10^{-8}$-$1,21 \times 10^{-9}$)
Carvalho, 2017	Fernandinho Mine - Future T. - Remolded S.	Rigid Wall Permeameter - Falling-Head Test	0-800	$e_0 = 0,80$	$7,45 \times 10^{-7}$ ($1,60 \times 10^{-6}$-$3,30 \times 10^{-7}$)
			0-800	$e_0 = 0,82$	$4,68 \times 10^{-7}$ ($1,90 \times 10^{-7}$-$2,80 \times 10^{-7}$)*
		Oedometer Test	200-800	0,71-0,66	$2,10 \times 10^{-8}$ ($2,50 \times 10^{-8}$-$1,30 \times 10^{-8}$)
			100-400	0,78-0,75	$1,55 \times 10^{-8}$ ($1,90 \times 10^{-8}$-$1,20 \times 10^{-8}$)*
Ferreira, 2018	Pontal Dam - Beach - Remolded S.	Flexible Wall Permeameter - Constant-Head Test	-	1,53-1,20	$2,21 \times 10^{-5}$ ($3,47 \times 10^{-5}$-$6,45 \times 10^{-6}$)
			-	0,66-0,56	$5,63 \times 10^{-8}$ ($8,37 \times 10^{-8}$-$2,10 \times 10^{-8}$)*
Miranda. 2018	Forquilha I Dam - Undisturbed S.	Flexible Wall Permeameter - Falling-Head Test	-	1,01-0,88	$6,55 \times 10^{-9}$ ($6,70 \times 10^{-9}$-$6,40 \times 10^{-9}$)*
	Forquilha I Dam - Remolded S.		-	0,84-0,65	$1,82 \times 10^{-6}$ ($3,48 \times 10^{-6}$-$1,67 \times 10^{-7}$)
Mohallem, 2018	Serra Azul Mine - Overflow - Remolded S.	Flexible Wall Permeameter - Falling-Head Test	-	0,81	$4,20 \times 10^{-8}$
	Serra Azul Mine - Underflow - Remolded S.		-	0,87-0,84	$1,25 \times 10^{-6}$ ($1,40 \times 10^{-6}$-$1,10 \times 10^{-6}$)*
Robertson et al., 2019	Fine Tailings - *In Situ*	Guelph Permeameter - Single Head Method 1 & 2	-	Unspecified	$2,50 \times 10^{-6}$
			-	1,33-0,95	$6,95 \times 10^{-6}$ ($6,20 \times 10^{-6}$-$7,70 \times 10^{-6}$)
	Berm Fill (Tailings) - *In Situ*		-	Unspecified	$1,83 \times 10^{-6}$ ($3,10 \times 10^{-6}$-$5,60 \times 10^{-7}$)
			-	0,86-0,70	$3,55 \times 10^{-5}$ ($3,90 \times 10^{-6}$-$3,20 \times 10^{-5}$)
	Slimes - *In Situ*	Guelph Permeameter - Single Head Method 1 & 2	-	1,62-1,15	$1,08 \times 10^{-6}$ ($2,30 \times 10^{-6}$-$4,90 \times 10^{-7}$)

*The highest values of hydraulic conductivity in parentheses are not associated with the highest values of void ratio.

Tailings (coarse and fine) results are presented in the white lines and the slimes results are presented in the gray lines. Source: elaborated by the author.

The range of variation of the hydraulic conductivity is very similar to the one presented by Vick (1990): 9,50 x 10^{-11} m/s (MORGENSTERN et al., 2016) to 2,01 x 10^{-4} m/s (SANTOS, 2004). However, the lowest k-value was obtained in an oedometer test in coarse tailings with e = 0,70, which does not match the expected values for the material. This value is even lower than the values obtained for slimes of the same TSF, analyzed by the same authors.

Moreover, Miranda (2018) presents undisturbed samples with void ratios e = 1,01 and e = 0,88 with hydraulic conductivities a hundred times lower than the values obtained for remolded samples of the same material with void ratios e = 0,65 and e = 0,84. It was expected that the samples with lower void ratios presented lower hydraulic conductivities – on a scale of five to ten times lower, not about a factor of a hundred.

Most of the samples shown in Table 2.8 were between the e = 0,60 and e = 0,90. For this range of void ratios, taking the average values of each author and excluding the sample analyzed by Morgenstern et al. (2016), considered as an outlier, the average value of the hydraulic conductivity of the tailings is 1,92 x 10^{-5} m/s, with a high standard deviation of 3,36 x 10^{-5} m/s.

In the tests that k was calculated to different confining stresses, there was a progressive reduction of its value with the increasing stresses, and void ratio reduction. Except for the sample analyzed by Morgenstern et al. (2016), which reduced three hundred times the initial value, the coarse tailings, in general, presented a variation of one-half to five times the initial value, following the usual reduction presented by Vick (1990). The slimes studied by Morgenstern et al. (2016) reduced three times the initial value in the oedometer test and, in the large strain consolidation test, at the final void ratio, the hydraulic conductivity was sixty times lower than the initial value.

2.4.7 ONE-DIMENSIONAL CONSOLIDATION

Both tailings and slimes are more compressible than similar natural soils with the same void ratios and under the same loading conditions. It occurs because of their grading characteristics, high particles' angularity, and loose depositional state (VICK, 1990).

According to Vick (1990), regardless of some slimes, tailings commonly do not present a clear break between the recompression line and the normal consolidation line, presenting in the (σ'_v,

e) space an extensive curvature even after the preconsolidation. Therefore, the compressibility indexes must be defined together with the stress range over which they apply.

The compressibility of tailings and slimes is affected mainly by the initial void ratio and density. The looser the material, the higher the compression under loading. Moreover, some tailings may show slow convergence of the compression curves in different initial densities to a singular NCL. The silt-sized gold tailings studied by Li et al. (2018) presented some convergence only at 20 MPa, which is much higher than the stresses in TSFs. It means that the in-situ specific volume is affected by the depositional density.

The compression index (C_c) of tailings is commonly between 0,05 and 0,10, and the C_c of slimes tends to be three to four times higher. However, it is hard to generalize the compressibility behavior of tailings because some materials present uncommon characteristics (VICK, 1990).

In coarse tailings, the primary consolidation is rapid. According to Vick (1990), coarse tailings present a coefficient of consolidation (C_v) between 5 x 10^{-1} to 10^{2} cm^2/s while slimes show similar C_v to natural clays, about 10^{-2} to 10^{-4} cm^2/s. The C_v has little correlation to void ratio variation and it can be more affected by permeability or stress-strain characteristics depending on the void ratio.

Vick (1990) states that tailings may have little secondary consolidation, and it may be associated with particle rearrangement and grain-to-grain sliding under loading. Even though, according to Robertson et al. (2019), one of the main causes of Feijão Dam I collapse was the ongoing internal strains due to creep under high shear stresses.

Table 2.9 presents the consolidation parameters of tailings generated in facilities located in the Quadrilátero Ferrífero found in the literature. The table displays the values obtained by the authors for each sample analyzed by them.

Regardless of void ratio and stress ranges, the C_c values fluctuate from 0,045 and 0,40, with an average of 0,12, in the tailings, and from 0,120 to 0,273, with an average of 0,20, in slimes. Except for the values of 0,40 and 0,25 given by Rezende (2013), the C_c values found for the iron ore tailings and slimes of the Quadrilátero Ferrífero are befitting to the ranges presented by Vick (1990).

Table 2.9 – Consolidation parameters of iron ore tailings from the Quadrilátero Ferrífero.

Authors	Sample	σ'_v (kPa)	e_i	e_f	C_c	C_r	σ'_{vc_C}* (kPa)	σ'_{vc_P}** (kPa)	C_v (cm²/s)	m_v (cm²/N)
Dornas, 2008	Forquilha III Dam - Tailings - Remolded Sample Bl. 14	12,5-100	< 0,70	-	0,082	-	-	-	-	-
		100-1600	< 0,70	-	0,139	-	-	-	-	-
	Forquilha III Dam - Tailings - Remolded Sample Bl. 19	12,5-100	< 0,70	-	0,047	-	-	-	-	-
		100-1600	< 0,70	-	0,110	-	-	-	-	-
Rezende, 2013	Fundão Dam - Tailings - Undisturbed Sample PT-000	12,5-3200	0,76	0,45	0,40	-	798	966	-	-
	Fundão Dam - Tailings - Undisturbed Sample PT-010	12,5-3200	1,33	0,79	0,25	-	85	44	-	-
	Fundão Dam - Tailings - Undisturbed Sample PT-043	12,5-3200	0,65	0,52	0,10	-	109	77	-	-
Ferreira, 2016	Germano Dam, Bay 3 - Slimes (stiff) - Remolded Sample	12,5-1600	0,8	-	0,139 (0,120-0,161)	0,022 (0,020-0,024)	566,67 (525-610)	-	0,012	-
	Germano Dam, Bay 3 - Slimes (firm) - Remolded Sample	12,5-1600	0,98	-	0,257 (0,251-0,260)	0,027 (0,024-0,032)	336,67 (310-377)	-	0,013	-
	Germano Dam, Bay 3 - Slimes (soft) - Remolded Sample	12,5-1600	1,09	-	0,265 (0,261-0,273)	0,022 (0,021-0,024)	151,33 (124-190)	-	0,014	-
Morgenstern et al., 2016	Fundão Dam - Tailings - Remolded Sample	3-100	0,86	0,82	0,049	0,00416	-	-	0,025	$1,6 \times 10^{-3}$
		100-300	0,82	0,79	0,045	0,00556	-	-	0,025	$4,4 \times 10^{-4}$
		300-600	0,79	0,77	0,064	0,00514	-	-	0,032	$3,2 \times 10^{-4}$
		600-3200	0,76	0,70	0,099	0,00415	-	-	0,093	$1,1 \times 10^{-4}$
	Fundão Dam - Remolded Sample - Slimes	2-1024	1,07	0,73	0,141	-	-	-	0,016	$5,2 \times 10^{-4}$
Carvalho, 2017	Fernandinho Mine - Future Tailings - AR-PCI-01 - Remolded Sample	12,5-1600	0,766	0,618	0,127	0,0131	-	170,7	0,0057	-
	Fernandinho Mine - Future Tailings - AR-PCF-06 - Remolded Sample	12,5-1600	0,81	0,688	0,108	0,0245	-	212,6	0,0042	-

Authors	Sample	σ'_v (kPa)	e_i	e_f	C_c	C_r	σ'_{vc_C}* (kPa)	σ'_{vc_P}** (kPa)	C_v (cm^2/s)	m_v (cm^2/N)
Ferreira, 2018	Pontal Dam, Beach - Remolded Sample	5-2400	0,972	0,685	0,088	-	-	-	-	-
Robertson et al., 2019	Feijão Dam I – Hist. Data - Coarse Tailings - Remolded Sample PI-01	6-1200	1,27	-	0,108	-	427	-	0,00019	-
	Feijão Dam I – Hist. Data - Fine Tailings - Remolded Sample PI-02A	6-1200	1,50	-	0,135	-	92	-	0,00024	-
	Feijão Dam I – Hist. Data - Coarse Tailings - Remolded Sample PI-03	6-1200	0,43	-	0,122	-	51	-	0,00028	-

*σ'_{vc_C} - past maximum effective vertical stress determined by Casagrande's method.

**σ'_{vc_P} - past maximum effective vertical stress determined by Pacheco Silva's method.

Tailings (coarse and fine) results are presented in the white lines and the slimes results are presented in the gray lines. Source: elaborated by the author.

The C_v, however, showed high variability. Both coarse tailings, and slime's samples studied by Ferreira (2016) and Morgenstern et al. (2016) exhibited similar values of C_v (average of 0,029) while the samples analyzed by Carvalho (2017) presented C_v ten times lower (average of 0,005), and the samples of Robertson et al. (2019) a hundred times lower (average of 0,00024).

The recompression index (C_r) ranged from 0,0041 to 0,025 in tailings, with an average of 0.0094. In the slime samples of Ferreira (2016) C_r ranged from 0,020 to 0,032, with an average of 0,024.

The high variability of the parameters may be associated not only with the different initial states of the samples collected by each author but also with the grading characteristics and particle's angularity. Different deposits show different iron (more angular particles) and silica contents, as it is presented in Table 2.2 and Table 2.3. Moreover, the compression and recompression indexes can also be affected by the adopted sample preparation and testing methodology, as will be discussed in 4.5.1.

2.4.8 STRENGTH PARAMETERS

According to Torrez-Cruz and Santamarina (2019), the frictional parameters of tailings are not significantly affected by their mineralogical composition. Nevertheless, tailings with more angular grains tend to have higher shear strength than similar natural soils under the same stress-state conditions. Vick (1990) states that, when compared with natural soils, the frictional angle of tailings is usually 3º to 5º higher, and most values are between 30º and 37º. The author also says that there is no significant variation of the frictional angle for coarse and tailings, and slimes.

Table 2.10 presents the critical state frictional angle (φ'_c) of the tailings generated in facilities located in the Quadrilátero Ferrífero found in the literature. It also displays values of peak undrained strength ratio ($s_{u,p}/p'_0$) of samples with contractive behavior, and critical undrained strength ratio ($s_{u,c}/p'_0$) of samples with contractive and brittle behavior. The table displays the values obtained by the authors for each different material studied by them. All parameters were determined after triaxial compression tests. When more than one sample was tested for the same material, it is shown the average value and the range of obtained values between parentheses. Furthermore, the tests were reinterpreted following the critical state approach when the stress paths were presented by the authors.

Table 2.10 – Strength parameters of iron ore tailings from the Quadrilátero Ferrífero.

Author	Sample	φ'_c	$s_{u,p}/p'_0$	$s_{u,c}/p'_0$
Presotti, 2002	Monjolo Dump (hydraulic fill)	35,2 (33,8-37,1)	-	-
Pereira, 2005	Germano Pit	32,2*	-	-
	Itabiruçu Dam	33,7*	0,45 (0,43-0,46)*	-
	Forquilha III Dam	36,2*	0,48 (0,44-0,54)*	-
	Forquilha II Dam	32,6*	0,34*	0,11 (0,06-0,14)*
	Campo Grande Dam	32,4*	0,54 (0,53-0,54)*	-
	Córrego do Doutor Dam	32,8*	0,35 (0,34-0,36)*	0,17 (0,13-0,23)*
Dornas, 008	Forquilha III Dam	38,2 (36,0-41,0)	0,33 (0,23-0,40)	0,18 (0,10-0,29)
Silva, 2010	Feijão Dam I	37,7 (34,1-41,3)	-	-
Silva, 2014	Itatiaiuçu Dam	34,7 (31,0*-37,0)	0,37 (0,29-0,53)	0,13 (0,05-0,18)*
Ferreira, 2016	Germano Dam, Bay 3 - Coarse Tailings	36,5*	-	-
	Germano Dam, Bay 3 - Slimes	39,2 (37,1-41,8)*	-	-
Morgenstern et al.,2016	Fundão Dam - Coarse Tailings	33,0	-	-
Carvalho, 2017	SD-02 Pile - Stored tailings	35,0 (30,5-37,7)	-	-
	Fernandinho Mine - Future tailings	34,5 (34,0-35,0)*	-	-
Ferreira, 2018	Pontal Dam - Arm I	34,4 (33,0-36,4)*	-	-
	Pontal Dam - Beach	35,9 (35,6-36,2)	-	-
Miranda, 2018	Forquilha I Dam	35,2 (32,1-38,0)	-	-
Mohallem, 2018	Serra Azul Mine - Underflow	30,5 (29,7-31,2)	-	-
	Serra Azul Mine - Overflow	30,1	-	-
Robertson et al., 2019	Feijão Dam I - Hist. Data - Coarse Tailings	35,3 (29,9-39,6)	-	-
	Feijão Dam I - Hist. Data - Fine Tailings	36,1 (34,5-36,9)	-	-
	Feijão Dam I - Coarse Tailings	34	0,51	0,01
	Feijão Dam I - Fine Tailings	33	0,42	0,005
General	Average	34,5	0,42	0,10
	Standard Deviation	2,2	0,08	0,08
	Maximum	29,7	0,23	0,005
	Minimum	41,8	0,54	0,29

*Values recalculated from the stress-paths presented by the authors.

Tailings (coarse and fine) results are presented in the white lines and the slimes results are presented in the gray lines. Source: elaborated by the author.

The average value of φ'_c = 34,5º is in the range of values presented by Vick (1990). Moreover, the standard deviation of 2,2º indicates that most of the φ'_c values are between 32,3º and 36,7º, which are also in the range presented by Vick (1990). The maximum value of φ'_c = 41,8º is

referent to a test that has shown dilatant behavior, and probably, has not reached the critical state.

Presotti (2002) has calculated ϕ'_c from the end of the triaxial tests. However, the author also presented a small "residual cohesion intercept" varying from 0 to 2,2 kPa (average of 0,6 kPa). As the effective stress paths of the tests were not made available by the author, they could not be reinterpreted. Thus, it is expected some variation of the ϕ'_c presented in Table 2.10 for the tailings disposed at Monjolo Dump.

Both peak and residual undrained shear strength ratios showed considerable variability. $s_{u,p}/p'_0$ ranging from 0,23 to 0,54 and $s_{u,c}/p'_0$ ranging from 0,005 to 0,29. As discussed in 2.3.6, the undrained strength is a state-dependent parameter. Thus, the undrained strength parameters are affected by variations of the confining stresses and sample void ratios.

It is relevant to mention that the shear strength is related to the three main modes of shear (see Figure 2.25 and Figure 2.26): compression, simple shearing, and extension, which mobilize the largest, the intermediate, and the smallest strengths, respectively (Sadrekarimi, 2014). Thus, as the values presented in Table 2.10 refer to triaxial compression tests, they are only representative of mobilized strength by compression so, it would be reckless to adopt these values as the only strength parameters in a state-of-the-art project.

Figure 2.25 – "Variation of mode of shear along a typical failure surface beneath a slope."

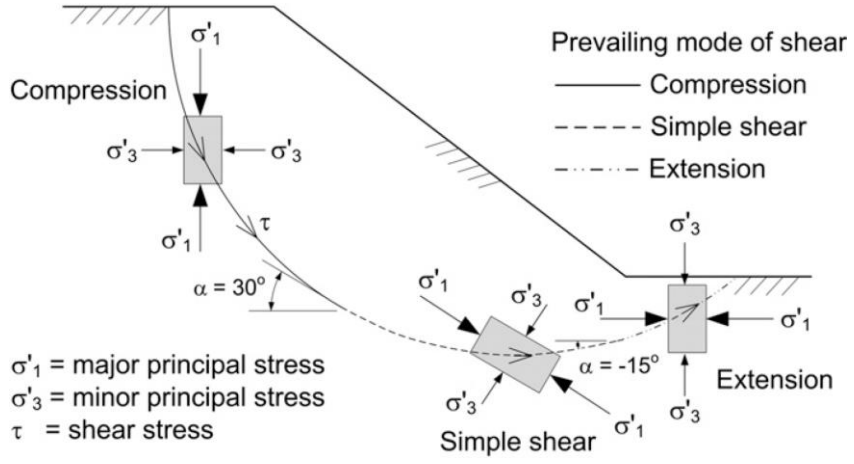

Source: Sadrekarimi, 2014.

Figure 2.26 – "Comparison of Bonnie silt in simple shear, triaxial compression and triaxial extension (all tests at initial confining stress of 80 kPa, 0,683 < e0 < 0,753)."

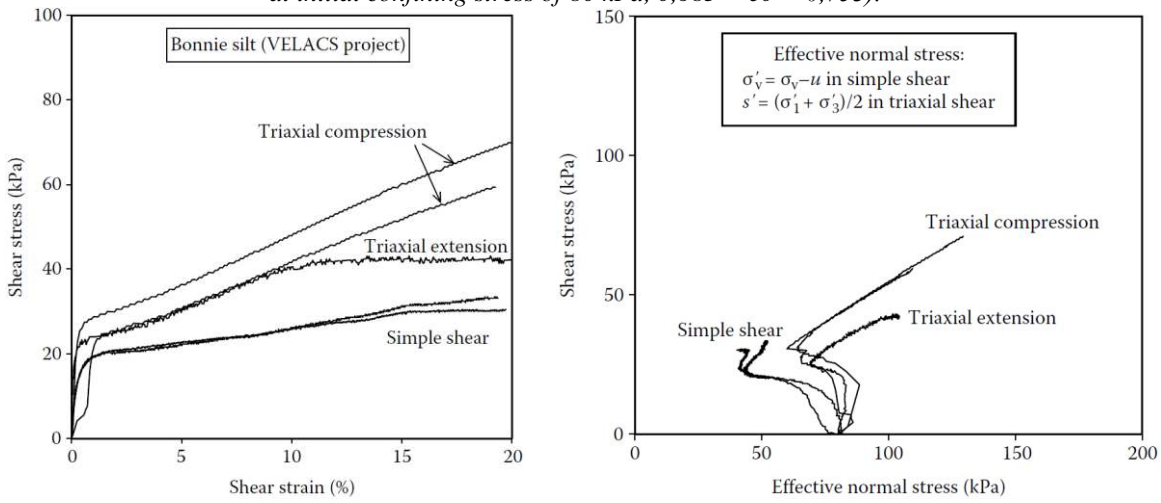

Source: Jefferies and Been, 2015.

2.4.9 CRITICAL STATE MODEL

Advanced modeling has been done for the two major TSFs of the Quadrilátero Ferrífero that have collapsed over the past years, Fundão Dam and Feijão Dam I. Both Morgenstern et al. (2016) and Robertson et al. (2019) have adopted NorSand to model the tailings behavior.

According to Shuttle and Jefferies (2010), NorSand is easy to use because it requires few parameters, most of them familiar to geotechnical engineers and others easy to understand and measure. The authors emphasize that, despite the name, NorSand can be adopted to model the behavior of "(…) any soil in which particle to particle interactions are controlled by contact forces and slip rather than bonds".

Besides the effect of void ratio on soil behavior, differently from more conventional critical state models, as Cam Clay, NorSand also accounts for the dilatant behavior of dense soils and liquefaction-related behaviors of loose non-cohesive materials (SHUTTLE AND JEFFERIES, 2010).

In addition to the critical state parameters introduced in 2.3, the elastic shear modulus (G_{max}) and the plastic modulus (H) are also input properties for NorSand.

2.4.9.1 Elastic Shear Modulus

According to Jefferies and Been (2015), a model that is rigid in shear is not the most suitable, since elastic shear strains are everywhere in the soil. Therefore, elastic shear properties, such as the elastic shear modulus, must be added to the model. G_{max} is then defined by Equation 2.37.

$$G_{max} = G_{ref} \cdot \left(\frac{p'}{p'_{ref}} \right)^{n} \qquad \text{Equation 2.37}$$

Where G_{ref} is the shear modulus at the confining stress p'_{ref}, p' is the current confining stress, and n is dependent on the type of soil. n = 0 indicates a constant modulus, n = 1 is associated with clays and sands usually present n = 0,5 (JEFFERIES AND BEEN, 2015).

According to Hitcher (1996), the elastic shear modulus is not affected by drainage conditions, but it is affected by soil's state – void ratio and confining stresses – and fabric. Thus, G_{max} is usually measured in the field. It can also be measured in the laboratory by using resonant columns tests or bender elements (more common). However, soil fabric, especially in loose deposits, may be lost during the sampling process (JEFFERIES and BEEN, 2015).

According to Jefferies and Been (2015), the last resource when G_{max} is not measured is to estimate it, based on the G_{max} of similar materials, and calibrate into the critical state model (such as NorSand) to fit the stress path of the triaxial tests data. However, some precision is lost in this approach.

2.4.9.2 Plastic Modulus

To determine the plastic parameters is essential to estimate the soil behavior since plastic strains are an elementary soil response to load. While the elastic shear modulus controls the magnitude of elastic strains, the work hardening defined by the plastic modulus (H) controls the magnitude of plastic strains for a specific stress increment. Higher values of H give stiffer stress-strain curves. Moreover, the undrained soil strength is highly affected by the plastic modulus (JEFFERIES and BEEN, 2015).

According to Jefferies and Been (2015), just as the elastic shear modulus, the plastic modulus may be at least in part correlated with soil particle arrangement. Thus, it is affected by the sample preparation. Nevertheless, there are no techniques to determine plastic modulus *in situ* yet.

The plastic modulus is then defined by iterative forward modeling (IFM). It consists of guessing different values of H until the adopted constitutive model converges to the best fit (JEFFERIES AND BEEN, 2015). Notice that the plastic modulus depends on the initial state parameter.

Therefore, it is subdivided into two constants H_0 and H_ψ and the plastic modulus is determined by Equation 2.38.

$$H = H_0 - H_\psi \cdot \psi \qquad \text{Equation 2.38}$$

Where, H_0 and H_ψ are constants.

2.4.9.3 Constitutive Model Properties

Table 2.11 presents the critical state model properties of the tailings generated in facilities located in the Quadrilátero Ferrífero found in the literature. The table displays the values obtained by the authors for each different material studied by them.

For both authors, the CSL is defined in the (p', q, e) space, where the void ratio is defined as e = ν – 1. As mentioned in 2.4.1, Robertson et al. (2019) worked with three different samples: fine tailings, average tailings, and coarse tailings. For each sample, it was defined both linear and curved critical state lines. All other characteristics were kept the same in all three samples.

Table 2.11 – Critical state model properties of iron ore tailings from the Quadrilátero Ferrífero.

Property		Morgenstern et al., 2016	Robertson et al., 2019
Semi-log. CSL	Γ	0,865	1,12/1,04/1,02
	λ	0,024	0,039
Curved CSL	A	-	1,29/1,22/1,19
	B	-	0,34
	C	-	0,11
M_{tc}		1,33	1,38
N		0,38	0,27
χ_{tc}		7,3	6
G_{max}		$G_{max} = 60(p'/p_{ref})^{0,45}$*	$G_{max} = 100(p'/p_{ref})^{0,5}$*
H_0		156	160
H_ψ		756	1037

*Where p_{ref} = 100 kPa

Source: elaborated by the author.

Torrez-Cruz and Santamarina (2019) exhibited that the critical state parameters of non-plastic tailings follow the same tendency of non-plastic soils. Therefore, inferences about non-plastic soil behavior may be used for non-plastic tailings concerning the differences associated with the particle size distribution, particle geometry, and mineralogy.

From Table 2.11, both values of λ_e determined by the authors are considerably small. According to Torrez-Cruz and Santamarina (2019), $\lambda < 0{,}10$ are associated with high hardness soils, such as soils composed mainly of quartz. Interesting notice that, based on the percent presented for Germano Pit and Germano Dam, by Pereira (2005) and Tolentino (2010), which are structures

located in the same mine as the Fundão Dam and whose tailings showed considerable similarity, the coarse tailings of Fundão Dam present considerable amounts of quartz, but both coarse and fine tailings of Feijão Dam I showed very low quartz content.

As stated in Torrez-Cruz and Santamarina (2019), the critical state strength ratio (M) of tailings is in the same range of non-plastic soils. Also, soils with angular particles tend to present higher M-values than soils constituted of round particles. According to Shuttle and Jefferies (2010), for silty tailings, not only high M-values are expected, but also χ_{tc} is expected to be out of the typical range for non-plastic soils (between 2,5 and 4,5).

M_{tc} = 1,33 and M_{tc} = 1,38 are equivalent to values of φ'_c = 33º and φ'_c = 34,1º, respectively. These values are considerably high, when compared to natural silty sand soils, but they are still lower than the average value of φ'_c = 34,5º presented on 2.4.8.

The values of χ_{tc} are also high, and both values are out of the typical range presented by Shuttle and Jefferies (2010) for natural soils.

3 METHODOLOGY

This chapter presents the methodology adopted to develop the laboratory and field tests describing the relevant sample, test preparation procedures, and equipment specifications.

For this work, samples of filtered iron ore tailings were collected at a mining complex located in the Quadrilátero Ferrífero, state of Minas Gerais, Brazil, where hematite is the main mineral exploited. In the process adopted at the mining complex, the underflow and overflow tailings are not separated, and the total tailings have been press filtered and deposited in the TSFs.

Because of the high production of tailings, the company is studying the feasibility of building dry stacks higher than 100 m. Whereas 100 m is the limit of the empirically based knowledge existent (see 2.2), it is a common concern of the company and us, researchers, to better understand the tailings behavior under different degrees of compaction and confining stresses.

The experimental program has been mainly developed at the Laboratório de Mecânica dos Solos of the Universidade Federal de Viçosa (LMS-UFV) and at the Laboratório de Geotecnia (LabGeo) at the Faculdade de Engenharia da Universidade do Porto (FEUP). Also, the water retention curves (see 3.8) of the tailings have been determined at the Laboratório de Física do Solo of UFV.

In addition, a trial embankment was built by mining company, in which were performed CPTu and field compaction quality-control tests that were made available for the research.

3.1 SAMPLE PREPARATION

Initially, the collected sample was dried at room temperature, loosened, sieved, and homogenized (see Figure 3.1). Then, the tailings were kept in airtight plastic bags, and before each test, the material was loosened, sieved, and homogenized again to avoid lumps.

Figure 3.1 – Sample preparation.

(a) Collected sample in a plastic bag; (b) Sample dried at room temperature; (c) Sample after loosening, sieving, and homogenizing. Source: elaborated by the author.

3.2 INDEX TESTS

Tests were performed to determine the Atterberg limits, maximum and minimum void ratios, particle size distribution, and specific gravity of the iron ore tailings. The samples used in the index tests were prepared according to the ABNT NBR 6457:2016.

3.2.1 PARTICLE SIZE DISTRIBUTION

The particle size analyses were conducted conforming to the ISO 17892-4:2016 and the ABNT NBR 7181:2016. It was run a total of twenty-four tests at LMS-UFV, one before the triaxial tests and the other twenty-three after the triaxial tests. The objective was to identify the evolution of the material – existence or not of particle crushing – due to static compaction and triaxial compression under the confining pressures of 100 kPa, 200 kPa, and 400 kPa.

Furthermore, it was run three additional tests at LabGeo: two of them performed to check the samples' uniformity, and another one performed with the material resulting from the standard Proctor test to check the evolution of the material due to dynamic compaction.

3.2.2 SPECIFIC GRAVITY

Three tests were performed to define the specific gravity of the filtered iron ore tailing sample. The tests followed the ISO 17892-3:2015 and the ABNT NBR 6458:2016. One test was done at LMS-UFV, and the other two tests were performed at LabGeo to verify the homogeneity of the samples sent to the lab.

3.2.3 ATTERBERG LIMITS

It was run a plasticity limit test and a liquid limit test for the studied sample conforming to the ABNT NBR 7180:2016 and the ABNT NBR 6459:2016, respectively.

3.2.4 MAXIMUM AND MINIMUM VOID RATIOS

It was run the minimum and maximum void ratios tests for the studied sample following the test method A.1 of ABNT NBR 16843:2020 and test method A of ABNT NBR 16840:2020, respectively.

3.3 PROCTOR COMPACTION TEST

The samples used in the compaction tests were prepared according to the ABNT NBR 6457:2016. The standard Proctor compaction tests were performed in both institutions, UFV and FEUP. The adopted procedures followed the ABNT NBR 7182:2016 and LNEC E 197:1966, respectively.

At LMS-UFV, to determine the compaction curve, it was run four tests, each test with five points with different water contents. It was used the standard Proctor mold (volume of 9,44 x 10^{-4} m³) and the hammer of 2,5 kg. For each point, the tailings were compacted in three layers, following the procedures of the ABNT NBR 7182:2016.

At LabGeo it was run an additional test with six points with different water contents to define the compaction curve of the sample sent to FEUP. On this test, it was also used the standard Proctor mold and the hammer of 2,5 kg. For each point, the soil was compacted in three layers following the LNEC E 197:1966.

3.4 TRIAXIAL COMPRESSION TEST

The testing methodologies adopted at LMS-UFV and LabGeo were both developed based on Head (1992). Moreover, both procedures were in conformity with ISO 17892-9:2018, ASTM D4767:2011(2020), and ASTM D7181:2020.

The triaxial compression tests were conducted to study the effect of tailings' compacity with four different degrees of compaction: 93%, 95%, 97%, and 100% of Proctor maximum dry unit weight. For each degree of compaction, to analyze the effect of the confining pressures, it was run five consolidated drained tests (CD) and five consolidated undrained tests (CU) under the effective confining stresses of 100 kPa, 200 kPa, 400 kPa, 800 kPa, and 1600 kPa. Additionally, it was done three extra CD tests – with DC = 93%, 95%, and 97% – and two extra CIU tests – with DC = 93% and 100% – under the effective confining stress of 1900 kPa.

The tests with effective confining pressures from 100 kPa to 400 kPa were conducted at LMS-UFV, while the tests with effective confining pressures above 400 kPa were conducted at LabGeo. All triaxial compression tests of the experimental program were performed in saturated and isotropically consolidated samples. It was adopted a minimum Skempton's porewater pressure coefficient B of 0,98 as the indicator of the complete saturation of the tested specimens.

To reach $B \geq 0{,}98$, at LabGeo the samples were first percolated with CO_2, then with de-aired water. The volumes of both substances used to percolate each sample were at least two times the voids volume of the sample. Later, always keeping the effective confining pressure of 10 kPa, it was applied back pressure to the specimens. The maximum back pressure necessary was 300 kPa.

At LMS-UFV, to reach $B \geq 0{,}98$, the samples were percolated only with de-aired water. Thus, higher back pressure was necessary to saturate the samples, 600 kPa. Furthermore, just as at LabGeo, when applying the backpressure, the effective confining stress was always kept equal to 10 kPa.

At both laboratories, the consolidation was done by increasing the chamber's pressure until the difference between backpressure and confining pressure reachs the desired effective consolidation stress. For shearing, it was adopted a controlled axial strain rate between 0,010 mm/min and 0,020 mm/min, while the confining pressure was kept approximately constant.

At LMS-UFV a conventional equipment, under the ASTM D4767:2011, was used to perform the test. At LabGeo, however, it was used chambers with enlarged and lubricated end platens, which allow larger axial strains than the conventional equipment (higher than 20%), keeping the sample's cylindrical geometry. Moreover, it was used a top platen-loading ram connection that allows the top cap to rotate during shearing and reduces tilting of the top cap. The equipment used also allows soil freezing at the end of the test, which permits taking the final water content more precisely. The Appendix A presents the description of the apparatus and the methodology adopted at LabGeo to perform the triaxial compression tests.

3.4.1 SAMPLE PREPARATION

At UFV it was adopted tailings samples ca. 50 mm in diameter x 100 mm long. Meanwhile, at FEUP it was used sixteen specimens ca. 72 mm in diameter x 144 mm long, and five samples ca. 60 cm in diameter x 120 mm.

Based on the water contents and dry unit weights determined on the standard Proctor test for each degree of compaction (93%, 95%, 97%, and 100%), the triaxial test specimens were prepared through static compaction using a split mold and a press (see Figure 3.2.a and Figure 3.2.b).

Figure 3.2 – Preparation of the triaxial compression test specimens.

(a) Press used to compact the samples; (b) Equipment used and portions of material separated for each layer; (c) Specimen being compacted; (d) Scarified layer after its compaction; (e) Prepared specimen beside the cylindrical ruler. Source: elaborated by the author.

The samples at UFV, were compacted in four layers assisted by a cylindrical ruler. For each layer, it was determined its corresponding volume and the exact mass of tailings, as shown in Figure 3.2.b and Figure 3.2.c. After the compaction of each layer, the material was scarified to avoid smooth planar surfaces between the compacted layers and improve the adherence between a layer and another (see Figure 3.2.d).

The specimens tested at LabGeo have followed the same preparation procedures, except for the fact that the specimens were compacted in six layers instead of four.

3.5 HYDRAULIC CONDUCTIVITY TEST

The hydraulic conductivity tests were performed in the same specimens molded for the triaxial test. Four tests (one for each degree of compaction) were conducted after the saturation stage, at 10 kPa of effective confining pressure, and thirty tests were performed after the isotropic consolidation stage, at the different effective confining stresses (100 kPa to 1900 kPa): eight specimens with DC = 93%, eight with DC = 95%, eight with DC = 97%, and six with DC = 100%.

The performed tests followed the procedures of the ASM D5084:2016 for constant head tests.

3.6 ISOTROPIC CONSOLIDATION

It was done seven isotropic consolidation tests: two with DC = 93% and ultimate mean effective stresses (p'_{ult}) of 1900 kPa and 3000 kPa; two with DC = 95% and p'_{ult} equal to 1900 kPa and 2100 kPa; one with DC = 97% and p'_{ult} = 1900 kPa; and two with DC = 100% and p'_{ult} equal to 1400 kPa and 1900 kPa.

The tests were performed in the triaxial test chamber. In each of them, the chamber's pressure was increased gradually and slowly enough to allow porewater pressure dissipation until reaching the target ultimate mean effective stress. Furthermore, all the tests with p'_{ult} = 1900 kPa were performed with two unloading-reloading cycles before reach the p'_{ult}.

The sample preparation followed the same procedure as the specimens used at the triaxial tests.

3.7 OEDOMETER TEST

The oedometer tests were conducted in loose and compacted samples, degrees of compaction of 93%, 95%, 97%, and 100% of standard Proctor. It was conducted thirteen tests: four unsaturated compacted tests with ultimate vertical effective stress ($\sigma'_{v,ult}$) equal to 3200 kPa, four saturated compacted tests with $\sigma'_{v,ult}$ equal to 3200 kPa, two saturated compacted tests with $\sigma'_{v,ult}$ equal to 6400 kPa, and three saturated loose tests with $\sigma'_{v,ult}$ equal to 2500 kPa, 3200 kPa and 6400 kPa.

In the saturated tests, the specimens were inundated right after the application of the seating load. Following the ABNT NBR16853:2020 and the ASTM D2435M:2011, the samples were submitted to a loading increment ratio equal to one, with a duration of 24 hours each, until reaching the ultimate load.

At the end of the loading process, the tailings were unloaded incrementally. The unloading increments had a shorter duration than the loading increments, and they not necessarily followed the increment ratio of one. No reloading was done in the oedometer tests.

3.7.1 SAMPLE PREPARATION

3.7.1.1 Loose specimen

The primary concern with preparing the loose specimens is to get homogeneous conditions with a high void ratio. Thus, it is necessary to determine the minimum water content to generate suction between the tailing grains and assure stable specimens after mold removal. For the oedometer test, the loose specimens were prepared with a void ratio of 1,30, and a water content of 7,5%.

For specimens' preparation, the tailing sample was moistened and homogenized with the established moisture content of 7,5%. The material was kept overnight in an airtight plastic bag to avoid moisture loss and allow the sample fines to be properly moistened.

Then, the specimens were molded directly into the floating ring following the moist tamping method presented by Jefferies and Been (2015). The ring, 50 mm in diameter and 19 mm thick, was filled in three layers: the first one 7 mm thick, and the two other layers 6 mm thick to reduce the effect of over compaction of the first layer.

Each layer was gently tamped and scarified in the end to avoid smooth planar surfaces between layers, just as it was done for the triaxial compression specimens. Figure 3.3 illustrates the specimen preparation procedure.

Figure 3.3 – Preparation of the oedometer test specimens compacted directly in the floating ring.

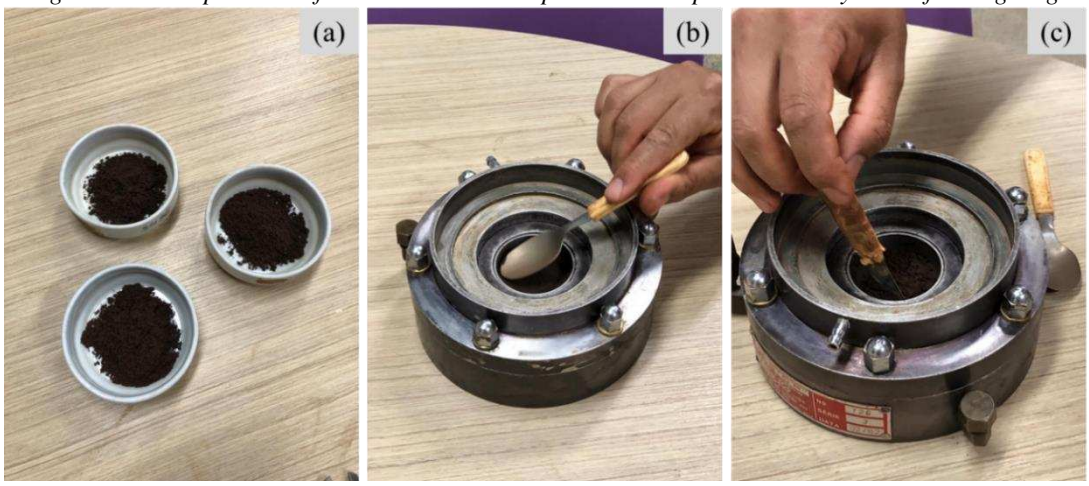

(a) Portions of material separated for each layer; (b) Placing and tamping of material; (c) Layer scarifying. Source: elaborated by the author.

3.7.1.2 Compacted specimens

Figure 3.4 – Preparation of the oedometer test carved specimens.

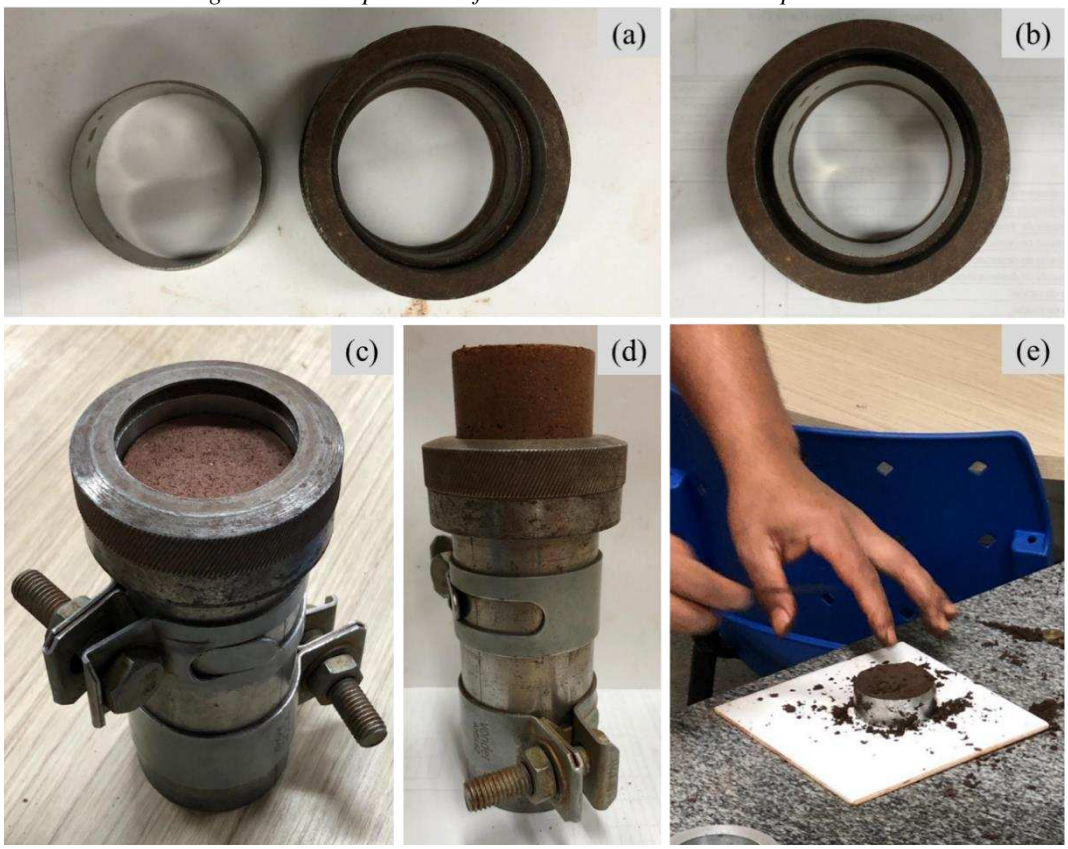

(a) Floating ring and mold; (b) Floating ring positioned inside the mold; (c) Set of molds to extract the compacted sample; (d) Floating ring positioned in the central part of the compacted sample; (e) Extracted sample being carved to fit the floating ring.

At UFV, the tailings were first compacted following the same procedure of triaxial compression tests (see 3.4.1). Then, the specimens were carved from the central portion of the compacted samples using the floating ring of the oedometer apparatus, just as illustrated in Figure 3.4.

At FEUP, the specimens were compacted directly in the floating ring, following the same procedure adopted for the loose specimens (3.7.1.1). Nevertheless, instead of gently tamping, the layers were compacted with a press.

3.8 SOIL-WATER CHARACTERISTIC CURVE

It has been defined the retention curves of the tailings sample compacted with 93% and 100% of the standard Proctor. A total of three specimens for each degree of compaction have been used. The retention curves were defined using the Richards' pressure chamber (see Figure 3.5) with five points of negative pressure (-10 kPa, -30 kPa, -60 kPa, -100 kPa and -1500 kPa) in accordance with the procedures presented in Teixeira and Behring (2017).

Figure 3.5 – Richards' pressure chambers of the Laboratório de Física do Solo – UFV.

Source: elaborated by the author.

3.8.1 SAMPLE PREPARATION

After compacting the samples following the same procedure of triaxial compression tests (see 3.4.1). It has carved specimens 5 cm thick from the central portion of the compacted mass.

3.9 FIELD TESTS

To evaluate the behavior of the filtered tailings compacted in the field, the mining company has built a trial embankment 15 m high compacted in lifts 0,5 m thick and minimum degree of compaction of 95% of standard Proctor. The company did not specify the exact dimensions of the trial embankment. However, according to them, the embankment was large enough to conventional trucks transporting the tailings and the compaction equipment traffic simultaneously. Also, the mining company has not indicated the equipment used to compact the filtered tailings, but they assured that the tailings have been compacted statically.

3.9.1 CPTU

The mining company performed two CPTu in the trial embankment whose test results were made available to the research.

According to the testing report, the cone used in the tests had a cone tip with a 10 cm² projected area, a 60º apex angle, and a 150 cm² friction sleeve. The tests were executed in the standard penetration speed (20 ± 5 mm/s) in accordance with the ABNT NBR 12069:1991. Additionally, no dissipation tests were performed since no significant excess of pore water pressure was registered during the CPTu tests.

3.9.2 COMPACTION QUALITY-CONTROL

In addition to the CPTu tests, to evaluate the quality of field compaction, the mining company determined the dry unit weight (γ_d) and water content (w) of 218 samples collected in different areas of the trial embankment. In each checked lift 0,5 m tick, it was collected a sample in the top portion of the layer and other in the base. The bulk unit weight (γ) was determined by the core cutter method, in accordance with the ABNT NBR 9813:2016, and the water content was determined following the procedures of the DNER-ME 213:1994.

The values of γ_d and w of each sample were compared with $\gamma_{d,max}$ and $w_{opt.}$ defined after standard Proctor tests performed every 1000 m^3 of compacted tailings. A total of 33 standard Proctor tests of reference were made available by the mining company together with the results of γ_d and w of the collected samples. The standard Proctor tests were performed according to the ABNT NBR 7182:2016.

3.10 EXPERIMENTAL PROGRAM

Table 3.1 summarizes all laboratory and *in situ* tests performed to characterize the filtered iron ore tailings.

Table 3.1 – Experimental Program.

Test	DC (%)	σ'_v or p' (kPa)	Quantity
Atterberg limits	-	-	1
Maximum void ratio	-	-	1
Minimum void ratio	-	-	1
Particle size distribution	-	-	27
Specific gravity	-	-	3
Standard Proctor compaction	-	-	5
Drained triaxial compression	93% of Proctor	100, 200, 400, 800, 1600, and 1900	6
	95% of Proctor	100, 200, 400, 800, 1600, and 1900	6
	97% of Proctor	100, 200, 400, 800, 1600, and 1900	6
	100% of Proctor	100, 200, 400, 800, and 1600	5
Undrained triaxial compression	93% of Proctor	100, 200, 400, 800, 1600, and 1900	6
	95% of Proctor	100, 200, 400, 800, and 1600	5
	97% of Proctor	100, 200, 400, 800, and 1600	5
	100% of Proctor	100, 200, 400, 800, 1600, and 1900	6
Isotropic consolidation	93% of Proctor	1900 and 3000	2
	95% of Proctor	1900 and 2100	2
	97% of Proctor	1900	1
	100% of Proctor	1400 and 1900	2
Oedometer - saturated sample	Loose Sample	2500, 3200, and 6400	3
	93% of Proctor	3200	1
	95% of Proctor	3200 and 6400	2
	97% of Proctor	3200	1
	100% of Proctor	3200 and 6400	2
Oedometer - unsaturated sample	93% of Proctor	3200	1
	95% of Proctor	3200	1
	97% of Proctor	3200	1
	100% of Proctor	3200	1
Flexible wall permeameter (constant-head test)	93% of Proctor	10, 100, 200, 400, 800, 1600, and 1900	9
	95% of Proctor	10, 100, 200, 400, 800, 1600, and 1900	9
	97% of Proctor	10, 100, 200, 400, 800, 1600, and 1900	9
	100% of Proctor	10, 100, 200, 400, 800, and 1600	7
Soil-water characteristic curve	93% of Proctor	-1500	3
	100% of Proctor	-1500	3
CPTu	-	-	2
In situ bulk unit weight & moisture content	-	-	218
Reference Proctor compaction	-	-	33

Source: elaborated by the author.

4 RESULTS AND DISCUSSION

This chapter describes the results and observations made from the experimental program presented in chapter 3. It will discuss the index properties, hydraulic conductivity, consolidation parameters, strength parameters, critical state and dilatancy parameters, plastic modulus, and elastic moduli of the tailings sample.

4.1 INDEX PROPERTIES

4.1.1 PARTICLE SIZE DISTRIBUTION

The particle size distribution curves obtained after testing, conform explained in 3.2.1, are plotted in Figure 4.1. The main aspects and percent of particle sizes are presented in Table 4.1 and Table 4.2, respectively.

Figure 4.1 – Particle size distribution curves of the studied sample.

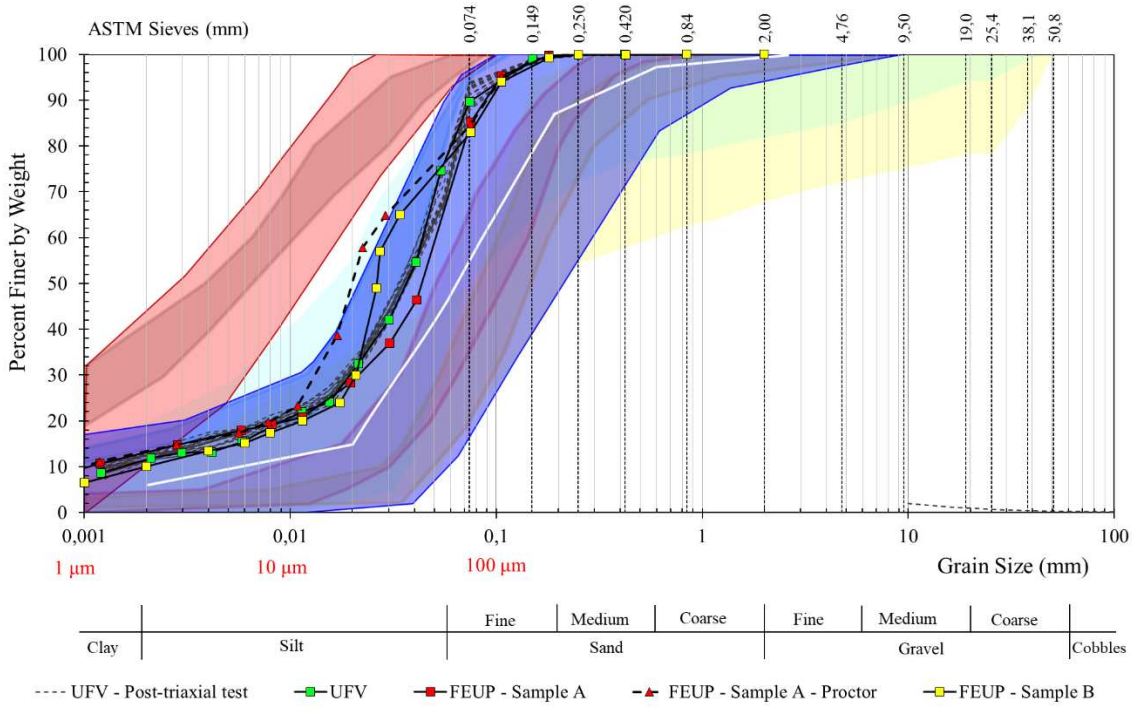

Source: elaborated by the author.

Table 4.1 – Main characteristics of the grain size distribution curves.

Sample	D_{50} (mm)	C_U	C_Z	Percent Fines < 0,075 mm
FEUP -Sample A	0,044	48,6	8,2	85,2
FEUP -Sample A - Proctor	0,020	24,2	7,0	84,7
FEUP- Sample B	0,026	15,4	7,2	83,0
UFV	0,037	28,8	5,6	89,6
UFV - Post-triaxial test avg.	0,035 (0,034-0,037)	34,9 (27,4-45,5)	6,1 (4,9-8,5)	91,7 (87,7-94,0)

Source: elaborated by the author.

Table 4.2 – Percent of particle sizes.

	Percent ABNT - NBR 6502:1995					
			Sand			
Sample	Clay < 0,002 mm	Silt 0,002 - 0,06 mm	Fine 0,06 - 0,2 mm	Medium 0,2 - 0,6 mm	Coarse 0,6 - 2,0 mm	Gravel > 2,0 mm
FEUP -Sample A	13,3	57,7	28,8	0,1	0,0	0,0
FEUP -Sample A - Proctor	13,4	66,4	17,6	2,6	0,0	0,0
FEUP- Sample B	10,3	67,7	21,6	0,4	0,0	0,0
UFV	12,0	67,5	19,9	0,6	0,0	0,0
UFV - Post-triaxial test avg.	12,0 (11,2-13,1)	63,0 (59,8-68,8)	24,4 (19,3-27,3)	0,51 (0,01-0,65)	0,07 (0,00-0,19)	0,0

Source: elaborated by the author.

The grain size distributions presented 83% to 94% of fines passing the nº 200 sieve, from which the majority are silt size particles. The samples UFV and FEUP - Sample A, presented in Figure 4.1, showed high similarity. Nonetheless, FEUP - Sample B showed some divergence on the central portion of the curve. The FEUP – Sample B, likewise the FEUP - Sample A - Proctor, exhibited higher content of particles ranging from 0,02 mm to 0,04 mm than the other samples.

When comparing FEUP - Sample A with FEUP - Sample A – Proctor the fines content increases in the central portion of the curve indicating some particle breakage due to dynamic compaction. On the other hand, UFV - Post-triaxial test samples did not show a significant difference from the UFV sample, indicating that samples compacted statically (with a press) did not significantly evolve.

Additionally, Figure 4.1 shows that the filtered tailings studied in this research are into the limits defined in 2.4.1 for tailings of the Quadrilátero Ferrífero. The grain size curves of the studied material are very similar to the upper limit of the samples of fine tailings of Feijão Dam I tested by Robertson et al. (2019). Furthermore, the values of D_{50}, C_U and C_Z are very consistent with the average values of the fine tailings of the Quadrilátero Ferrífero, presented in Table 2.1. The high values of C_U and C_Z are a consequence of the tail of fines shown by the curves, likewise the other tailings from the Quadrilátero Ferrífero. Therefore, the material could also be classified as relatively poorly graded instead of well graded.

4.1.2 SPECIFIC GRAVITY

It was determined the specific gravity of the three samples: UFV, FEUP - Sample A, and FEUP - Sample B. The G_s of each sample are presented in Table 4.3. The three values were consistent and showed an average value of 3,205 g/cm^3.

Table 4.3 – Specific gravity of the studied sample.

Sample	G_s (g/cm^3)
UFV	3,218
FEUP - Sample A	3,184
FEUP - Sample B	3,213
Average	**3,205**

Source: elaborated by the author.

The specific gravity of the analyzed tailings is considerably close to the average value (G_s = 3,71 g/cm^3) presented in subsection 2.4.2 for the tailings of the Quadrilátero Ferrífero, when compared to the range of variation (2,38 – 5,22). Moreover, even though the grain size distributions presented 83% to 94% of fines passing the nº 200 sieve, the G_s = 3,205 g/cm^3 is consistent with the samples in Table 2.4 that presented high quartz content: Germano Pit and Córrego do Doutor Dam (Pereira, 2005), Fernandinho Mine – Future Tailings (Carvalho, 2017), and Pontal Dam – Beach (Ferreira, 2018).

4.1.3 ATTERBERG LIMITS

As most iron ore tailings displayed in Table 2.5, the plasticity limit and liquid limit tests indicated that the studied tailings are non-plastic. Following the Unified Soil Classification System (USCS), explained in the ASTM D2487:2017, the material is classified as silt or silt with sand, depending on the particle size distribution curve.

4.1.4 MAXIMUM AND MINIMUM VOID RATIOS

With an average water content of 0,66%, the sample dried at room temperature presented e_{min} = 0,60 and e_{max} = 1,18, and respective $\gamma_{d,max}$ = 19,70 kN/m^3 and $\gamma_{d,min}$ = 14,46 kN/m^3.

The maximum void ratio is consistent with the void ratios of 1,08, 1,13 and 1,24 of the loose specimens prepared for the one-dimensional consolidation tests, which the results are presented in 4.5.1. Moreover, the maximum dry unit weight is a little bit lower, but still compatible, with $\gamma_{d,max}$ = 20,71 kN/m^3 and $\gamma_{d,max}$ = 21,05 kN/m^3 obtained after the standard Proctor tests (see 4.2).

The slight variation of $\gamma_{d,max}$ is partially explained by the fines content increase identified after the standard Proctor test, indicating some breakage of the material (see 4.1.1). The particles' breakage results in the rearrange of the material, and the broken particles tend to fill the voids resulting in higher dry unit weights.

The values of e_{min} and e_{max} are very coherent with the average values found in 2.4.1 for the iron ore tailings of the Quadrilátero Ferrífero (e_{min} = 0,66 and e_{max} = 1,22).

4.2 MAXIMUM DRY UNIT WEIGHT AND OPTIMUM WATER CONTENT

The dry unit weight-water content curves defined after the standard Proctor tests performed at LMS-UFV and LabGeo-FEUP are plotted in Figure 4.2. In both curves, the optimum water content was $w_{opt.}$ = 11,7%, and the maximum dry unit weight presented a small variation $(\gamma_{d,max})_{FEUP}$ = 20,71 kN/m^3 and $(\gamma_{d,max})_{UFV}$ = 21,05 kN/m^3.

The divergence of the values of dry unit weight found at UFV and FEUP may be associated with the variability of the samples or the intensity of particle breakage in each test. Comparing to the parameters presented in 2.4.5, the values of $w_{opt.}$ and $\gamma_{d,max}$ are into the one standard deviation range of the set, which means that the values are considerably close to the average values calculated for the other samples of the Quadrilátero Ferrífero (w_{opt} = 13,0% and $\gamma_{d,max}$ = 19,75 kN/m^3).

Figure 4.2 – Dry unit weight-water content and saturation curves of the studied sample.

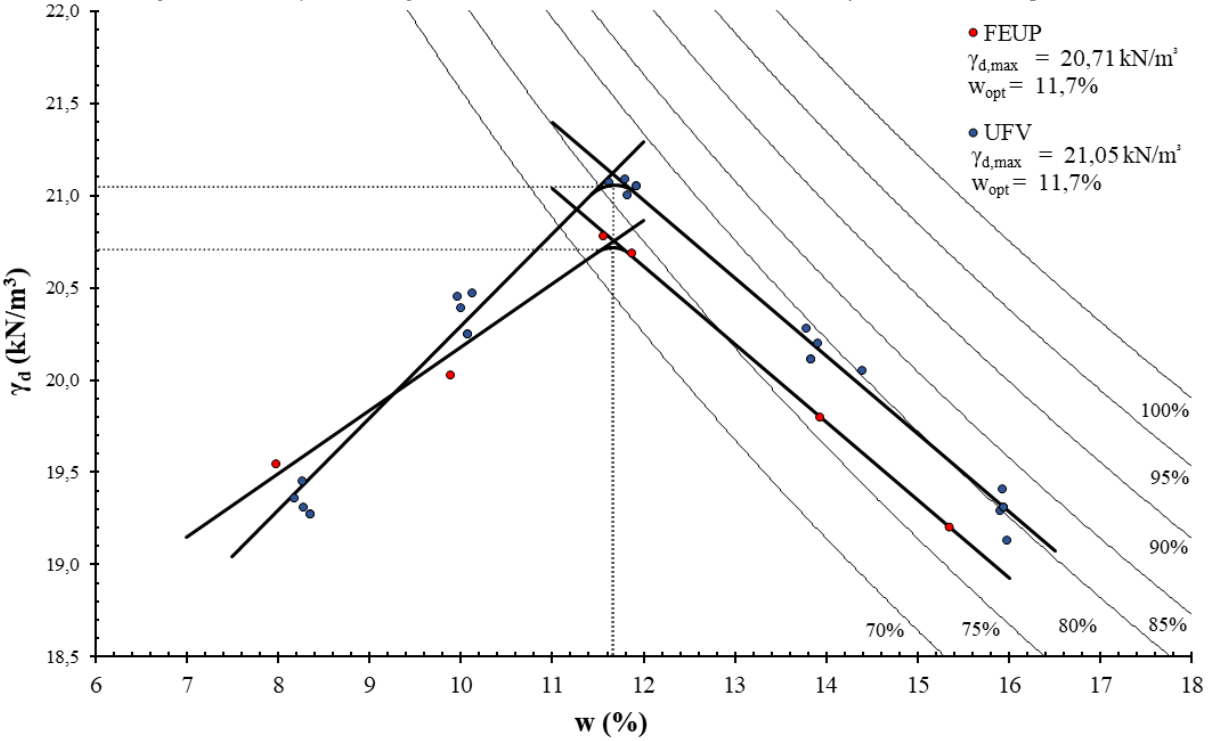

Source: elaborated by the author.

To check the degree of saturation (S) of the material compacted wet of optimum, it was also plotted the saturation curves in Figure 4.2. The saturation curves were defined by Equation 4.1, adopting the average G_s = 3,205 kg/m^3.

$$S = \frac{G_s \cdot \gamma_d \cdot w}{\gamma_w \cdot (G_s - \gamma_d)} \qquad \text{Equation 4.1}$$

Figure 4.2 shows that the filtered tailings compacted wet of optimum at levels higher than 90% of the maximum dry unit weight will present degrees of saturation raging from approximately 73% to 82%. Table 4.4 shows the precise variation of S wet of optimum on both dry unit weight-water content curves defined at FEUP and UFV. The values of the degree of saturation in Table 4.4 were calculated adopting for each sample its specific gravity – G_s = 3,184 kN/m^3, FEUP - Sample A, and G_s = 3,218 kN/m^3, UFV.

As presented by Crystal et al. (2018) and illustrated in Figure 2.5, materials with S higher than 85% are likely to behave as saturated. The degrees of saturation for each of the studied degrees of compaction wet of optimum given in Table 4.4 indicates that the lower the DC, the higher the S. However, with degrees of compaction higher than 90% of standard Proctor, none of the samples (FEUP and UFV) presented degrees of saturation higher than 85%.

Table 4.4 – Degree of saturation related to each degree of compaction wet of optimum.

Curve	DC (%)	S (%)
FEUP	100	73,5
	97	76,5
	95	77,5
	93	78,2
	90	78,5
UFV	100	75,5
	97	78,9
	95	80,0
	93	80,8
	90	81,3

Source: elaborated by the author.

Even though the material does not reach S = 85%, it is close to reaching saturation, and water infiltration must be prevented at all costs when compacting wet of optimum. Additionally, as stated by Lupo and Hall (2010) (section 2.2), when stacking the tailings, as they are gradually loaded, the material will tend to consolidate, extruding the air existent in the internal voids, reducing the void ratio, and increasing saturation, if the deposited tailings are compressible. As will be discussed in section 4.5, the compressibility will be dependent on the degree of compaction and the confining stresses.

In agreement with Trindade et al. (2008), it is worth mentioning that the compaction wet of optimum leads to a disperse soil structure, which is a synonym of lower shear strength

resistance, lower permeability, and higher deformability when comparing to the compaction dry of optimum, which ensures a flocculated structure.

4.2.1 COMPACTION QUALITY-CONTROL

The values of γ_d and w of the 218 samples collected in the trial embankment and the $\gamma_{d,max}$ and $w_{opt.}$ determined after the 33 standard Proctor tests performed by the mining company are presented in Figure 4.3 along with the dry unit weight-water content curves defined after the standard Proctor tests performed at LMS-UFV and LabGeo-FEUP. In addition, Table 4.5 and Table 4.6 show statistical data from the field tests.

The standard proctors performed by mining company exhibit average values of w_{opt} and $\gamma_{d,max}$ similar to the ones found in this research. Also, the one standard deviation range indicates high concentration of values between $\gamma_{d,max}$ = 20,33 kN/m^3 and $\gamma_{d,max}$ = 22,13 kN/m^3, and w_{opt} between 11% and 12,6%. However, the maximum and minimum values diverge significantly from the average. Two samples have even shown pairs of values (w_{opt}, $\gamma_{d,max}$) above the zero air voids curve (S = 100%), just as other 42 samples of core cutter tests. These results suggest considerable variability of the characteristics of the tailings in some portions of the trial embankment.

Figure 4.3 – Dry unit weight-water content curves of FEUP and UFV, and field tests results.

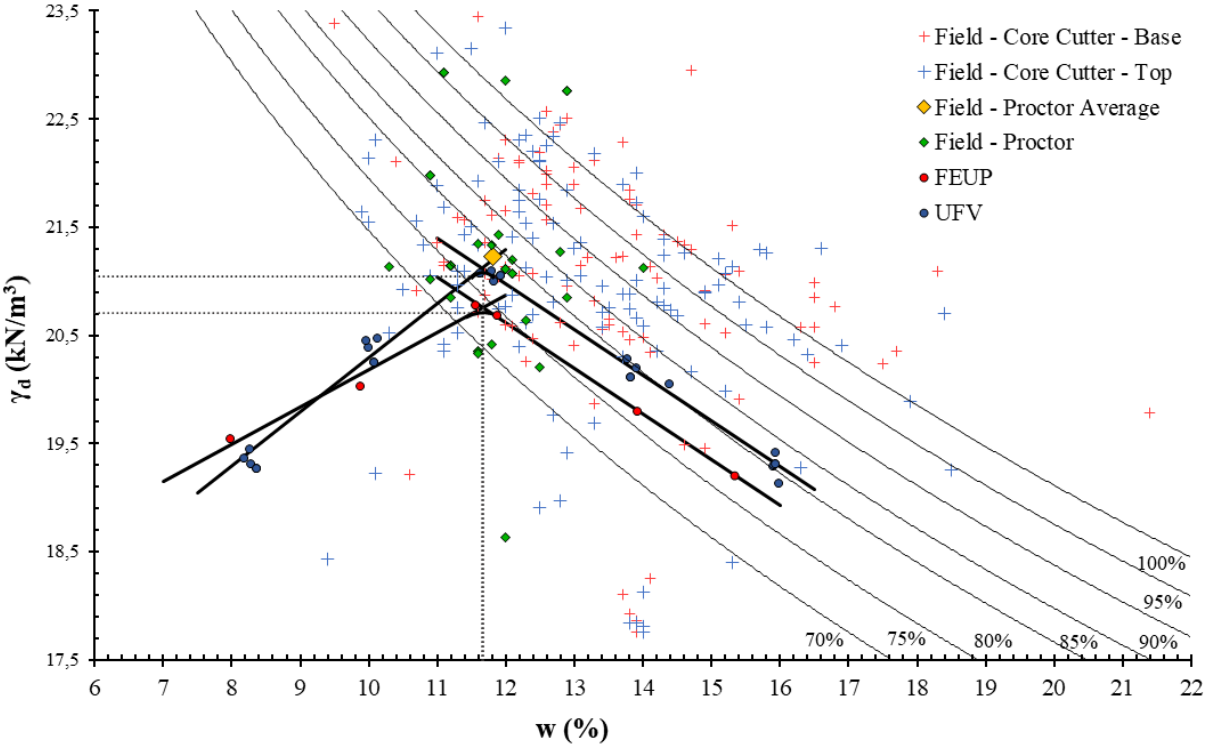

Source: elaborated by the author.

Table 4.5 – Statistics of standard Proctor and field tests performed by the mining company.

Statistics	$\gamma_{d,max}$ (kN/m³)	$w_{opt.}$ (%)	$\gamma_{d,field}$ (kN/m³)	w_{field} (%)	DC (%)	$w_{dev.}$ (%)
average	21,23	11,8	21,00	13,3	99,4	1,5
stdev.s	0,90	0,8	1,09	1,9	4,3	1,9
max	22,93	14,0	23,45	21,40	115,00	10,20
min	18,63	10,3	17,76	9,40	87,34	-2,90

Source: elaborated by the author.

Table 4.6 – Number of samples compacted equal or bellow each of the studied degree of compaction.

Samples	≤ 93%	≤ 95%	≤ 97%	≤ 100%	> 100%
Total (218)	11	16	56	140	78
$w_{opt.}$ (5)	0	0	2	3	2
< $w_{opt.}$ (34)	3	3	5	22	12
> $w_{opt.}$ (179)	8	13	49	115	64

Source: elaborated by the author.

Taking the FEUP and UFV curves as references, the average w_{field} = 13,3% is equivalent to DC between 95% and 97%. Nevertheless, the average $\gamma_{d,field}$ = 21,00 kN/m³ is equivalent to DC_{field} = 98,9%, adopting the average $\gamma_{d,max}$ = 21,23 kN/m³ as reference (see Table 4.5).

Additionally, Table 4.6 shows that 82% of the field samples indicate compaction wet of optimum. Moreover, from the 218 field tests, 78 show a degree of compaction higher than 100% of standard Proctor and, from these 78 tests, 64 show water content above the optimum. If no significant divergence between the standard Proctor test samples of reference and the core cutter samples was identified, it could indicate that portions of the embankment were compacted wet of optimum with higher compaction energy.

Analyzing Figure 4.3, it is also possible to identify the field tests that present values of dry unit weight and water content higher than the maximum dry unit weight and optimum water content of the standard Proctors of reference (samples on the top right of the chart). Nonetheless, a homogeneous material could never achieve a state of DC > 100% compacted wet of optimum, even if compacted with higher energy. Thus, the results strongly indicate the variability of the material in the field and turns on the alert that a unique sample is not enough to characterize the behavior of a dry stack.

It is relevant mentioning that increasing the compaction energy without reducing the water content increases the degree of dispersion of the soil structure and the degree of saturation without a significant increase of dry unit weight (TRINDADE et al. 2008).

Finally, when comparing the sampling position – top or base of the layer – in Figure 4.3, there is no significant divergence of γ_d and w. It suggests that the same degree of compaction was achieved in the top and the base of the layers. Nevertheless, the compaction equipment or the

number of passes still need to be adjusted, since Table 4.6 shows a significant variation of the degrees of compaction throughout the trial embankment.

4.3 HYDRAULIC CONDUCTIVITY

The hydraulic conductivity test results are presented in Table 4.7 and Figure 4.4, in which the hydraulic conductivity is plotted against the void ratios of the specimens. The void ratios fluctuated from 0,64 to 0,47, and Figure 4.4 shows a tendency of permeability decreasing with the reduction of the void ratio. The specimens compacted with higher void ratios – lower degrees of compaction – showed higher hydraulic conductivities, except for the specimens tested at 10 kPa of confining stresses, which presented almost the same permeability.

Rezende (2013) and Ferreira (2018) have determined the hydraulic conductivity (k) of tailings' samples in similar ranges of void ratios – 0,65 to 0,52 and 0,66 to 0,56, respectively –. Rezende (2013) defined k of about 10^{-6} m/s from oedometer tests, and Ferreira (2018) k of about 10^{-8} m/s from constant-head tests in flexible wall permeameter. The hydraulic conductivities determined for the studied sample, in Table 4.7, range from 6,23 x 10^{-8} m/s to 4,10 x 10^{-7} m/s, showing no similarity with the results of the other authors.

Comparing the highest and the lowest values, the factor of reduction of the hydraulic conductivity with decreasing void ratio is about 6,6 times, which is higher than the maximum expected reduction factor stated by Vick (1990) for coarse tailings (5 times) and lower than the maximum expected reduction factor stated for slimes (10 times). The value is consistent with the material since it is classified as a fine tailing composed predominantly of silt size particles.

The result of the KC equation (Equation 2.36), adjusted by Chapuis and Aubertin (2003) to predict the hydraulic conductivity of tailings based on their void ratio is also plotted in Figure 4.4. As the input of the equation, it was adopted the average specific gravity (G_s = 3,205 g/m^3) and average specific surface (S_p = 402,44 m^2/kg). The specific surface was determined from the grain size distribution curves displayed in 4.1.1, according to the methodology presented by Chapuis and Légaré (1992).

In the studied range of void ratios, the KC equation of Chapuis and Aubertin (2003) is not adherent to the test results. The measured hydraulic conductivities are higher than the ones determined by the KC equation. Also, the reduction rate is higher than the one predicted by the KC equation, indicating that the studied tailings are more sensitive to void ratio reduction.

Table 4.7 – Hydraulic conductivity determined at the triaxial chambers.

DC	p' (kPa)	e_0	k (m/s)
	10	0,64	4,09E-07
	100	0,61	3,69E-07
	200	0,61	2,88E-07
	400	0,58	1,38E-07
93%	807	0,57	2,90E-07
	800	0,57	4,10E-07
	1598	0,55	2,92E-07
	1603	0,56	3,53E-07
	1899	0,56	1,62E-07
	10	0,61	3,83E-07
	100	0,59	1,79E-07
	200	0,58	1,24E-07
	400	0,57	9,65E-08
95%	801	0,56	3,14E-07
	799	0,54	2,11E-07
	1600	0,52	1,65E-07
	1602	0,54	1,94E-07
	1906	0,54	1,58E-07
	10	0,58	3,43E-07
	100	0,57	1,46E-07
	200	0,56	1,09E-07
	400	0,55	8,54E-08
97%	801	0,53	1,76E-07
	801	0,52	2,13E-07
	1601	0,51	1,08E-07
	1600	0,52	1,58E-07
	1901	0,50	1,65E-07
	10	0,54	4,09E-07
	100	0,53	1,14E-07
	200	0,52	9,14E-08
100%	400	0,51	7,14E-08
	807	0,49	9,83E-08
	1605	0,49	6,23E-08
	1600	0,47	7,29E-08

Source: elaborated by the author.

Figure 4.4 – Hydraulic conductivity against void ratio.

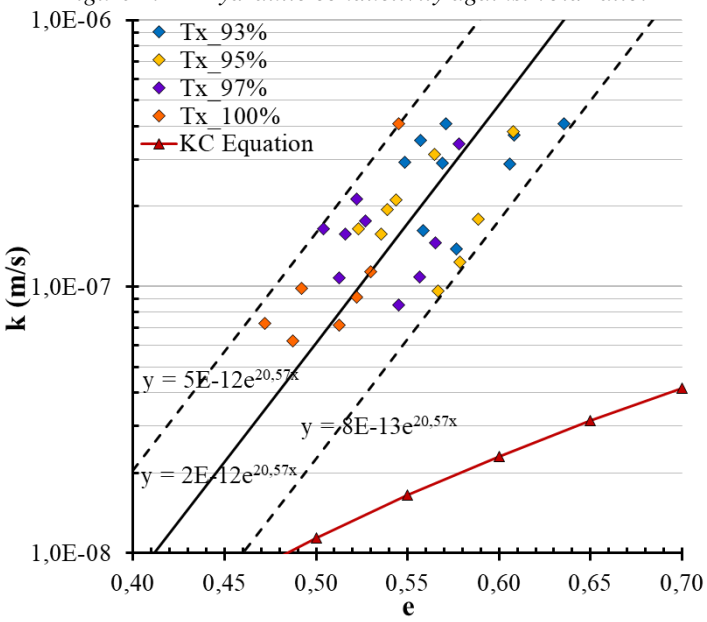

Source: elaborated by the author.

Table 4.8 – Power law relationship between void ratio and hydraulic conductivity.

Average	$\boldsymbol{k = 2 \times 10^{-12} \cdot exp^{20,57e}}$	**Equation 4.2**
Lower Limit	$k = 8 \times 10^{-13} \cdot exp^{20,57e}$	Equation 4.3
Upper Limit	$k = 5 \times 10^{-12} \cdot exp^{20,57e}$	Equation 4.4

Source: elaborated by the author.

Notice that in Equation 2.36, the hydraulic conductivity is inversely proportional to the specific surface, and the specific surface is inversely proportional to the particles' diameters. Thus, the results of KC equation compared to the measured hydraulic conductivities suggest that the clay size particles may be agglomerated or bonded into silt size particles and the material in its in-situ state may present different hydraulic behavior than the one predicted by the equation.

To confirm this hypothesis, it would be necessary to define the particle size distributions through laser testing or hydrometer testing without the use of a deflocculant, and recalculate the specific surface and hydraulic conductivity with the KC-equation.

The power-law relationship that better fits the data and its deviation boundaries are presented in Figure 4.4 and Table 4.8. From the equations, the measured values are between 0,4 and 2,5 times the average values.

4.4 SOIL-WATER CHARACTERISTIC CURVES

The soil-water characteristic curves are presented as a function of water content in Figure 4.5 and a function of saturation in Figure 4.6. In Figure 4.6, the sample Char_93_S1 show degrees of saturation above 100%. The inconsistency presented by Char_93_S1 may be associated with some variation of the specific gravity since the sample presented consistent results in Figure 4.5.

Figure 4.5 – Soil-water characteristic curves determined for DC = 93% and DC = 100%. Water content against suction.

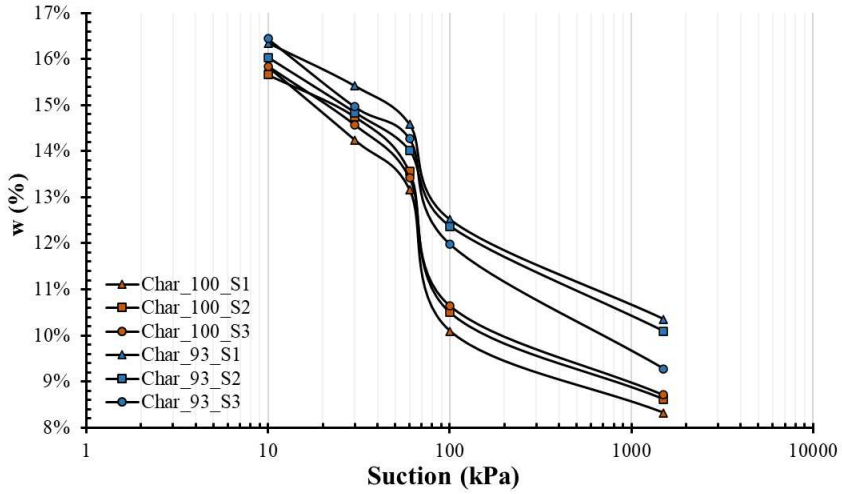

Source: elaborated by the author.

Figure 4.6 – Soil-water characteristic curves determined for DC = 93% and DC = 100%. Saturation against suction.

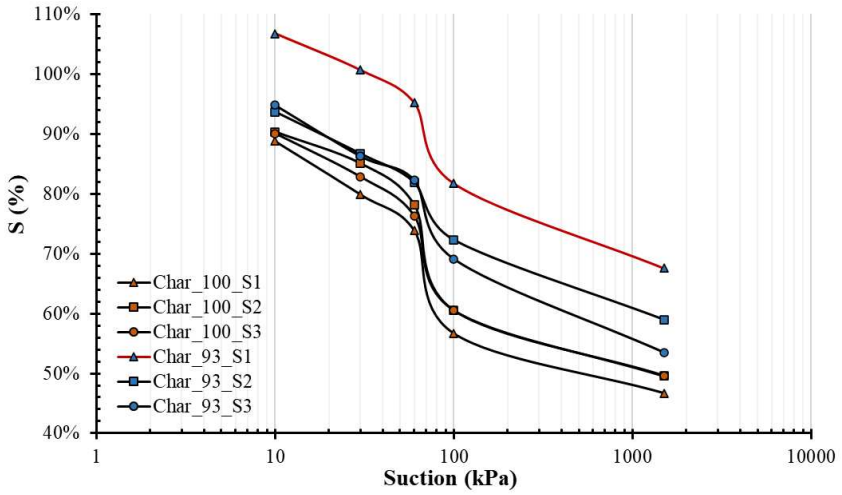

Source: elaborated by the author.

Notice that the specimens used in the test were carved from samples compacted into the split mold used to prepare the specimens of the triaxial test. As high energy is required to achieve the degrees of compaction of 93% and 100% of the standard Proctor, carving the sample may disturb the compacted material driving it to a looser state. It implies that, for the same degrees of compaction, and the same range of water content, the suction may be even lower than it was measured in the tests.

4.5 CONSOLIDATION

4.5.1 ONE-DIMENSIONAL CONSOLIDATION

Figure 4.7 presents the results of the oedometer tests performed in the saturated specimens, and the full curves with the unloading stages are in Appendix B. The primary one-dimensional consolidation parameters determined for each sample are in Table 4.9.

Figure 4.7 – Compression curves of saturated specimens.

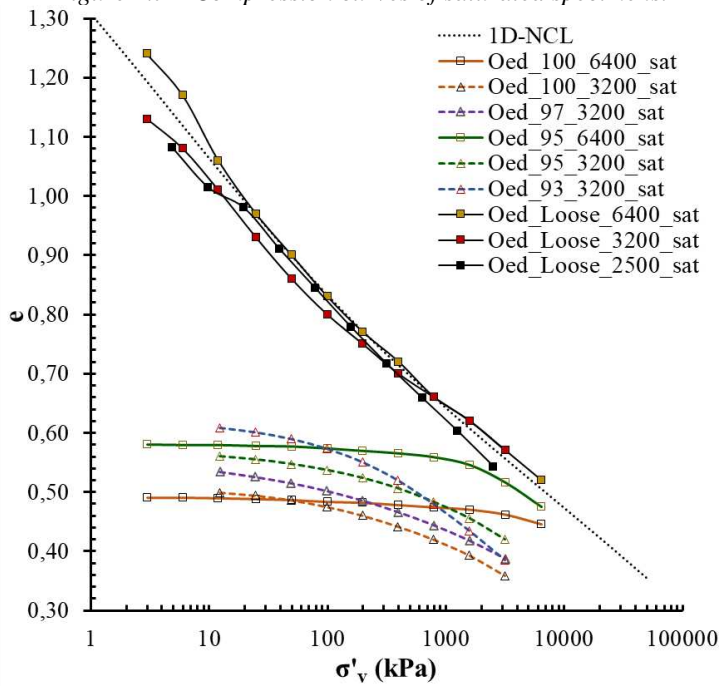

Dashed lines: carved specimens; solid lines: specimens compacted directly in the floating ring; dotted line: projection of the average one-dimensional normal consolidation line. Source: elaborated by the author.

The loose specimens showed significant convergence. All three tests showed steeper curvature, with an average compression index (C_c) of 0,235 until 100 kPa/300 kPa. Under higher vertical stresses, the material became less compressible, with $C_{c,avg}$ = 0,175. It seems that in the initial stages, as the specimens are in a very loose state, the particles are freer to rearrange themselves.

As the vertical stress increases, the space between the particles gets more restricted, and the material becomes less compressible.

Just as it was observed by Li et al. (2018) for gold ore tailings, the compression curves from the different degrees of compaction did not converge to the NCL even at 6400 kPa. Following Li et al. (2018), the slow convergence of the compression curves indicates that the differences of initial states, as an effect of the degree of compaction, can only be erased by large strains at high confining stresses.

Table 4.9 – One-dimensional consolidation parameters.

DC	Lab.	Sample	σ'_v	C_c	C_r	C_v (cm²/s)
Loose	LabGeo	Oed_Loose_6400_sat	3-200	0,245	0,000	-
			200-6400	0,166		
		Oed_Loose_3200_sat	3-6	0,166	0,000	-
			6-100	0,239		
			100-3200	0,166		
	LMS	Oed_Loose_2500_sat	5-300	0,222	0,027	0,019 (0,016-0,023)
			300-2500	0,196		
93%	LMS	Oed_93_3200_sat	800-1600	0,149	0,024	0,031 (0,026-0,035)
			1600-3200	0,165		
		Oed_93_3200_unsat	800-1600	0,096	0,024	-
			1600-3200	0,123		
95%	LabGeo	Oed_95_6400_sat	800-1600	0,044	0,003	-
			1600-3200	0,099		
			3200-6400	0,135		
	LMS	Oed_95_3200_sat	800-1600	0,092	0,025	0,025 (0,018-0,034)
			1600-3200	0,119		
		Oed_95_3200_unsat	800-1600	0,098	0,026	-
			1600-3200	0,124		
97%	LMS	Oed_97_3200_sat	800-1600	0,087	0,026	0,023 (0,016-0,030)
			1600-3200	0,101		
		Oed_97_3200_unsat	800-1600	0,090	0,028	-
			1600-3200	0,112		
100%	LabGeo	Oed_100_6400_sat	800-1600	0,013	0,003	-
			1600-3200	0,028		
			3200-6400	0,054		
	LMS	Oed_100_3200_sat	800-1600	0,089	0,027	0,027 (0,014-0,034)
			1600-3200	0,114		
		Oed_100_3200_unsat	800-1600	0,063	0,027	-
			1600-3200	0,086		

Saturated test results are presented in the white lines and the unsaturated test results are presented in the gray lines. Source: elaborated by the author.

Except for the curve Oed_93_3200_sat, all carved samples (dashed lines) presented similar compression and recompression indexes. However, their behavior was different from the samples compacted directly in the floating ring (solid lines), which showed a long flat recompression stage, see Figure 4.8.

The recompression indexes (C_r) were measured as the average slope of the first two unloading stages since no intermediate unloading\reloading stages were performed. The carved specimens

showed significantly higher reloading indexes ($C_{r,avg}$ = 0,026) than the specimens compacted in the floating ring ($C_{r,avg}$ = 0,003).

As mentioned in 4.4, some differences in behavior between the carved samples and the samples compacted directly in the floating ring were expected. However, during unloading, it was expected similar behavior for both types of specimens. Nevertheless, the specimens compacted in the floating ring presented flatter unloading curves expanding less than the carved ones.

Figure 4.8 – Compression curves of DC = 95% and DC = 100%.

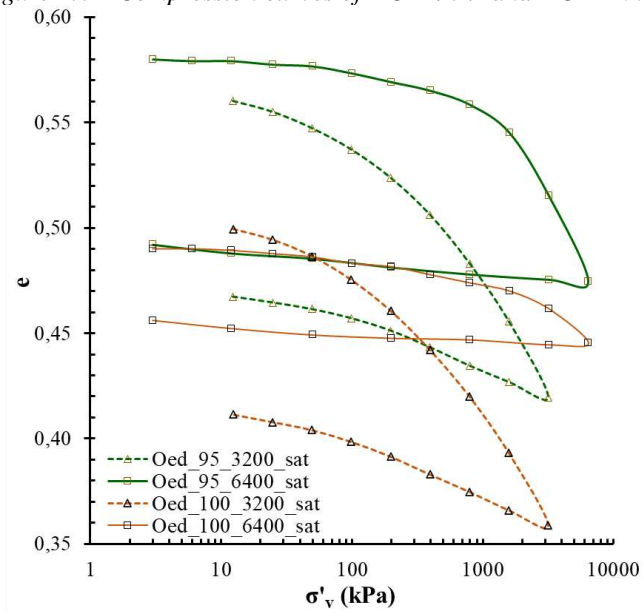

Dashed lines: carved specimens; solid lines: specimens compacted directly in the floating ring. Source: elaborated by the author.

Comparing Oed_95_6400_sat with Oed_100_6400_sat it is possible to verify the tendency of samples compacted with higher degrees of compaction to be more overconsolidated, so less compressible. The specimen compacted to 100% of the standard Proctor shows a significant change of curvature only after σ'_v = 1600 kPa, while the specimen with DC = 95% of the standard Proctor starts changing the slope after σ'_v = 400 kPa.

To see the effect of the degree of saturation in the compressibility of the tailings, the two sets of oedometers prepared at UFV (saturated and unsaturated) were plotted in Figure 4.9. The effect of suction was accounted for in the effective vertical stress of the unsaturated curves. Based on the range of saturation presented in Table 4.4, the suction range for the initial states of the unsaturated samples was checked in the soil-water characteristic curves (see Figure 4.6). The values of suction varied depending on the degree of compaction and compaction curve of

reference (FEUP or UFV), ranging from -44,5 kPa to -80 kPa and an average of -66,1 kPa, which was adopted to calculate the effective vertical stress of the unsaturated samples.

As discussed in sections 2.2 and 4.2, when the unsaturated specimens are loaded, the air is extruded from their internal voids, the degree of saturation increases, and there is a reduction of the suction. However, the decrease of the suction was not accounted for when plotting the unsaturated curves. The same negative pore water pressure was adopted for all points of the curves. This simplification is acceptable because the suction is negligible compared to the magnitude of the final loading stages.

Except for Oed_93_3200_sat, both saturated and unsaturated specimens showed similar behaviors, with curves relatively parallel to each other, except for the initial stages, in which the unsaturated curves are shifted and show steeper slopes due to the suction that, in these stages, is relevant compared to the magnitude of the loading.

Figure 4.9 – Compression curves of saturated and unsaturated specimens.

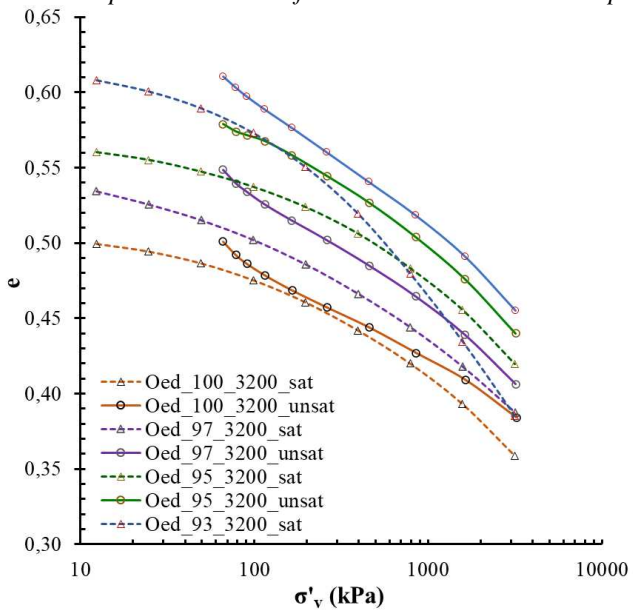

Dashed lines: saturated specimens; solid lines: unsaturated specimens. Source: elaborated by the author.

While the compression index of the samples with degrees of compaction of 95% and 97% showed significant similarity, saturated or unsaturated, the unsaturated specimen with DC = 100% showed a lower compressibility index, indicating that the unsaturated material was less compressible. The samples with DC = 93% showed the same behavior as the samples with DC = 100%. Nevertheless, Oed_93_3200_sat was considered an outlier because of its unusual behavior compared to the other tests.

It is noteworthy mentioning that, when compared with the samples compacted directly in the mold, the unsaturated specimen compacted to 100% of the standard Proctor still shows higher compression and recompression indexes.

The compression and recompression indexes of the carved samples are consistent with the indexes of the other tailings from the Quadrilátero Ferrífero presented in 2.4.7, except for the ones shown by Morgenstern et al., 2016 for the tailings of Fundão Dam, which were consistent with the indexes shown by samples Oed_95_6400_sat and Oed_100_6400_sat, compacted directly in the floating ring.

For the saturated carved samples, it was also determined the vertical coefficient of consolidation (Cv). Cv was determined for each stage of consolidation and, in Table 4.9, it is displayed the average, minimum, and maximum values of each sample. The values presented in Table 4.9 are consistent with the values presented by Morgenstern et al., 2016 for the tailings of Fundão Dam.

4.5.2 ISOTROPIC CONSOLIDATION

Figure 4.10 presents the results of the isotropic consolidation tests. They are also displayed individually in Appendix C. The isotropic compression and recompression indexes of the samples are presented in Table 4.10.

Table 4.10 – Isotropic consolidation parameters.

DC	Sample	p' (kPa)	λ	κ	κ/λ
93%	Iso_93_1900kPa	240-400	0,0125	0,0035	0,283
		880-1600	0,0342	0,0052	0,151
	Iso_93_3000kPa	500-1100	0,0299	-	-
		1100-3000	0,0420	-	-
95%	Iso_95_1900kPa	170-400	0,0083	0,0037	0,446
		1060-1600	0,0186	0,0050	0,267
	Iso_95_2100kPa	600-1150	0,0181	-	-
		1150-2100	0,0286	-	-
97%	Iso_97_1900kPa	520-680	0,0104	0,0039	0,371
		940-1900	0,0172	0,0090	0,521
100%	Iso_100_1400kPa	45-500	0,0065	-	-
		500-1400	0,0095	-	-
	Iso_100_1900kPa	55-270	0,0060	0,0032	0,541
		1000-1600	0,0111	0,0047	0,420

Source: elaborated by the author.

Figure 4.10 shows the tendency of the compression curve to get more flattened with the increase of the degree of compaction and reduction of the initial void ratio, which is associated with the increment of the OCR. Samples with higher degrees of compaction and lower initial void ratios

are more distant from the normal consolidation line and the recompression extends to higher loading stages, resulting in flattened curves. It is also verified when comparing the compression indexes in Table 4.10, which also presents low recompression indexes that indicate slight swelling of the material after unloading and helps to explain the flattened curves resultant of the samples compacted with a higher degree of compaction.

Following Vick (1990), all compression curves presented an extensive curvature. Both the compression and the recompression indexes of all curves are not constant. The parameters tend to increase with the increase of confining pressure. In the same sample, the recompression index determined in the first unloading/reloading cycle is smaller than the one determined in the second unloading/reloading cycle. Except for the specimen with DC = 97%, the average recompression index calculated after the first unloading/reloading cycle was κ_{avg} = 0,0036 and the average recompression index calculated after the second unloading/reloading cycle was κ_{avg} = 0,0050. This characteristic may be associated with the evolution of the tailings with the increase of the confining stresses resulted from particle crushing and shattering.

Figure 4.10 – Compression curves of the isotropic consolidation tests.

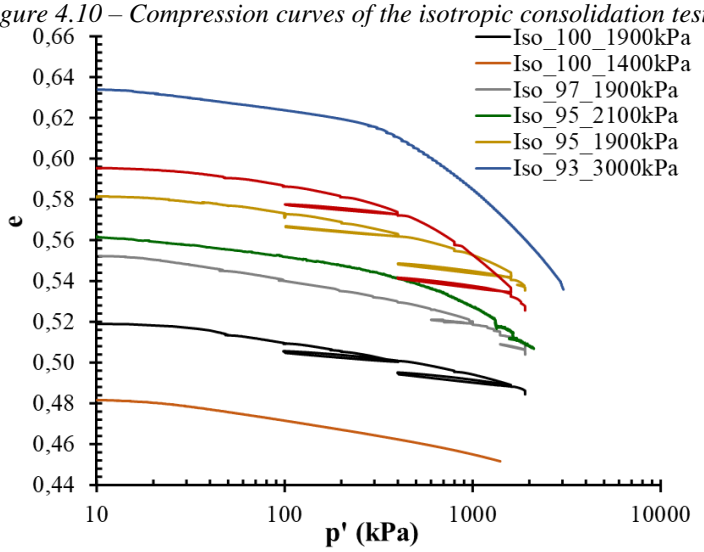

Source: elaborated by the author.

To compare the results of the isotropic consolidation tests with the one-dimensional consolidation tests, the results of saturated samples of the oedometer test were plotted with the results of the isotropic consolidation tests in the (p', e) space in Figure 4.11.

The effective mean stresses (p') of the oedometer tests were calculated by Equation 4.7, which is derived from Equation 2.4. The coefficient of earth pressure at rest (K_0) was determined by Equation 4.6 (MAYNE and KULHAWY, 1982), where the OCR was calculated as the ratio of

the vertical stress at the overconsolidated curve (compacted curve) to the vertical stress at the NCL – the average NCL, presented in 4.5.1, was used to calculate the OCR –.

$$p' = \sigma'_v \cdot \frac{(1 + 2K_0)}{3} \qquad \text{Equation 4.5}$$

$$K_{0,OC} = (1 - \sin\varphi'_c) \cdot OCR^{\sin\varphi'_c} \qquad \text{Equation 4.6}$$

Figure 4.11 shows that the isotropic compression curves are more consistent with the one-dimensional compression curves of the samples compacted directly in the floating ring of the oedometer test than with the curves of the carved specimens. It strengthens the hypothesis that carved specimens of very dense materials tend to be disturbed during preparation.

Figure 4.11 – Compression curves of the saturated oedometer tests plotted with the compression curves of the isotropic consolidation tests.

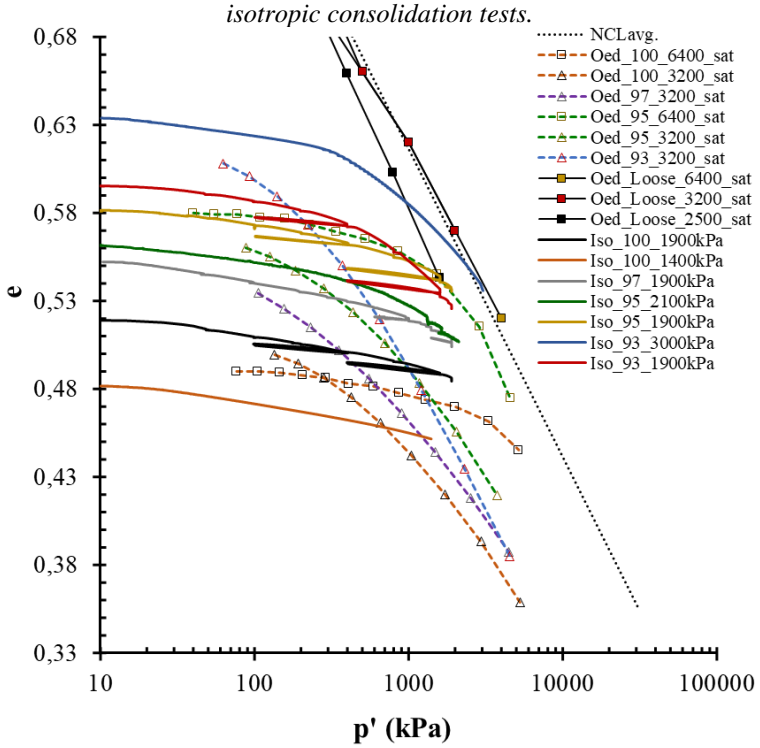

Source: elaborated by the author.

Moreover, in Figure 4.11, the sample Iso_93_3000kPa tends to reach the normal consolidation line at 3000 kPa ($\sigma'_v \approx 4900$ kPa). Nonetheless, isotropic consolidation tests in loose samples must be performed to confirm it because there is some inaccuracy in plotting the oedometer test and isotropic consolidation test results together. Even determining the mean effective stresses of the oedometer tests, one-dimensional and isotropic loading inflicts different boundary conditions on the specimens.

4.6 TRIAXIAL COMPRESSION TESTS

The results of the triaxial compression tests are presented in Figure 4.12 and detailed by degree of compaction in Appendix D.

Figure 4.12 – Triaxial test results.

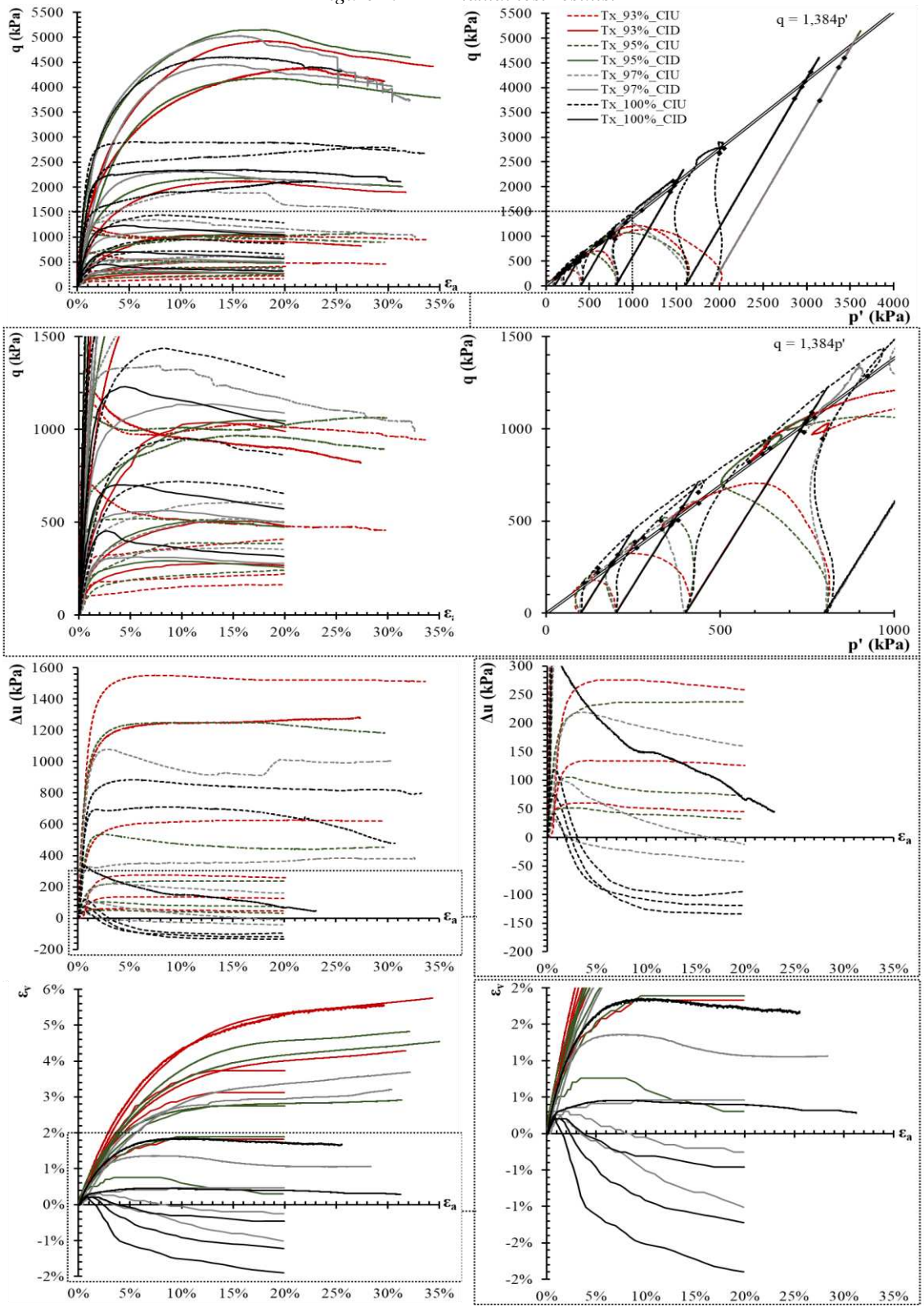

Source: elaborated by the author.

The following subsections will discuss the properties determined after the triaxial test results.

4.6.1 CRITICAL STATE LINE

Figure 4.13 and Figure 4.14 presents the critical state line defined in the (p', q) space and (p', e) space, respectively. A curved critical state line was initially defined in the (p', e) space, for each degree of compaction. The curved CSLs are plotted separately in Appendix E, and Table 4.11 presents the equations of each curved CSL.

Figure 4.13 – Critical state line defined in the (p', q) space.

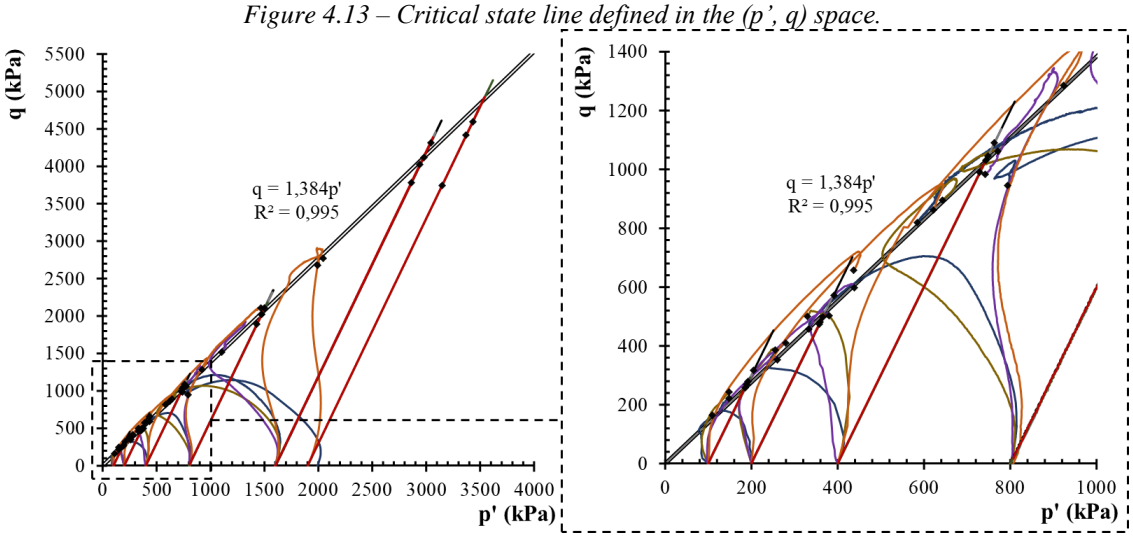

Source: elaborated by the author.

The critical state line in the (p', q) space was determined by linear regression of the last data points of each test. The resulting line showed a good fit to the data with a high $R^2 = 0,995$. The resultant critical friction ratio, $M_{tc} = 1,384$, is very similar to $M_{tc} = 1,38$ found by Robertson et al. (2019). Moreover, the equivalent frictional angle, $\varphi'_c = 34,2º$, is close to the average value, $\varphi'_c = 34,5º$, of other iron ore tailings of the Quadrilátero Ferrífero, presented in 2.4.8.

The curved critical state lines of each degree of compaction converged to a similar locus. The lines did not show significant evolution from a degree of compaction to another. Only the CSL referent to DC = 100% deviated significantly from the others. Nevertheless, the samples compacted to 100% of Proctor maximum dry unit weight and consolidated under 100kPa, 200 kPa, and 400 kPa have shown strong dilatant behavior.

According to Been (1999), dense (dilatant) samples hardly reach the critical state in a conventional triaxial apparatus because of the formation of shear planes and the tendency to localization. Thus, the CSL referent to DC = 100% is shifted because the samples have not

reached the critical state yet. Also, it is possible to affirm that all samples have converged to the same critical state locus.

Figure 4.14 – Critical state line defined in the (p', e) space.

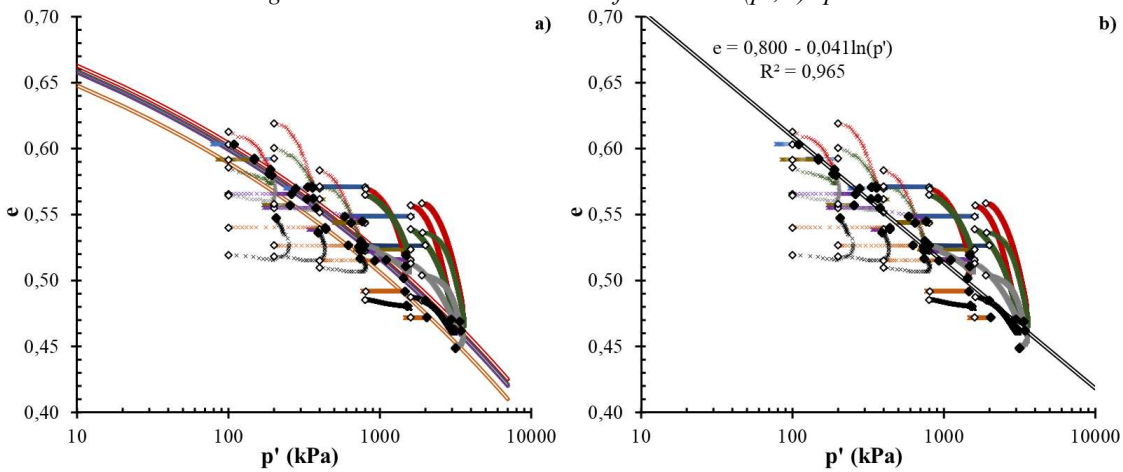

a) Curved critical state lines of the four studied degrees of compaction; b) CSL of the four studied degrees of compaction represented as a unique semi-logarithmic line. Source: elaborated by the author.

Table 4.11 – Equations of the CSLs defined for each degree of compaction.

DC	Equation	
93%	$e = 0{,}805 - 0{,}201\left(\frac{p'}{p'_{ref}}\right)^{0{,}15}$	Equation 4.7
95%	$e = 0{,}801 - 0{,}201\left(\frac{p'}{p'_{ref}}\right)^{0{,}15}$	Equation 4.8
97%	$e = 0{,}800 - 0{,}201\left(\frac{p'}{p'_{ref}}\right)^{0{,}15}$	Equation 4.9
100%	$e = 0{,}790 - 0{,}201\left(\frac{p'}{p'_{ref}}\right)^{0{,}15}$	Equation 4.10
semi-log	$e = 0{,}800 - 0{,}041 \ln(p')$	Equation 4.11

Source: elaborated by the author.

The CSL shows a wide curvature for the analyzed stress range – 100 kPa to 3400 kPa – and the semi-logarithmic form, presented in Figure 4.14, fits well the data ($R^2 = 0{,}965$) within the range. The semi-log CSL was adopted to calibrate the NorSand model used to estimate H and G_{max} in subsection 4.6.5.

The curved CSLs and semi-logarithmic CSL were plotted with the isotropic compression curve of Iso_93_3000kPa in Figure 4.15. The curvature of the curved CSLs and the isotropic compression curve, Iso_93_3000kPa, are similar after 300 kPa of confining stress. Furthermore, the slope of the semi-log critical state line ($\lambda = 0{,}041$) is very consistent with the compression index of Iso_93_3000kPa for p' between 1100 kPa and 3000 kPa ($\lambda = 0{,}042$). The similarity

between the curves is an evidence that the critical state line is well defined for the studied stress range.

Figure 4.15 – Curved critical state lines compared to the isotropic consolidation test (Iso_93_3000kPa).

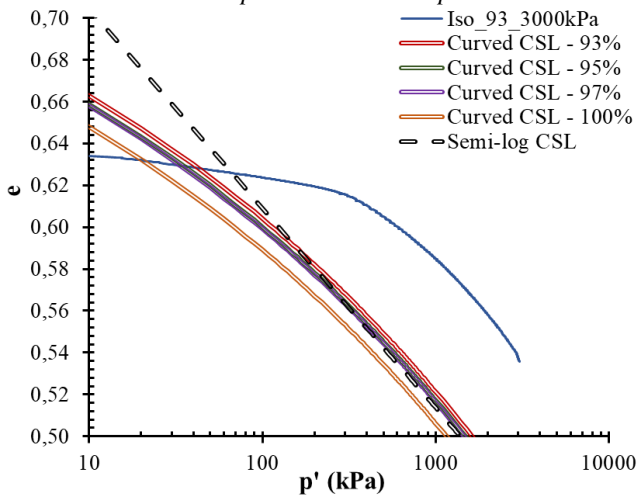

Source: elaborated by the author.

Comparing to the critical state lines, defined in the (p', e) space, for other iron ore tailings of the Quadrilátero Ferrífero, the CSL presented $\Gamma = 0{,}800$, closer to $\Gamma = 0{,}865$, determined by Morgenstern et al. (2016), and $\lambda = 0{,}041$, closer to $\lambda = 0{,}039$, defined by Robertson et al. (2019). In other words, at p' = 1,0 kPa, the CSL here defined has approximately the same void ratio as the CSL defined by Morgenstern et al. (2016). However, its gradient is analogous to the CSL determined by Robertson et al. (2019).

4.6.2 STATE PARAMETER

The initial state parameter of each specimen was determined using as a reference both the semi-logarithmic and the curved critical state lines. As curved CSL, it was adopted the line referent to DC = 93% because it was determined after the loosest specimens, which are more likely to reach the critical state locus, as explained in 4.6.1. The state parameters are presented in Table 4.12 and Figure 4.16.

Analyzing the state parameters, in Table 4.12, with the triaxial plots presented in Appendix D, it is interesting to verify that under low confining stresses the specimens compacted to 93% of the standard Proctor already show contractive behavior. This behavior is consonant with the positive state parameters presented in Table 4.12. As the degree of compaction increases the state parameters get negative until reach a dilatant condition under low confining stresses for

DC = 97% (at p'= 100 kPa and 200 kPa) and DC = 100% (at p' = 100 kPa, 200 kPa, and 400 kPa).

Table 4.12 – State parameters determined adopting the unique semi-log CSL and adopting the curved CSL of DC = 93% as unique curved CSL.

DC	Trx.	p'0 (kPa)	ψsemi-log	ψcurved
93%	CID	100	0,004	0,009
		200	0,039	0,037
		400	0,032	0,026
		807	0,047	0,039
		1603	0,063	0,057
		1899	0,071	0,066
	CIU	100	-0,006	-0,001
		200	0,012	0,010
		400	0,018	0,012
		800	0,048	0,040
		1598	0,054	0,048
		1991	0,041	0,036
95%	CID	100	-0,024	-0,019
		200	0,020	0,018
		400	0,020	0,014
		801	0,042	0,034
		1602	0,045	0,038
		1906	0,049	0,044
	CIU	100	-0,017	-0,012
		200	-0,023	-0,025
		400	0,010	0,004
		799	0,021	0,013
		1600	0,029	0,023
97%	CID	100	-0,045	-0,040
		200	-0,022	-0,024
		400	0,000	-0,006
		801	0,004	-0,004
		1601	0,019	0,012
		1901	0,017	0,011
	CIU	100	-0,043	-0,038
		200	-0,026	-0,027
		400	-0,013	-0,019
		801	-0,001	-0,008
		1600	0,022	0,015
100%	CID	100	-0,090	-0,085
		200	-0,062	-0,064
		400	-0,042	-0,048
		800	-0,038	-0,045
		1605	-0,007	-0,013
	CIU	100	-0,069	-0,064
		200	-0,054	-0,056
		400	-0,036	-0,042
		807	-0,031	-0,038
		1600	-0,022	-0,029
		1902	-0,002	-0,008

Source: elaborated by the author.

Figure 4.16 – State parameter versus effective mean stress plot.

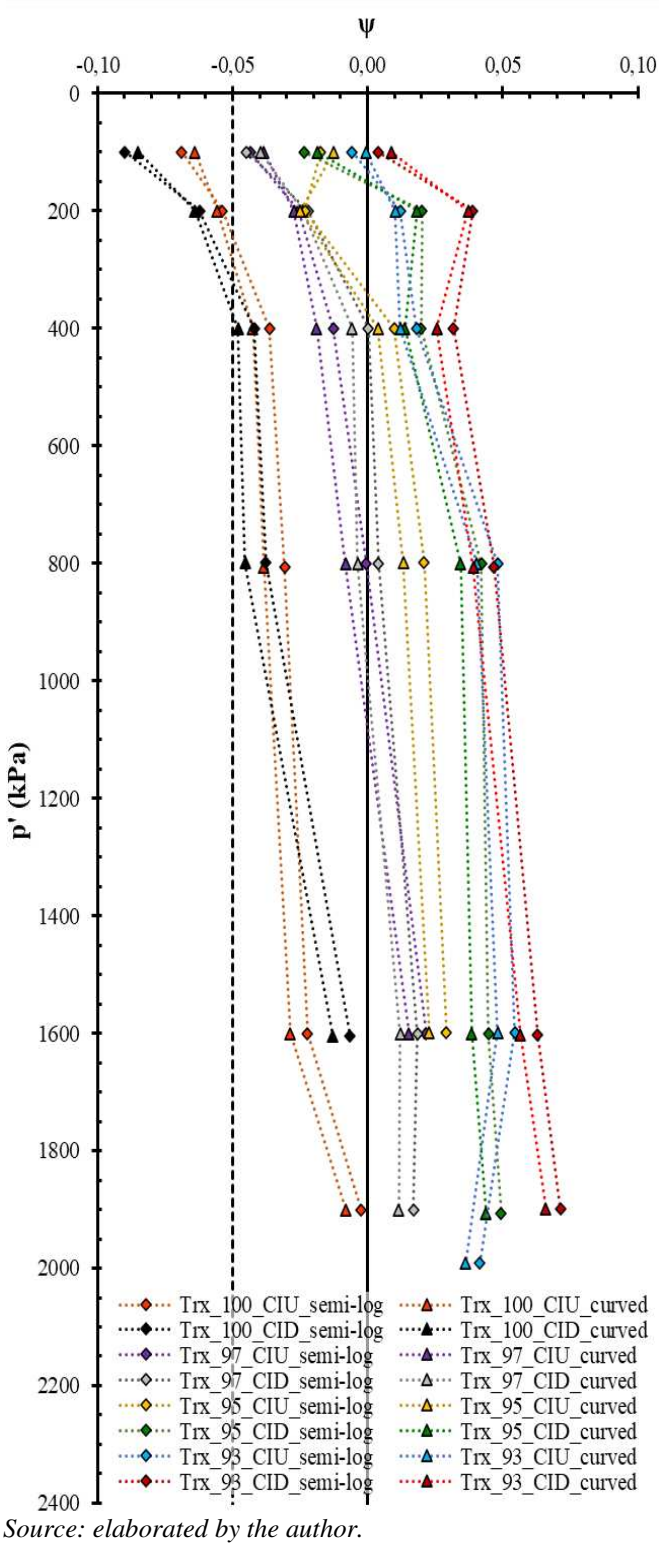

Source: elaborated by the author.

All samples within this interval between contractive and dilatant behavior show a lightly dilatant behavior, which means that the samples start to show the tendency to gain resistance under undrained conditions. However, they still preserve some characteristics of contractive behavior – such as the generation of positive pore water pressure and the tendency to reduce in volume – until considerably large strains, when it dilates to the critical state. Due to these characteristics, according to Jefferies and Been (2015), "it is the lightly dilatant soils that tend to cause the most trouble for engineering predictions, design and remediation."

Note that for high confining stresses (800 kPa, 1600 kPa, and 1900 kPa), not even the samples compacted with DC = 100% showed a dilatant behavior. It suggests that, for stacks, in which the tailings will be submitted to this range of confining stresses, the standard Proctor is not the most appropriate compaction energy. Therefore, higher compaction energy, such as modified Proctor, must be evaluated.

Figure 4.16 shows the tendency of the state parameters to increase both with the reduction of the degree of compaction and the increment of confining stresses. Figure 4.16 also shows that only four samples presented $\psi < -0,05$: Trx_100_CID_100kPa, Trx_100_CID_200kPa, Trx_100_CIU_100kPa and Trx_100_CIU_200kPa.

According to Jefferies and Been (2015), soils denser than $\psi < -0,05$ present strain-hardening behavior (dilatant) while soils looser than $\psi > -0,05$ show a strain-softening behavior (lightly dilatant and contractive soils). Nevertheless, as will be discussed in 4.6.3, the samples Trx_97_CID_100kPa and Trx_100_CID_400kPa, which have state parameters between -0,04 and -0,05, have also presented dilatant behavior.

It is noteworthy mentioning that, depending on the CSL used as referential, the state parameters of Trx_97_CID_100kPa and Trx_100_CID_400kPa are $\psi = -0,045$ and $\psi = -0,048$, respectively. The values are considerably close to $\psi = -0,05$. Therefore, it is possible to affirm that the results are still consistent with the boundary defined by Jefferies and Been (2015).

4.6.2.1 CPTu

The results of the CPTus are presented in Figure 4.17 and Figure 4.18. They show the measured parameters: cone tip resistance corrected for unequal end area (q_t), sleeve friction (fs), and penetration pore pressure (u_2); the normalized parameters: normalized cone resistance (Q_{tn}), normalized friction ratio (F_r), and normalized porewater pressure (B_q); the soil behavior type

index (I_c) proposed by Robertson (2009), and the state parameters calculated using Plewes et al. (1992) and Robertson (2010).

Figure 4.17 – Results of CPTu-01. Measured parameters, normalized parameters, I_c, and ψ.

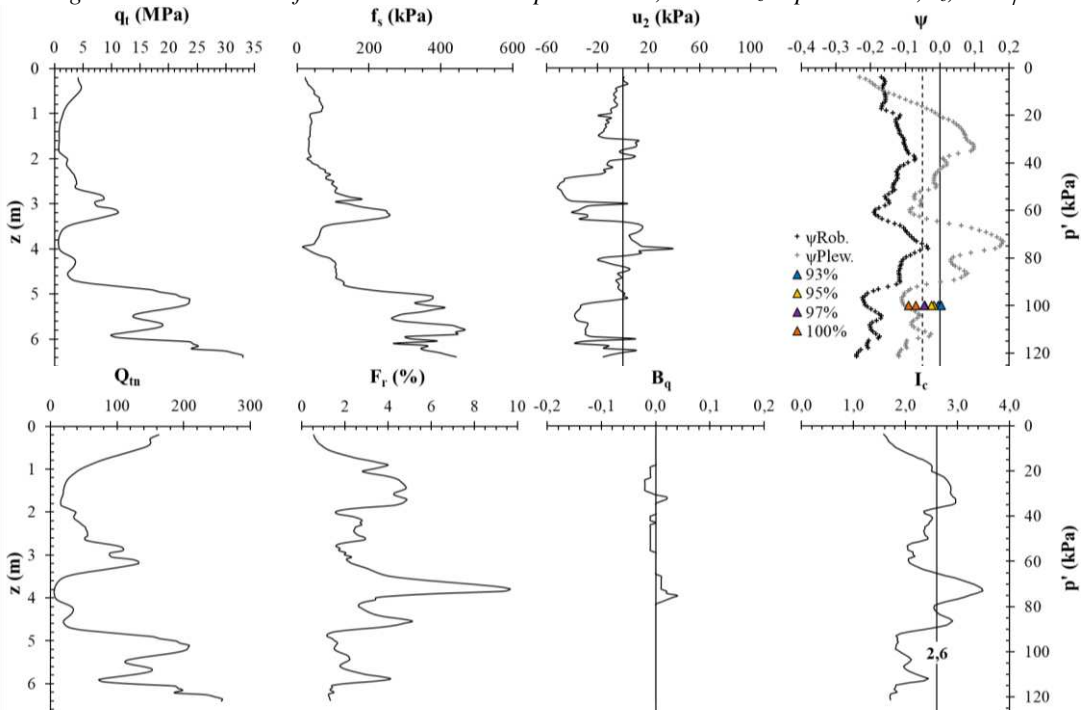

Source: elaborated by the author

In the state parameter plot it is also plotted the boundary of ψ = -0,05, suggested by Jefferies and Been (2015), and the state parameters obtained by the triaxial tests for p' = 100 kPa and p'= 200 kPa.

The CPTu data were normalized adopting the average bulk unit weight, γ = 23,79 kN/m^3, determined after $\gamma_{d,avg.}$ and $w_{avg.}$ presented in Table 4.5, and considering the non-existence of piezometric profile, since minor penetration pore pressure was recorded during the tests.

To characterize the in-situ state parameters using Plewes et al. (1992), it was adopted a lateral stress coefficient K_0 = 0,7. This value was adopted because, based on the compaction quality-control tests, most of the trial embankment has shown a degree of compaction higher than 95% of standard Proctor unit weight, and the consolidation tests have shown that the material hardly achieves the normal consolidation line (see 4.5).

The I_c ranges from 1,62 to 3,49, indicating that the tailings go from sand-like to clay-like behavior in the CPTu profiles. Nevertheless, 93,5% of the material is between 1,62 and 2,95, from which 41,5% is between 1,62 and 2,05, classified as sand to silty sand according to Robertson (2009), 35,2% is between 2,05 and 2,60, classified as silty sand to sandy silt

according to Robertson (2009), and 16,79% is between 2,60 and 2,95, classified as clayey silt to silty clay (ROBERTSON, 2009). The CPTu suggests that the tailings present mainly sand-like to transitional behavior with punctual zones of clay-like behavior. At a certain point, the classification is consistent with the lab test results that, following the USCS, characterized the material as silt or silt with sand.

Figure 4.18 – Results of CPTu-02. Measured parameters, normalized parameters, I_c, and ψ.

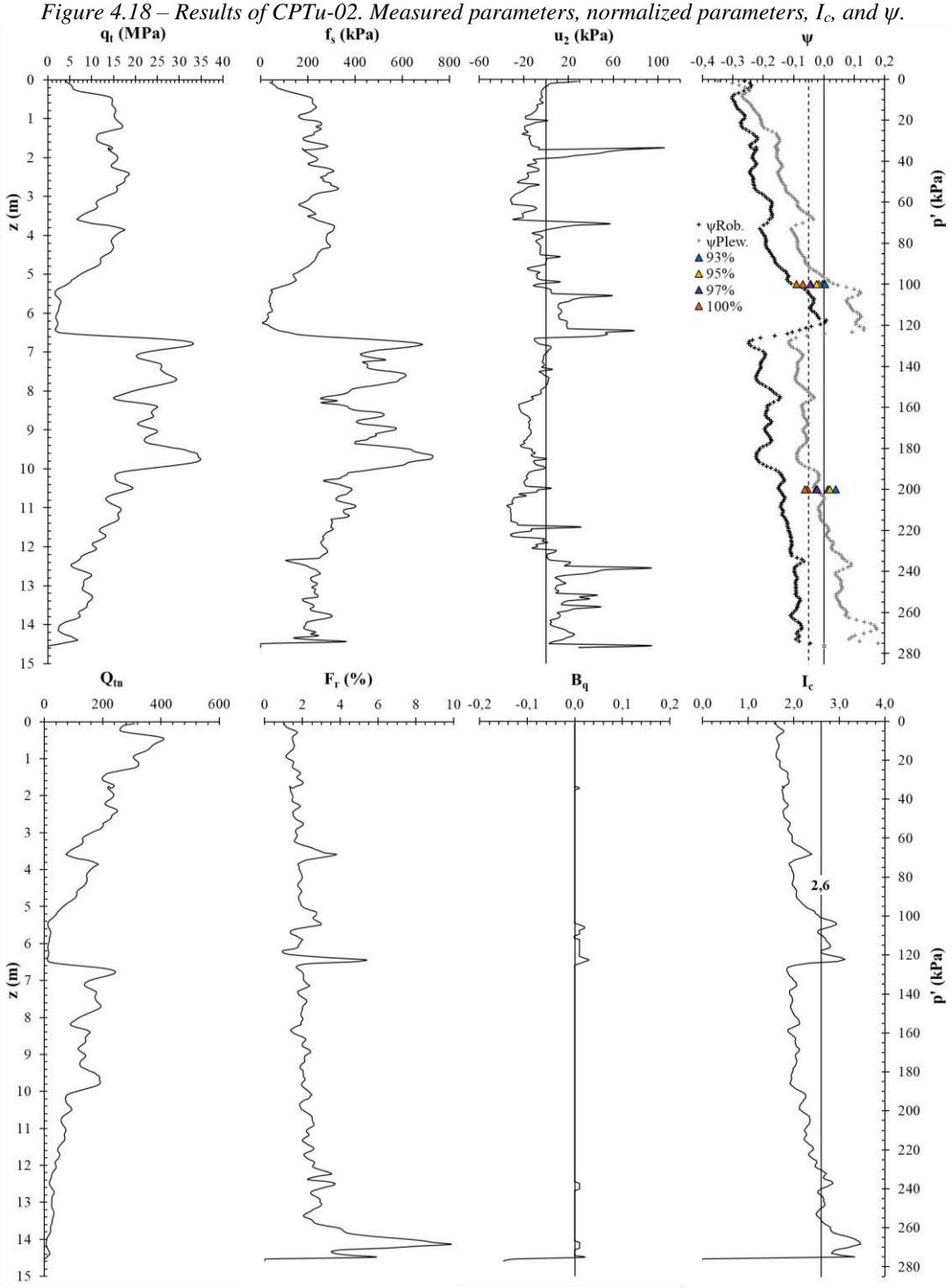

Source: elaborated by the author

The Q_{tn} ranging from 5,74 to 408,69 indicates the variability of the material deposited in the trial embankment. Additionally, in line with Robertson et al. (2017), the layers with low Q_{tn} are expected to be contractive at large strains.

Based on the layers with low Q_{tn} and the state parameters of the laboratory specimens, plotted in Figure 4.17 and Figure 4.18, it is possible to affirm that the state parameters estimated using the methodology of Plewes et al. (1992) are more consistent than the ones estimated using Robertson (2010).

Figure 4.17 shows that at p'= 100 kPa, ψ estimated using Plewes et al. (1992), is equivalent to ψ of the specimens with DC = 100%, while ψ estimated using Robertson (2010) did not show any equivalence. Moreover, in Figure 4.18, at p' = 100 kPa, ψ estimated using Plewes et al. (1992) is a little bit higher them ψ referent to DC = 93%, while ψ estimated using Robertson (2010) correspond to ψ referent to DC = 100%. However, the low value of Q_{tn} indicates that the material has a contractive behavior at p' = 100 kPa, which is more consistent with the state parameter defined using Plewes et al. (1992).

The comparison between the state parameters of the laboratory samples with the ones estimated with the CPTu also shows the variability of the degree of compaction of the trial embankment since, for the same confining stress (p'= 100%), CPTu-01 showed ψ equivalent to DC = 100% and CPTu-02 showed ψ equivalent to DC = 93%.

Regardless of the variation due to the fluctuation of the degree of compaction (see 4.2.1), it was also expected to see a constant increase of the state parameter throughout the depth of the trial embankment, due to the increasing stress levels, as was observed in the triaxial tests. Nevertheless, both CPTus show variability along with the profile, and they are not consistent with each other (see Figure 4.19).

CPTu-01 does not show a constant increase of the state parameter with the depth increase. Instead, it shows layers of loose tailings, approximately 1,0 m thick between 1,0 m and 2,0 m deep and between 3,6 m and 4,6 m deep, showing peaks of high state parameters at these depths. The CPTu-02, on the other hand, presents an increase in the state parameter at a constant rate until c.a. 6,4 m deep, then there is a shift in the profile, and the same behavior is observed again.

The ψ profile of CPTu-01 may be associated with high variability of the material or poor control of the compaction where the test was performed. The high variation of the state parameter at

low depths may be associated with adopting thicker layers or using inappropriate compaction equipment.

Figure 4.19 – Analysis of ψ profile: a) CPTu-01 and b) CPTu-02.

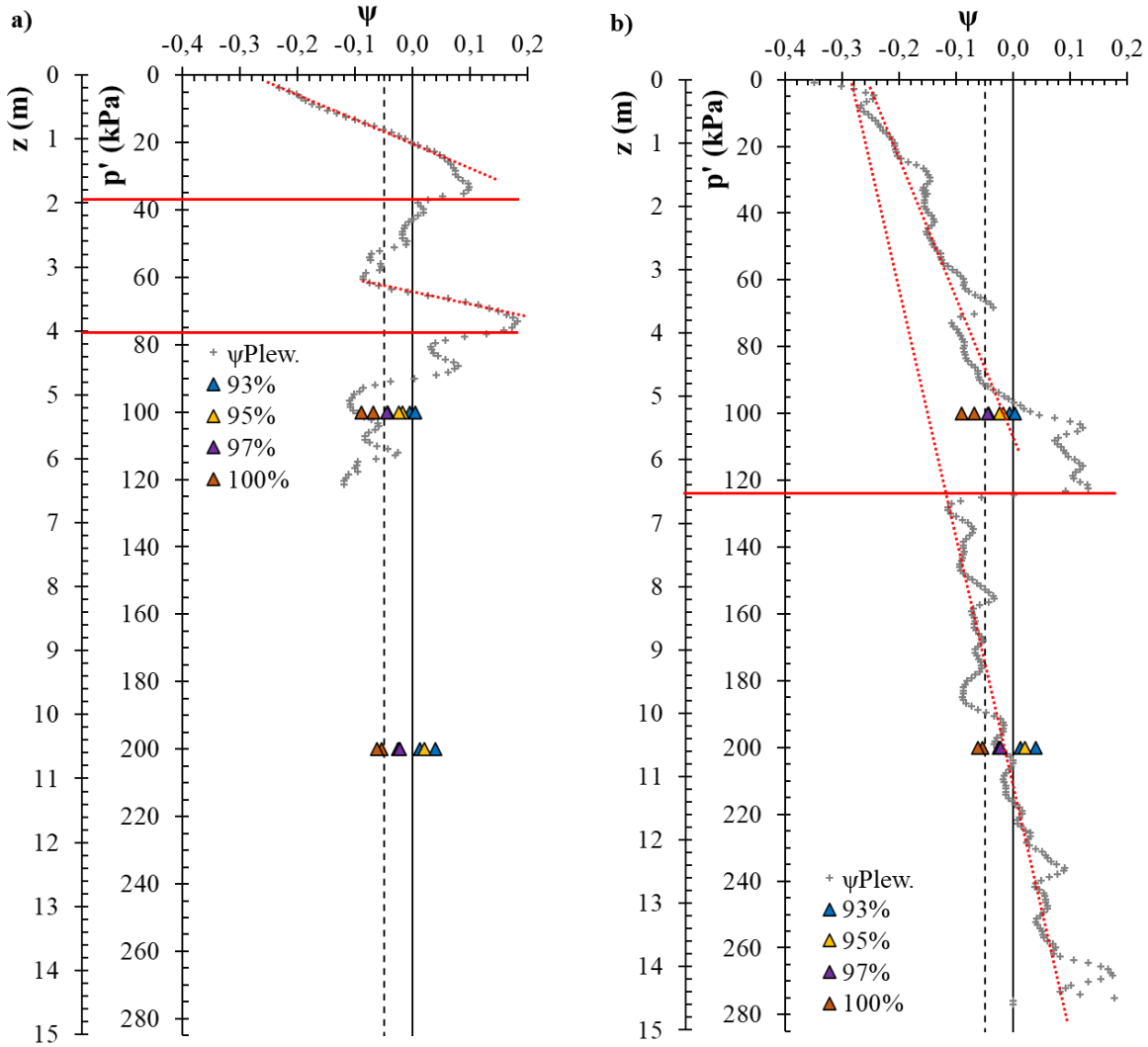

Source: elaborated by the author

The material intercepted by CPTu-02 seems to be more homogeneous than the material intercepted by CPTu-01 since there is no abrupt change in the ψ profile of CPTu-02. Furthermore, the ψ profile of CPTu-02 shows that the adopted degree of compaction seems to have changed after the 8,5 m of the embankment raised, and a lower degree of compaction was adopted in the top portion of the embankment.

4.6.3 DILATANCY

Following the critical state approach for peak strength and dilatancy (2.3.5), it was determined the stress-dilatancy and state-dilatancy parameters of the studied tailings. For this, it was

identified the drained tests in which the samples presented a fully dilatant behavior: Trx_97_CID_100kPa, Trx_100_CID_100kPa, Trx_100_CID_200kPa, and Trx_100_CID_400kPa. Figure 4.20 shows these test results.

Figure 4.20 – Results of the CID triaxial test in which the specimens have shown a fully dilatant drained behavior.

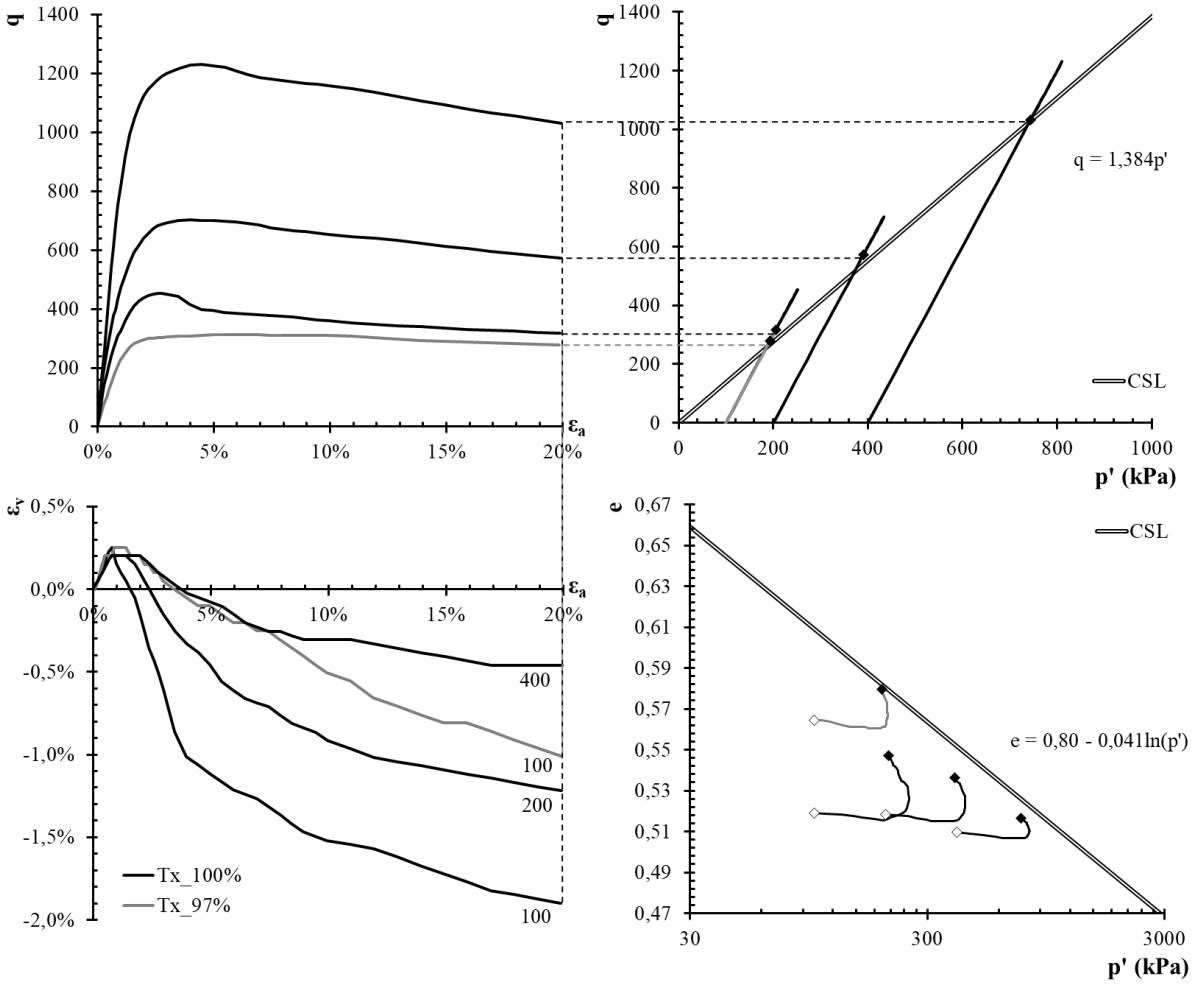

Source: elaborated by the author

The maximum dilatancy and, consequently, the peak strength of the samples have been mobilized with axial strain between 2,19% and 2,78%. From each of the samples, it was calculated the D_{min}, ψ at maximum dilatancy, and η_{max}. The parameters were then plotted in Figure 4.21a and b, from which were determined N, χ_{tc}, and M_{tc}. Table 4.13 presents the determined parameters.

Table 4.13 – Stress-dilatancy and state-dilatancy parameters.

M_{tc}	1,384
N_{tc}	0,0058
χ_{tc}	8,16

Source: elaborated by the author

M_{tc} determined from the (p',q) plot presented in Figure 4.13 was confirmed by the (D_{min}, η_{max}) plot. Both N and χ_{tc} were out of the conventional range exhibited by natural soils (N ranging from 0,2 to 0,45; χ_{tc} ranging from 2,5 to 4,5). When comparing to the parameters of Morgenstern et al. (2016) and Robertson et al. (2019), χ_{tc} is even higher than the value of χ_{tc} = 7,3 presented by Morgenstern et al. (2016), and N was very low, not being close to any of the values determined by the authors.

Figure 4.21 – Stress-dilatancy and state-dilatancy plots.

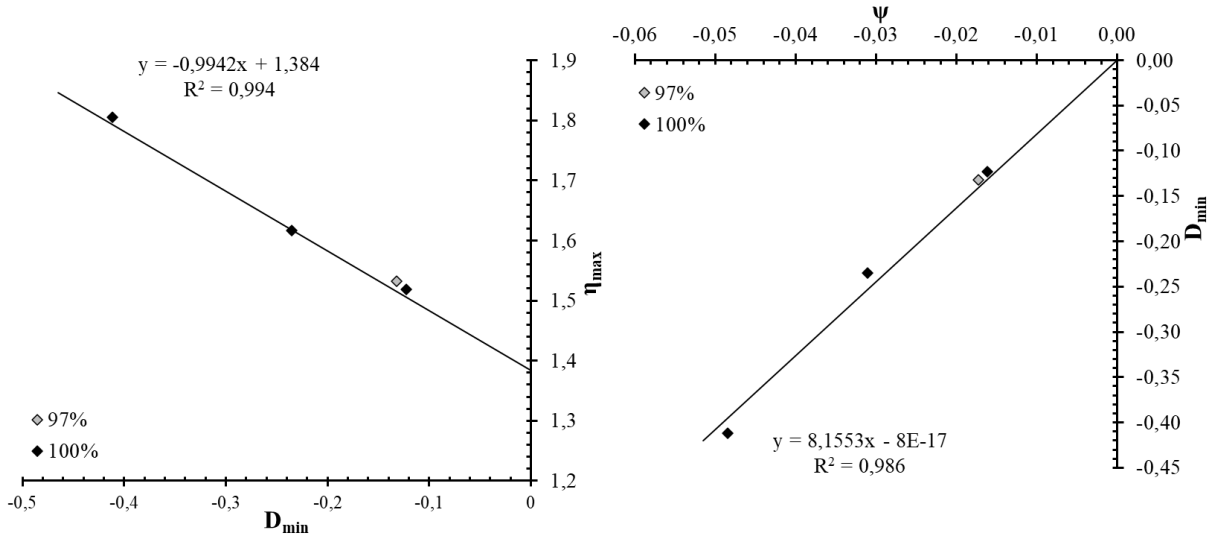

Source: elaborated by the author

It is noteworthy mentioning that only four samples showed fully dilatant behavior, and the obtained parameters are out of the common ranges. Moreover, Trx_100_CID_100kPa (most dilatant sample) showed rapid strength loss (brittle behavior) after the peak was reached, and this behavior was not observed in the other dilatant samples. Therefore, to confirm the parameters of dilatancy and to analyze the brittle response of dilatant samples under drained load conditions, it would be pertinent to run tests in denser specimens, compacted using higher levels of energy, such as modified Proctor.

4.6.4 UNDRAINED STRENGTH

Three samples of CIU tests have shown a contractive brittle behavior (see Figure 4.22): Trx_93_CIU_800kPa, Trx_93_CIU_1600kPa, and Trx_93_CIU_1900kPa. These samples were then used to calculate the peak undrained strength, the critical undrained strength, and the brittle index of the tailings. The undrained strengths were also normalized by the initial mean effective stresses. The results are presented in Table 4.14.

Table 4.14 – Undrained strength parameters.

Sample	$\psi_{semi-log}$	Peak		Critical		I_B
		$s_{u,p}$	$s_{u,p}/p_0'$	$s_{u,c}$	$s_{u,c}/p_0'$	
Trx_93_CIU_800kPa	0,048	352,63	0,44	228,53	0,29	0,35
Trx_93_CIU_1600kPa	0,054	607,33	0,38	409,80	0,26	0,33
Trx_93_CIU_1900kPa	0,041	572,58	0,29	472,44	0,24	0,17

Source: elaborated by the author

Figure 4.22 – Results of the CIU triaxial tests in which the specimens have shown a contractive brittle behavior.

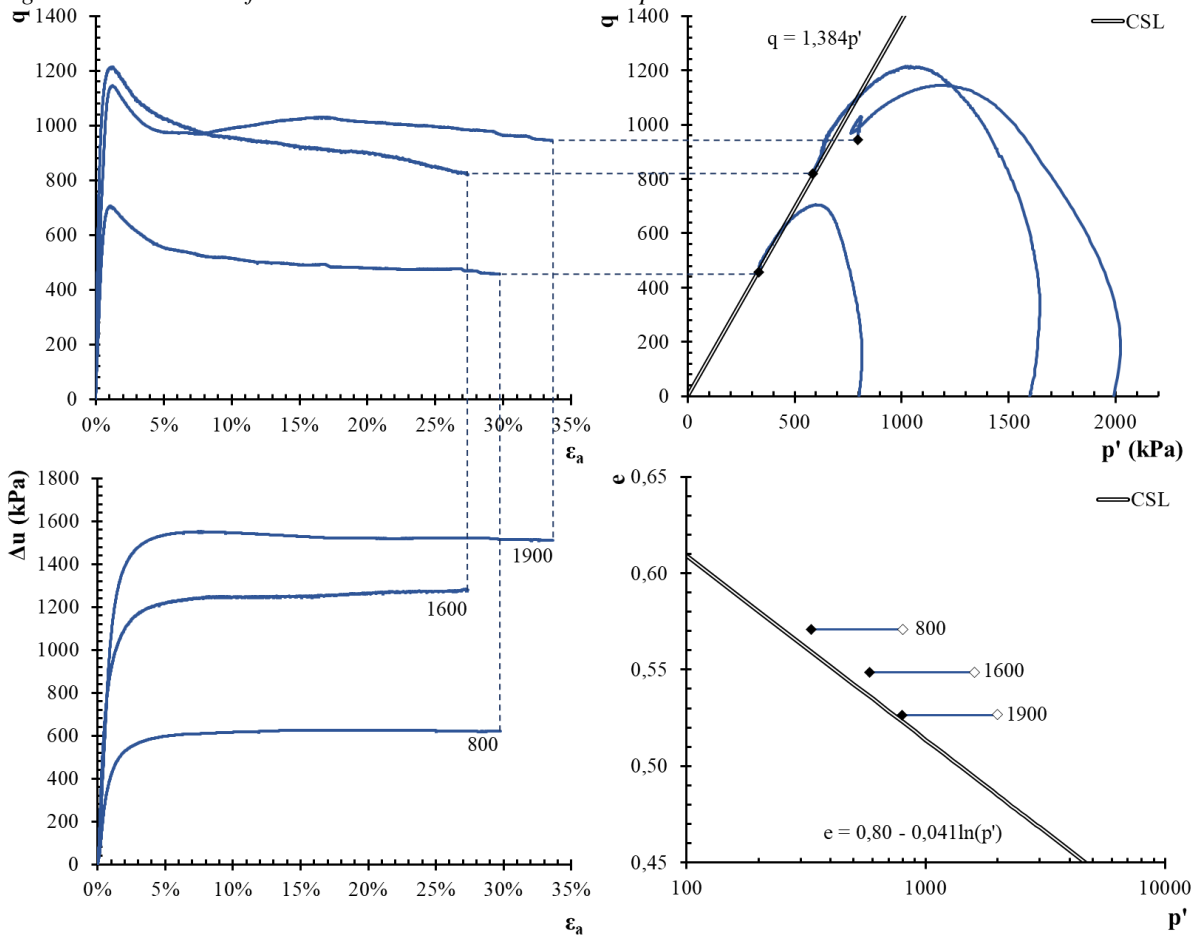

Source: elaborated by the author

The peak undrained strength ratios are in a similar range to other iron ore tailings from the Quadrilátero Ferrífero (see 2.4.8). However, the critical undrained strength ratios are higher than the references. The considerably high values of critical undrained strength result in low values of the brittleness index, indicating that the samples did not present much loss of strength after the peak, especially the specimen of 1900 kPa, whose peak and critical undrained strengths are very close.

Nevertheless, Figure 4.22 shows that right after the peak, at approximately 2% of axial strain, most of the strength loss happens with less than 5% of strain deformation. This behavior is

identified in all three samples (see Appendix D) and, despite the low brittleness index, the material presents a quick loss of strength, showing a brittle response.

Notice that the undrained strength ratios are not constant when comparing the three samples. The ratios gradually decrease from 800 kPa to 1900 kPa. It would suggest that at 800 kPa and 1600 kPa, the material is still not fully contractive. However, the state parameters of the samples are very similar, although the end of the tests Trx_93_CIU_800kPa and Trx_93_CIU_1600kPa are a little bit shifted from the average semi-logarithmic CSL.

Therefore, it would be appropriate to run additional tests at higher stresses and the same degree of compaction to check if the undrained shear behavior of Tx_93%_CIU_1900kPa is confirmed. Moreover, it must be emphasized that it just represents one mode of shear (see 2.4.8), and the other modes of shear (simple shear and extension) should also be evaluated.

4.6.5 ELASTIC SHEAR MODULUS AND PLASTIC MODULUS

Neither the elastic shear modulus (G_{max}) nor the plastic modulus (H) could be measured through the experimental program. The parameters were estimated initially based on the parameters of Morgenstern et al. (2016) and Robertson et al. (2019), then calibrated with NorSand into the *NorTXL.xls (Release 2)*, from Jefferies and Been (2015).

All triaxial tests were modeled into the spreadsheet, and it was verified that the models were more sensitive to the variation of G_{max} than H. When analyzing the terms of the plastic modulus, it was observed that changing H_0 affected more the model's behavior than changing H_ψ. However, H_0 was almost the same for both Morgenstern et al. (2016) and Robertson et al. (2019). Because the critical state parameters λ and M_{tc} of the studied tailing are close to the parameters presented by Robertson et al. (2019), to calibrate the models, it was adopted H_0 and H_ψ equal to the values defined by Robertson et al. (2019): **$H_0 = 160$ and $H_\psi = 1037$**.

With H fixed, G_{max} was adjusted until finding the best fit to the triaxial tests data. To recreate the elastic behavior in the *NorTXL.xls (Release 2),* the inputs are Gmax @ p0 (G_{max} at the initial mean stress), G_exp (the exponent n defined in 2.4.9.1), and ν (Poisson's ratio). The model did not show significant variation from changing G_exp. Thus, the value was kept constant G_exp = 0,4. Moreover, some variation was observed when reducing the Poisson's ratio, but it was kept constant $\nu = 0{,}2$ as suggested by Shuttle and Jefferies (2010).

It is worth noting that, even for undrained tests, it was adopted the drained Poisson's ratio (ν = 0,2). According to Jefferies and Been (2015), the Poisson's ratio is considered constant when calibrating the model because the undrained behavior is a "boundary condition effect." Therefore, the unique elastic parameter changed during calibration was Gmax @ p0.

Besides Gmax @ p0, the initial OCR also had to be adjusted, so the model could better fit the test data. First, the OCR of each sample was estimated by comparing the compression curves of each degree of compaction with the average 1D-NCL (see 4.5.1). Nonetheless, the calibration in *NorTXL.xls (Release 2)* was affected only by OCRs lower than four. Thus, the final OCR was mainly defined based on the better fit of the model to the test data since the OCRs defined from the compression curves for the lower confining stresses were considerably high.

The calibration results are in Appendix F. Figure 4.23 presents the synthesis of the elastic shear moduli defined for each specimen calibrated into NorSand. The results are also plotted by the degree of compaction in Appendix G, and Table 4.15 shows the equations of the trendlines defined for each degree of compaction.

Figure 4.23 – G_{max} estimated after NorSand calibration.

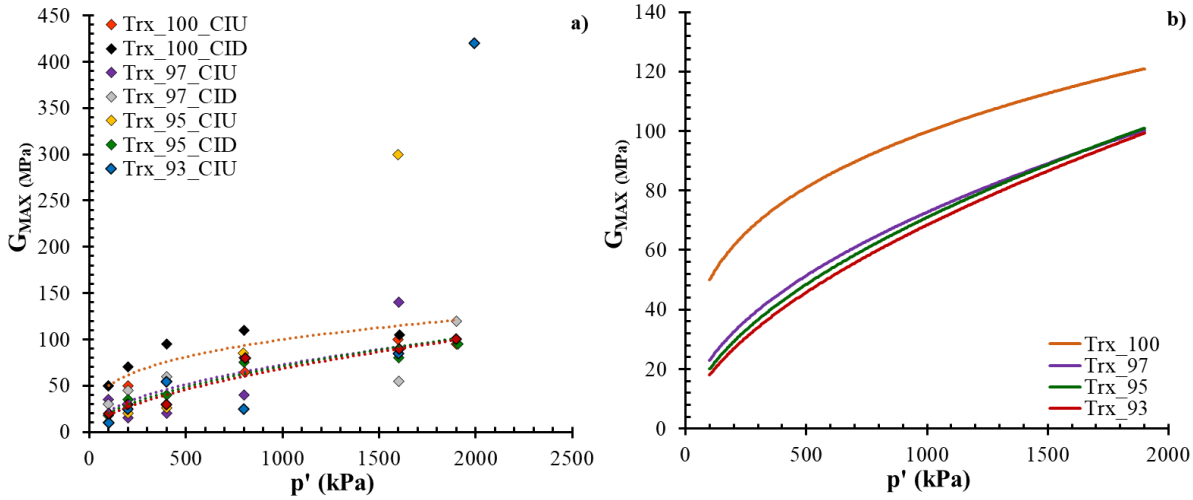

a) G_{max} estimated for each of the confining stresses of the four studied degrees of compaction; b) Trendlines determined after values of G_{max} of each degree of compaction. Source: elaborated by the author

Despite the outliers, the samples compacted to 93%, 95%, and 97% of the standard Proctor presented very similar trendlines indicating no significant change of the elastic shear modulus when increasing the degree of compaction from 93% to 97%. A relevant change of the elastic shear modulus was identified only for DC = 100%.

Table 4.15 – G_{max} equation for each degree of compaction.

DC	Equation	
93%	$G_{MAX} = 18\left(\frac{p'}{p'_{ref}}\right)^{0,58}$	Equation 4.12
95%	$G_{MAX} = 20\left(\frac{p'}{p'_{ref}}\right)^{0,55}$	Equation 4.13
97%	$G_{MAX} = 22\left(\frac{p'}{p'_{ref}}\right)^{0,52}$	Equation 4.14
100%	$G_{MAX} = 50\left(\frac{p'}{p'_{ref}}\right)^{0,30}$	Equation 4.15

*Where, p'_{ref} = 100 kPa
Source: elaborated by the author

Compared to Morgenstern et al. (2016) and Robertson et al. (2019), the calibrated G_{max} equations result in elastic shear moduli considerably lower than those defined by both authors. Thus, to confirm the values of G_{max} would be pertinent to perform seismic field tests or further laboratory tests using bender elements or vibrating columns.

4.6.6 SECANT ELASTIC MODULI

In addition to the elastic properties already defined, the drained and undrained secant elastic moduli ($E_{50,D}$ and $E_{50,U}$) were also determined from the results of the CID and CIU tests.

The secant moduli were defined as the slope of the line starting at the origin and ending at the point of the stress-strain curve equivalent to 50% of the maximum deviatoric stress. The moduli determined for each specimen were then plotted in the space (p', E_{50}), and the trendlines for each degree of compaction were defined.

Figure 4.24 and Figure 4.25 show the synthesis of the drained and undrained secant elastic moduli, respectively. Table 4.16 and Table 4.17 present the equations of the trendlines defined for each degree of compaction, and Appendix H shows the results plotted separately by the degree of compaction.

Figure 4.24 – $E_{50,D}$ determined after triaxial tests.

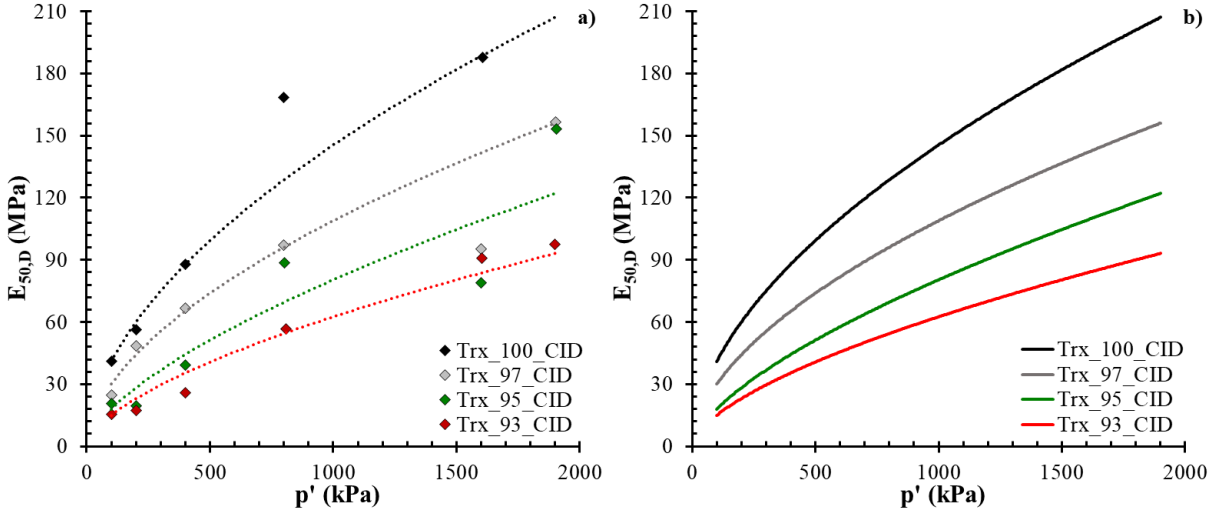

a) $E_{50,D}$ determined for each of the confining stresses of the four studied degrees of compaction; b) Trendlines determined after values of $E_{50,D}$ of each degree of compaction. Source: elaborated by the author.

Table 4.16 – $E_{50,D}$ equation for each degree of compaction.

DC	Equation	
93%	$E_{50,D} = 15\left(\frac{p'}{p'_{ref}}\right)^{0,62}$	Equation 4.16
95%	$E_{50,D} = 18\left(\frac{p'}{p'_{ref}}\right)^{0,65}$	Equation 4.17
97%	$E_{50,D} = 30\left(\frac{p'}{p'_{ref}}\right)^{0,56}$	Equation 4.18
100%	$E_{50,D} = 41\left(\frac{p'}{p'_{ref}}\right)^{0,55}$	Equation 4.19

*Where, p'_{ref} = 100 kPa
Source: elaborated by the author.

Figure 4.25 – $E_{50,U}$ determined after triaxial tests.

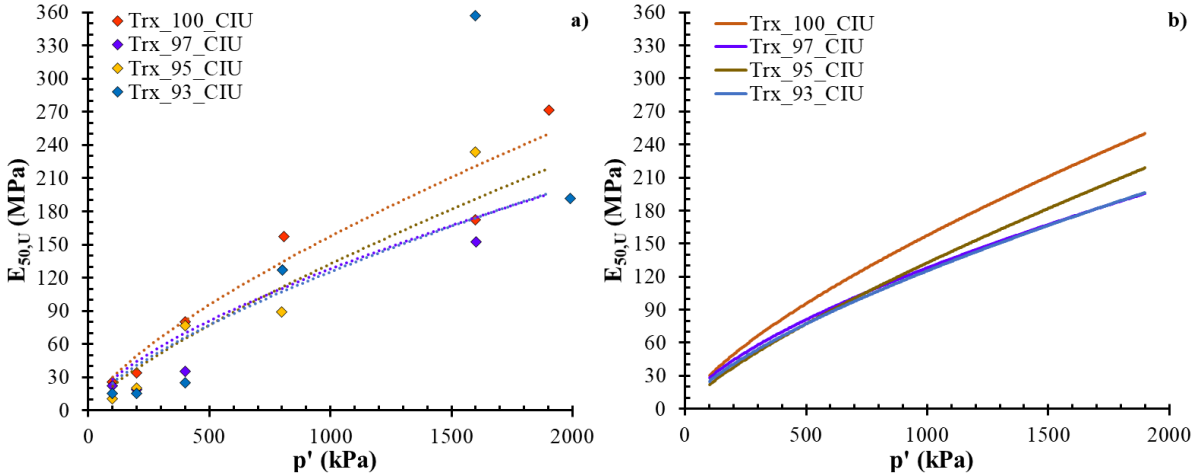

a) $E_{50,U}$ determined for each of the confining stresses of the four studied degrees of compaction; b) Trendlines determined after values of $E_{50,U}$ of each degree of compaction. Source: elaborated by the author.

Table 4.17 – $E_{50,U}$ equation for each degree of compaction.

DC	Equation	
93%	$E_{50,U} = 25\left(\frac{p'}{p'_{ref}}\right)^{0,70}$	Equation 4.20
95%	$E_{50,U} = 22\left(\frac{p'}{p'_{ref}}\right)^{0,78}$	Equation 4.21
97%	$E_{50,U} = 28\left(\frac{p'}{p'_{ref}}\right)^{0,66}$	Equation 4.22
100%	$E_{50,U} = 30\left(\frac{p'}{p'_{ref}}\right)^{0,72}$	Equation 4.23

*Where, p'_{ref} = 100 kPa
Source: elaborated by the author.

Figure 4.24 shows clear trends of $E_{50,D}$, with little outliers, for each degree of compaction. The higher the degree of compaction, the higher the $E_{50,D}$, indicating the increase of the stiffness with the increase of the degree of compaction. Meanwhile, Figure 4.25 shows more dispersion of $E_{50,U}$ and, except for DC = 100%, the trendlines of each degree of compaction are significantly close to each other, not showing a clear variation of the stiffness with DC under undrained conditions.

4.7 SUMMARY OF PROPERTIES

The properties defined in this chapter are summarized in Table 4.18. Notice that for "one-dimensional consolidation" and "isotropic consolidation" were presented the parameters considered more representative of the tailings' behavior. Nonetheless, section 4.5 must be consulted to check the particularities of the compression and recompression indexes presented in Table 4.18.

Table 4.18 – Summary of properties.

Index Properties		**Critical State Properties**		
D_{50} (mm):	0,035 (0,026-0,044)	**Semi-log. CSL**	Γ:	0,800
C_U:	34,4 (15,4-48,6)		λ_e:	0,041
C_Z:	6,2 (4,9-8,5)	**Curved CSL**	A:	0,805
% Fines (< 0,075 mm):	91,1(94,0-83,0)		B:	0,201
G_s (g/cm^3):	3,205 (3,184-3,218)		C:	0,15
LL, LP, IP:	non-plastic		M_{tc}:	1,384
e_{min}:	0,60		N_{tc}:	0,0058
e_{max}:	1,18		χ_{tc}:	8,16
w_{opt}:	11,70%	**Plastic Modulus**		
$\gamma_{d,max}$ (kN/m^3):	20,88 (20,71-21,05)		H_0:	160
Hydraulic conductivity			H_ψ:	1037
$k = 2 \times 10^{-12} \cdot exp^{20,57e}$		**Elastic Moduli**		
One-Dimensional Consolidation		**DC = 93%**	$G_{MAX} = 18\left(\frac{p'}{p'_{ref}}\right)^{0,58}$	
C_c*$_{(loose)}$:	0,235/0,175		$E_{50,D} = 15\left(\frac{p'}{p'_{ref}}\right)^{0,62}$	
C_r:	0,003		$E_{50,U} = 25\left(\frac{p'}{p'_{ref}}\right)^{0,7}$	
C_v (cm^2/s):	0,025 (0,014-0,035)	**DC = 95%**	$G_{MAX} = 20\left(\frac{p'}{p'_{ref}}\right)^{0,55}$	
*Depedent on σ'v			$E_{50,D} = 18\left(\frac{p'}{p'_{ref}}\right)^{0,65}$	
Isotropic Consolidation			$E_{50,U} = 22\left(\frac{p'}{p'_{ref}}\right)^{0,78}$	
λ*$_{(ISO\_93\_3000kPa)}$:	0,0299/0,0420	**DC = 97%**	$G_{MAX} = 22\left(\frac{p'}{p'_{ref}}\right)^{0,52}$	
κ*:	0,0042 (0,0032-0,0052)		$E_{50,D} = 30\left(\frac{p'}{p'_{ref}}\right)^{0,56}$	
*Depedent on p'			$E_{50,U} = 28\left(\frac{p'}{p'_{ref}}\right)^{0,66}$	
Strength Parameters		**DC = 100%**	$G_{MAX} = 50\left(\frac{p'}{p'_{ref}}\right)^{0,30}$	
φ'$_c$:	34,2°		$E_{50,D} = 41\left(\frac{p'}{p'_{ref}}\right)^{0,55}$	
$(s_u/\sigma'_v)_{peak}$:	0,29 - 0,44		$E_{50,U} = 30\left(\frac{p'}{p'_{ref}}\right)^{0,72}$	
$(s_u/\sigma'_v)_{critical}$:	0,24 - 0,29		*Where, p'$_{ref}$ = 100 kPa	

Source: elaborated by the author.

5 CONCLUSIONS

The studied tailings exhibited characteristics consistent with other iron ore tailings of the Quadrilátero Ferrífero, presented in section 2.4. The particle size distribution curves of the samples compacted statically did not show significant divergence from the initial sample. Nonetheless, the dynamically compacted specimen showed a fines content increase in the central portion of the curve. It evidences the tailings' evolution due to dynamic, but not static compaction.

The higher the degree of compaction, the lower the hydraulic conductivity. The hydraulic conductivity determined after the constant head tests were proportional to the void ratio of each specimen. For the studied range of void ratios, k varied from 6,23 x 10^{-8} m/s to 4,10 x 10^{-7} m/s, which is equivalent to a factor of reduction of approximately ten times. The k measured was higher than the k predicted by the KC equation, which suggests that the clay size particles tend to agglomerate. Furthermore, the hydraulic conductivity was more sensitive to the void ratio variation than predicted by the KC equation.

Increasing the degree of compaction also resulted in compressibility decrease. Higher degrees of compaction (97% and 100%) showed flattened compression curves. Therefore, the tailings compacted to 100% of standard Proctor unit weight are less susceptible to excessive strains and saturation (as a function of consolidation) than the tailings compacted to 97%, 95%, and 93% of the standard Proctor. Moreover, for the range of studied degrees of compaction and saturation, the tailings presented low suction, and the material's compressibility is only affected by the suction under low confining stresses.

The one-dimensional consolidation tests showed that with σ'_v = 6,4 MPa, the sample compacted to 95% of the standard Proctor unit weight did not reach the normal consolidation line. Plotting the oedometer and the isotropic consolidation tests in the same plot showed that the loosest specimen compacted with DC = 93% (e_0 = 0,63) reaches the NCL with p' = 3,0 MPa ($\sigma'_v \approx$ 4,9 MPa). This result indicates that the degree of compaction's effect can only be erased by large strains with 3,0 MPa of confining stress.

However, as mentioned in section 4.5.2, the convergence of the sample Iso_93_3000kPa with the normal consolidation line must be confirmed by defining the NCL after isotropic consolidation tests in looser samples. Since the boundary conditions implied by the oedometer tests and the isotropic consolidation tests are different.

The recompression curves presented low indexes, which indicate minor swelling of the tailing when unloaded. It is consistent with the flattened compression curves of the samples with higher degrees of compaction, which are highly overconsolidated. Furthermore, it was also identified that the compression and recompression indexes tend to change with the increase of the confining stress.

The variation of the compression and recompression indexes suggests that the tailings tend to evolve with the increase of confining stresses. The evolution of the material also affects the CSL that tends to be curved. However, for the range of stresses evaluated in the triaxial compression tests (100 kPa – 3400 kPa), the CSL presented a wide curvature, so the semi-logarithmic CSL fitted the data well. Notice that the evolution of the curves may be associated with particle crushing and shattering. This should be confirmed by doing laser grain size distribution tests and scanning electron microscopy (SEM) tests before and after the compaction and the very high confining stress application.

Regardless of the outliers and the strong dilatant samples, the triaxial compression tests converged to the same critical state line. No significant difference due to the degree of compaction or sample variation (UFV, FEUP – Sample A, or FEUP – Sample B) was identified.

The state parameters were consistent with the boundary of $\psi = -0,05$ defined by Jefferies and Been (2015), and a transition of behavior from the samples with DC = 93% to the samples with DC = 100% was identified. The samples with DC = 93% presented positive state parameters or $\psi \approx 0,00$, showing mainly a contractive behavior. Most of the samples with DC = 95% and DC = 97% showed a light dilatant behavior, with some negative state parameters, but always higher than -0,05. Lastly, samples with DC = 100% presented dilatant behavior for low confining stresses, $\psi < -0,05$ or $\psi \approx -0,05$, and light dilatant behavior for high confining stresses, $\psi > -0,05$.

The loose drained samples, just as observed by Robertson et al. (2019) for the tailings of Feijão Dam I, showed peak before reaching the critical state, and the dense drained samples exhibited dilatancy parameters higher than those obtained by Morgenstern et al. (2016) and Robertson et al. (2019) for iron ore tailings.

The high dilatancy is coherent with steep stress-strain curves presented by the dense samples. The peak strength in both drained (dense samples) and undrained (loose samples) tests was reached with an axial strain of approximately 2%. Under the undrained condition, the material

showed rapid strength loss right after the peak. However, this behavior was not confirmed under drained conditions since only the sample Trx_100_CID_100kPa showed a brittle response after the peak.

The tailings did not show much strength loss after the peak. However, the undrained strength ratio was not constant from 800 kPa to 1900 kPa of confining stress. It suggests that for higher confining pressures or looser states, the undrained strength ratio may be lower.

Considering K_0 = 0,7, and γ = 23,79 kN/m^3, the confining stress of p'= 800 kPa is reached in the base of an embankment of 42 m high. It means that, after 42 m of lifting, even the tailings compacted to 100% of standard Proctor, will show light dilatant behavior.

It is relevant mentioning that, differently of DC = 93% and DC = 95%, with p'= 800 kPa the samples with DC = 97% and DC = 100% still dilate without significant intermediate strength loss (see Appendix D). With p' = 1600 kPa only the sample with DC = 100% keep showing the same behavior until, with p' = 1900 kPa (equivalent to 100 m high), the tailings with DC = 100% stops dilating.

At this point a designer may be inclined to assume that since there is no significant strength loss until 1900 kPa would be possible to build a dry stack 100 m high with DC = 100% without further studies. Nevertheless, before affirming it, the other modes of shear – simple shearing and extension – must be analyzed. As Figure 2.26 (section 2.4.8) shows, the same material under similar initial state conditions shows higher strength loss in simple shear, and lower final strength, in extension. Additionally, as Figure 2.25 presents, in the basal zone of a stack – higher confining pressure – the main modes of shear will be simple shearing and extension.

Both $E_{50,U}$ and G_{max} did not show significant variation from DC = 93% to DC = 97%. Only for DC = 100%, a notable increase was observed. Differently, $E_{50,D}$ showed a gradual increment for each degree of compaction. The elastic shear moduli estimated after NorSand calibration were lower than expected for the material. The parameters were even lower than the secant elastic moduli. Therefore, bender elements or vibrating column tests must be performed to confirm G_{max} referent to each studied degree of compaction.

The characteristics displayed in chapter 4 are related to a sample of filtered iron ore tailings from a specific mining complex located in the Quadrilátero Ferrífero. Its representability is dependent on the variability of the *in-situ* material. The standard Proctor tests done for quality-

control of the trial embankment, presented in 4.2.1, showed that the field samples converged to average values of optimum water content and maximum dry unit weight close to the ones found at LMS and LabGeo. However, some samples showed considerable variation.

Variability of both the material and the degree of compaction was identified in the trial embankment. Mapping the tailings' variations is essential to stack the material in an adequate initial state. Each of the main variations must be characterized, and the proper degree of compaction and optimum water content must be specified. Using the same specification of DC and w_{opt} for different materials may result in saturated and loose portions of tailings.

Additionally, the compaction quality-control tests revealed parts of the trial embankment with DC > 100% and $w_{field} > w_{opt}$. It also indicates variability of the tailings instead of suggesting that higher compaction energy was used during compaction. Increasing the compaction's energy to achieve higher degrees of compaction without reducing the water content will not substantially improve the characteristics of the stack. Moreover, the higher the degree of compaction, the lower the void ratio. Consequently, for constant water content, the material will be more likely to saturate without significant gain of compacity.

Reducing the water content prevents saturation. Thus, it is adequate to compact dry of optimum because when stacking, depending on its compressibility, the material will tend to consolidate, reducing the void ratio and increasing saturation. The normalized pore water pressure profiles of the CPTus (presented in 4.6.2.1) were negligible. However, the material was under low confining stresses (p'_{max} = 280 kPa). Under higher loading conditions, the tailings stacked wet of optimum will tend to consolidate and may saturate. Furthermore, an excess of pore water pressure may be generated in the saturated zones, depending on the rate of lifting and the total height of the stack.

The CPTus performed in the trial embankment were consistent with the compaction quality-control tests. They registered the considerable variation of the behavior along with the profile of the embankment. Moreover, the state parameters predicted using Plewes et al. (1992) were more consistent with the state parameter determined in the laboratory than the ones estimated by using Robertson (2010).

The parameters obtained in this research added to the ranges and average parameters of iron ore tailings presented in section 2.4 are a good initial reference for conceptual project designs. However, the behavior of each material is associated with the combination of their intrinsic

characteristics and state. Thus, when developing an engineering project, in which the tailings will have geomechanical or hydraulic importance, the characterization of the material and its variations is essential.

5.1 FUTURE RESEARCH

The research covered a relevant range of characteristics of studied sample of the iron ore tailings. Nevertheless, further research is necessary, as it follows:

i) To map the range of variability of the tailings in the mining complex, to characterize the most relevant of them.

ii) To do x-ray diffraction testing to determine the mineral contents of the tailings.

iii) To perform tests under higher confining stresses to verify the evolution of the material, confirm the undrained behavior of the lower degrees of compaction, and evaluate the tendency of even the tailings compacted to 100% of the standard Proctor unit weight to become contractive.

iv) To test samples with higher levels of compaction to confirm the parameters of dilatancy and to analyze their behavior under high confining stresses.

v) To determine the particle size distribution through conventional hydrometer test with and without deflocculant to check particle agglomeration.

vi) To determine the particle size distribution through laser and run SEM tests before and after applying high confining stresses to check particle evolution.

vii) To model a dry stack using appropriate constitutive models that incorporate the main aspects of the tailings behavior, considering the initial state condition of each degree of compaction and different lifting rates, to check the stresses and strains resultant of each condition.

viii) To perform isotropic consolidation tests in loose samples to confirm the isotropic normal consolidation line.

ix) To perform direct simple shear and triaxial extension tests to determine the drained and undrained parameters associated with the different modes of shear.

x) To run bender elements or vibrating column tests to confirm G_{max} for each degree of compaction. Also, run seismic tests, such as SCPTu, in the trial embankment to analyze the G_{max} *in situ*.

xi) To perform tests to characterize the unsaturated behavior of the iron ore tailings.

BIBLIOGRAPHY

Alves, A. R. (2009). *Disposição compartilhada de rejeito e estéril gerados no Processo de extração de minério de ferro.* Dissertação (Mestrado em Geotecnia) - Universidade de Brasília , Distrito Federal.

AMERICAN SOCIETY FOR TESTING AND MATERIALS. (2011). *D2435M: Standard test methods for one-dimensional consolidation properties of soils using incremental loading.* West Conshohocken.

AMERICAN SOCIETY FOR TESTING AND MATERIALS. (2011/2020). *D4767: Standard test method for consolidated undrained triaxial compression test for cohesive soils.* West Conshohocken.

AMERICAN SOCIETY FOR TESTING AND MATERIALS. (2016). *D5084: Standard test methods for measurement of hydraulic conductivity of saturated porous materials using a flexible wall permeameter.* West Conshohocken.

AMERICAN SOCIETY FOR TESTING AND MATERIALS. (2017). *D2487: Standard Practice for Classification of Soils for Engineering Purposes (Unified Soil Classification System).* West Conshohocken.

AMERICAN SOCIETY FOR TESTING AND MATERIALS. (2020). *D7181: Standard test method for consolidated drained triaxial compression test for soils.* West Conshohocken.

ASSOCIAÇÃO BRASILEIRA DE NORMAS TÉCNICAS. (1991). *NBR 12069: Soil - Cone penetration test (CPT) "in situ" - Method of test.* Rio de Janeiro.

ASSOCIAÇÃO BRASILEIRA DE NORMAS TÉCNICAS. (20020). *NBR 16843: Soil - Determination of minimum index void ratio of cohesionless soil.* Rio de Janeiro.

ASSOCIAÇÃO BRASILEIRA DE NORMAS TÉCNICAS. (2016). *NBR 6457: Soil samples - Preparation for compactation and characterization tests.* Rio de Janeiro.

ASSOCIAÇÃO BRASILEIRA DE NORMAS TÉCNICAS. (2016). *NBR 6458: Gravel grains retained on the 4,8 mm mesh sieve - Determination of the bulk specific gravity, of the apparent specific gravity and of water absortion.* Rio de Janeiro.

ASSOCIAÇÃO BRASILEIRA DE NORMAS TÉCNICAS. (2016). *NBR 6459: Soil - Liquid limit determination.* Rio de Janeiro.

ASSOCIAÇÃO BRASILEIRA DE NORMAS TÉCNICAS. (2016). *NBR 7180: Soil - Plasticity limit determination.* Rio de Janeiro.

ASSOCIAÇÃO BRASILEIRA DE NORMAS TÉCNICAS. (2016). *NBR 7181: Grain size analysis.* Rio de Janeiro.

ASSOCIAÇÃO BRASILEIRA DE NORMAS TÉCNICAS. (2016). *NBR 7182: Soil - Compaction test.* Rio de Janeiro.

ASSOCIAÇÃO BRASILEIRA DE NORMAS TÉCNICAS. (2016). *NBR 9813: Soil - "In situ" determination of the apparent specific gravity using a core cutter.* Rio de Janeiro.

ASSOCIAÇÃO BRASILEIRA DE NORMAS TÉCNICAS. (2020). *NBR 16840: Soil - Determination of the maxium index void ratio of cohesionless soils* . Rio de Janeiro.

ASSOCIAÇÃO BRASILEIRA DE NORMAS TÉCNICAS. (2020). *NBR 16853: Soil - One-dimensional consolidation test.* Rio de Janeiro.

Atkinson, J. H. (2007). *The mechanics of soils and foundations* (2nd ed.). New York: Taylor & Francis.

AUSTRALIA. (2016). *Leading Practice Sustainable Development Program for the Mining Industry.* Department of Industry, Science, Energy and Resources. Department of Foreign Affairs and Trade.

Barthelmy, D. (1997). *Mineralogy Database*. Acesso em 26 de February de 2021, disponível em Webmineral: http://webmineral.com/

Been, K. (1999). The critical state line and its application to soil liquefaction. Em P. V. Lade, & J. A. Yamamuro, *Physics and Mechanics of Soil Liquefaction* (pp. 195-204). Rotterdam: Balkema.

BRAZIL. (2020). *Brazilian Mineral Yearbook - Main Metallic Commodities.* National Mining Agency - ANM, Brasília.

BRAZIL. (2020). *Mineral Sector Bulletin.* Secretariat of Geology, Mining and Mineral Transformation - SMM, Brasília.

Budhu, M. (2010). *Soil mechanics and foundations* (3rd ed.). John Wiley & Sons.

Carvalho, W. D. (2017). *Sistema de disposição compartilhada de estéreis e rejeitos desaguados da mina de Fernandinho.* Dissertação (Mestrado em Engenharia Geotécnica) - Universidade Federal de Ouro Preto, Ouro Preto.

Chapuis, R. P., & Aubertin, M. (2003). *Predicting the coefficient of permeability of soils using the Kozeny-Carman equation.* Rapport technique, Montréal.

Chapuis, R., & Légaré, P. (1992). A Simple Method for Determining the Surface Area of Fine Aggregates and Fillers in Bituminous Mixtures. *ASTM International*, 177-186.

Crystal, C., Hore, C., & Ezama, I. (2018). Filter-Pressed Dry Stacking: Design Considerations Based on Practical Experience. *Tailings and Mine Waste*, 209-219.

CSN. (2020). *Filtragem de Rejeitos*. Acesso em 28 de December de 2020, disponível em CSN - Companhia Siderúrgica Nacional: https://esg.csn.com.br/csn-passa-filtrar-100-dos-rejeitos-em-casa-de-pedra/

Dauce, P. D., Castro, G. B., Lima, M. M., & Lima, R. M. (2019). Characterisation and magnetic concentration of an iron ore tailings. *Journal of Materials Research and Technology, 8*(1), 1052-1059.

Davies, M. (2011). Filtered dry stacked tailings: the fundamentals. *Proceedings Tailings and Mine Waste 2011*, 9.

Davies, M. P., & Rice, S. (2001). An alternative to conventional tailing management – " dry stack " filtered tailings. *Proceeding of Tailings and Mine Waste*, 411-420.

Davies, M., Lupo, J., Martin, T., McRoberts, E., Musse, M., & Ritchie, D. (2010). Dewatered tailings practice - Trends and observations. *Tailings and Mine Waste'10 - Proceedings of the 14th International Conference on Tailings and Mine Waste*, 133-142.

DEPARTAMENTO NACIONAL DE ESTRADAS DE RODAGEM. (1994). *DNER-ME 213/94: Solos - Determinação do teor de umidade* . Rio de Janeiro.

Dixon-Hardy, D. W., & Engels, J. M. (2007). Methods for the disposal and storage of mine tailings. *Land Contamination and Reclamation, 15*(3), 301-317.

Door, J. V. (1969). *Physiographic, stratigraphic, and structural development of the Quadrilatero Ferrifero, Minas Gerais, Brazil.* US Government Printing Office. Washington: U.S. Government Printing Office.

Dornas, A. L. (2008). *Análise do comportamento geotécnico da barragem forquilha iii para a geometria atual e para alteamentos futuros pelo método de montante.* Dissertação (Mestrado em Engenharia Geotécnica) - Universidade Federal de Ouro Preto, Ouro Preto.

Endo, I., Delgado, C. E., Oliveira, M. M., Zapparoli, A. d., Carlos, D. U., Galbiatti, H. F., . . . Moura, L. G. (2019). *Estratigrafia e Arcabouço Estrutural do Quadrilátero Ferrífero: Nota Explicativa do Mapa Geológico do Quadrilátero Ferrífero, Minas Gerais, Brasil. Escala 1:150.000.* Departamento de Geologia da Escola de Minas – UFOP - Centro de Estudos Avançados do Quadrilátero Ferrífero, Ouro Preto.

Farina, F., Albert, C., Martínez Dopico, C., Aguilar Gil, C., Moreira, H., Hippertt, J. P., . . . Lana, C. (2016). The Archean–Paleoproterozoic evolution of the Quadrilátero Ferrífero (Brasil): Current models and open questions. *Journal of South American Earth Sciences, 68*, 4-21.

Ferreira, D. B. (2018). *Liquefação de rejeitos de minério de ferro – estudo de caso: sistema pontal em Itabira/MG.* Dissertação (Mestrado em Geotecnia) - Universidade Federal de Ouro Preto, Ouro Preto.

Ferreira, D. S. (2016). *Análise do comportamento geotécnico de aterro experimental executado sobre um depósito de rejeitos finos.* Dissertação (Mestrado em Geotecnia) - Universidade Federal de Ouro Preto, Ouro Preto.

Gomes, R. B., De Tomi, G., & Assis, P. S. (2016). Iron ore tailings dry stacking in Pau Branco mine, Brazil. *Journal of Materials Research and Technology, 5*(4), 339-344.

Head, K. H. (1992). *Manual of Soil Laboratory Testing - Volume 2: Permeability, shear strength and compressibility tests* (1st ed., Vol. II). Chichester: John Wiley & Sons Ltd.

Head, K. H. (1992). *Manual of Soil Laboratory Testing - Volume 3: Effective Stress Tests* (1st ed., Vol. II). Chichester: John Wiley & Sons Ltd.

Hitcher, P.-Y. (1996). Elastic Properties of Soils. *Journal of Geotechnical Engineering, 122*(8), 641–648.

Hore, C., & Luppnow, D. (2014). Karara Iron Ore TSF – design considerations for a unique large scale dry stack facility. *Proceedings of Tailings and Mine Waste*, 1-11.

Huang, X., Ranade, R., & Li, V. (2013). Feasibility Study of Developing Green ECC Using Iron Ore Tailings Powder as Cement Replacement. *Journal of Materials in Civil Engineering, 25*(7), 923-931.

INTERNATIONAL STANDARDS ORGANIZATION. (2015). *17892-3: Geotechnical investigation and testing - Laboratory testing of soil - Part 3: Determination of particle density.* Brussels.

INTERNATIONAL STANDARDS ORGANIZATION. (2016). *17892-4: Geotechnical investigation and testing - Laboratory testing of soil - Part 4: Determination of particle size distribution.* Brussels.

INTERNATIONAL STANDARDS ORGANIZATION. (2018). *17892-9: Geotechnical investigation and testing - Laboratory testing of soil - Part 9: Consolidated triaxial compression tests on water saturated soils.* Brussels.

Jefferies, M., & Been, K. (2015). *Soil Liquefaction: a critical state approach* (2nd ed.). CRC Press.

Jesus, C. A., & Joaquim, L. G. (2018). *Brazilian Mineral Summary.* National Mining Agency - ANM.

Knappett, J., & Craig, R. F. (2012). *Craig ' s Soil Mechanics.* CRC press.

Laboratório Nacional de Engenharia Civil. (1967). *E 197-1966: Solos - Ensaio de compactação.* Lisboa.

Li, W., Coop, M. R., Senetakis, K., & Schnaid, F. (2018). The mechanics of a silt-sized gold tailing. *Engineering Geology, 241*, 97-108.

Lima, R. M., & Abreu, F. D. (2020). Characterization and concentration by selective flocculation/magnetic separation of iron ore slimes from a dam of Quadrilátero Ferrífero – Brazil. *Journal of Materials Research and Technology, 9*(2), 2021-2027.

Lupo, J., & Hall, J. (2010). Dry stack tailings - Design considerations. *Tailings and Mine Waste'10 - Proceedings of the 14th International Conference on Tailings and Mine Waste*, 327-334.

Luz, A. B., & Lins, F. A. (2018). Introdução ao Tratamento de Minérios. Em A. B. Luz, S. C. França, P. F. Braga, & CETEM/MCTIC (Ed.), *Tratamento de Minérios* (6th ed., pp. 1-23). Rio de Janeiro.

Maranha das Neves, E. (2016). *Mecânica dos Estados Críticos: solos saturados e não saturados* (1st ed.). Lisboa: ITS Press.

Mayne, P., & Kulhawy, F. (June de 1982). K0-OCR relationships in soil. *Journal of the Geotechnical Engineering Division, 108*(6), 851-872.

Miranda, T. M. (2018). *Análise do potencial de liquefação de um rejeito de minério de ferro por meio de ensaios de laboratório e de campo.* Dissertação (Mestrado em Geotecnia) - Universidade Federal de Ouro Preto, Ouro Preto.

Mohallem, S. D. (2018). *Análise de sistema de co-disposição dos rejeitos de minério de ferro gerados na mina serra azul – Itatiaiuçu/MG.* Dissertação (Mestrado Profissional em Engenharia Geotécnica) – Universidade Federal de Ouro Preto, Ouro Preto.

Morgenstern, N. R., Vick, S. G., Viotti, C. B., & Watts, B. D. (2016). *Report on the Immediate Causes of the Failure of the Fundão Dam.* Fundão Tailings Dam Review Panel .

Pereira, E. L. (2005). *Estudo do potencial de liquefação de rejeitos de minério de ferro sob carregamento estático.* Dissertação (Mestrado em Engenharia Civil) – Escola de Minas, Universidade Federal de Ouro Preto, Ouro Preto.

Pires, K. d., Mendes, J. J., Figueiredo, V. C., Silva, F. L., Krüger, F. L., Vieira, C. B., & Araújo, F. G. (2019). Mineralogical Characterization of Iron Ore Tailings from the Quadrilatero Ferrifero, Brazil, by Eletronic Quantitative Mineralogy. *Materials Research, 22*(1).

Plewes, H. D., Davies, M. P., & Jefferies, M. G. (1992). CPT based screening procedure for evaluating liquefaction susceptibility. *Proceedings of the 45th Canadian Geotechnical Conference*, 41-49.

Presotti, E. D. (2002). *Influência do teor de ferro nos parâmetros de resistência de um rejeito de minério de ferro.* Dissertação (Mestrado em Geotecnia) - Universidade Federal de Ouro Preto, Ouro Preto.

Reynolds, O. (December de 1885). On the dilatancy of media composed of rigid particles in contact, with experimental illustrations. *Philosophical Magazine and Journal of Science, 20*, 469-481.

Rezende, V. A. (2013). *Estudo do comportamento de barragem de rejeito arenoso alteada por montante.* Dissertação (Mestrado em Engenharia Geotécnica) – Escola de Minas, Universidade Federal de Ouro Preto, Ouro Preto.

Robertson, P. (2010). Estimating in-situ state parameter and friction angle in sandy soils from the CPT. *2nd International Symposium on Cone Penetration Testing, CPT'10*, 2-43.

Robertson, P. K. (2009). Interpretation of cone penetration tests – a unified approach. *Canadian Geotechnical Journal, 46*(11), 1337–1355.

Robertson, P. K., de Melo, L., Williams, D. J., & Wilson, G. W. (2019). *Report of the Expert Panel on the Technical Causes of the Feijão Dam I.* VALE S.A.

Robertson, P. K., Viana da Fonseca, A. V., Ulrich, B., & Coffin, J. (2017). Characterization of unsaturated mine waste: a case history. *Canadian Geotechnical Journal, 54*(12), 1752-1761.

Roscoe, K. H., Schofield, A. N., & Wroth, C. P. (1958). On The Yielding of Soils. *Géotechnique, 8(1)*, 22-53.

Rowe, P. W. (1962). The stress dilatancy relation for static equilibrium of an assembly of particles in contact. *Proceedings of the Royal Society of London A, 269*, 500-527.

Sadrekarimi, A. (2014). Effect of the Mode of Shear on Static Liquefaction Analysis. *Journal of Geotechnical and Geoenvironmental Engineering, 140*(12).

Santos, A. G. (2004). *Influência do teor de ferro na condutividade hidráulica saturada de um rejeito de minério de ferro.* Dissertação (Mestrado em Engenharia Civil) – Universidade Federal de Ouro Preto, Ouro Preto.

Schofield, A., & Wroth, C. (1968). *Critical State Soil Mechanics.* London: McGraw-hill.

SHUTTLE, D., & JEFFERIES, M. (2010). Norsand: description, calibration, validation and applications. *Geo-frontiers congress 2005–Soil constitutive models: evaluation, selection, and calibration.* , 204-236.

Silva, J. P. (2014). *Avaliação da influência do regime de fluxo no comportamento geotécnico de uma barragem de rejeito alteada pelo método de montante.* Dissertação (Mestrado em Engenharia Civil) - Escola Politécnica da Universidade de São Paulo, São Paulo.

Silva, J. P., Mendes, M. B., Milonas, J. G., Pirete, W., & Souza, W. J. (2013). Geotechnical parameters of iron ore tailings from the Quadrilátero Ferrífero after different treatments and ore processing. *Proceedings of the 16th International Seminar on Paste and Thickened Tailings* (pp. 261-271). Perth: Australian Centre for Geomechanics.

Silva, W. P. (2010). *Estudo do potencial de liquefação estática de uma barragem de rejeito alteada para montante aplicando a metodologia de Olson (2001).* Dissertação (Mestrado em Engenharia Geotécnica) – Universidade Federal de Ouro Preto, Ouro Preto.

Taylor, D. W. (1948). *Fundamentals of Soil Mechanics.* New York: John Wiley & Sons.

Teixeira, W. G., & Bhering, S. B. (2017). Retenção de água no solo pelos métodos da mesa de tensão e da câmara de Richards. Em P. C. Teixeira, G. K. Donagemma, A. Fontana, & W. G. Teixeira (Eds.), *Manual de métodos de análise de solo* (3 ed., pp. 34-46). Brasília: Embrapa.

Terzaghi, K., Peck, R. B., & Mesri, G. (1996). *Soil Mechanics in Engineering Practice* (3rd ed.). New York: John Wiley & Sons.

Tolentino, M. V. (2010). *Estudo da viabilidade técnica do aproveitamento do resíduo arenoso da mineração do itabirito.* Dissertação (Mestrado em Ciência e Tecnologia dos Materiais), Centro de Desenvolvimento da Tecnologia Nuclear - CDTN, Belo Horizonte.

Torres-Cruz, L. A., & Santamarina, J. C. (2019). The Critical State Line of Non-Plastic Tailings. *Canadian Geotechnical Journal, 57*, 1508-1517.

Trindade, T. P., Carvalho, C. A., Lima, D. C., Barbosa, P. S., & Silva, C. H. (2008). *Compactação de solos: fundamentos teóricos e práticos* (1 ed.). (UFV, Ed.) Viçosa.

VALE S.A. (2020). *Dry Iron Ore Processing*. Acesso em 1 de 12 de 2020, disponível em Repair and development: http://www.vale.com/brasil/EN/aboutvale/reports/atualizacoes_brumadinho/Pages/dry-processing.aspx

Vick, S. G. (1990). *Planing, Design, and Analysis of Tailings Dams* (2nd ed.). Vancouver: BiTech.

Wroth, C. P. (1984). The interpretation of in situ soil tests. *Géotechnique*(34(4)), 449–489.

APPENDIX A – Description of triaxial compression test procedures at LabGeo – FEUP

A.1 Triaxial Apparatus

According to Soares (2014), the high pressure triaxial cell used at LabGeo was built at the Imperial College of London (ICL). The triaxial apparatus works exactly as the conventional ones. However, the triaxial chamber and the pipelines are made of stainless steel and copper to resist the high pressures applied during the tests (see Figure A.1). The chamber and the pressure transducers reach a limiting pressure of 10 MPa and the internal and external load cells of the equipment reach a maximum load of 100 kN.

Figure A.1 – a) Oil hydraulic press with a high-pressure triaxial cell; b) Detail of a soil specimen while being placed inside the high-pressure triaxial cell

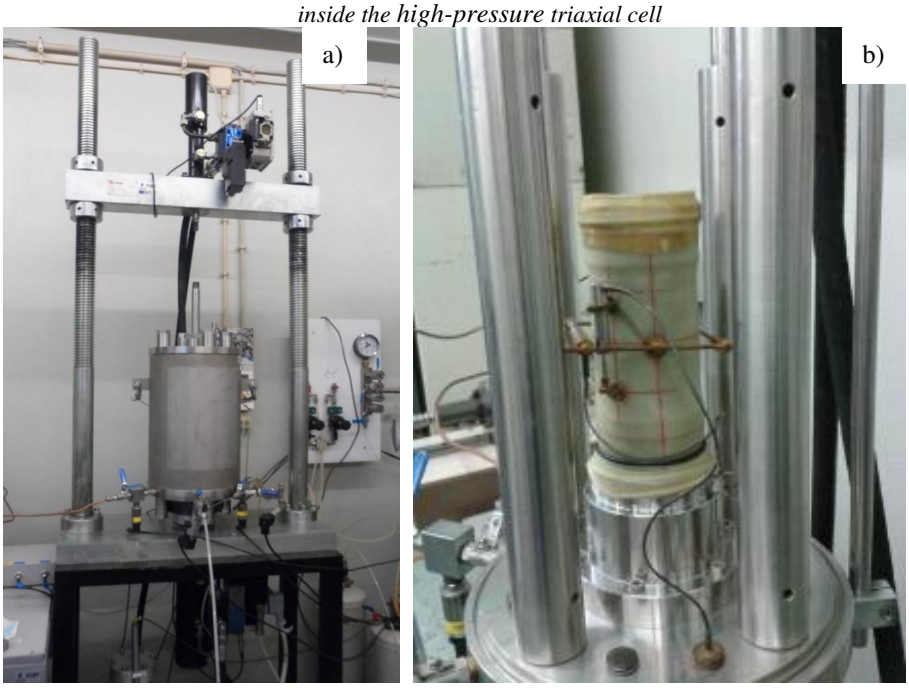

Source: Soares, 2014.

The oil hydraulic press used to perform high-pressure tests was developed by the Institute of Mechanical Engineering and Industrial Management of the University of Porto (INEGI), under specifications of the LabGeo (SOARES, 2014).

The oil hydraulic press is constituted of motor and hydraulic pump with limit pressure of 250 bar, which allows to perform static tests with maximum load of 50 kN and cyclic tests with maximum load of 10 kN. The hydraulic unit and servo actuator are composed of a hydraulic cylinder with both displacement and load transducers that allows the application of cyclic loads with frequencies between 0,001 Hz and 2,00 Hz. Moreover, it is constituted of an electrical panel with the protection of the motor and an emergency button (SOARES, 2014).

The whole system is coupled with a computer with the software DynaTester V2.0®. The software controls the tests and the data acquisition for both static and cyclic tests and admits several test stages.

A.2 Instrumentation

At LabGeo the triaxial tests used to be performed with both external and internal instrumentation. The internal instrumentation was used to measure the axial and radial strains, so volumetric strain and void ratio variation, important to define the critical state, could be determined during and after the saturation stage.

According to Soares (2014), as internal instrumentation, it was used linear displacement transducers (LDT), which are basically strain gauges attached to a metal strip (see Figure A.2.a and Figure A.2.b); hall effects, electromagnetic devices as the ones presented in Figure A.1.c; or miniature linear variable differential transformers (mini LVDT), which are waterproof and high pressure resistant contactless linear position sensors that work just as the LVDTs used as external instrumentation.

Figure A.2 – a) LDT; b) LDT attached to the specimen; c) Hall effects coupled to the specimen.

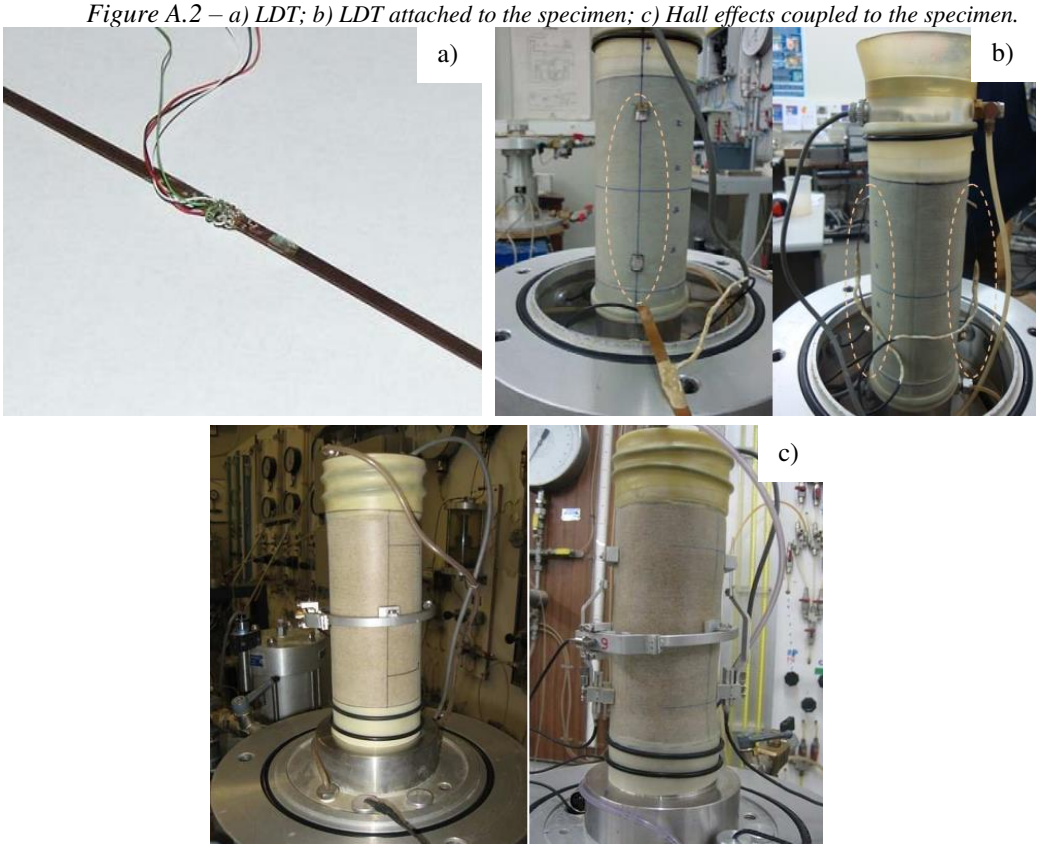

Source: adapted from Costa (2009), Bedin (2010) and Rocha (2010).

However, the internal instrumentation did not present the desirable accuracy. Its accuracy was limited to samples with low volumetric strain during saturation that did not show structural collapse, the opposite behavior of what is expected for loose samples, usually used to determine the critical state locus.

Therefore, nowadays, to determine void ration variation during saturation, the internal instrumentation is no more used and has been substituted by the end-of-test soil freezing technique, detailed in subsection A.7.

The external instrumentation constituted of linear variable differential transformers (LVDT) and automatic volume change gauges are, on the other hand, accurate and irreplaceable equipment essential to determine the void ratio of saturated samples.

The LVDT are used to measure external displacements. They must be vertically positioned coupled to the piston, so the relative displacement is registered, as the piston movements during the test. Figure A.3 shows a LVDT used at LabGeo, which has a maximum displacement range of 50 mm, enough for loose specimens to achieve the critical state (COSTA, 2009).

Figure A.3 – LVDT (LabGeo-FEUP).

Source: Soares, 2014.

The automatic volume change gauge must be used with fully saturated specimens. According to Costa (2009), they consist of a hydraulic cylinder whose piston is connected to a LVDT that registers the piston's displacements with the water volume variation (see Figure A.4).

Figure A.4 – Automatic volume change gauge. a) Schematic representation; b) Illustration of a VJ Tech® model.

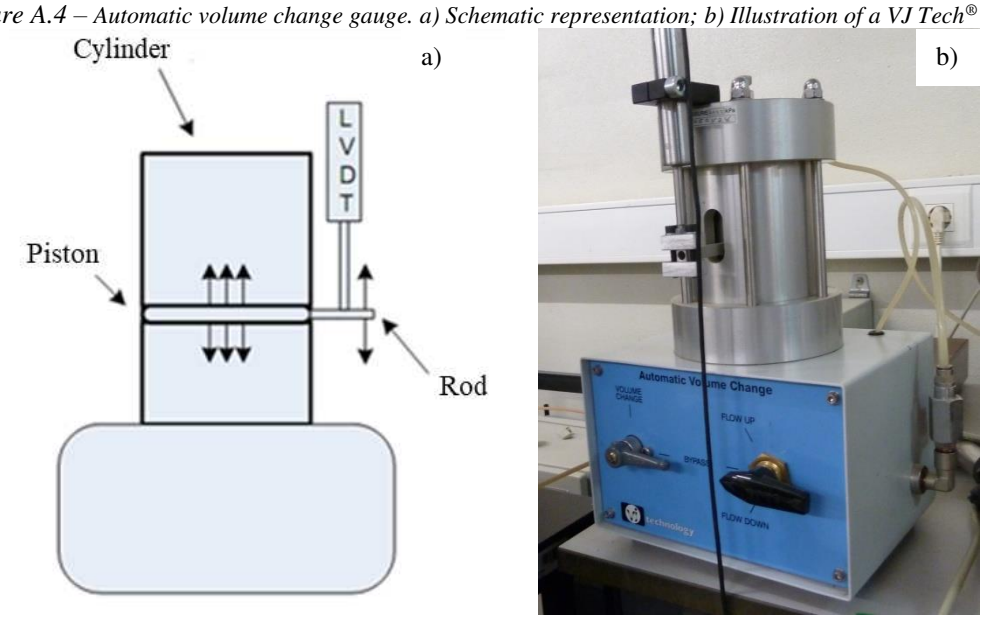

Source: Soares, 2014 (adapted from Costa, 2009)

A.3 Platens

At the LabGeo, it is used lubricated end platens in the triaxial tests. The lubricated end platens consist of a "sandwich" of two discs of standard triaxial latex membrane filled with a thin layer of silicone grease (JEFFERIES AND BEEN, 2015), as it is illustrated in Figure A.5. According to Rowe and Barden (1964), the lubricated end platens are important to minimize the influence of the platen restraint on stresses and allow uniform strains in the ends of the specimen.

Figure A.5 – a) Schematic representation of a lubricated end platen; b) Lubricated end platen (LabGeo-FEUP).

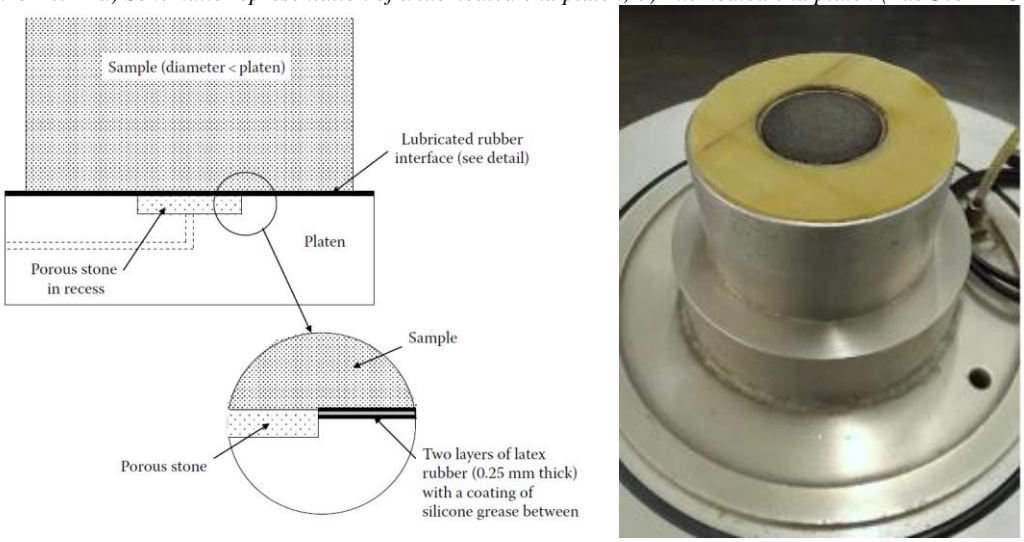

Source: Jefferies and Been (2015), LabGeo (2019).

To use lubricated end platens, smaller porous stones must be used in the ends of the specimen. According to Jefferies and Been (2015), for a specimen of 71 mm of diameters a porous stone of 30 mm of diameter is adequate.

Reducing the size of the porous stones do not affect the drainage of coarse soils, since they are considerably permeable, but it may interfere in the drainage of low permeable soils. Moreover, as the flow boundary is changed, the properties associated with the consolidation stage, such as the consolidation coefficient, cannot be measured.

To have uniform radial strains in the ends of the specimens, since the dilative specimens tend to expand, larger platens are used, at least 5 mm larger than the specimen's diameter, as it is also illustrated in Figure A.5.

Furthermore, the top platen-loading ram connection is done as illustrated in Figure A.6, and the piston end loosely fits into the top cap cylindrical guide hole in a perfect alienation. This type of connection allows the rotation of the top cap during the shearing stage reducing tilting of the top of the specimen and contributing for more uniform stress distribution and radial strains.

Figure A.6 – a) Detail of the top cap cylindrical guide hole; b) Top platen-loading ram connection.

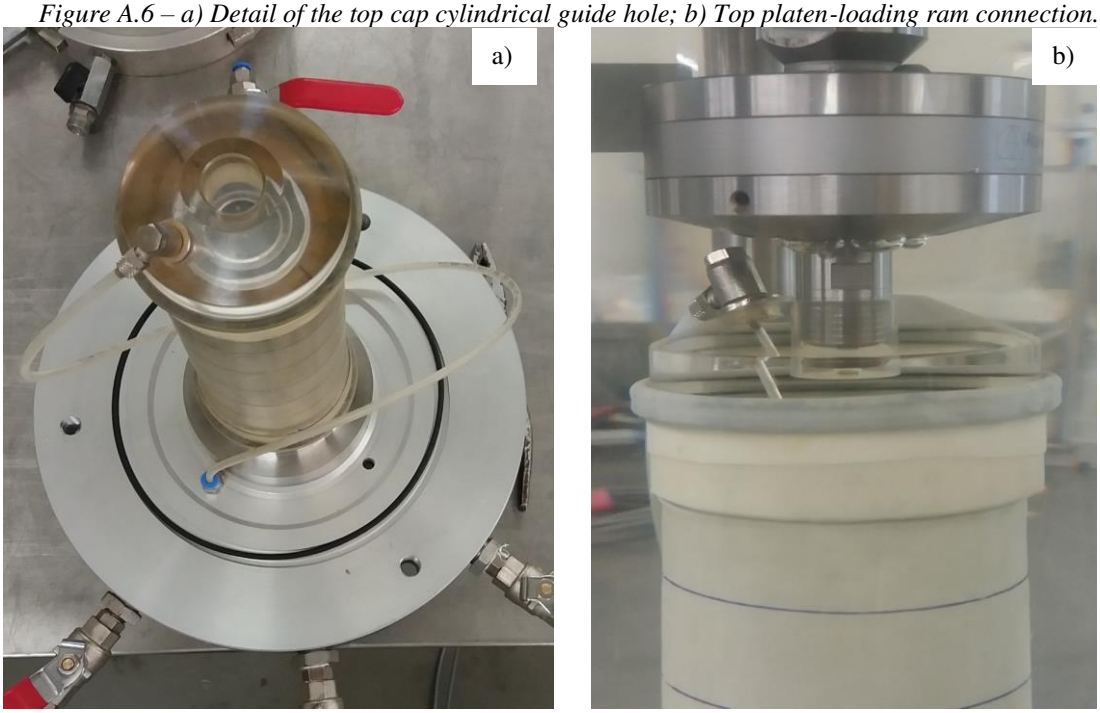

Source: Besenzon, 2019.

The larger lubricated end platens and loose top platen-load ram connection permit to take the tests to higher axial strains (up to 35%) than the one achieved in the conventional triaxial apparatus (between 15% and 20%) without stress-strain concentration at the specimen ends.

A.4 Sample Preparation

To determine the critical state line (CSL), at LabGeo, the samples are prepared using mainly the moist tamping method, which permits to make homogeneous specimens with high void ratios. The moist tamping method is low time-consuming, does not segregate the soil particles, and allows the operator to control the final density much more readily than other methods, such as wet and dry pluviation (Chang et al., 2011)

When dealing with loose specimens, first, it is determined the water content necessary to generate suction between the particles of the soil and keep the specimen's shape after the split mold removal.

After that, the mass of dry sample is mixed with the necessary amount of water to obtain the defined water content. The mixture is let to cure for at least 16h to allow the fines in the sample to become properly wet (JEFFERIES AND BEEN, 2015).

Based on the dimensions of the specimen and predefined void ratio, the weight of moist sample (W_{mt}) necessary to make the specimen is defined. The specimen is then compacted in five or six layers of equal thickness. However, to avoid over compaction of the bottom layers due to the compaction of the succeeding layers, the weight of soil necessary for each layer (W_i) is defined, in a way that the bottom layers are initially under-compacted, and the proper degree of compaction is achieved at the end of the specimen's compaction. The weight of each layer is calculated by Equation A.1, defined by Jefferies and Been (2015).

$$W_i = \frac{W_{mt}}{n}\left[1 + \frac{U_n}{100} \cdot \left(\frac{2n_i - n + 1}{n - 1}\right)\right] \qquad \text{Equation A.1}$$

Where, U_n is the percent under-compaction, equal to 100% for the first layer and linearly vary from the bottom to the top, and i = 1…n and with bottom layer i = 1.

After the layer weights are determined, the specimens are prepared according to the procedures described by Viana da Fonseca et al. (2011) and Soares and Viana da Fonseca (2016) (see Figure A.7), as it follows:

Figure A.7 – Triaxial specimens preparation.

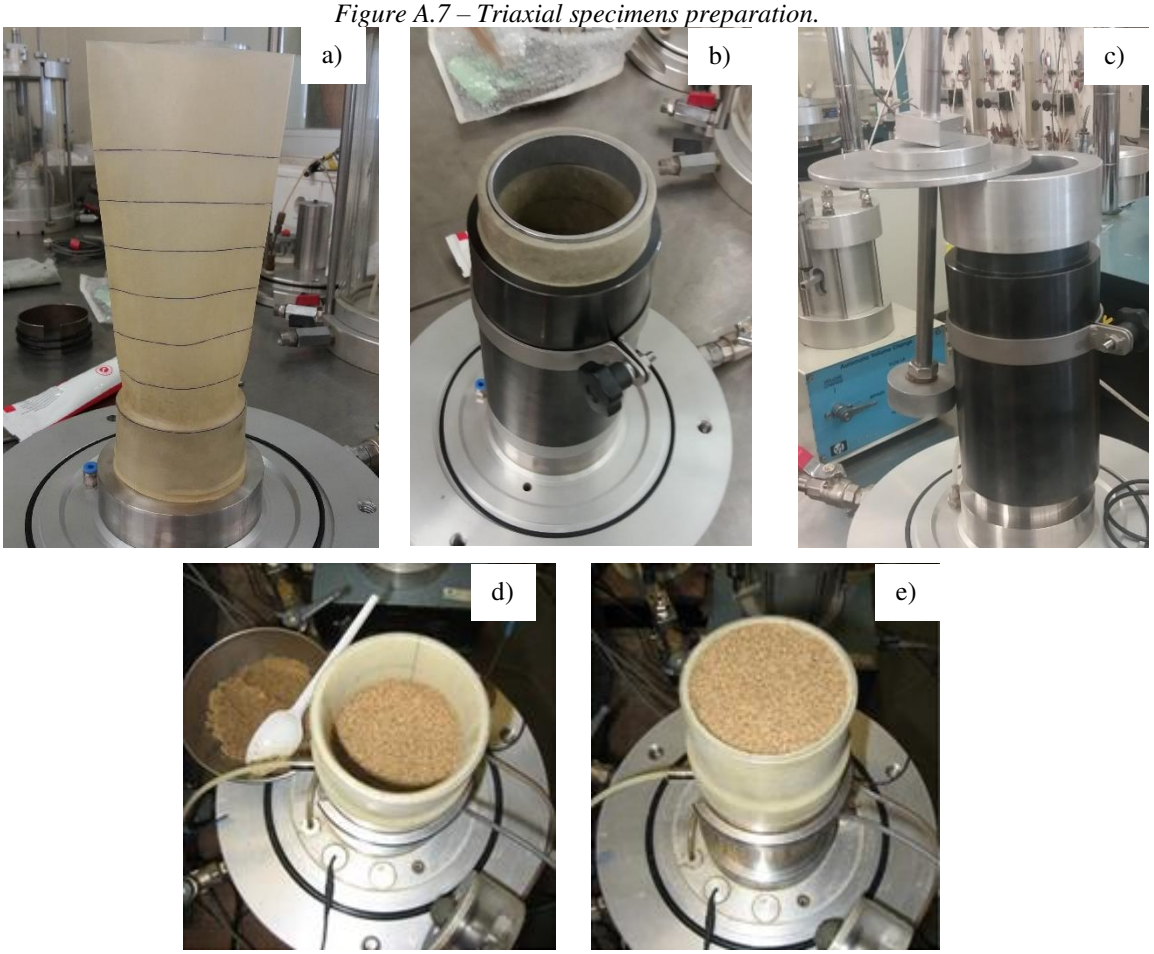

a) Latex membrane with guiding lines attached to the base; b) Bipartite mold placed on the base; c) Tamper with adjustable stop; d) Intermediate layer being prepared; e) Specimen after final layer has been prepared. Source: adapted from Viana da Fonseca et al (2011) and Besenzon (2019).

i) Guiding lines are drawn in the latex membrane indicating the thickness of the layers.

ii) A paper filter is placed in the base of the cell to avoid fines passing through the porous stone.

iii) The membrane is attached to the base of the chamber using two O-rings.

iv) A cylindrical metallic bipartite mold is placed on the base and the membrane is subsequently adjusted. A 50 kPa of vacuum pressure is applied between the mold and the membrane for a perfect stretch.

v) The soil is placed and compacted using a tamper with an adjustable stop, which assures uniform samples. Before tamping, the tamper is adjusted, so its foot stops on the top of the layer.

vi) Once the specimen is finished, the top cap is placed, and the membrane is wrapped on it using two O-rings.

vii) A small vacuum (negative pressure between 10 kPa to 15 kPa) is applied to the top for safe removal of the mold without soil collapse. The final dimensions of the specimen are then measured helped by a caliper.

viii) Finally, the Perspex (or stainless steel for high-pressure tests) chamber is mounted on the base and then properly closed and filled with water; the internal pressure is replaced by the surrounding water confining pressure, (positive 10 to 15 kPa).

For this research, however, the moist tamping method was not used to prepare the specimens since the material was compacted in much denser states. Based on the results of the proctor compaction test (see section 4.2), to each degree of compaction, the specimens were prepared in six layers using a press, just as it was described in 3.4.1.

A.5 Saturation

A.5.1 Carbon Dioxide Treatment

As the carbon dioxide (CO_2) is more soluble in water than air, the carbon dioxide treatment is used to reduce the time and back pressure required to saturate the specimen.

The methodology adopted at LabGeo is the same as the one described by Jefferies and Been (2015). It consists in injecting CO_2 in the sample from the bottom platen pipeline to the top platen pipeline, which is left with the end open under water to verify the bubble rate – a bubble rate of one to five bubbles per second is recommended to avoid collapse of the sample due to increase in pore pressure by not properly venting the CO_2, or creation of preferential pathways due to a large flux of CO_2.

Since the CO_2 is heavier than the air, by bubbling CO_2 from the bottom to the top, the air is easily exuded from the specimen, and the carbon dioxide treatment approximately takes one to two hours to be completed.

A.5.2 De-Aired and Deionized Water Percolation

At the LabGeo, in the water percolation stage, it is used de-aired and deionized water to saturate the specimen. Deionized water is used to avoid any chemical reaction between the seeping fluid and the tailings, and the amount of water used in the process is approximately twice the specimen's void volume.

The deionized water is seeped from the bottom to the top of the specimen. The flow inside the specimen is generated by a constant hydraulic gradient created applying a water pressure of 10 kPa at the bottom of the specimen. The triaxial chamber's pressure is set with 20 kPa to avoid sample collapse during percolation (see Figure A.8).

Figure A.8 – Specimen's saturation by water percolation.

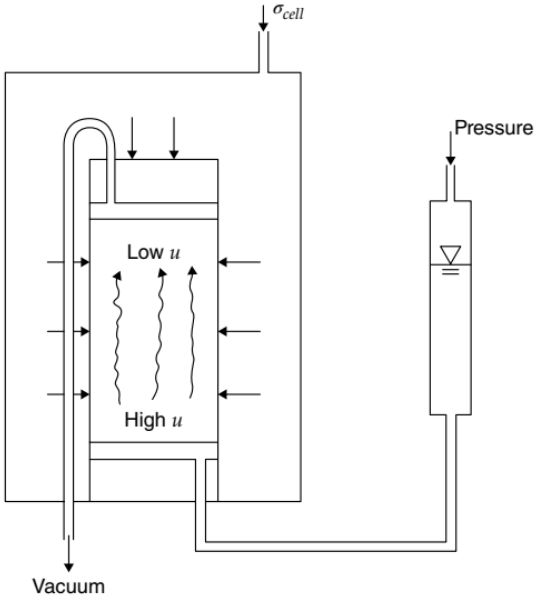

Source: Lade, 2016.

According to Besenzon (2019), after the predicted water volume is percolated through the specimen, a good practice is to check the drainage pipelines for air bubbles. The process of percolation generally takes ten to twelve hours in tailings specimens.

A.5.3 Back pressure

To apply back pressure consists in gradually increasing the pore pressure enough to the water dissolve the air remaining in the specimen's voids, pipelines, and connections. Meanwhile the back pressure is raised, the chamber's pressure (confining pressure) is also increased keeping an effective stress of 10 kPa to maintain the integrity of the specimen.

For the studied tailings, the saturation process was completed with a maximum back pressure of 300 kPa and respective chamber's pressure of 310 kPa, when Skempton's porewater pressure coefficient B was 0,98.

Even though Head (1992) and the international legislation, ISO 17892-9:2018, ASTM D4767:2011, and ASTM D7181:2020, define B = 0,95 as reference of saturation for triaxial tests, for soft soils B = 0,95 is equivalent to approximately 97% of saturation, which means that the sample would not be fully saturated (BESENZON, 2019). Therefore, at LabGeo to guarantee the fully saturation of the specimens a minimum B parameter of 0,98 is adopted.

Moreover, when working with bender elements, additionally to the Skempton's coefficient B, the compression P wave velocity is also measured to assure the specimen's saturation. The P wave velocity is strongly affected by the water completely filling or not the internal voids of the soil. As stated by Ferreira (2008), while the soil is being saturated, the P wave velocity maintains approximately constant and it only increases, reaching values close to the velocity of the sound in the water (around 1500 m/s), when the internal voids of the material are filled with water – completely saturated.

A.6 Isotropic consolidation and Shearing

At LabGeo, the isotropic consolidation and shearing stages of consolidated triaxial compression tests follow the procedures of the ISO 17892-9:2018.

After the saturation stage is completed, the drainage vales are closed, and the chamber's pressure (confining pressure) is raised until the difference between the back pressure and the chamber's pressure is equal to the desirable effective consolidation pressure. Then, the appropriate drainage valves are open and the consolidation to the test stress conditions is done.

Finally, monotonic, or cyclic axial stress is applied under stain-control or stress-control. For this research, monotonic tests were performed with constant strain rate, increasing the axial strain up to 35% until the critical state was reached.

It is noteworthy to mention that the monotonic shear strain rate depends on if the shearing stage occurs under drained or undrained conditions. While under undrained conditions the shear rate depends only on the data acquisition frequency of the software, under drained conditions the shear rate must be compatible to the excess pore pressure dissipation rate. Therefore, the

maximum rate (v_{max}) is dependent of the permeability of the soil and may be calculated by Equation A.2, defined in the ISO 17892-9:2018.

$$v_{max} = \frac{H_c \cdot \varepsilon_a}{15 \cdot t_{100}} \qquad \text{Equation A.2}$$

Where, H_c is the height of the specimen at the end of consolidation, ε_a is the axial strain that will be achieved at the end of the test, and t_{100} is the time of complete consolidation.

Even though it may usually be performed with higher shear strain rates, at LabGeo, the drained tests are performed with a rate of 0.01 mm/min and the undrained tests with a rate of 0.05 mm/min.

A.7 End-of-Test Soil Freezing

The post-shearing and post-consolidation void ratios can be determined in accordance with the method B of section *11.2 Specimen Properties After Consolidation* of the ASTM D7181:2020, which explains the determination of the specimen characteristics after post-consolidation using the final water content.

A limitation of the method explained in the ASTM D7181:2020 is when dealing with soils with high permeability that can absorb water from (or exude water to) the porous stones and drainage lines during the specimen removal from the triaxial chamber. Therefore, to minimize it, Sladen and Handford (1987) proposed the end-of-test soil freezing technique, which resulted to be a very accurate method to preserve the specimen condition at the end of the test, and it is adopted at LabGeo.

With the soil freezing, the volume of water inside the specimen is kept constant. Thus, as the specimen is saturated, it is possible to determine the post-shearing void ratio by Equation A.3.

$$G \cdot w_f = S \cdot e_f \qquad \text{Equation A.3}$$

As the volume changes are precisely measured during consolidation and shearing, the post-consolidation void ratio is determined by Equation A.4, and the post-saturation void ratio is determined by Equation A.5.

$$e_0 = e_f + \frac{\Delta V}{V_s} \qquad \text{Equation A.4}$$

$$e_{sat.} = e_0 + \frac{\Delta V}{V_s} \qquad \text{Equation A.5}$$

Where, e_0 is the void ratio after the consolidation (beginning of shearing stage) and $e_{sat.}$ is the void ratio after the specimen saturation.

The Figure A.9 presents the sample Trx_95%_CID_800kPa frozen after testing, as an example of the end-of-test soil freezing technique.

Figure A.9 – Frozen sample after triaxial compression test.

Source: LabGeo, 2020.

According to Besenzon (2019), although the end-of-test soil freezing technique gives precise measurements of the void ratio at the end of each stage of the triaxial test, it is reasonable to compare the results with other measurements. Therefore, additional verification is done at LabGeo by measuring the approximate sample axial shortening during saturation.

The axial shortening is verified by measuring the relative displacement between the top cap and the piston end (see Figure A.6). As presented in A.3, the piston end loosely fits into the top cap cylindrical guide hole in a perfect alienation (see Figure A.6). Thus, 1 mm marks are drawn on the piston end and are used as a reference to measure relative displacements of the sample

during saturation. The magnitude of the axial shortening is then compared with the magnitude of the volume variation determined after the end-of-test soil freezing.

A.8 Bibliography

AMERICAN SOCIETY FOR TESTING AND MATERIALS. (2011). *D4767: Standard test method for consolidated undrained triaxial compression test for cohesive soils.* West Conshohocken.

AMERICAN SOCIETY FOR TESTING AND MATERIALS. (2020). *D7181: Standard test method for consolidated drained triaxial compression test for soils.* West Conshohocken.

Bedin, J. (2010). *Estudo do comportamento geomecânico de resíduos de mineração.* Tese (Doutorado em Engenharia Civil) - Universidade Federal do Rio Grande do Sul, Porto Alegre.

Besenzon, D. (2019). Conventional triaxial testing for determination of mechanical behavior of gold tailings. *Report of the course on Experimentation in Geotechnics*, Doctoral Program in Civil Engineering, Faculdade de Engenharia da Universidade do Porto, Porto, Portugal.

Chang, N., Heymann, G. & Clayton, C. R. I. (2011). The effect of fabric on the behaviour of gold tailings. *Géotechnique*, 61(3),187–197.

Costa, C. (2009) *Development of a monitoring system for control of triaxial tests of soils.* Dissertação (Mestrado em Automação, Instrumentação e Controle) - Universidade do Porto, Porto.

Ferreira, C. (2008). *The use of seismic wave velocities in the measurement of stiffness of a residual soil*. Tese (Doutorado em Engenharia Civil) - Universidade do Porto, Porto, Portugal.

Head, K. H. (1992). *Manual of Soil Laboratory Testing - Volume 2: Permeability, shear strength and compressibility tests* (1st ed., Vol. II). Chichester: John Wiley & Sons Ltd.

INTERNATIONAL STANDARDS ORGANIZATION. (2018). *17892-9: Geotechnical investigation and testing - Laboratory testing of soil - Part 9: Consolidated triaxial compression tests on water saturated soils.* Brussels.

Jefferies, M., & Been, K. (2015). *Soil Liquefaction: a critical state approach* (2nd ed.). CRC Press.

LABORATÓRIO DE GEOTECNIA DA FACULDADE DE ENGENHARIA DA UNIVERSIDADE DO PORTO (2019). *Relatório de ensaios.* Porto, Portugal: LabGeo, 2019.

LABORATÓRIO DE GEOTECNIA DA FACULDADE DE ENGENHARIA DA UNIVERSIDADE DO PORTO (2020). *Relatório de ensaios: ensaios de compressão triaxial com medição de permeabilidade.* Porto, Portugal: LabGeo, 2020.

Lade, P. V. (2016). *Triaxial testing of soils*. John Wiley & Sons.

Rocha, J.M.M.da (2010). *Definição das condições de liquefacão em triaxial à luz da teoria dos estados críticos e avaliação de risco por razão de velocidades de ondas sísmicas numa areia dunar.* Dissertação (Mestrado Integrado em Engenharia Civil) - Universidade do Porto, Porto, Portugal.

Rowe, P. W., & Barden, L. (1964). Importance of free ends in triaxial testing. *Journal of the Soil Mechanics and Foundations Division*, 90(1), 1-27.

Sladen, J. A. & Handford, G., (1987). A potential systematic error in laboratory testing of very loose. *Canadian Geotechnical Journal*, 24(3), 462–466.

Soares, M. (2014). *Evaluation of Soils Liquefaction Potential Based on Laboratory Data - Major Factors and Limit Boundaries*. Tese (Doutorado em Engenharia Civil) - Universidade do Porto, Porto, Portugal.

Soares, M. & Viana da Fonseca, A. (2016). Factors Affecting Steady State Locus in Triaxial Tests. *Geotechnical Testing Journal*, 39(6), 1056-1078.

Viana da Fonseca, A., Coop, M.R., Fahey, M. & Consoli, N. (2011). The interpretation of conventional and non-conventional laboratory tests for challenging geotechnical problems. *Keynote Lecture IS'Seoul, in 'Deformation Characteristics of Geomaterials*, 1, 84-119.

APPENDIX B – Oedometer Test Results

B.1 Loose State

Figure B.1 – Oedometer test results, loose state. Oed_Loose_2500_sat tested at UFV; Oed_Loose_3200_sat and Oed_Loose_6400_sat tested at FEUP.

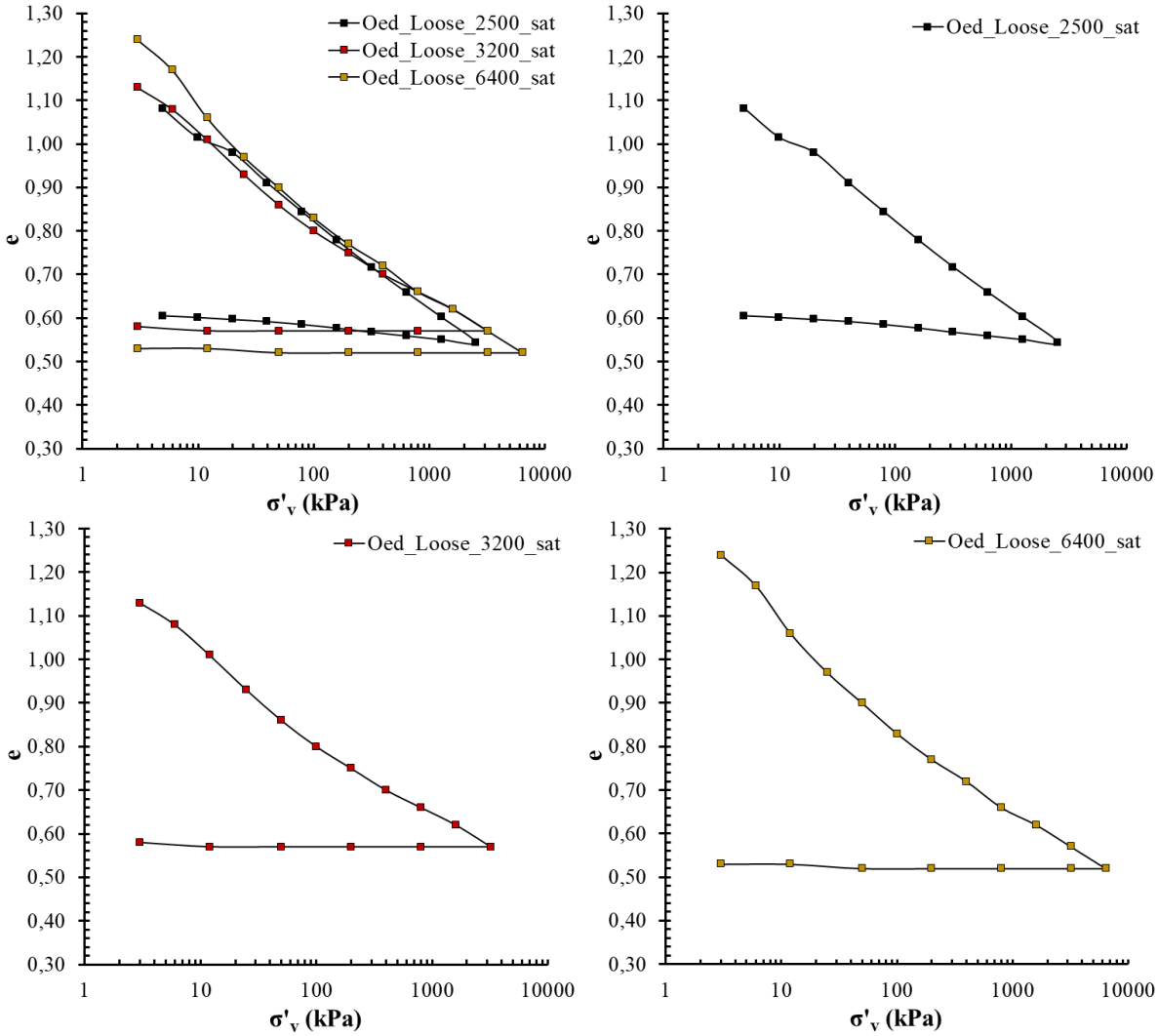

Source: elaborated by the author.

B.2 DC = 93%

Figure B.2 – Oedometer test results, DC =93%. Both samples tested at UFV.

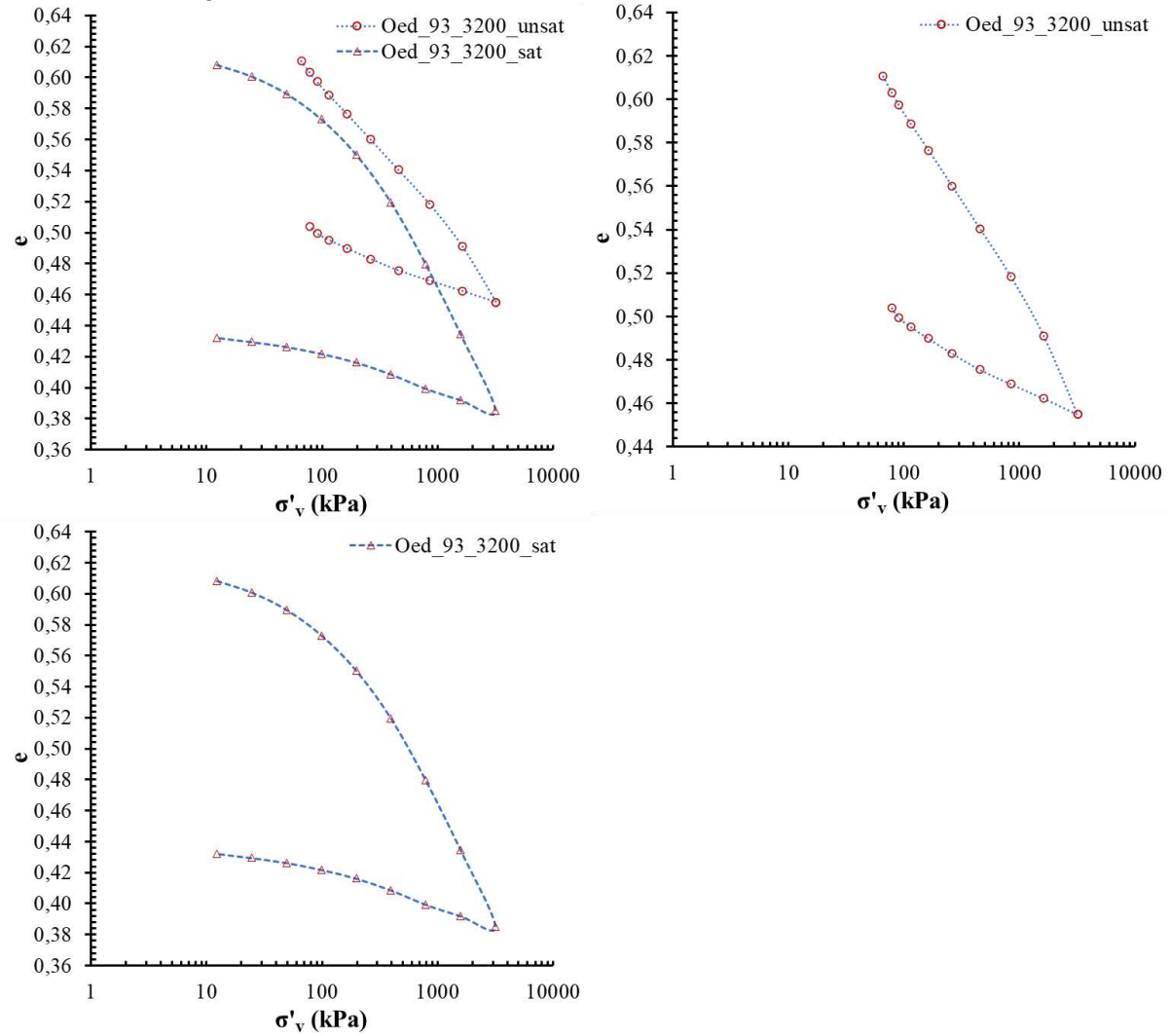

Source: elaborated by the author.

B.3 DC = 95%

Figure B.3 – Oedometer test results, DC =95%. Oed_95_3200_unsat and Oed_95_3200_sat tested at UFV; Oed_95_6400_sat tested at FEUP.

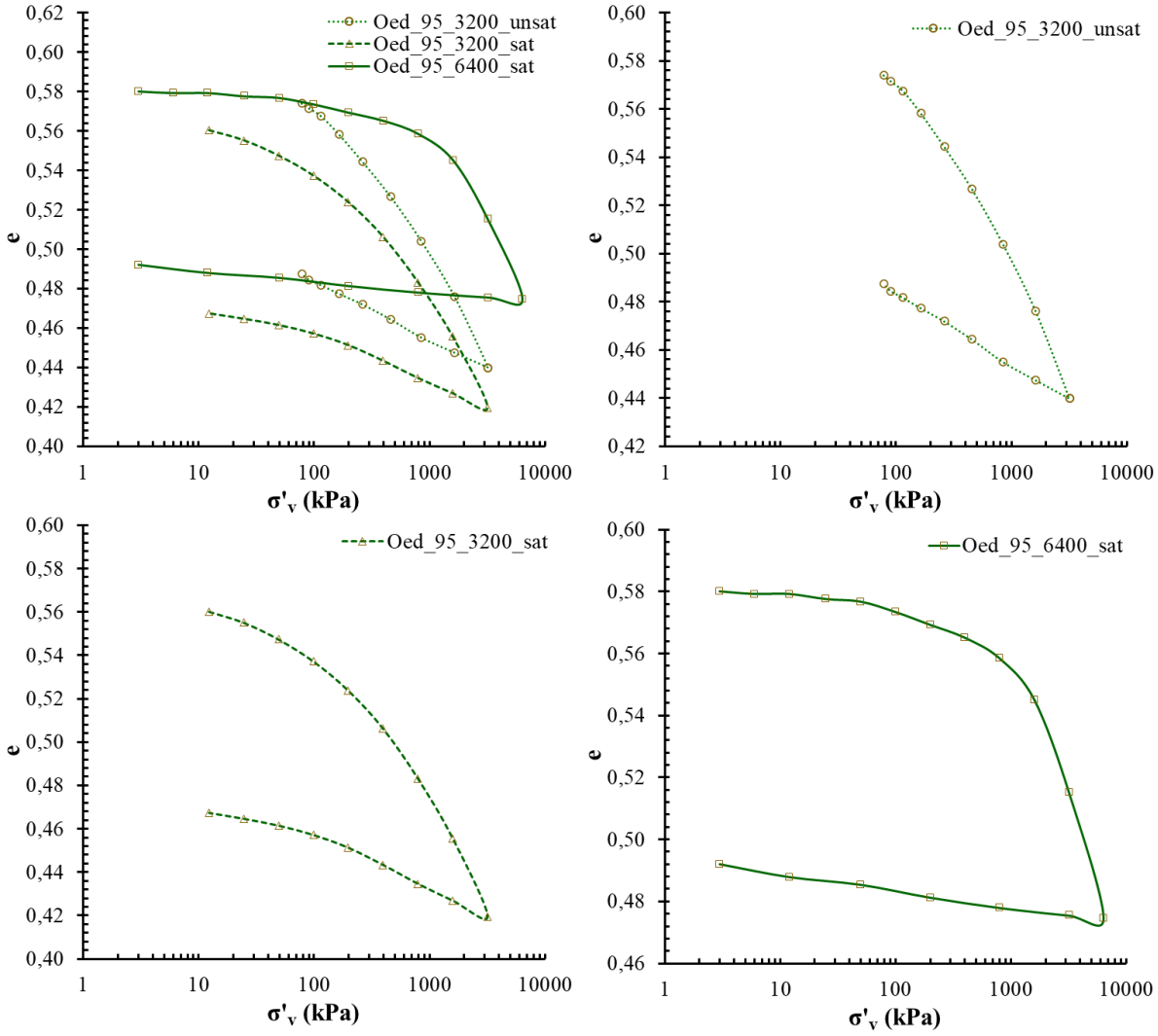

Source: elaborated by the author.

B.4 DC = 97%

Figure B.4 – Oedometer test results, DC =97%. Both samples tested at UFV.

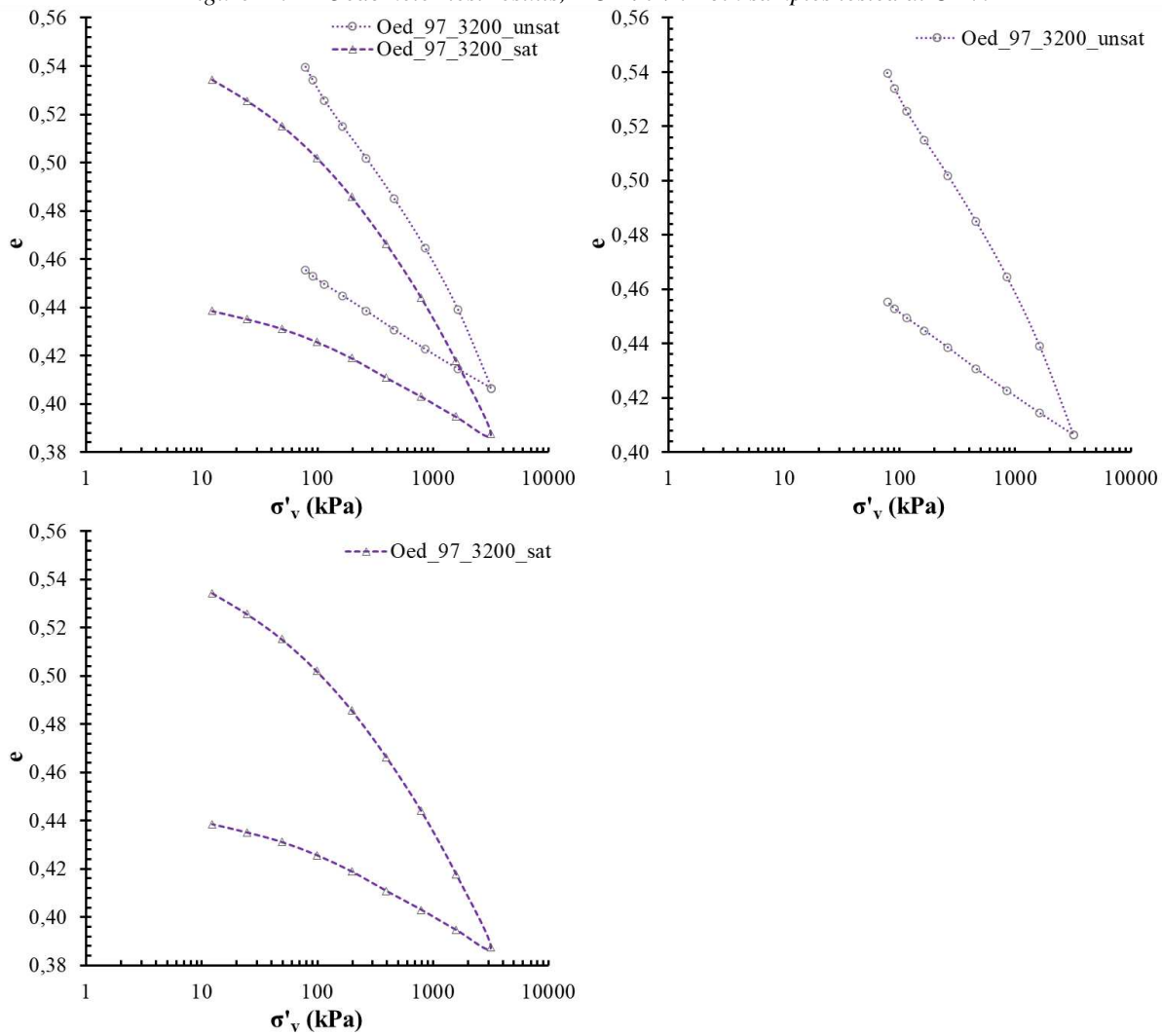

Source: elaborated by the author.

B.5 DC = 100%

Figure B.5 – Oedometer test results, DC =100%. Oed_100_3200_unsat and Oed_100_3200_sat tested at UFV; Oed_100_6400_sat tested at FEUP.

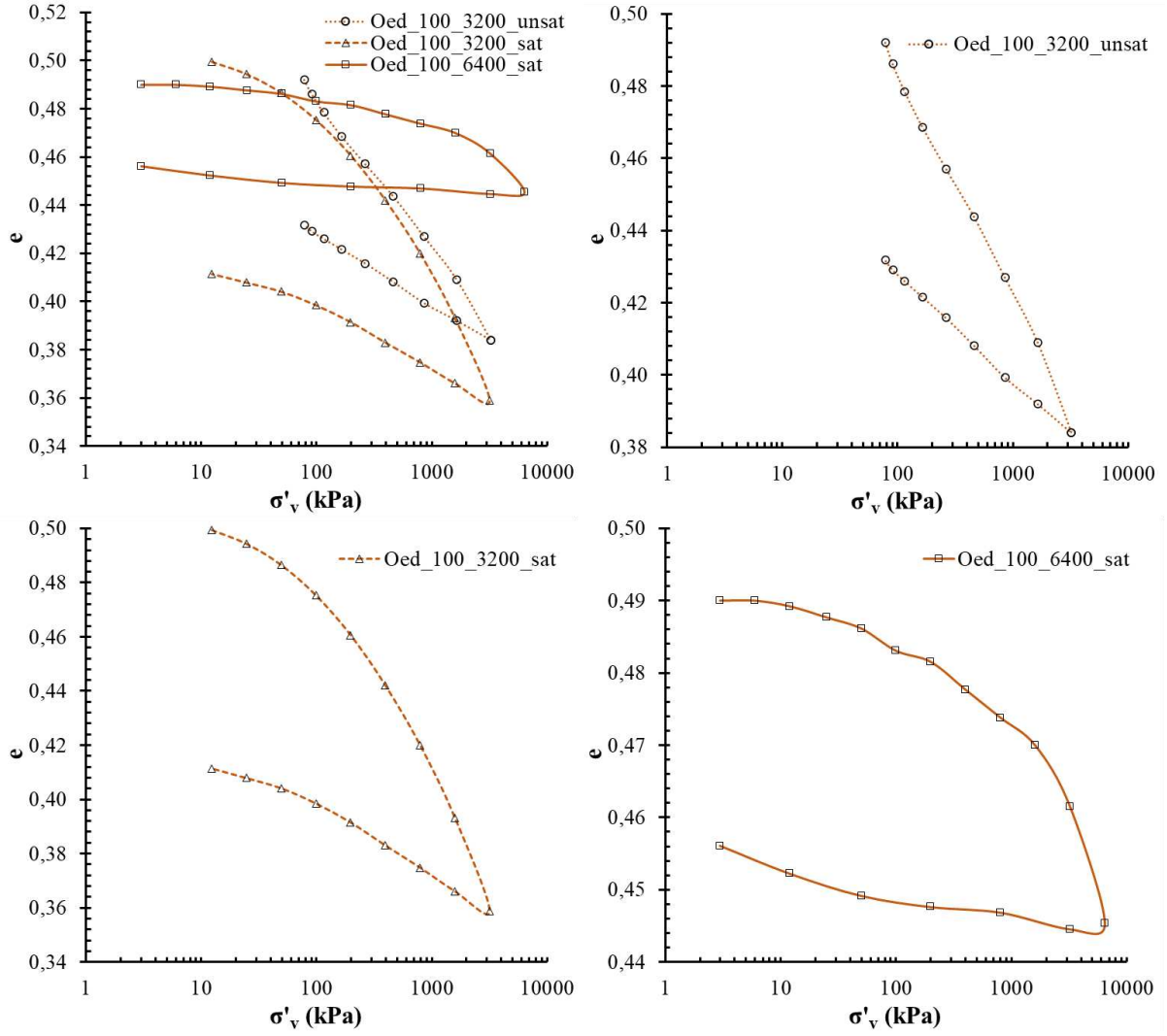

Source: elaborated by the author.

APPENDIX C – Isotropic Consolidation Test Results

C.1 DC = 93%

Figure C.1 – Isotropic consolidation test results, DC =93%.

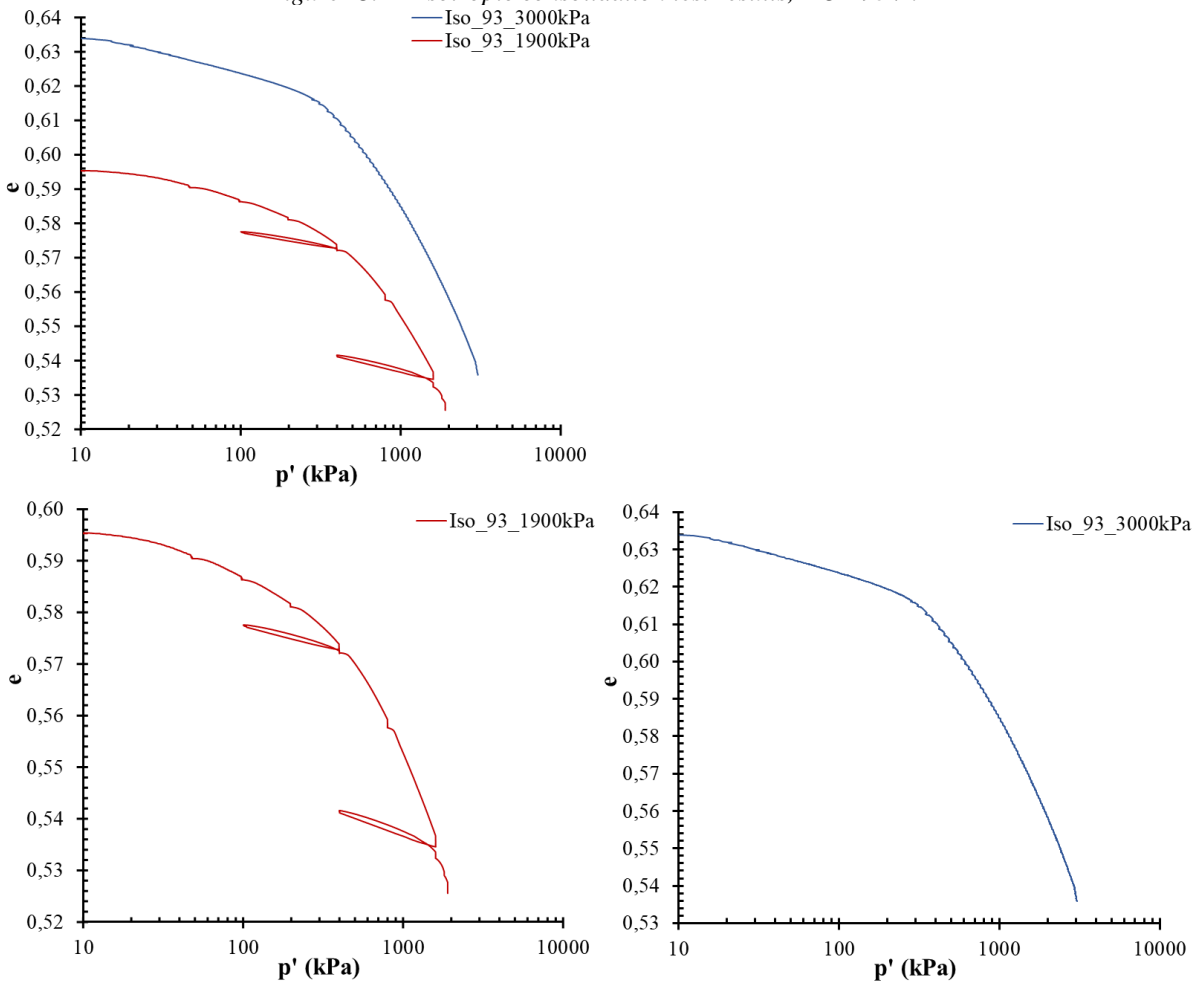

Source: elaborated by the author.

C.2 DC = 95%

Figure C.2 – Isotropic consolidation test results, DC =95%.

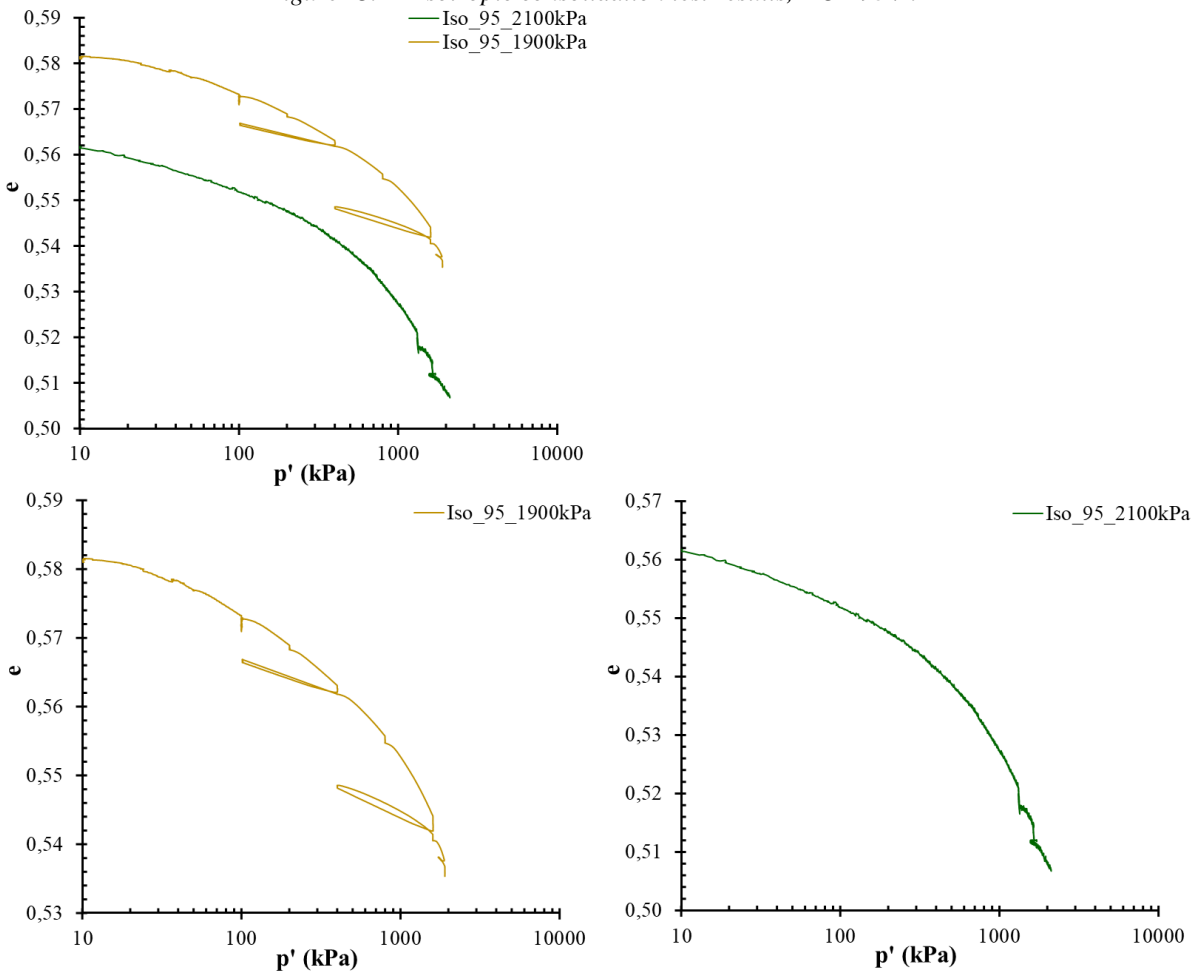

Source: elaborated by the author.

C.3 DC = 97%

Figure C.3 – Isotropic consolidation test results, DC =97%.

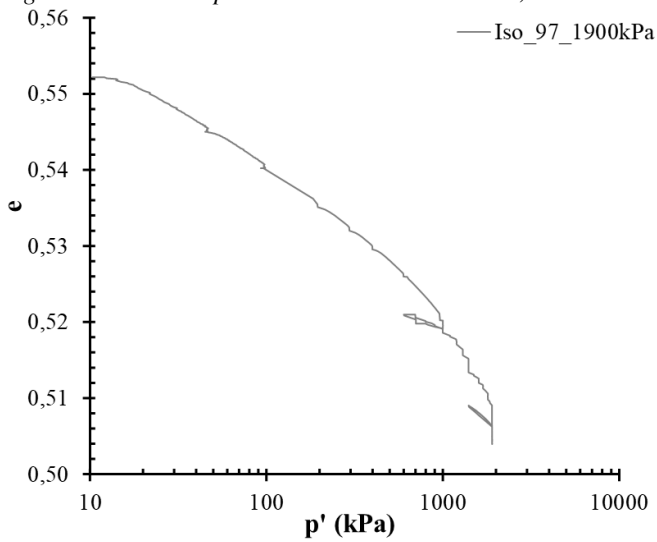

Source: elaborated by the author.

C.4 DC = 100%

Figure C.4 – Isotropic consolidation test results, DC =100%.

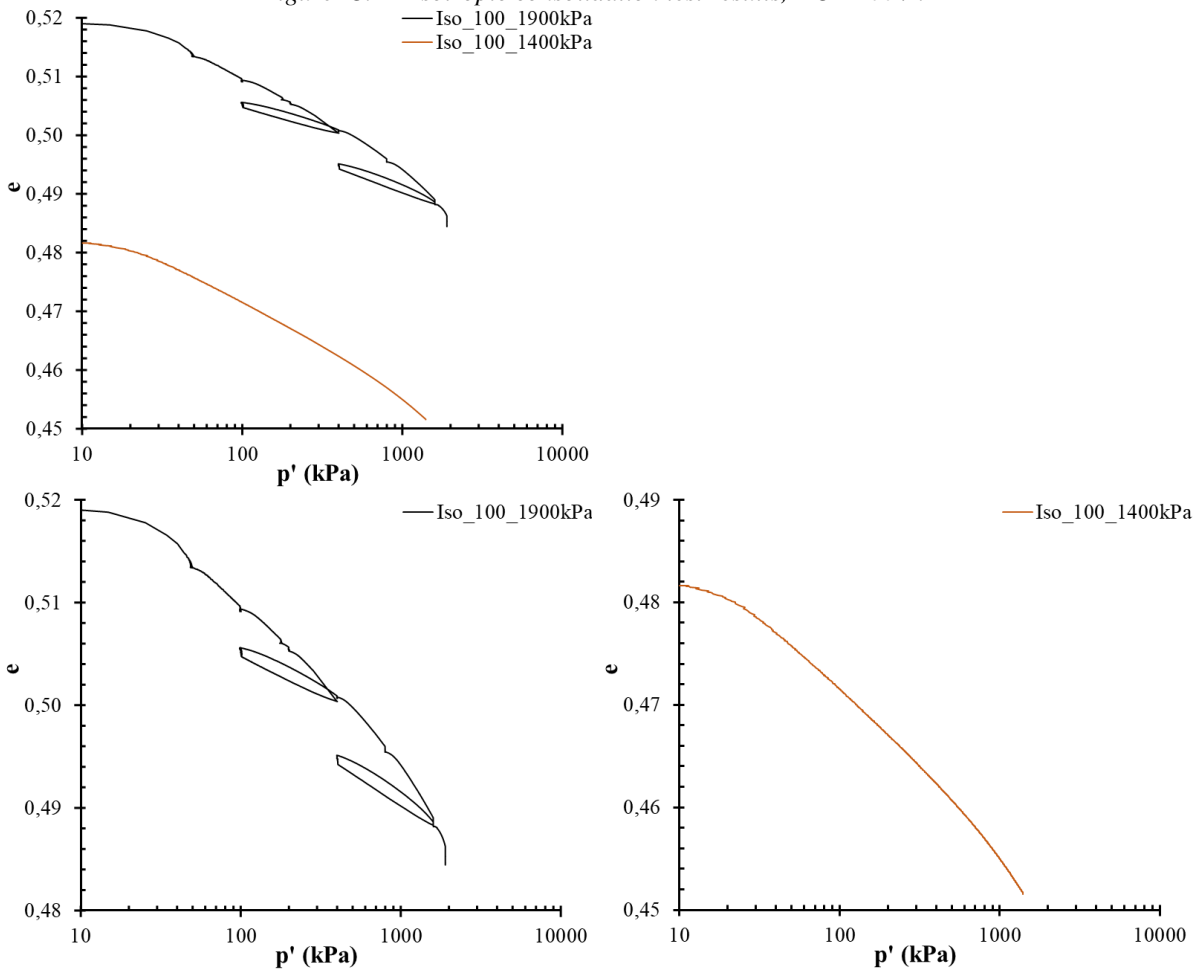

Source: elaborated by the author.

APPENDIX D – Triaxial Compression Test Results

D.1 DC = 93%

Figure D.1 – Triaxial test results, DC = 93%. In red, the drained tests, and in blue, the undrained tests.

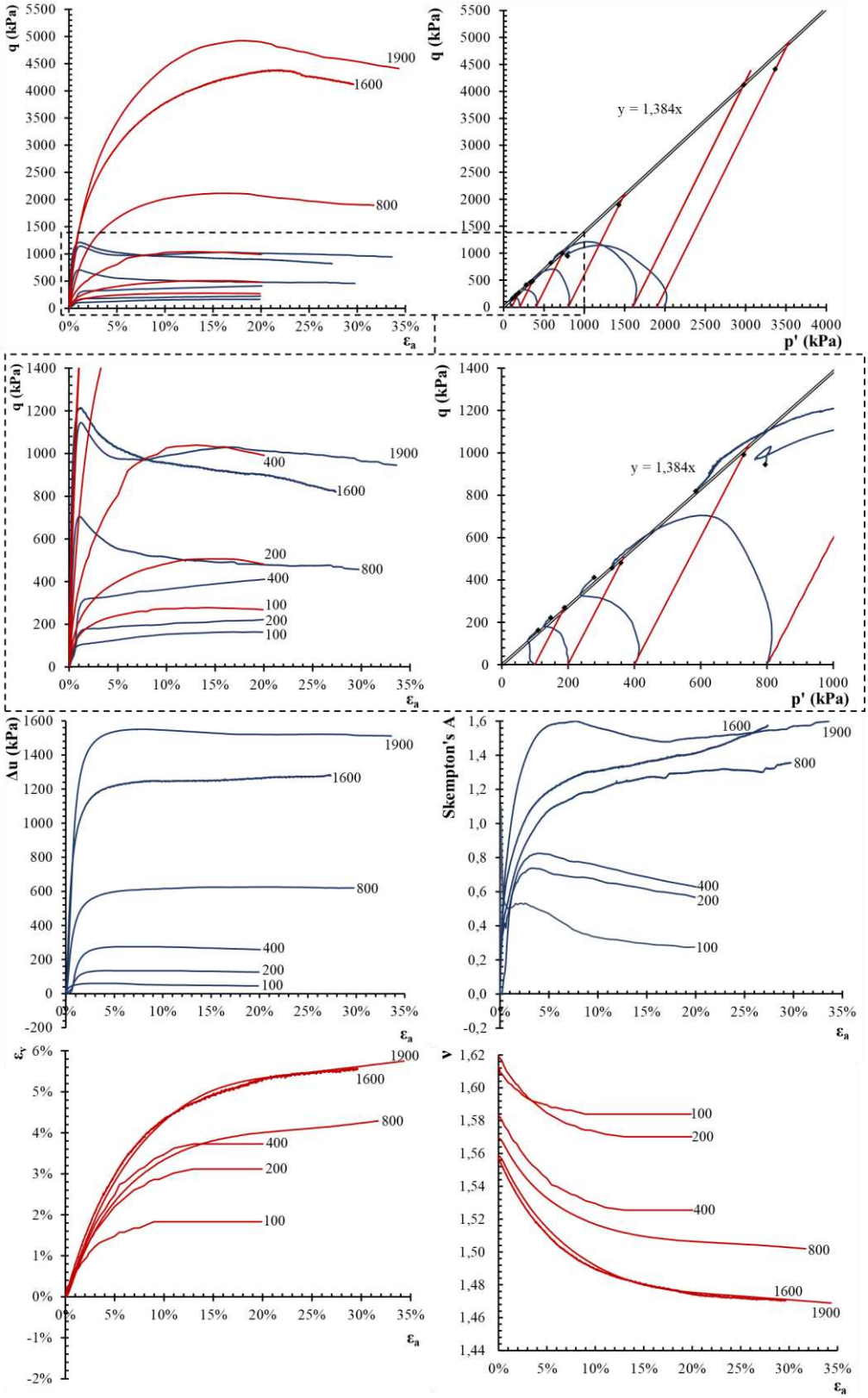

Source: elaborated by the author.

D.2 DC = 95%

Figure D.2 – Triaxial test results, DC = 95%. In green, the drained tests, and in yellow, the undrained tests.

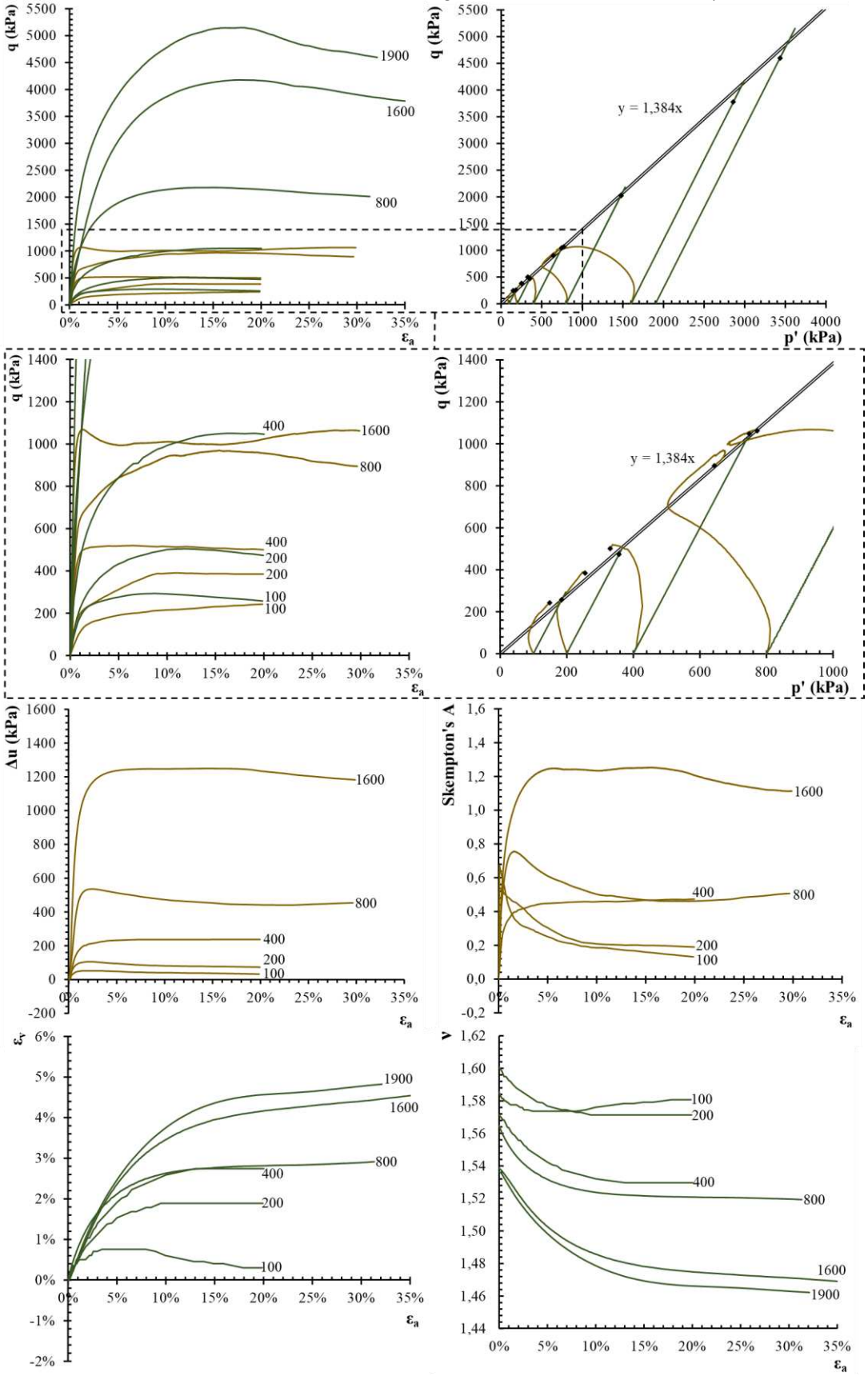

Source: elaborated by the author.

D.3 DC = 97%

Figure D.3 – Triaxial test results, DC = 97%. In gray, the drained tests, and in purple, the undrained tests.

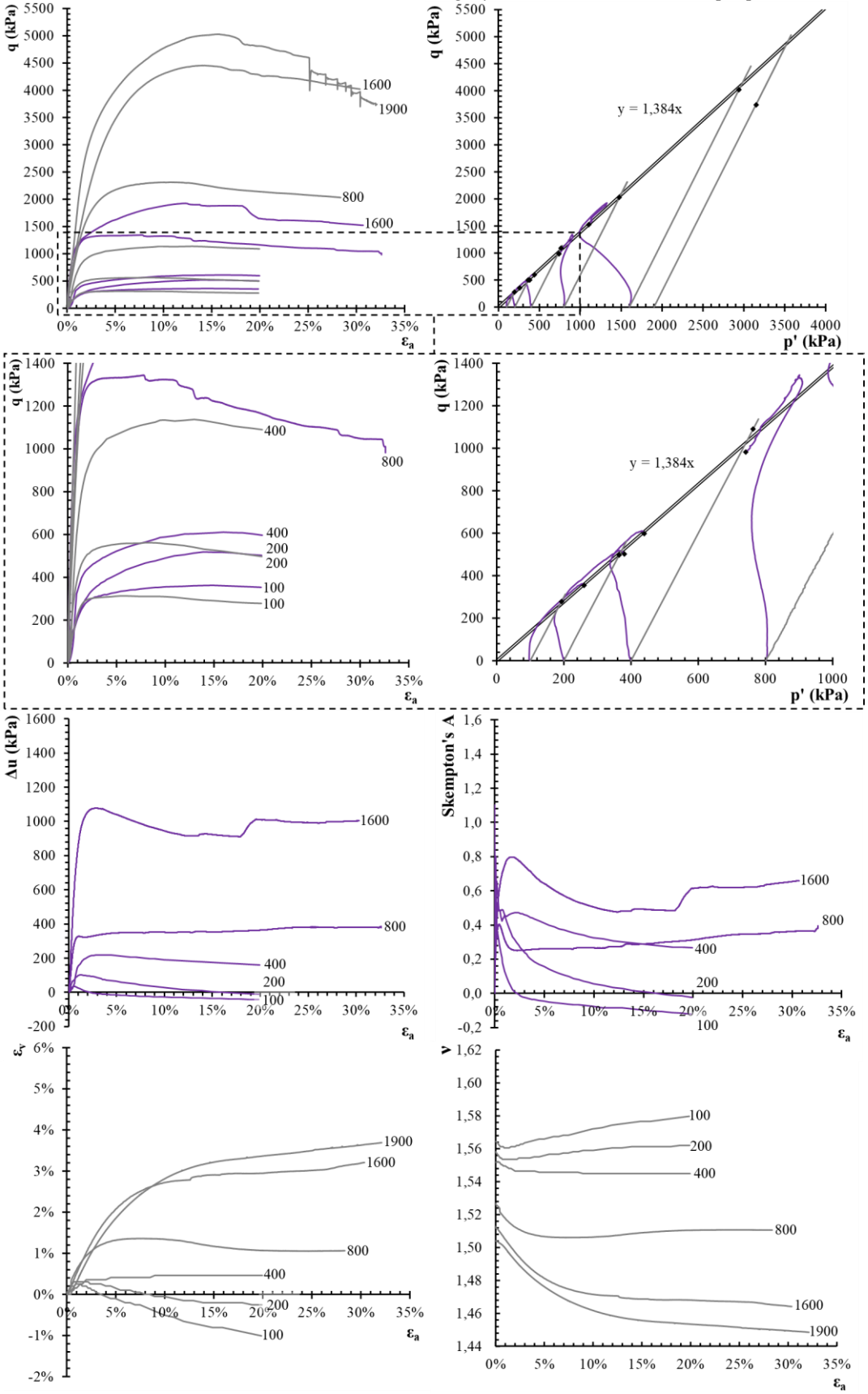

Source: elaborated by the author.

D.4 DC = 100%

Figure D.4 – Triaxial test results, DC = 97%. In black, the drained tests, and in orange, the undrained tests.

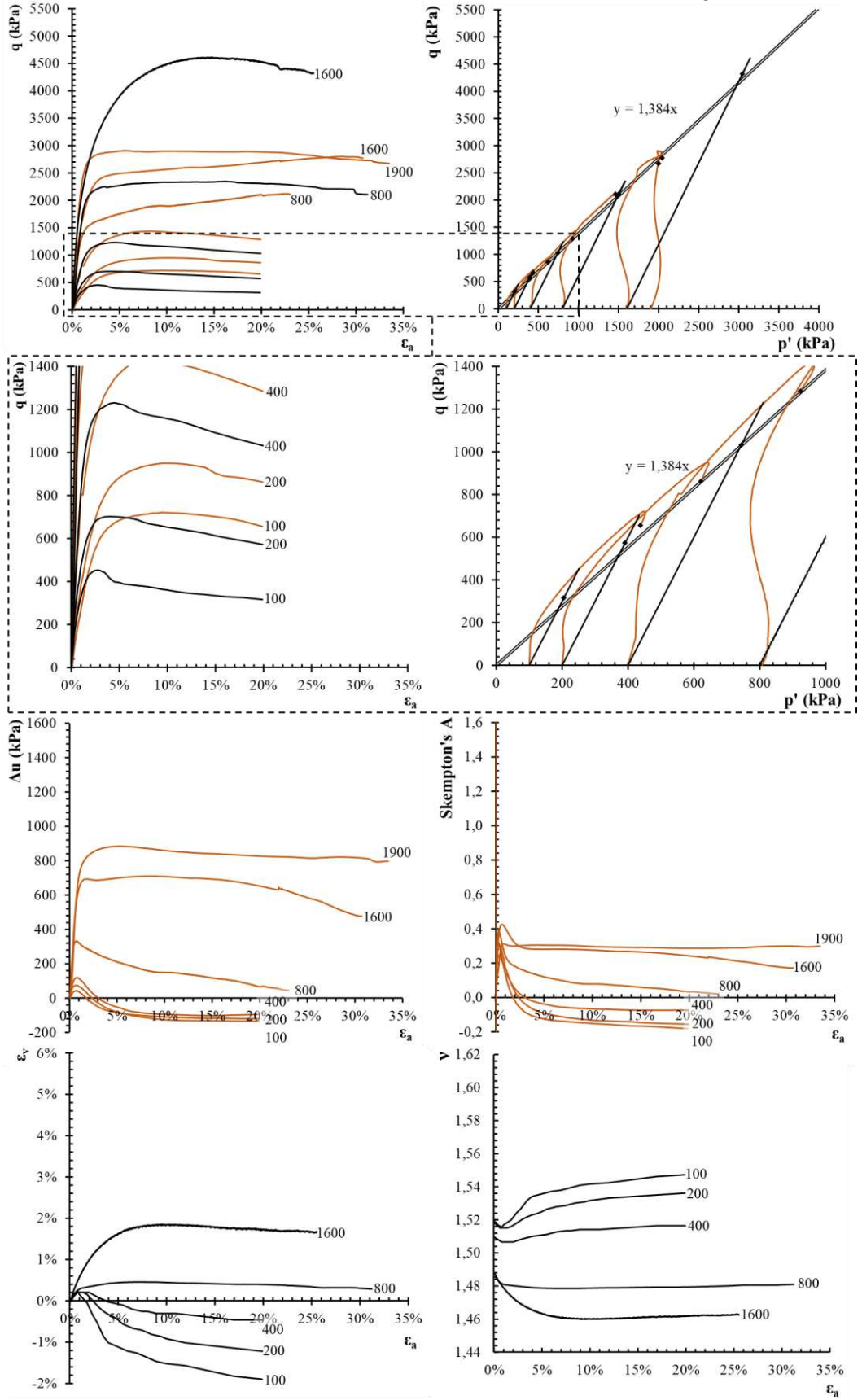

Source: elaborated by the author.

APPENDIX E – Critical State Lines

Figure E.1 – Critical state line defined in the (p', e) space.

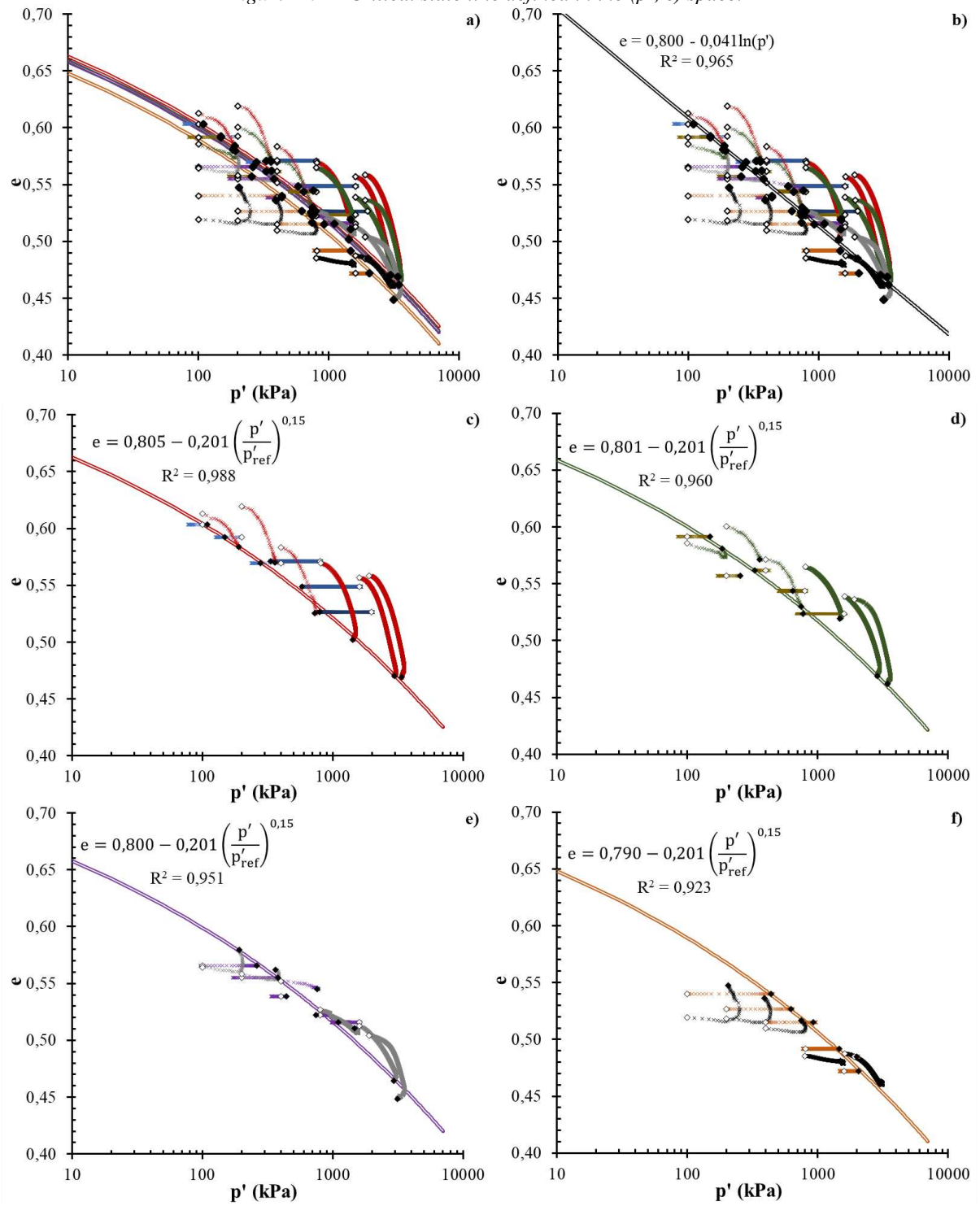

a) Curved critical state lines of the four studied degrees of compaction; b) CSL of the four studied degrees of compaction represented as a unique semi-logarithmic line; c) Curved CSL – DC = 93%; d) Curved CSL – DC = 95%; e) Curved CSL – DC = 97%; and f) Curved CSL – DC = 100%. Source: elaborated by the author.

APPENDIX F – Norsand Calibration

F.1 DC = 93%

Table F.1 – NorSand calibration into NorTXL.xls (Release 2) – DC = 93% – Summary.

	CID						CIU					
	100kPa	**200kPa**	**400kPa**	**800kPa**	**1600kPa**	**1900kPa**	**100kPa**	**200kPa**	**400kPa**	**800kPa**	**1600kPa**	**1900kPa**
CSL parameters												
Γ	0,8	0,8	0,8	0,8	0,8	0,8	0,8	0,8	0,8	0,8	0,8	0,8
λ	0,041	0,041	0,041	0,041	0,041	0,041	0,041	0,041	0,041	0,041	0,041	0,041
Plasticity												
M_{tc}	1,384	1,384	1,384	1,384	1,384	1,384	1,384	1,384	1,384	1,384	1,384	1,384
N	0,0058	0,0058	0,0058	0,0058	0,0058	0,0058	0,0058	0,0058	0,0058	0,0058	0,0058	0,0058
χ_{tc}	8,16	8,16	8,16	8,16	8,16	8,16	8,16	8,16	8,16	8,16	8,16	8,16
H_0	160	160	160	160	160	160	160	160	160	160	160	160
H_ψ	1037	1037	1037	1037	1037	1037	1037	1037	1037	1037	1037	1037
($H = H_0 - H_\psi.\psi$...)	156,1	119,7	127,1	111,6	95,4	110,2	166,0	147,6	141,2	110,2	103,6	117,0
Elasticity												
G_{max} @ p_0	20	30	30	80	90	100	10	25	55	25	85	420
G_exp	0,4	0,4	0,4	0,4	0,4	0,4	0,4	0,4	0,4	0,4	0,4	0,4
ν	0,2	0,2	0,2	0,2	0,2	0,2	0,2	0,2	0,2	0,2	0,2	0,2
(Ir...)	200,0	150,0	75,0	100,0	56,3	52,6	100	125	137,5	31,25	53,13	210,95
k	0,006	0,008	0,016	0,012	0,021	0,02	0,012	0,010	0,009	0,038	0,022	0,005
Initial soil state												
ψ_0	0,004	0,039	0,032	0,047	0,062	0,048	-0,006	0,012	0,018	0,048	0,054	0,041
e_0	0,613	0,619	0,583	0,570	0,557	0,558	0,603	0,592	0,570	0,571	0,549	0,527
p_0	100	200	400	800	1600	1900	100	200	400	800	1600	1991
K_0	1,0	1,0	1,0	1,0	1,0	1,0	1,0	1,0	1,0	1,0	1,0	1,0
(σ_1...)	100	200	400	800	1600	1900	100	200	400	800	1600	1991
OCR ("R")	1,6	1,55	1,5	1,35	1,2	1,15	1,55	1,5	1,45	1,3	1,3	1,12

Source: elaborated by the author.

Figure F.1 – NorSand calibration into NorTXL.xls (Release 2) – Trx_93_CID_100kPa.

Soil properties….

CSL parameters

Γ =	**0,8**	---
λ =	**0,041**	*on base e*

Plasticity

M_{tc} =	**1,384**	
N =	**0,0058**	*(typ 0.2 - 0.3)*
χ_{tc} =	**8,16**	*often taken as 4*
H_0 =	**160**	*> H_23*
H_ψ =	**1037**	
($H = H_0 - H_\psi.\psi$...)	*156,071*	*(typ 60 - 400)*

Elasticity

G_{max} @ p_0=	**20**	MPa
G_exp =	**0,4**	*elastic exponent*
ν =	**0,20**	
(Ir ...)	*200*	---
k=	*0,0060*	---

Initial soil state…

ψ_0 =	**0,0038**	
=> e_0 =	*0,613*	
p_0 =	**100**	***kPa***
K_0 =	**1**	---
(sig1 ...)	*100*	
OCR ("R") =	**1,6**	---

Drained or undrained… **Drained**

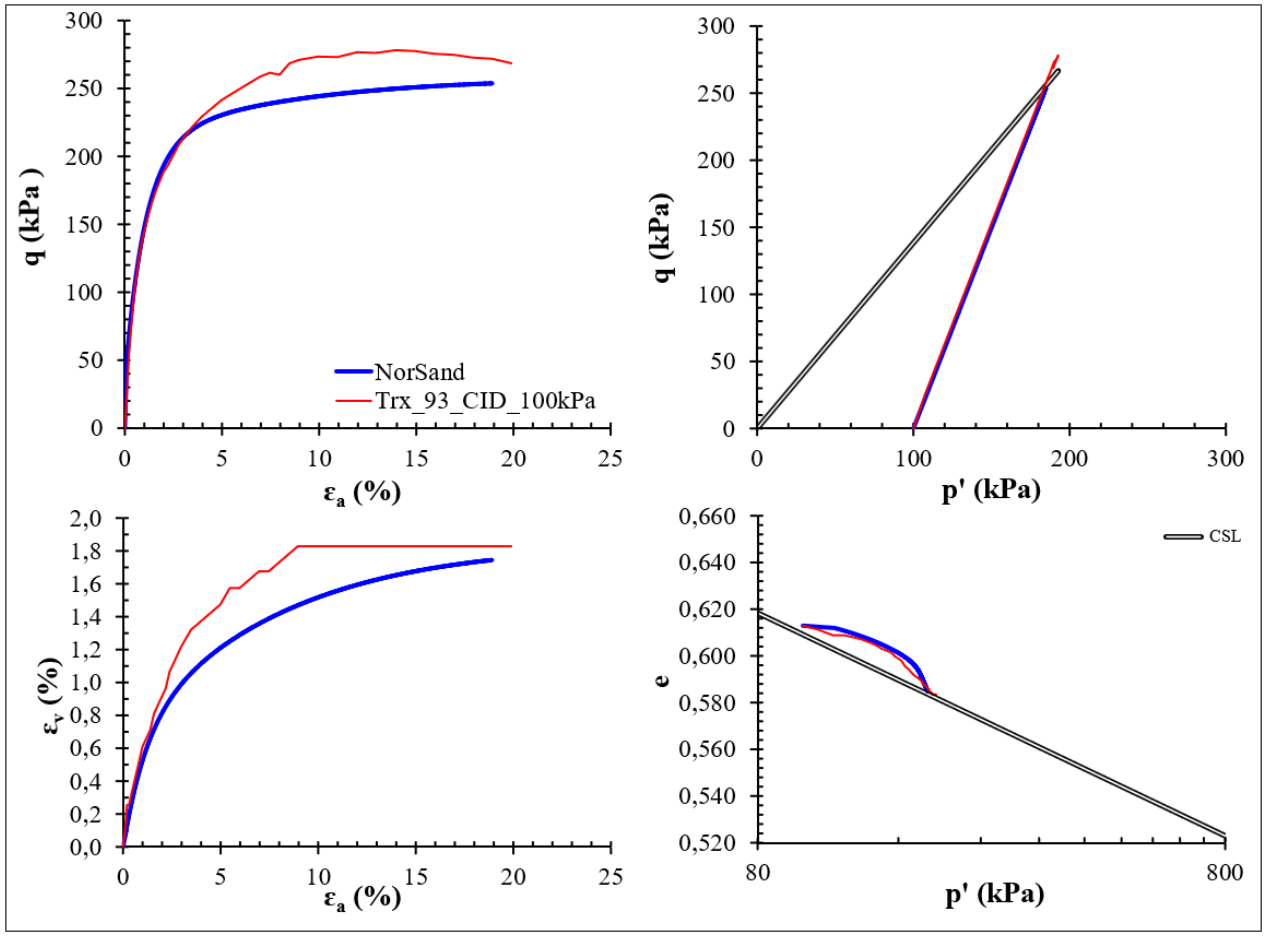

Source: elaborated by the author.

Figure F.2 – NorSand calibration into NorTXL.xls (Release 2) – Trx_93_CID_200kPa.

Soil properties….

CSL parameters

Γ =	**0,8**	**---**
λ =	**0,041**	*on base e*

Plasticity

M_{tc} =	**1,384**	
N =	**0,0058**	*(typ 0.2 - 0.3)*
χ_{tc} =	**8,16**	*often taken as 4*
H_0 =	**160**	*> H_24*
H_ψ =	**1037**	
(H = H_0 - H_ψ.ψ...)	*119,674*	*(typ 60 - 400)*

Elasticity

G_{max} @ p_0=	**30**	MPa
G_exp =	**0,4**	*elastic exponent*
ν =	**0,20**	
(Ir ...)	*150*	**---**
k=	*0,0081*	**---**

Initial soil state…

ψ_0 =	**0,0389**	
=> e_0 =	*0,619*	
p_0 =	**200**	***kPa***
K_0 =	**1**	**---**
(sig1...)	*200*	
OCR ("R") =	**1,55**	**---**

Drained or undrained… **Drained**

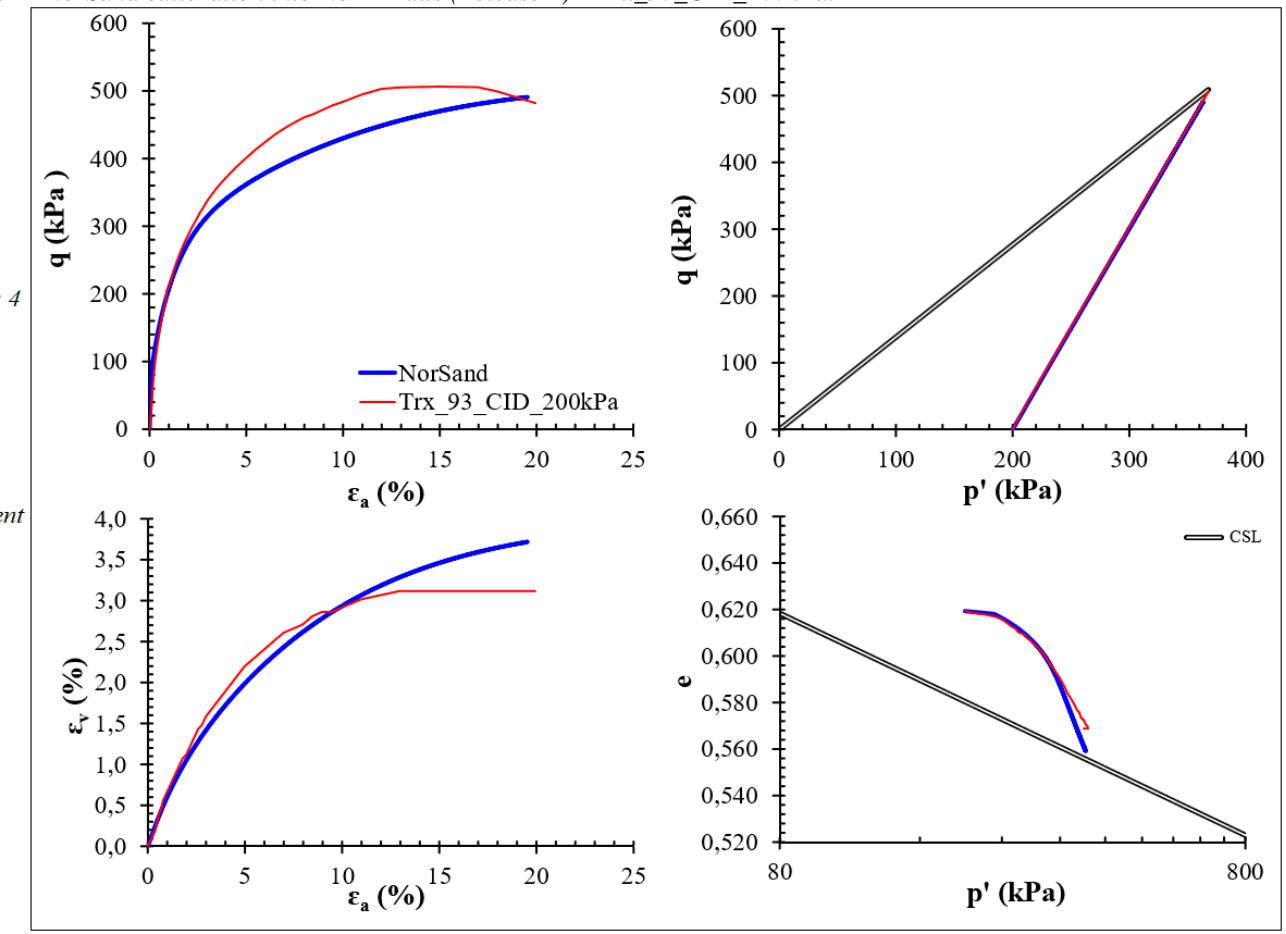

Source: elaborated by the author.

Figure F.3 – NorSand calibration into NorTXL.xls (Release 2) – Trx_93_CID_400kPa.

Soil properties….

CSL parameters

Γ = **0,8** ---

λ = **0,041** *on base e*

Plasticity

M_{tc} = **1,384**

N = **0,0058** *(typ 0.2 - 0.3)*

χ_{tc} = **8,16** *often taken as 4*

H_0 = **160** *> H_31*

H_ψ = **1037**

(H = H_0 - H_ψ.ψ...) *127,099* *(typ 60 - 400)*

Elasticity

G_{max} @ p_0= **30** MPa

G_exp = **0,4** *elastic exponent*

ν = **0,20**

(Ir ...) *75* ---

k= *0,0158* ---

Initial soil state…

ψ_0 = **0,0317**

=> **e_0** = *0,583*

p_0 = **400** ***kPa***

K_0 = **1** ---

(sig1...) *400*

OCR ("R") = **1,5** ---

Drained or undrained… **Drained**

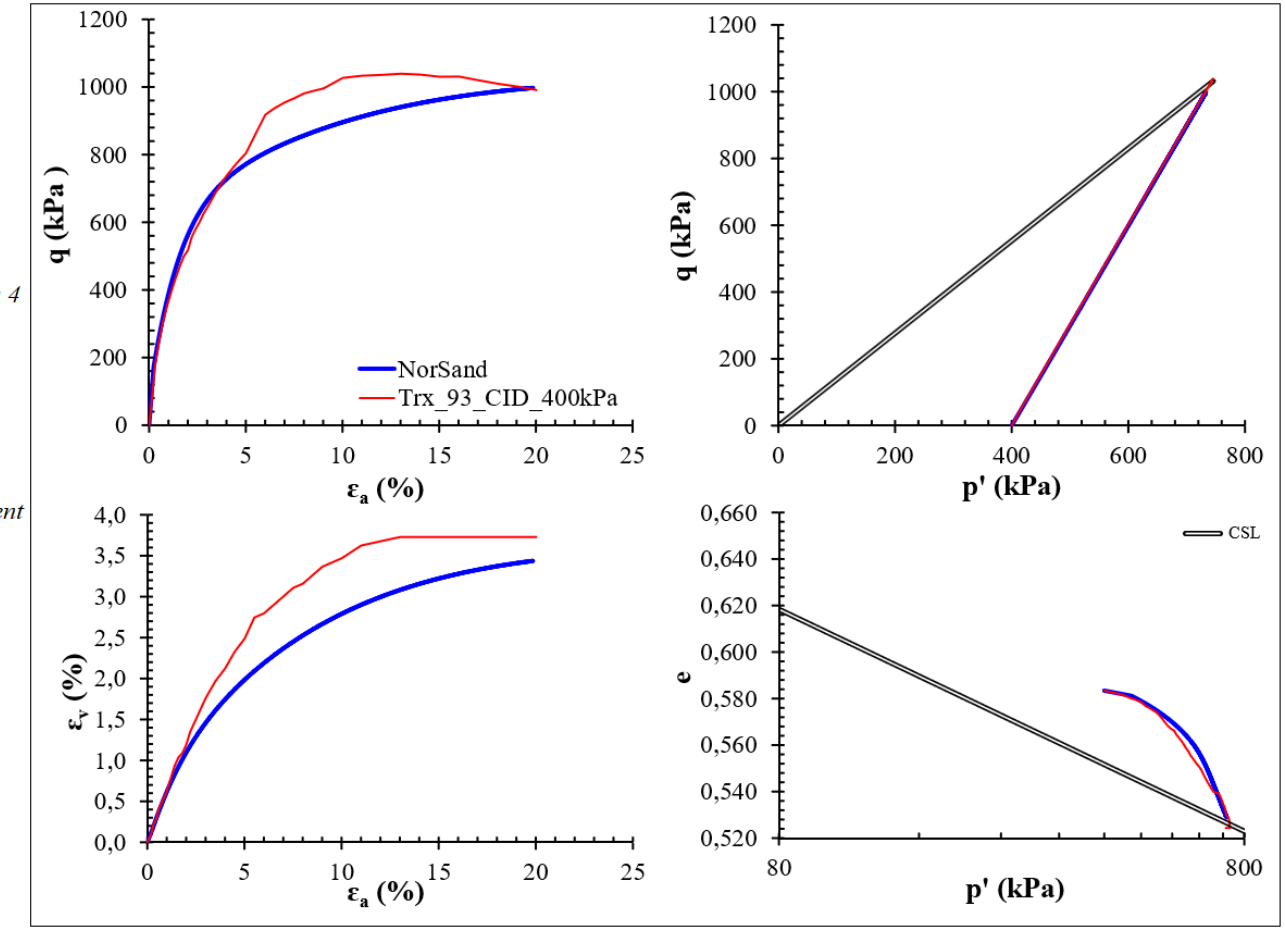

Source: elaborated by the author.

Figure F.4 – NorSand calibration into NorTXL.xls (Release 2) – Trx_93_CID_800kPa.

Soil properties….

CSL parameters

Γ =	**0,8**	---
λ =	**0,041**	*on base e*

Plasticity

M_{tc} =	**1,384**	
N =	**0,0058**	*(typ 0.2 - 0.3)*
χ_{tc} =	**8,16**	*often taken as 4*
H_0 =	**160**	*> H 26*
H_ψ =	**1037**	
($H = H_0 - H_{\psi}\,\psi$...)	*111,261*	*(typ 60 - 400)*

Elasticity

G_{max} @ p_0=	**80**	MPa
G_exp =	**0,4**	*elastic exponent*
ν =	**0,20**	
(Ir ...)	*100*	---
k=	*0,0118*	---

Initial soil state…

ψ_0 =	**0,0470**	
=> e_0 =	*0,570*	
p_0 =	**800**	***kPa***
K_0 =	**1**	---
(sig1...)	*800*	
OCR ("R") =	**1,35**	---

Drained or undrained… **Drained**

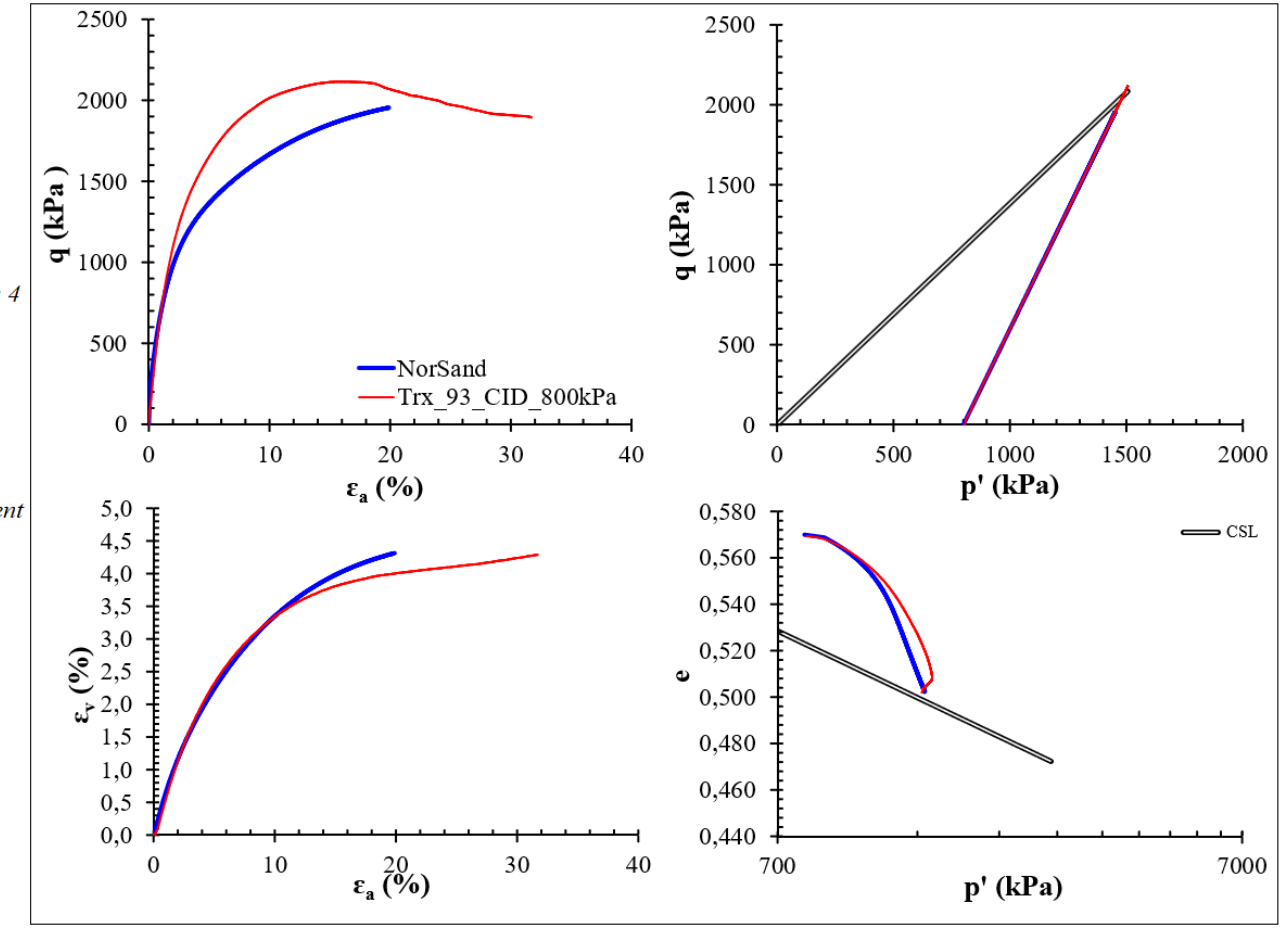

Source: elaborated by the author.

Figure F.5 – NorSand calibration into NorTXL.xls (Release 2) – Trx_93_CID_1600kPa.

Soil properties….

CSL parameters

Γ = **0,8** ---

λ = **0,041** *on base e*

Plasticity

M_{tc} = **1,384**

N = **0,0058** *(typ 0.2 - 0.3)*

χ_{tc} = **8,16** *often taken as 4*

H_0 = **160** *> H 38*

H_ψ = **1037**

(H = H_0 - H_ψ ψ...) *95,3643* *(typ 60 - 400)*

Elasticity

G_{max} @ p_0 = **90** MPa

G_exp = **0,4** *elastic exponent*

ν = **0,20**

(Ir ...) *56,25* ---

k= *0,0208* ---

Initial soil state…

ψ_0 = **0,0623**

=> e_0 = *0,557*

p_0 = **1600** ***kPa***

K_0 = **1** ---

(sig1...) *1600*

OCR ("R") = **1,2** ---

Drained or undrained… **Drained**

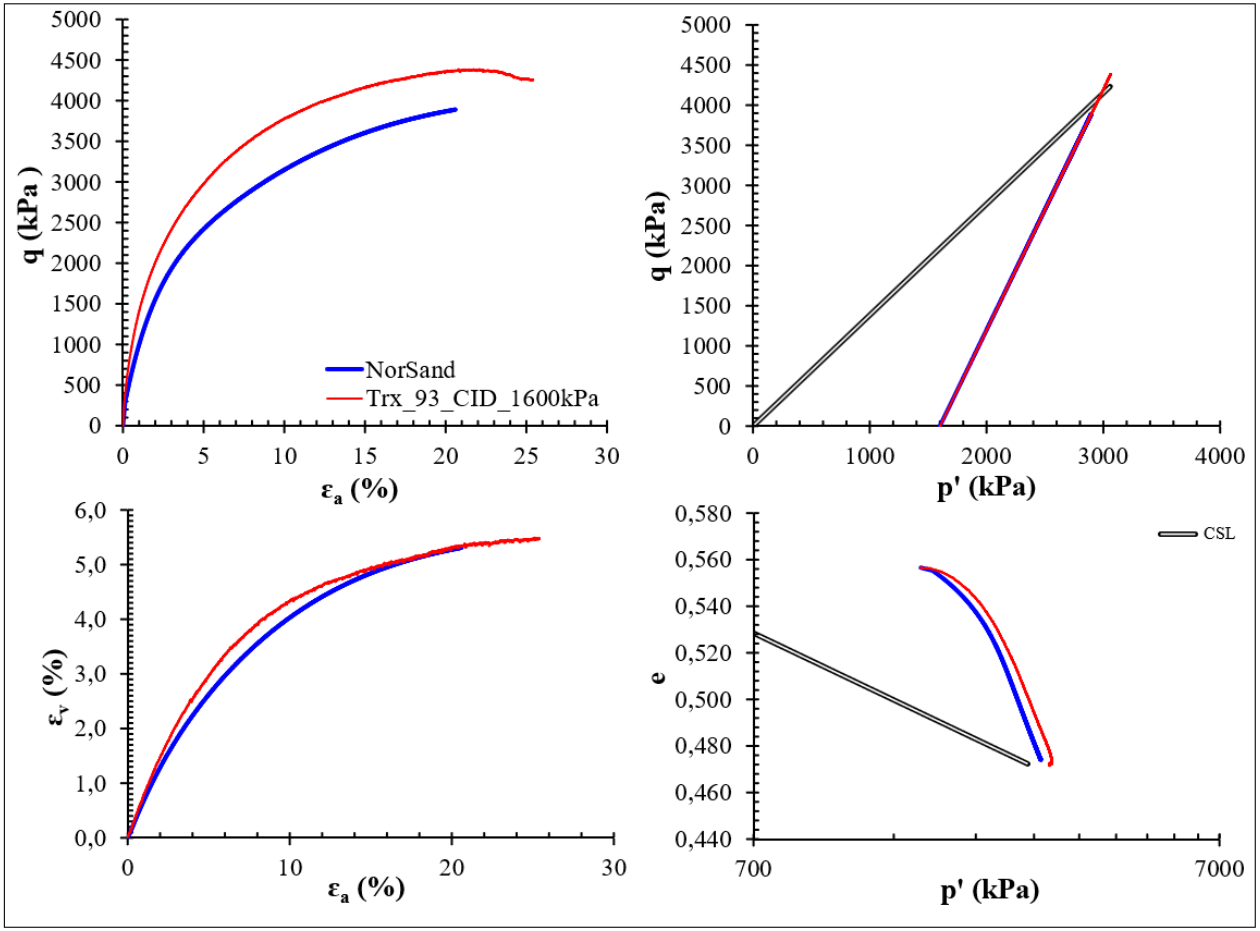

Source: elaborated by the author.

Figure F.6 – NorSand calibration into NorTXL.xls (Release 2) – Trx_93_CID_1900kPa.

Soil properties….

CSL parameters

Γ = **0,8** ---

λ = **0,041** *on base e*

Plasticity

M_{tc} = **1,384**

N = **0,0058** *(typ 0.2 - 0.3)*

χ_{tc} = **8,16** *often taken as 4*

H_0 = **160** *> H 41*

H_ψ = **1037**

(H = H_0 - H_ψ...) *85,9543* *(typ 60 - 400)*

Elasticity

G_{max} @ p_0= **100** MPa

G_exp = **0,4** *elastic exponent*

ν = **0,20**

(Ir ...) *52,6316* ---

k= *0,0222* ---

Initial soil state…

ψ_0 = **0,0714**

=> ***e_0*** = *0,558*

p_0 = **1900** ***kPa***

K_0 = **1** ---

(sig1...) *1900*

OCR ("R") = **1,15** ---

Drained or undrained… **Drained**

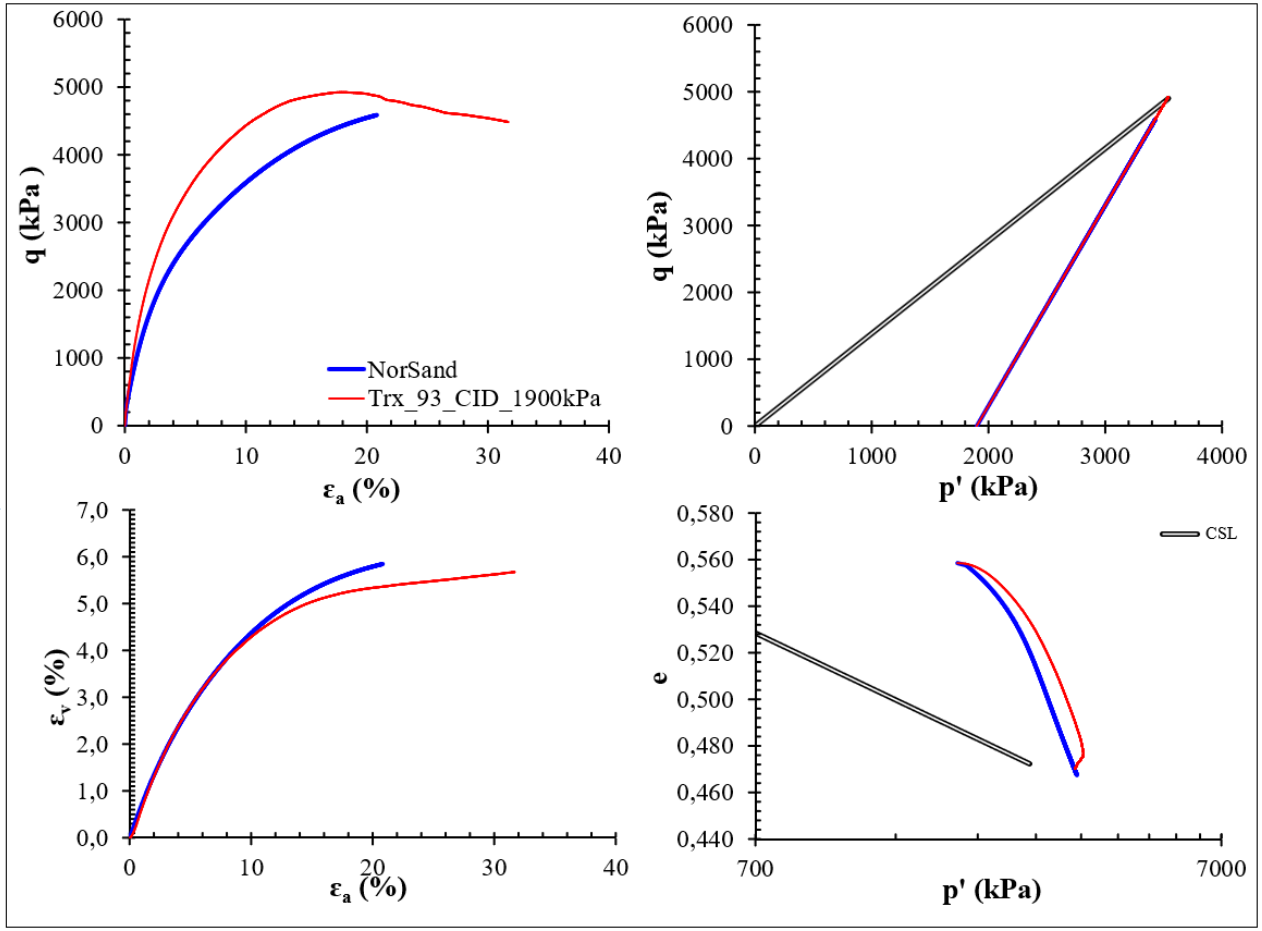

Source: elaborated by the author.

Figure F.7 – NorSand calibration into NorTXL.xls (Release 2) – Trx_93_CIU_100kPa.

Soil properties….

CSL parameters

Γ =	**0,8**	---
λ =	**0,041**	*on base e*

Plasticity

M_{tc} =	**1,384**	
N =	**0,0058**	*(typ 0.2 - 0.3)*
χ_{tc} =	**8,16**	*often taken as 4*
H_0 =	**160**	*> H 27*
H_ψ =	**1037**	
($H = H_0 - H_\psi.\psi$...)	*165,979*	*(typ 60 - 400)*

Elasticity

G_{max} @ p_0=	**10**	MPa
G_exp =	**0,4**	*elastic exponent*
ν =	**0,20**	
(Ir ...)	*100*	---
k=	*0,0120*	---

Initial soil state…

ψ_0 =	**-0,0058**	
=> e_0 =	*0,603*	
p_0 =	**100**	***kPa***
K_0 =	**1**	---
(sig1...)	*100*	
OCR ("R") =	**1,55**	---

Drained or undrained… **Undrained**

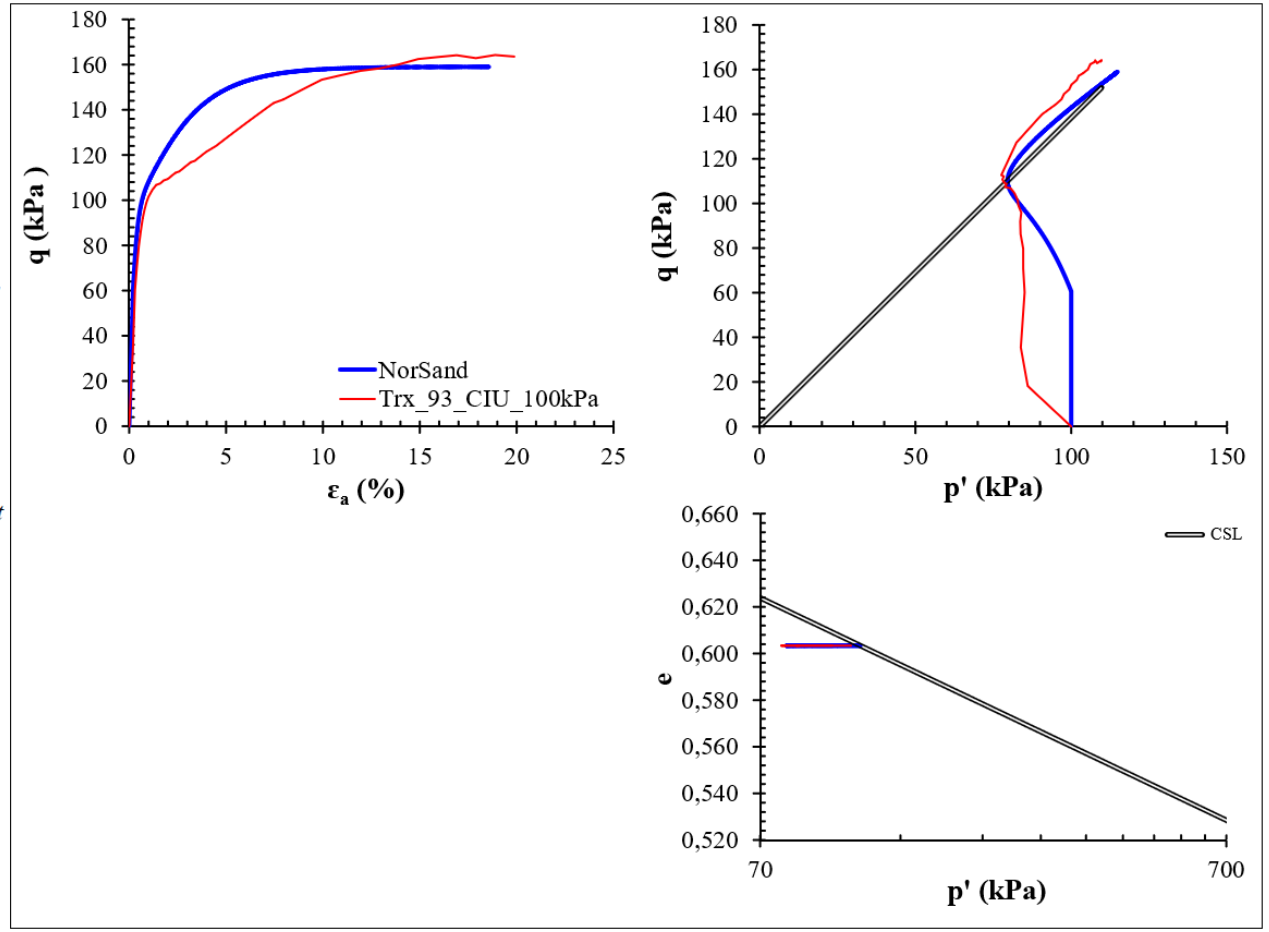

Source: elaborated by the author.

Figure F.8 – NorSand calibration into NorTXL.xls (Release 2) – Trx_93_CIU_200kPa.

Soil properties….

CSL parameters

Γ =	**0,8**	---
λ =	**0,041**	*on base e*

Plasticity

M_{tc} =	**1,384**	
N =	**0,0058**	*(typ 0.2 - 0.3)*
χ_{tc} =	**8,16**	*often taken as 4*
H_0 =	**160**	*> H_25*
H_ψ =	**1037**	
(H = H_0 - H_ψ ψ...)	*147,556*	*(typ 60 - 400)*

Elasticity

G_{max} @ p_0=	**25**	MPa
G_exp =	**0,4**	*elastic exponent*
ν =	**0,20**	
(Ir ...)	*125*	---
k=	*0,0096*	---

Initial soil state…

ψ_0 =	**0,0120**	
=> e_0 =	*0,592*	
p_0 =	**200**	***kPa***
K_0 =	**1**	---
(sig1...)	*200*	
OCR ("R") =	**1,5**	---

Drained or undrained… **Undrained**

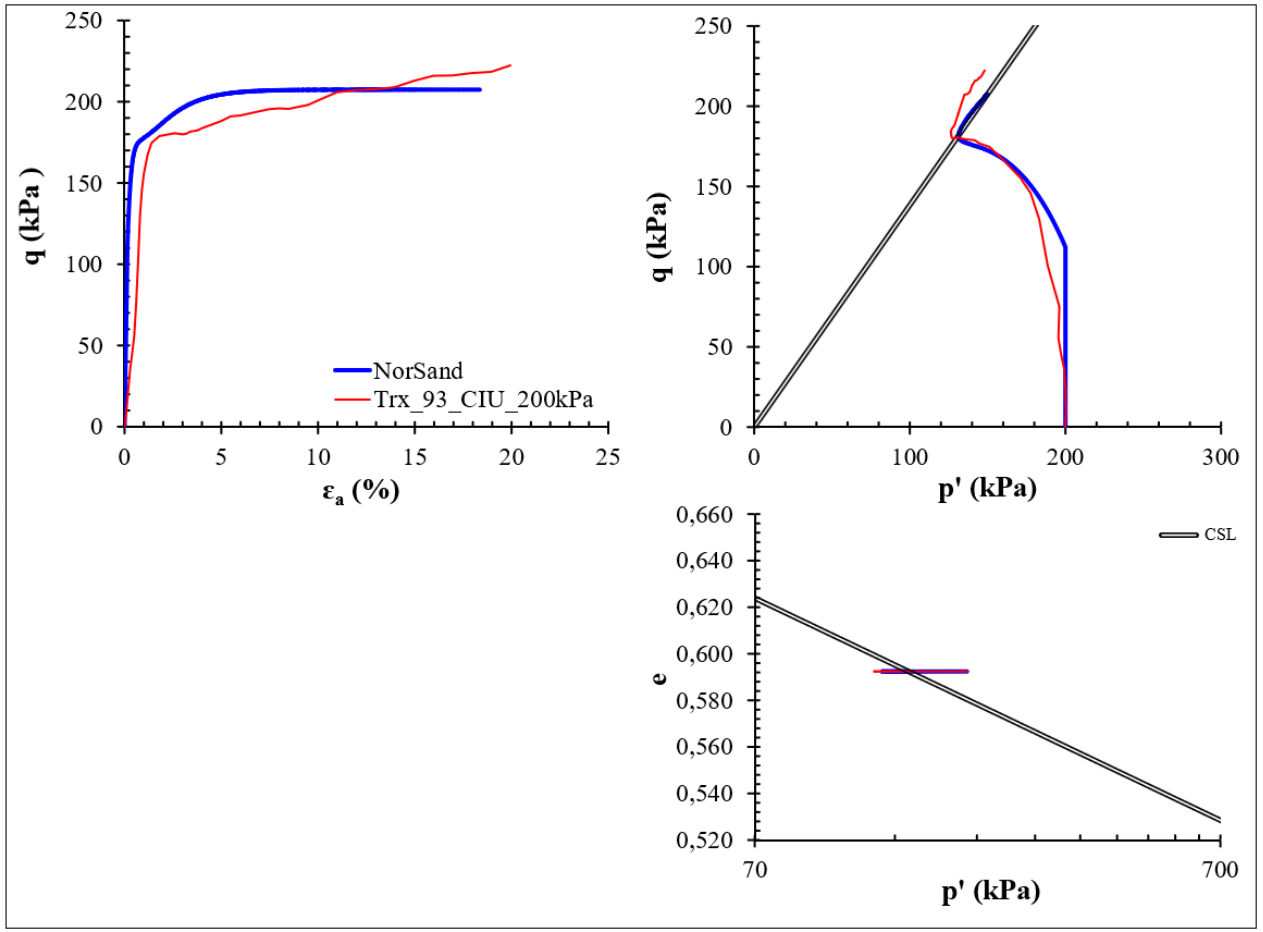

Source: elaborated by the author.

Figure F.9 – NorSand calibration into NorTXL.xls (Release 2) – Trx_93_CIU_400kPa.

Soil properties….

CSL parameters

Γ = **0,8** ---

λ = **0,041** *on base e*

Plasticity

M_{tc} = **1,384**

N = **0,0058** *(typ 0.2 - 0.3)*

χ_{tc} = **8,16** *often taken as 4*

H_0 = **160** *> H_24*

H_ψ = **1037**

(H = H_0 - H_ψ...) *141,241* *(typ 60 - 400)*

Elasticity

G_{max} @ p_0= **55** MPa

G_exp = **0,4** *elastic exponent*

ν = **0,20**

(Ir ...) *137,5* ---

k= *0,0086* ---

Initial soil state…

ψ_0 = **0,0181**

=> e_0 = *0,570*

p_0 = **400** ***kPa***

K_0 = **1** ---

(sig1...) *400*

OCR ("R") = **1,45** ---

Drained or undrained… **Undrained**

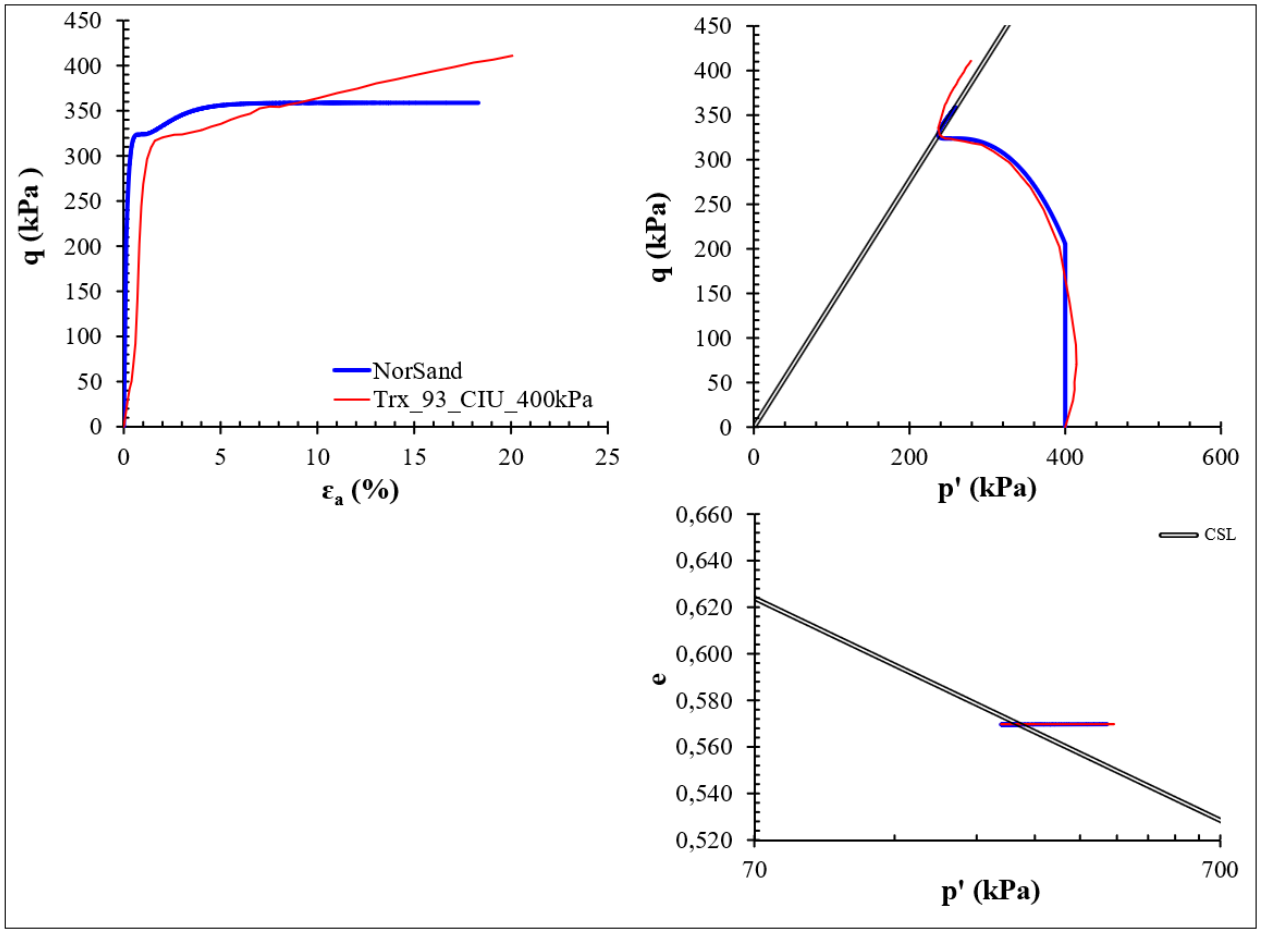

Source: elaborated by the author.

Figure F.10 – NorSand calibration into NorTXL.xls (Release 2) – Trx_93_CIU_800kPa.

Soil properties….

CSL parameters

Γ =	**0,8**	**---**
λ =	**0,041**	*on base e*

Plasticity

M_{tc} =	**1,384**	
N =	**0,0058**	*(typ 0.2 - 0.3)*
χ_{tc} =	**8,16**	*often taken as 4*
H_0 =	**160**	*> H_210*
H_ψ =	**1037**	
(H = H_0 - H_ψ ψ...)	*110,157*	*(typ 60 - 400)*

Elasticity

G_{max} @ p_0=	**25**	MPa
G_exp =	**0,4**	*elastic exponent*
ν =	**0,20**	
(Ir ...)	*31,25*	**---**
k=	*0,0377*	**---**

Initial soil state…

ψ_0 =	**0,0481**	
=> e_0 =	*0,571*	
p_0 =	**800**	***kPa***
K_0 =	**1**	**---**
(sig1...)	*800*	
OCR ("R") =	**1,3**	**---**

Drained or undrained… **Undrained**

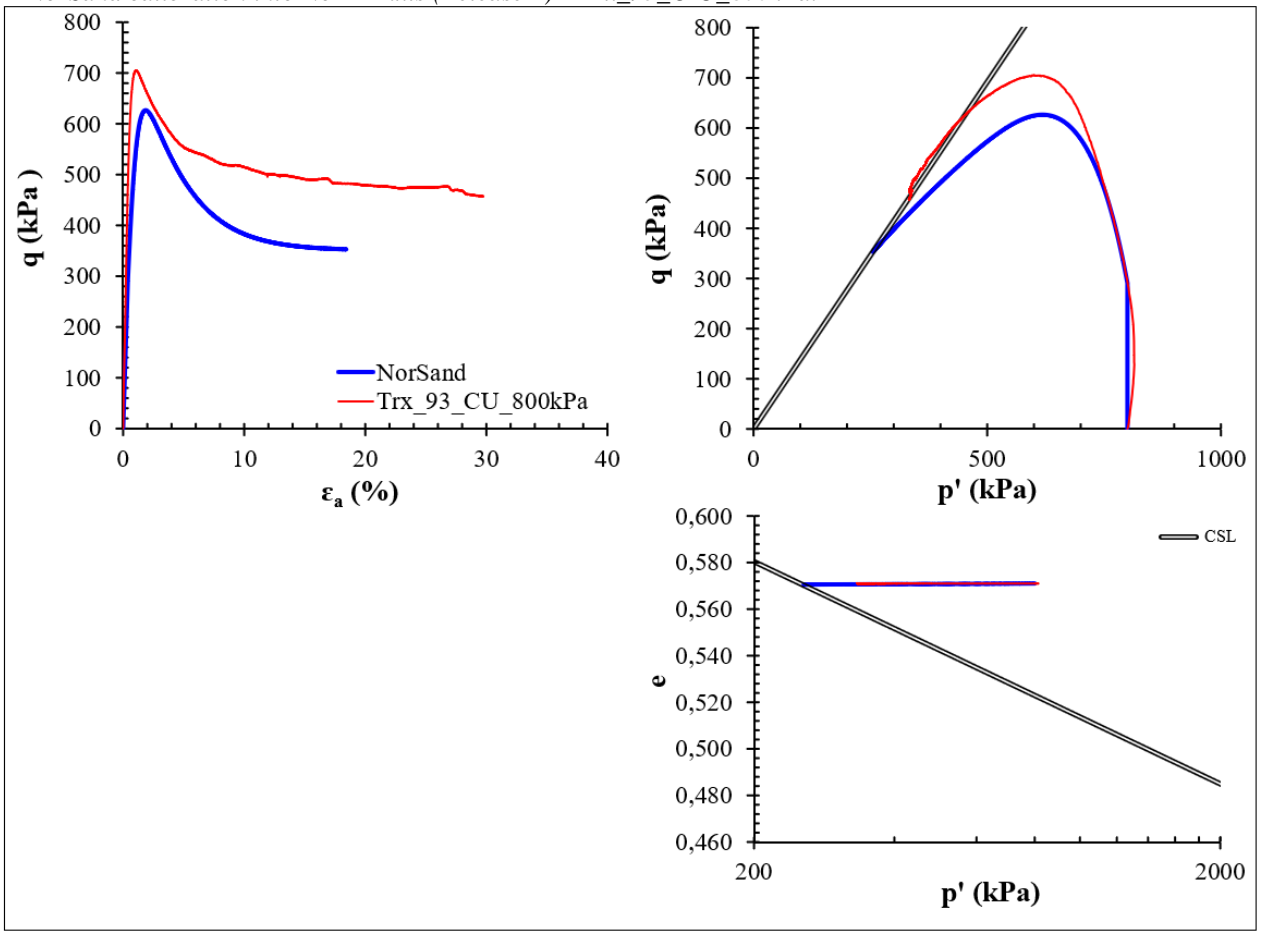

Source: elaborated by the author.

Figure F.11 – NorSand calibration into NorTXL.xls (Release 2) – Trx_93_CIU_1600kPa.

Soil properties….

CSL parameters

Γ = **0,8** ---

λ = **0,041** *on base e*

Plasticity

M_{tc} = **1,384**

N = **0,0058** *(typ 0.2 - 0.3)*

χ_{tc} = **8,16** *often taken as 4*

H_0 = **160** *> H 40*

H_ψ = **1037**

(H = H_0 - H_ψ ψ...) *103,603* *(typ 60 - 400)*

Elasticity

G_{max} @ p_0= **85** MPa

G_exp = **0,4** *elastic exponent*

ν = **0,20**

(Ir ...) *53,125* ---

k= *0,0219* ---

Initial soil state…

ψ_0 = **0,0544**

=> e_0 = *0,549*

p_0 = **1600** ***kPa***

K_0 = **1** ---

(sig1...) *1600*

OCR ("R") = **1,3** ---

Drained or undrained… **Undrained**

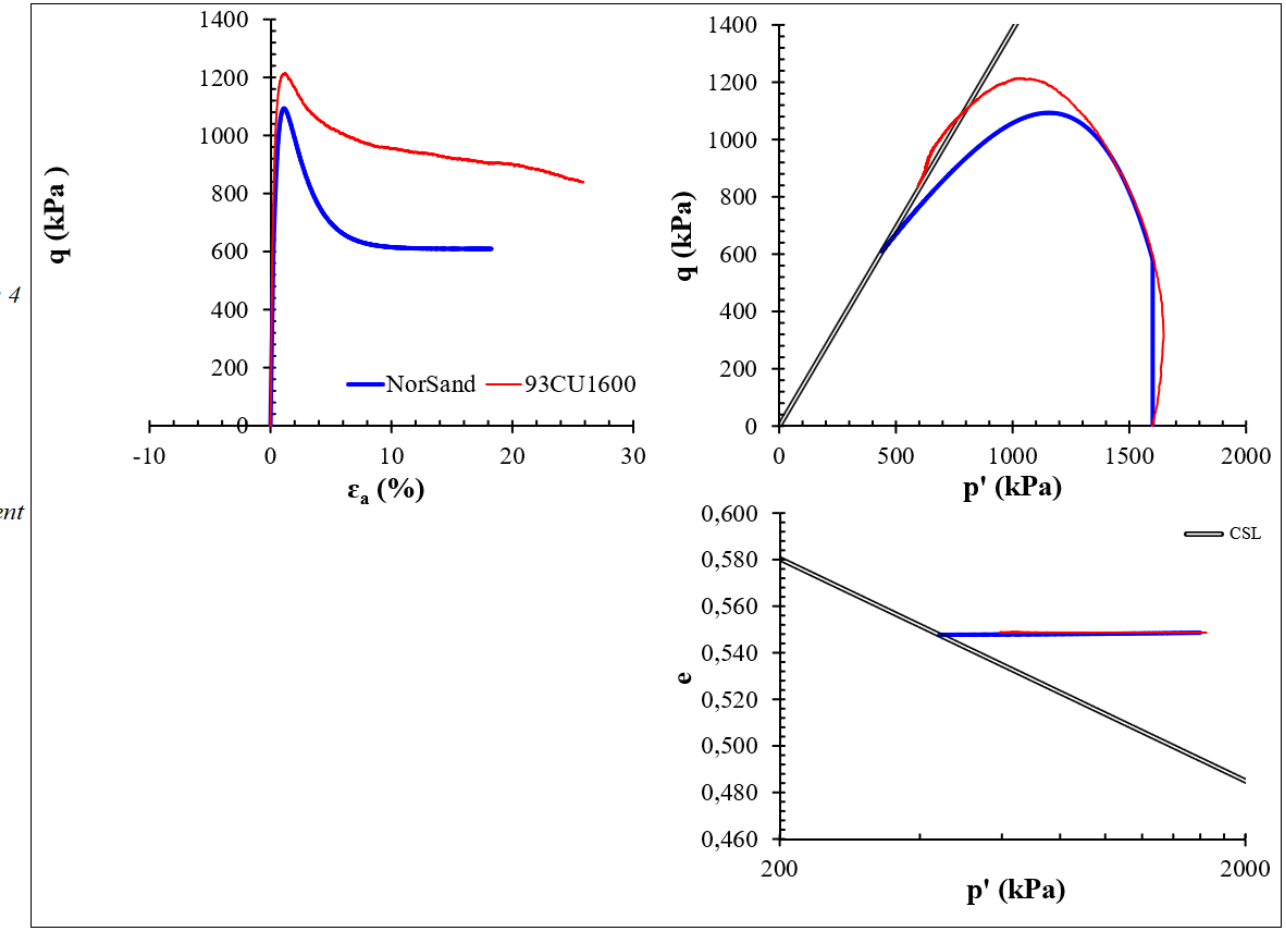

Source: elaborated by the author.

Figure F.12 – NorSand calibration into NorTXL.xls (Release 2) – Trx_93_CIU_1900kPa.

Soil properties….

CSL parameters

Γ = **0,8** ---

λ = **0,041** *on base e*

Plasticity

M_{tc} = **1,384**

N = **0,0058** *(typ 0.2 - 0.3)*

χ_{tc} = **8,16** *often taken as 4*

H_0 = **160** *> H_21*

H_ψ = **1037**

(H = H_0 - H_y.y...) *116,994* *(typ 60 - 400)*

Elasticity

G_{max} @ p_0 = **420** MPa

G_exp = **0,4** *elastic exponent*

ν = **0,20**

(Ir ...) *210,949* ---

k= *0,0054* ---

Initial soil state…

ψ_0 = **0,0415**

=> e_0 = *0,527*

p_0 = **1991** ***kPa***

K_0 = **1** ---

(sig1...) *1991*

OCR ("R") = **1,12** ---

Drained or undrained… Undrained

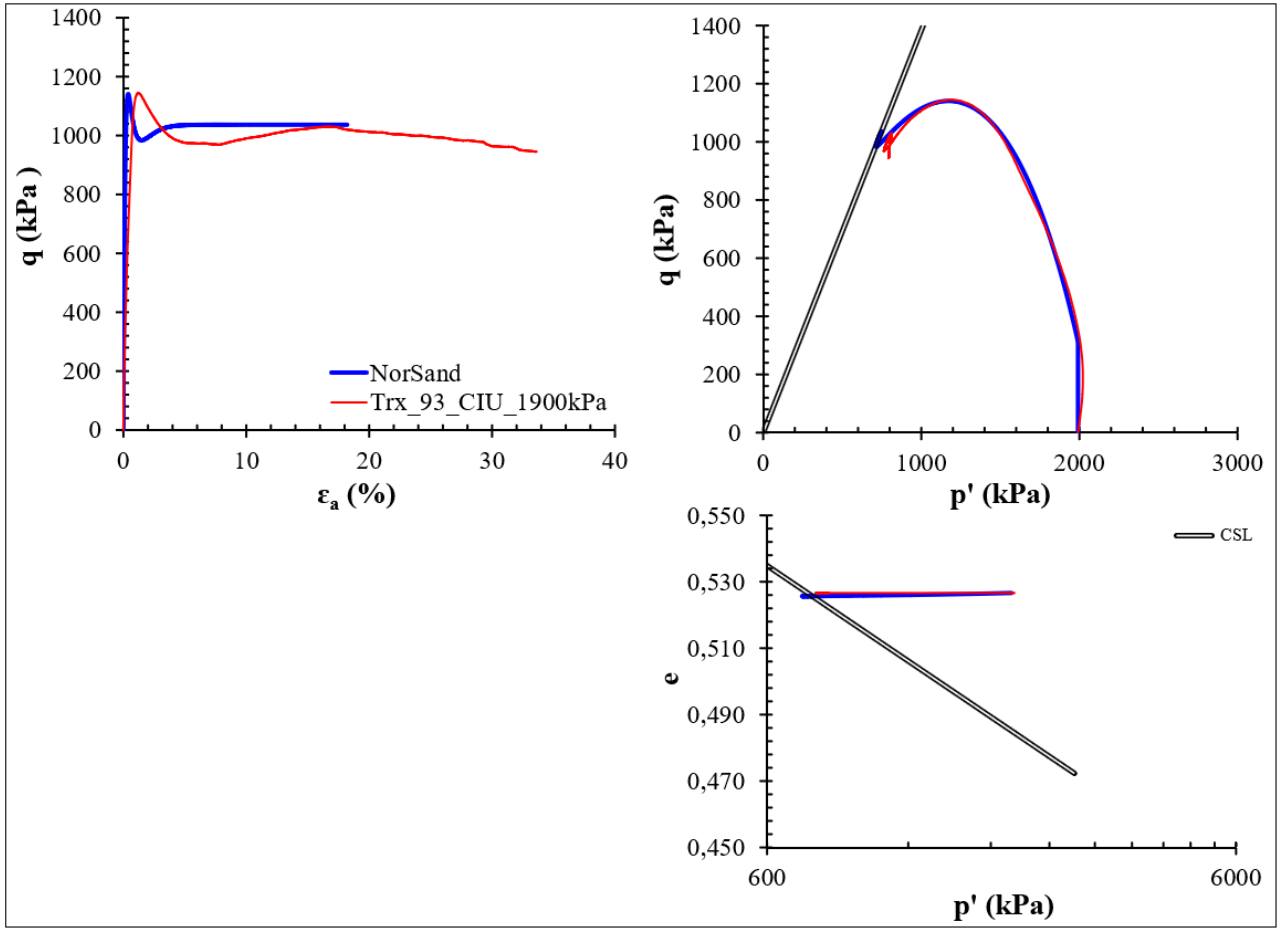

Source: elaborated by the author.

F.2 DC = 95%

Table F.2 – NorSand calibration into NorTXL.xls (Release 2) – DC = 95% – Summary.

	CID						CIU				
	100kPa	**200kPa**	**400kPa**	**800kPa**	**1600kPa**	**1900kPa**	**100kPa**	**200kPa**	**400kPa**	**800kPa**	**1600kPa**
CSL parameters											
Γ	0,8	0,8	0,8	0,8	0,8	0,8	0,8	0,8	0,8	0,8	0,8
λ	0,041	0,041	0,041	0,041	0,041	0,041	0,041	0,041	0,041	0,041	0,041
Plasticity											
M_{tc}	1,384	1,384	1,384	1,384	1,384	1,384	1,384	1,384	1,384	1,384	1,384
N	0,0058	0,0058	0,0058	0,0058	0,0058	0,0058	0,0058	0,0058	0,0058	0,0058	0,0058
χ_{tc}	8,16	8,16	8,16	8,16	8,16	8,16	8,16	8,16	8,16	8,16	8,16
H_0	160	160	160	160	160	160	160	160	160	160	160
H_ψ	1037	1037	1037	1037	1037	1037	1037	1037	1037	1037	1037
($H = H_0 - H_\psi.\psi$...)	184,6	139,2	139,5	116,4	113,5	108,8	178,1	184,0	149,8	138,3	129,8
Elasticity											
G_{max} @ p_0	18	35	40	75	80	95	10	20	26	85	300
G_exp	0,4	0,4	0,4	0,4	0,4	0,4	0,4	0,4	0,4	0,4	0,4
ν	0,2	0,2	0,2	0,2	0,2	0,2	0,2	0,2	0,2	0,2	0,2
(Ir...)	180,0	175,0	100,0	93,8	50,0	50,0	100,0	100,0	65,0	106,3	187,5
k	0,0	0,0	0,0	0,0	0,0	0,0	0,0	0,0	0,0	0,0	0,0
Initial soil state											
ψ_0	-0,024	0,020	0,020	0,042	0,045	0,049	-0,017	-0,023	0,010	0,021	0,029
e_0	0,59	0,60	0,57	0,56	0,54	0,54	0,59	0,56	0,56	0,54	0,52
p_0	100	200	400	800	1600	1900	100	200	400	800	1600
K_0	1,0	1,0	1,0	1,0	1,0	1,0	1,0	1,0	1,0	1,0	1,0
(σ_1...)	100	200	400	800	1600	1900	100	200	400	800	1600
OCR ("R")	1,60	1,55	1,50	1,40	1,30	1,25	1,60	1,55	2,25	1,20	1,22

Source: elaborated by the author.

Figure F.13 – NorSand calibration into NorTXL.xls (Release 2) – Trx_95_CID_100kPa.

Soil properties….

CSL parameters

Γ =	**0,8**	**---**
λ =	**0,041**	*on base e*

Plasticity

M_{tc} =	**1,384**	
N =	**0,0058**	*(typ 0.2 - 0.3)*
χ_{tc} =	**8,16**	*often taken as 4*
H_0 =	**160**	*> H 23*
H_ψ =	**1037**	
(H = H_0 - H_ψ...)	*184,551*	*(typ 60 - 400)*

Elasticity

G_{max} @ p_0=	**18**	MPa
G_exp =	**0,4**	*elastic exponent*
ν =	**0,20**	
(Ir ...)	*180*	**---**
k=	*0,0066*	**---**

Initial soil state…

ψ_0 =	**-0,0237**	
=> e_0 =	*0,585*	
p_0 =	**100**	***kPa***
K_0 =	**1**	**---**
(sig1...)	*100*	
OCR ("R") =	**1,6**	**---**

Drained or undrained… **Drained**

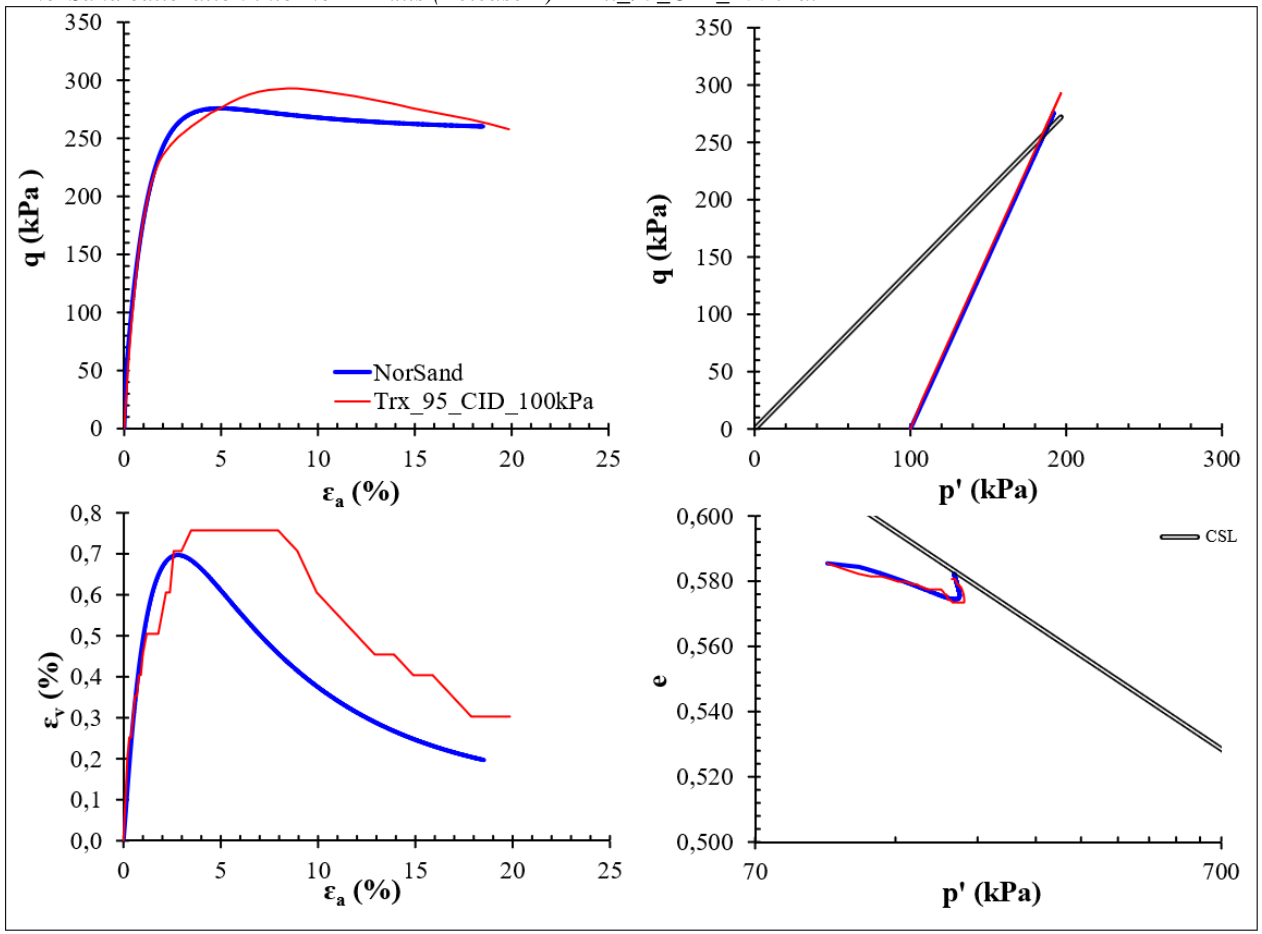

Source: elaborated by the author.

Figure F.14 – NorSand calibration into NorTXL.xls (Release 2) – Trx_95_CID_200kPa.

Soil properties….

CSL parameters

Γ =	**0,8**	---
λ =	**0,041**	*on base e*

Plasticity

M_{tc} =	**1,384**	
N =	**0,0058**	*(typ 0.2 - 0.3)*
χ_{tc} =	**8,16**	*often taken as 4*
H_0 =	**160**	*> H_23*
H_ψ =	**1037**	
(H = H_0 - H_ψψ...)	*139,189*	*(typ 60 - 400)*

Elasticity

G_{max} @ p_0=	**35**	MPa
G_exp =	**0,4**	*elastic exponent*
ν =	**0,20**	
(Ir ...)	*175*	---
k=	*0,0069*	---

Initial soil state…

ψ_0 =	**0,0201**	
=> e_0 =	*0,600*	
p_0 =	**200**	***kPa***
K_0 =	**1**	---
(sig1...)	*200*	
OCR ("R") =	**1,55**	---

Drained or undrained… **Drained**

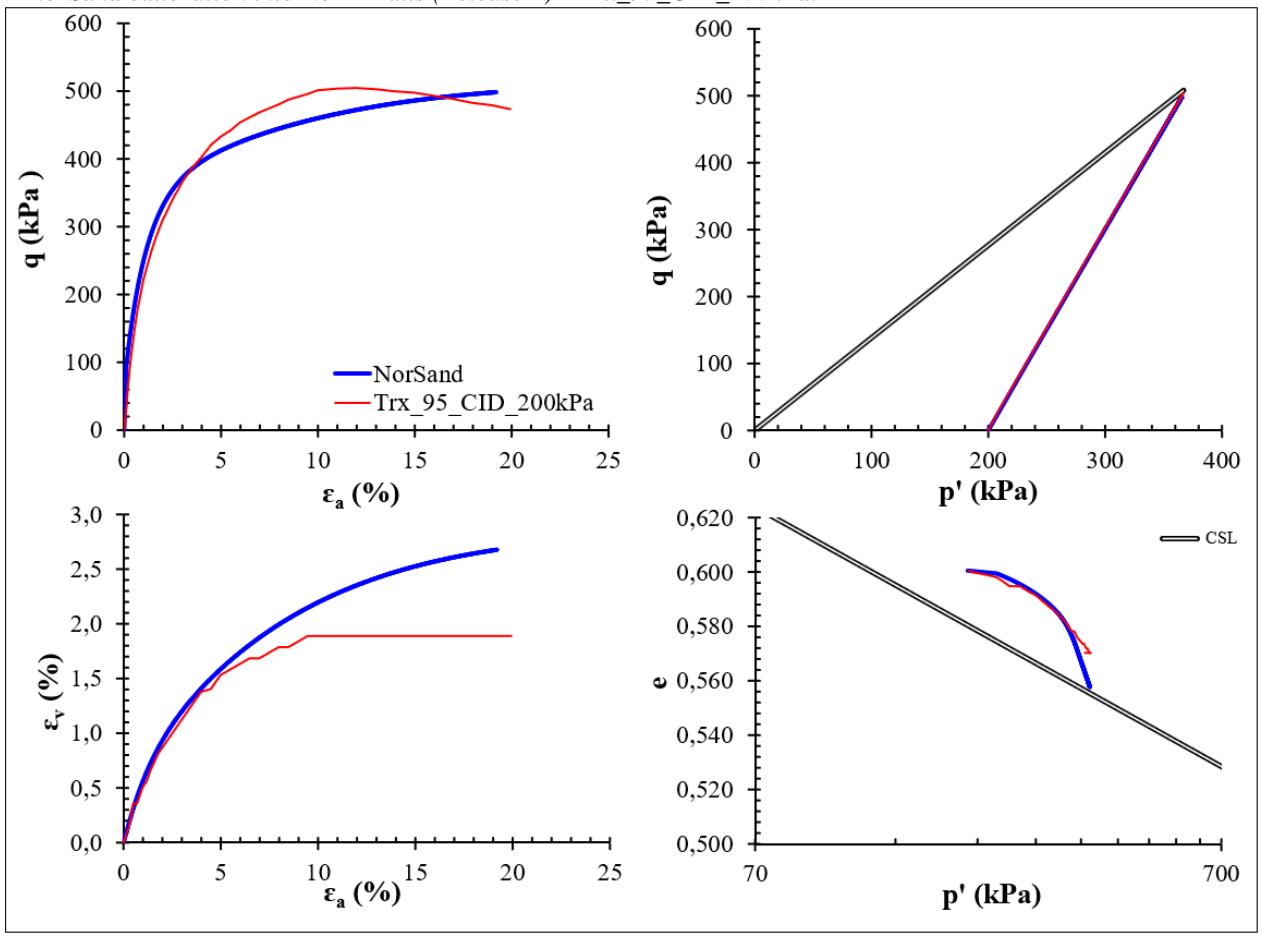

Source: elaborated by the author.

Figure F.15 – NorSand calibration into NorTXL.xls (Release 2) – Trx_95_CID_400kPa.

Soil properties….

CSL parameters

Γ =	**0,8**	---
λ =	**0,041**	*on base e*

Plasticity

M_{tc} =	**1,384**	
N =	**0,0058**	*(typ 0.2 - 0.3)*
χ_{tc} =	**8,16**	*often taken as 4*
H_0 =	**160**	*> H_26*
H_ψ =	**1037**	
(H = H_0 - H_{ψ} ψ...)	*139,522*	*(typ 60 - 400)*

Elasticity

G_{max} @ p_0=	**40**	MPa
G_exp =	**0,4**	*elastic exponent*
ν =	**0,20**	
(Ir ...)	*100*	---
k=	*0,0118*	---

Initial soil state…

ψ_0 =	**0,0197**	
=> e_0 =	*0,571*	
p_0 =	**400**	***kPa***
K_0 =	**1**	---
(sig1...)	*400*	
OCR ("R") =	**1,5**	---

Drained or undrained… **Drained**

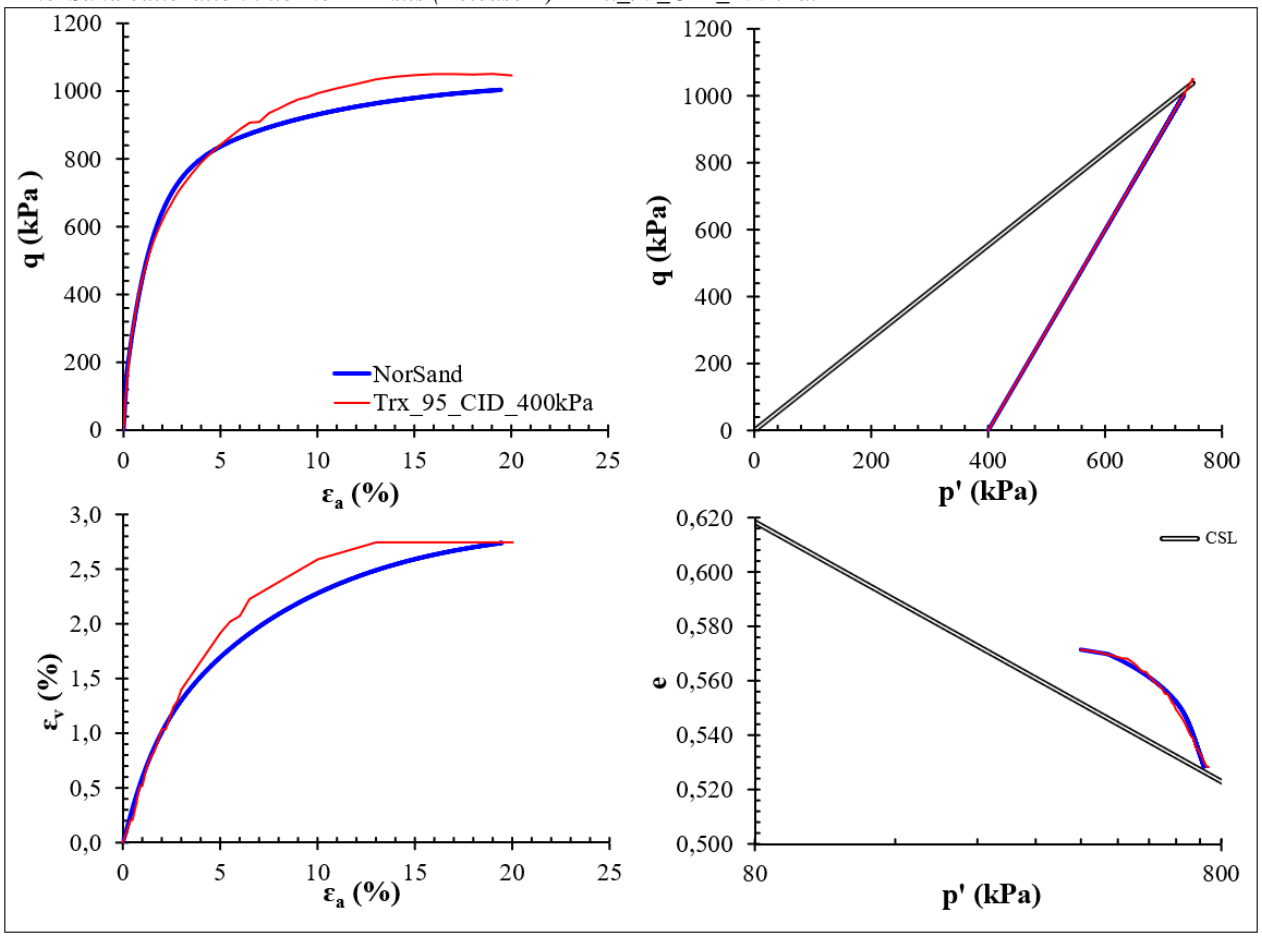

Source: elaborated by the author.

Figure F.16 – NorSand calibration into NorTXL.xls (Release 2) – Trx_95_CID_800kPa.

Soil properties….

CSL parameters

Γ =	**0,8**	**---**
λ =	**0,041**	*on base e*

Plasticity

M_{tc} =	**1,384**	
N =	**0,0058**	*(typ 0.2 - 0.3)*
χ_{tc} =	**8,16**	*often taken as 4*
H_0 =	**160**	*> H_27*
H_ψ =	**1037**	
(H = H_0 - H_{ψ} ψ...)	*116,424*	*(typ 60 - 400)*

Elasticity

G_{max} @ p_0=	**75**	MPa
G_exp =	**0,4**	*elastic exponent*
ν =	**0,20**	
(Ir ...)	*93,75*	**---**
k=	*0,0125*	**---**

Initial soil state…

ψ_0 =	**0,0420**	
=> e_0 =	*0,565*	
p_0 =	**800**	***kPa***
K_0 =	**1**	**---**
(sig1 ...)	*800*	
OCR ("R") =	**1,4**	**---**

Drained or undrained… **Drained**

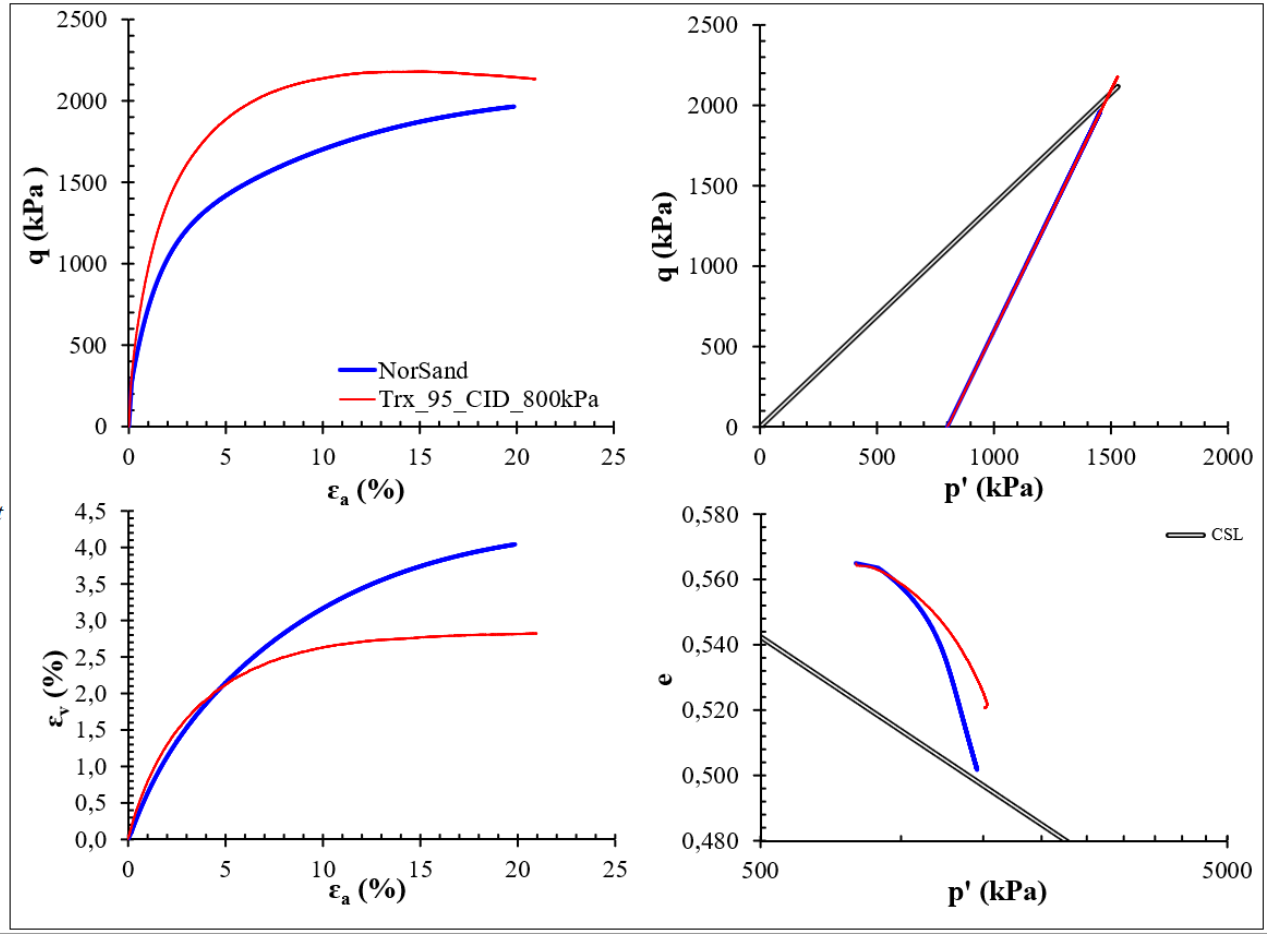

Source: elaborated by the author.

Figure F.17 – NorSand calibration into NorTXL.xls (Release 2) – Trx_95_CID_1600kPa.

Soil properties….

CSL parameters

Γ =	**0,8**	---
λ =	**0,041**	*on base e*

Plasticity

M_{tc} =	**1,384**	
N =	**0,0058**	*(typ 0.2 - 0.3)*
χ_{tc} =	**8,16**	*often taken as 4*
H_0 =	**160**	*> H_42*
H_ψ =	**1037**	
(H = H_0 - H_{ψ} ψ...)	*113,548*	*(typ 60 - 400)*

Elasticity

G_{max} @ p_0=	**80**	MPa
G_exp =	**0,4**	*elastic exponent*
ν =	**0,20**	
(Ir ...)	*50*	---
k=	*0,0231*	---

Initial soil state…

ψ_0 =	**0,0448**	
=> e_0 =	*0,539*	
p_0 =	**1600**	***kPa***
K_0 =	**1**	---
(sig1...)	*1600*	
OCR ("R") =	**1,3**	---

Drained or undrained… **Drained**

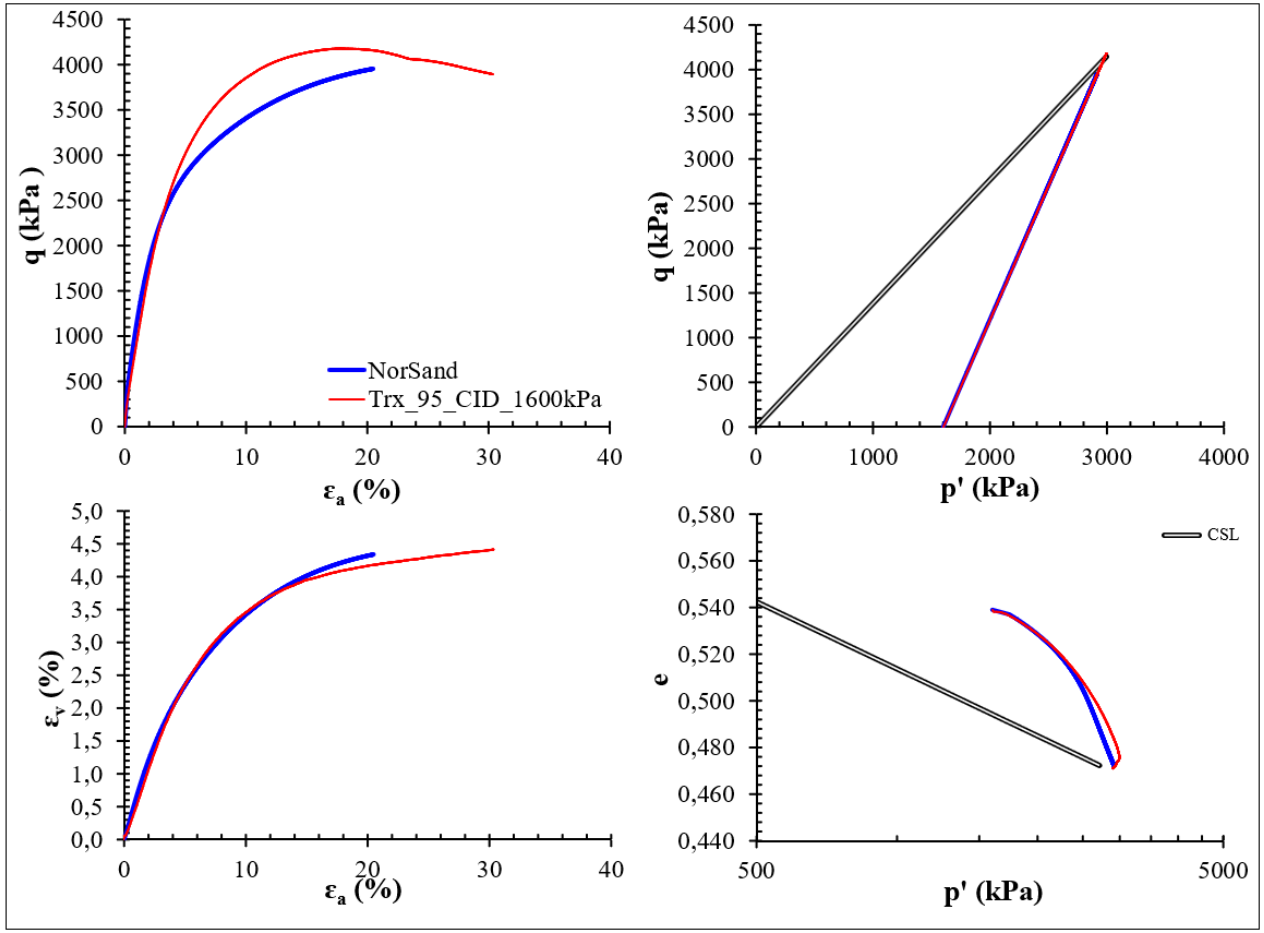

Source: elaborated by the author.

Figure F.18 – NorSand calibration into NorTXL.xls (Release 2) – Trx_95_CID_1900kPa.

Soil properties….

CSL parameters

Γ =	**0,8**	**---**
λ =	**0,041**	*on base e*

Plasticity

M_{tc} =	**1,384**	
N =	**0,0058**	*(typ 0.2 - 0.3)*
χ_{tc} =	**8,16**	*often taken as 4*
H_0 =	**160**	*> H_42*
H_ψ =	**1037**	
(H = H_0 - H_{ψ} ψ...)	*108,843*	*(typ 60 - 400)*

Elasticity

G_{max} @ p_0=	**95**	MPa
G_exp =	**0,4**	*elastic exponent*
ν =	**0,20**	
(Ir ...)	*50*	**---**
k=	*0,0230*	**---**

Initial soil state…

ψ_0 =	**0,0493**	
=> e_0 =	*0,536*	
p_0 =	**1900**	***kPa***
K_0 =	**1**	**---**
(sig1 ...)	*1900*	
OCR ("R") =	**1,25**	**---**

Drained or undrained… **Drained**

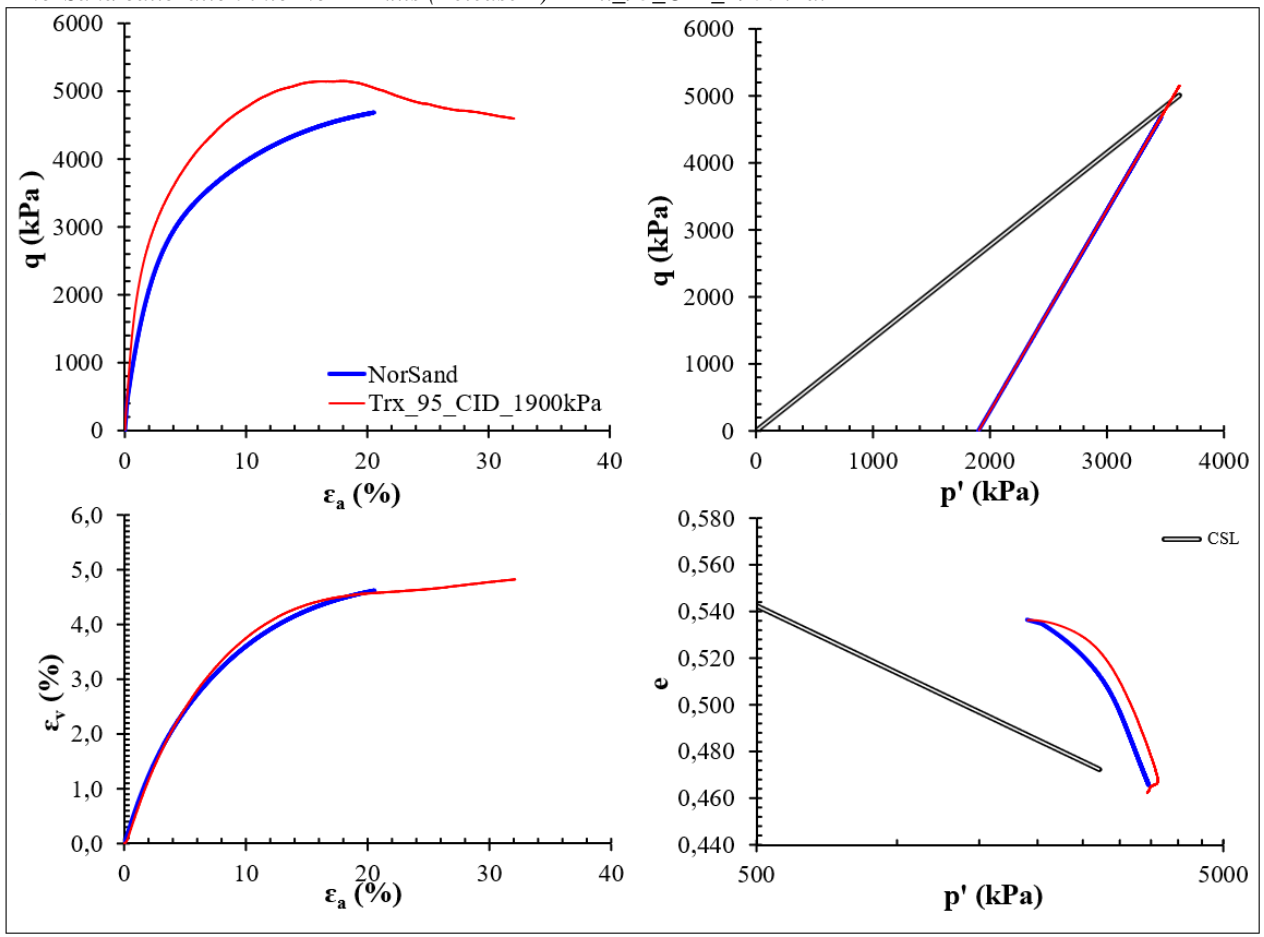

Source: elaborated by the author.

Figure F.19 – NorSand calibration into NorTXL.xls (Release 2) – Trx_95_CIU_100kPa.

Soil properties….

CSL parameters			
Γ =	**0,8**	---	
λ =	**0,041**	*on base e*	
Plasticity			
M_{tc} =	**1,384**		
N =	**0,0058**	*(typ 0.2 - 0.3)*	
χ_{tc} =	**8,16**	*often taken as 4*	
H_0 =	**160**	*> H_27*	
H_ψ =	**1037**		
(H = H_0 - H_{ψ} ψ...)	*178,06*	*(typ 60 - 400)*	
Elasticity			
G_{max} @ p_0=	**10**	MPa	
G_exp =	**0,4**	*elastic exponent*	
ν =	**0,20**		
(Ir ...)	*100*	---	
k=	*0,0119*	---	

Initial soil state…

ψ_0 =	**-0,0174**	
=> ***e*** $_0$ =	*0,592*	
p_0 =	**100**	***kPa***
K_0 =	**1**	---
(sig1 ...)	*100*	
OCR ("R") =	**1,6**	---

Drained or undrained… <u>Undrained</u>

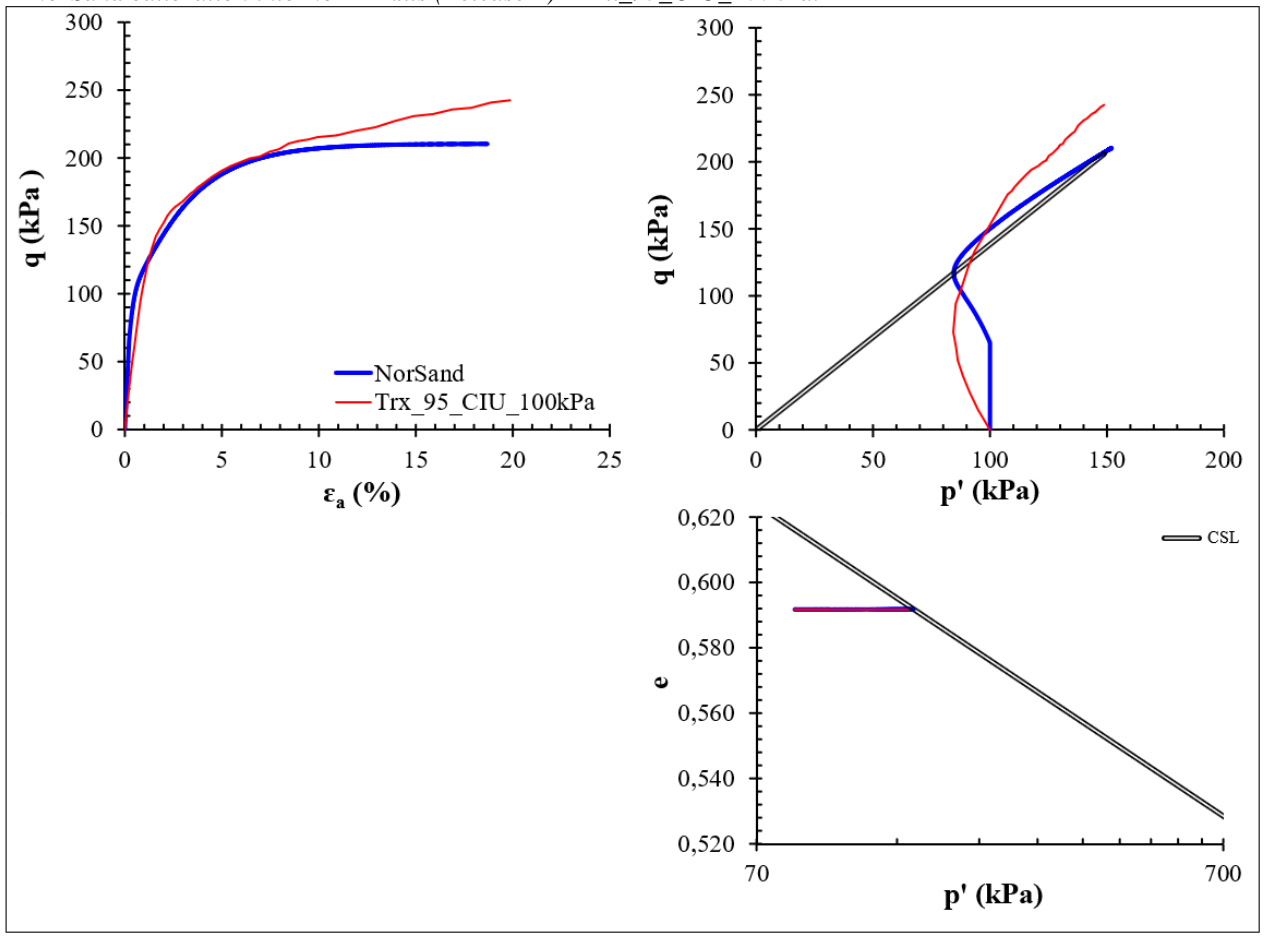

Source: elaborated by the author.

Figure F.20 – NorSand calibration into NorTXL.xls (Release 2) – Trx_95_CIU_200kPa.

Soil properties….

CSL parameters

Γ = **0,8** ---

λ = **0,041** *on base e*

Plasticity

M_{tc} = **1,384**

N = **0,0058** *(typ 0.2 - 0.3)*

χ_{tc} = **8,16** *often taken as 4*

H_0 = **160** *> H 26*

H_ψ = **1037**

(H = H_0 - H_ψ ψ...) *184,047* *(typ 60 - 400)*

Elasticity

G_{max} @ p_0 = **20** MPa

G_exp = **0,4** *elastic exponent*

ν = **0,20**

(Ir ...) *100* ---

k= *0,0117* ---

Initial soil state…

ψ_0 = **-0,0232**

=> e_0 = *0,557*

p_0 = **200** ***kPa***

K_0 = **1** ---

(sig1...) *200*

OCR ("R") = **1,55** ---

Drained or undrained… **Undrained**

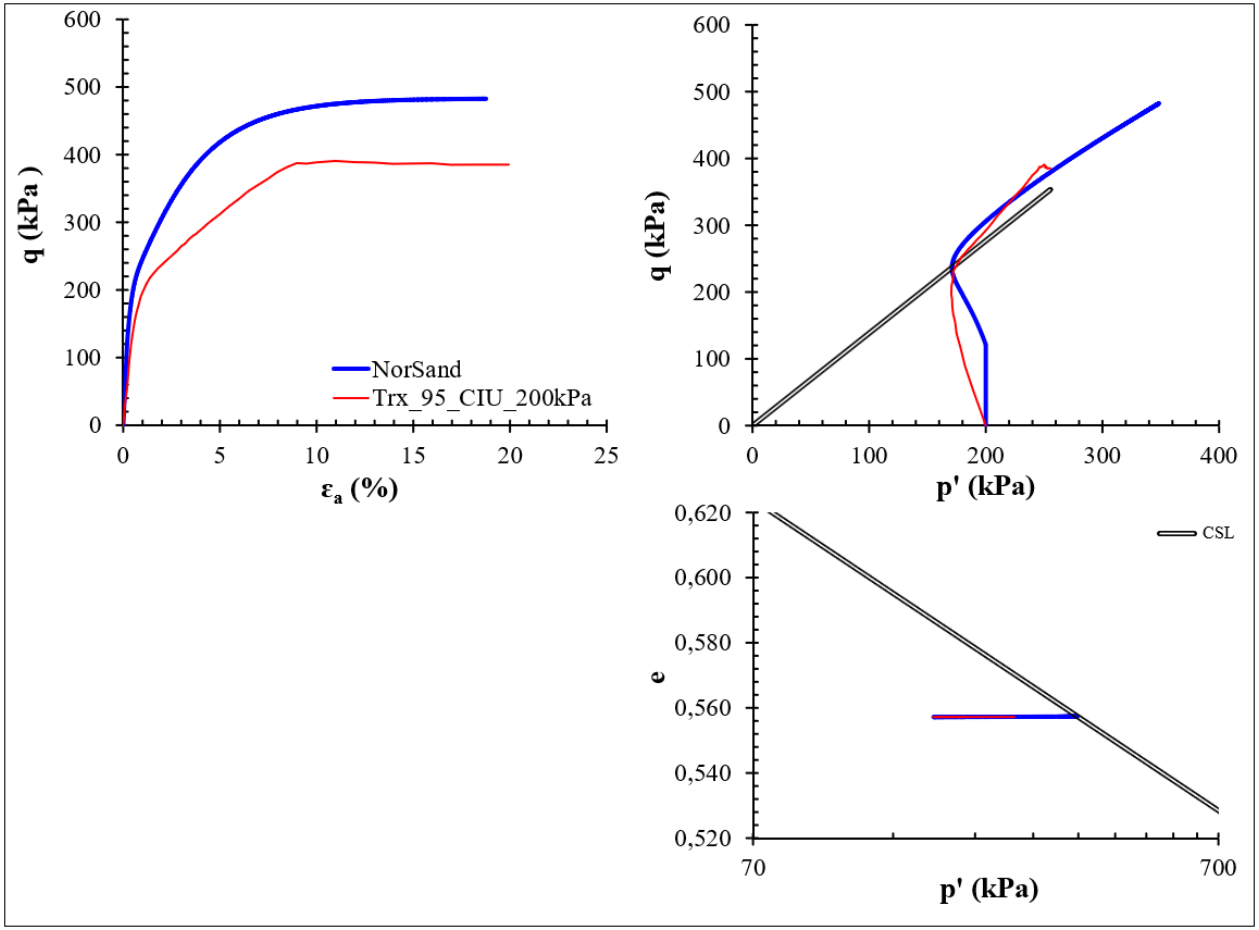

Source: elaborated by the author.

Figure F.21 – NorSand calibration into NorTXL.xls (Release 2) – Trx_95_CIU_400kPa.

Soil properties….

CSL parameters

Γ = **0,8** ---

λ = **0,041** *on base e*

Plasticity

M_{tc} = **1,384**

N = **0,0058** *(typ 0.2 - 0.3)*

χ_{tc} = **8,16** *often taken as 4*

H_0 = **160** *> H 33*

H_ψ = **1037**

(H = H_0 - H_{ψ} ψ...) *149,799* *(typ 60 - 400)*

Elasticity

G_{max} @ p_0 = **26** MPa

G_exp = **0,4** *elastic exponent*

ν = **0,20**

(Ir ...) *65* ---

k= *0,0180* ---

Initial soil state…

ψ_0 = **0,0098**

=> e_0 = *0,562*

p_0 = **400** ***kPa***

K_0 = **1** ---

(sig1...) *400*

OCR ("R") = **2,25** ---

Drained or undrained… **Undrained**

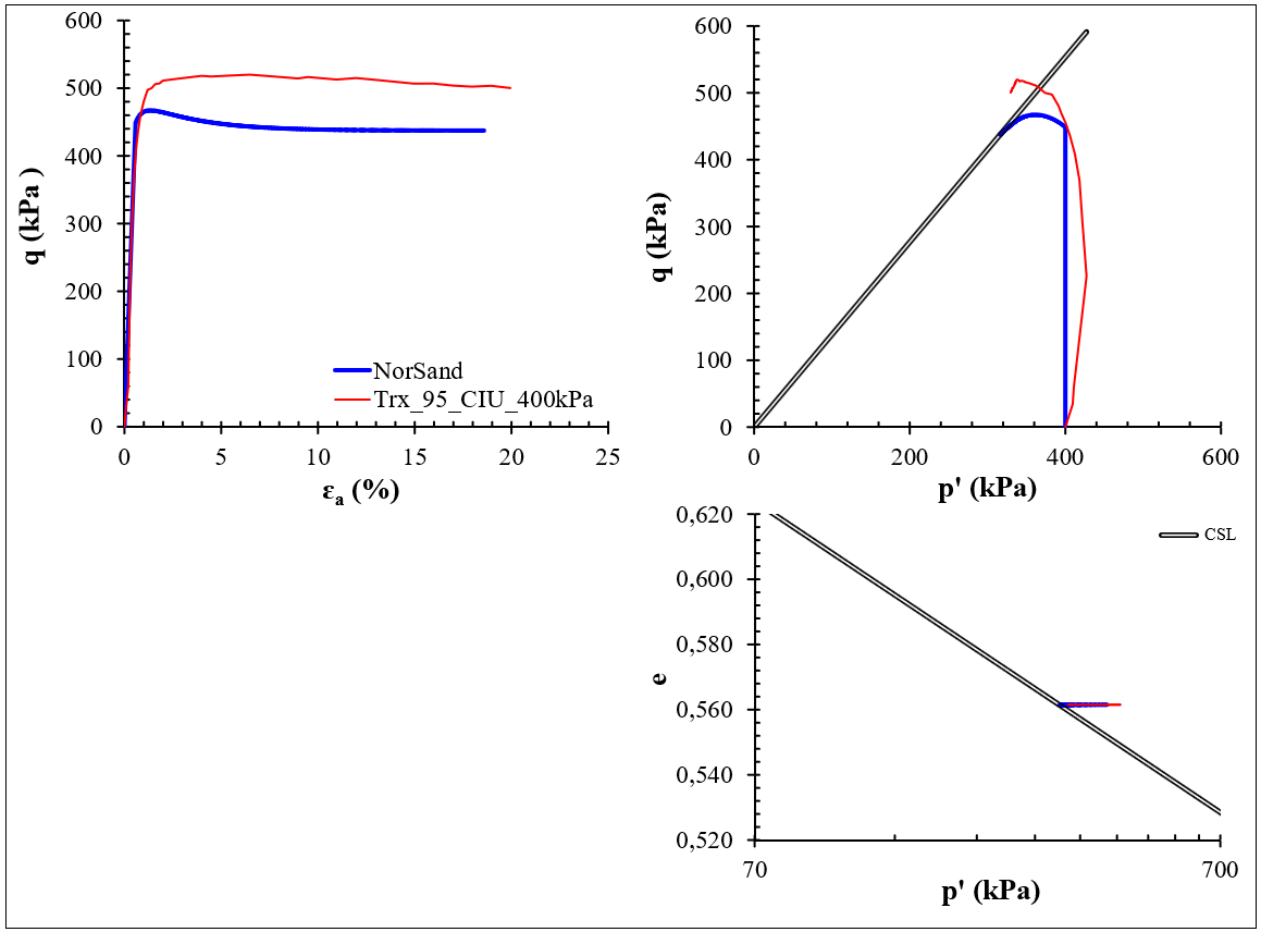

Source: elaborated by the author.

Figure F.22 – NorSand calibration into NorTXL.xls (Release 2) – Trx_95_CIU_800kPa.

Soil properties….

CSL parameters

Γ =	**0,8**	---
λ =	**0,041**	*on base e*

Plasticity

M_{tc} =	**1,384**	
N =	**0,0058**	*(typ 0.2 - 0.3)*
χ_{tc} =	**8,16**	*often taken as 4*
H_0 =	**160**	*> H_25*
H_ψ =	**1037**	
(H = H_0 - H_ψ ψ...)	*138,305*	*(typ 60 - 400)*

Elasticity

G_{max} @ p_0=	**85**	MPa
G_exp =	**0,4**	*elastic exponent*
ν =	**0,20**	
(Ir ...)	*106,25*	---
k=	*0,0109*	---

Initial soil state…

ψ_0 =	**0,0209**	
=> e_0 =	*0,544*	
p_0 =	**800**	***kPa***
K_0 =	**1**	---
(sig1...)	*800*	
OCR ("R") =	**1,2**	---

Drained or undrained… **Undrained**

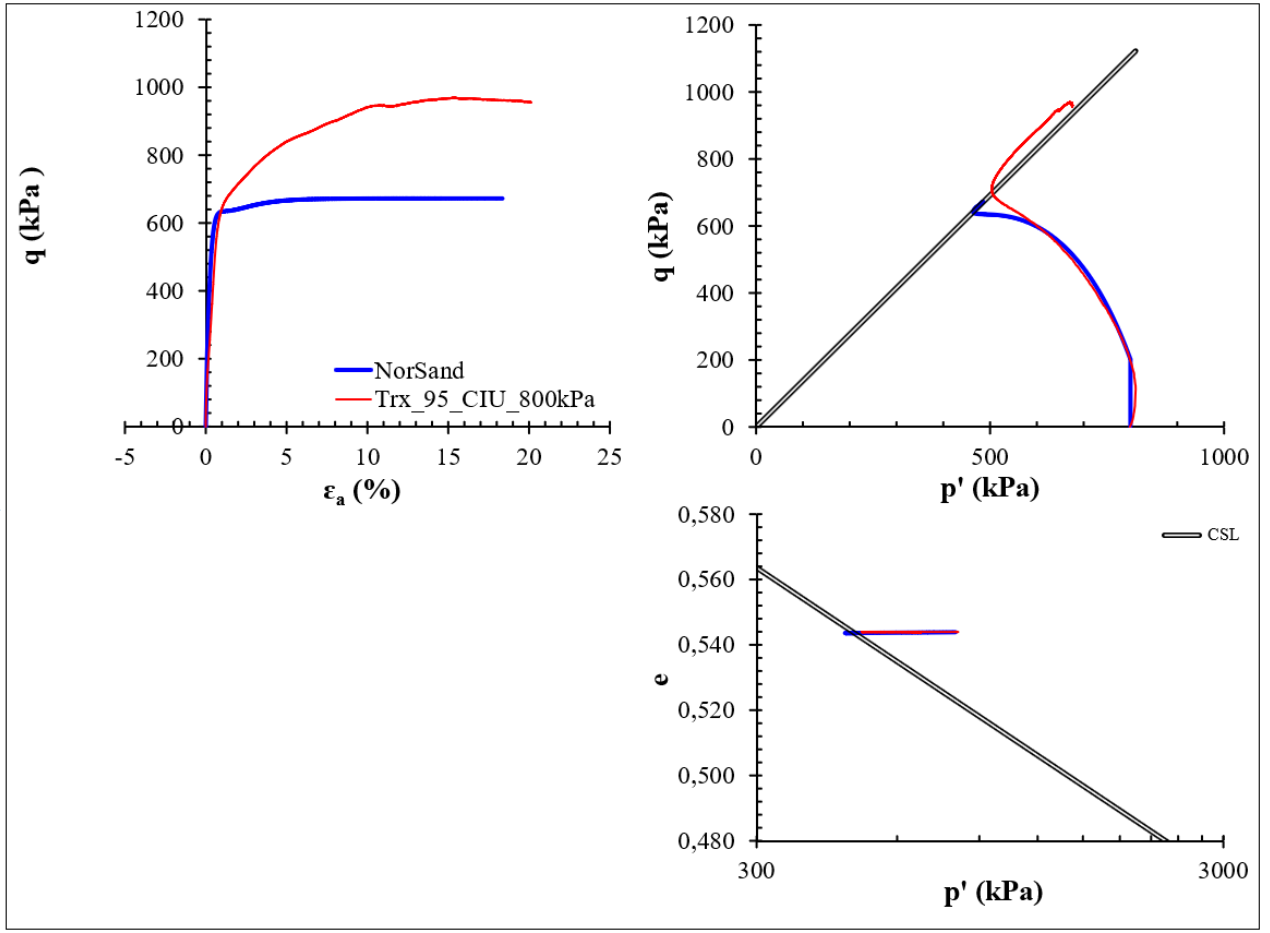

Source: elaborated by the author.

Figure F.23 – NorSand calibration into NorTXL.xls (Release 2) – Trx_95_CIU_1600kPa.

Soil properties….

CSL parameters

Γ =	**0,8**	---
λ =	**0,041**	*on base e*

Plasticity

M_{tc} =	**1,384**	
N =	**0,0058**	*(typ 0.2 - 0.3)*
χ_{tc} =	**8,16**	*often taken as 4*
H_0 =	**160**	*> H_22*
H_ψ =	**1037**	
(H = H_0 - H_ψ ψ...)	*129,798*	*(typ 60 - 400)*

Elasticity

G_{max} @ p_0=	**300**	MPa
G_exp =	**0,4**	*elastic exponent*
ν =	**0,20**	
(Ir ...)	*187,5*	---
k=	*0,0061*	---

Initial soil state…

ψ_0 =	**0,0291**	
=> e_0 =	*0,523*	
p_0 =	**1600**	***kPa***
K_0 =	**1**	---
(sig1...)	*1600*	
OCR ("R") =	**1,22**	---

Drained or undrained… **Undrained**

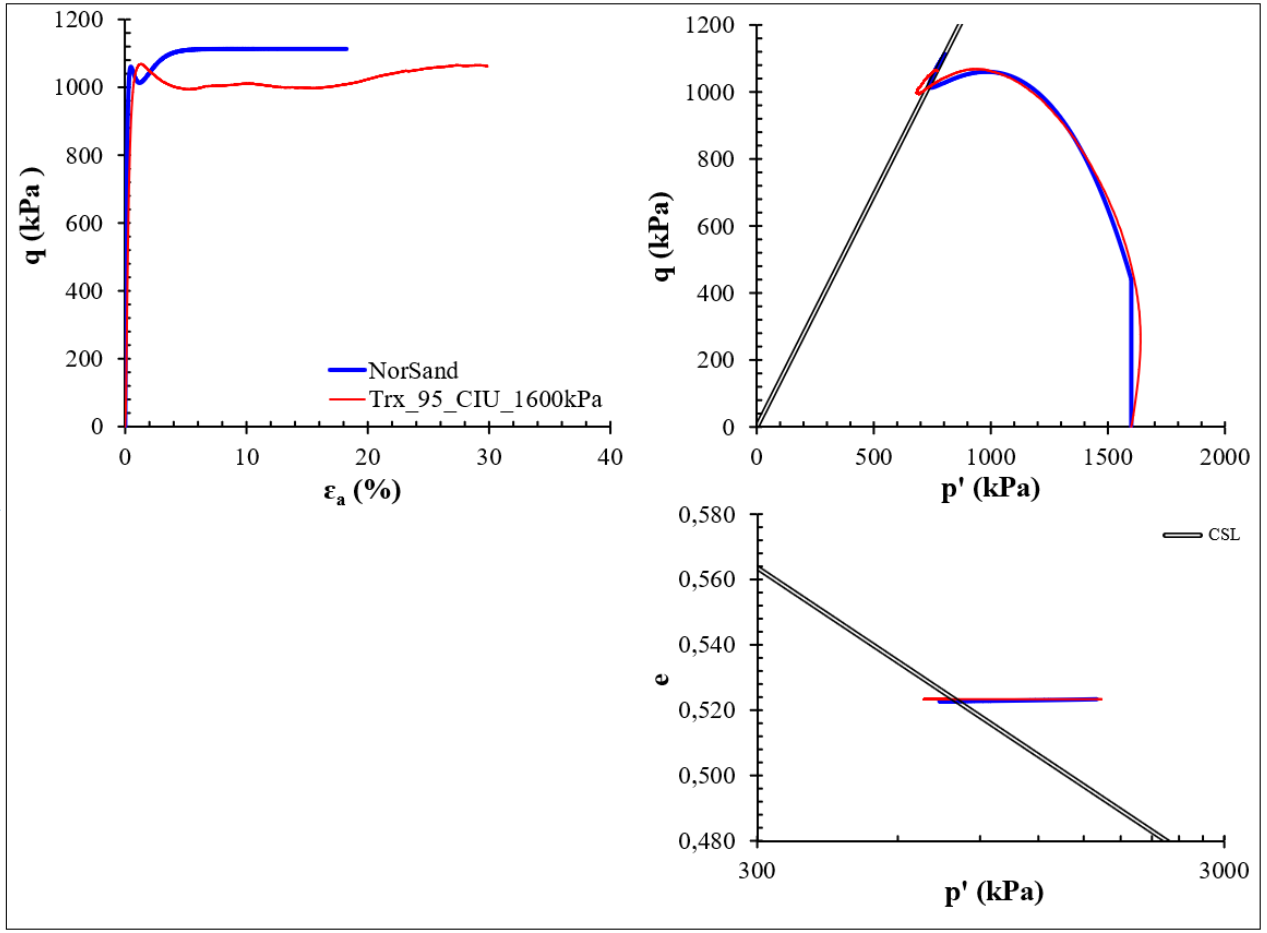

Source: elaborated by the author.

F.3 DC = 97%

Table F.3 – NorSand calibration into NorTXL.xls (Release 2) – DC = 97% – Summary.

	CID						CIU				
	100kPa	**200kPa**	**400kPa**	**800kPa**	**1600kPa**	**1900kPa**	**100kPa**	**200kPa**	**400kPa**	**800kPa**	**1600kPa**
CSL parameters											
Γ	0,8	0,8	0,8	0,8	0,8	0,8	0,8	0,8	0,8	0,8	0,8
λ	0,041	0,041	0,041	0,041	0,041	0,041	0,041	0,041	0,041	0,041	0,041
Plasticity											
M_{tc}	1,384	1,384	1,384	1,384	1,384	1,384	1,384	1,384	1,384	1,384	1,384
N	0,0058	0,0058	0,0058	0,0058	0,0058	0,0058	0,0058	0,0058	0,0058	0,0058	0,0058
χ_{tc}	8,16	8,16	8,16	8,16	8,16	8,16	8,16	8,16	8,16	8,16	8,16
H_0	160	160	160	160	160	160	160	160	160	160	160
H_ψ	1037	1037	1037	1037	1037	1037	1037	1037	1037	1037	1037
($H = H_0 - H_\psi.\psi$...)	206,4	183,0	159,8	155,9	140,8	142,3	205,0	186,5	173,3	160,6	137,6
Elasticity											
G_{max} @ p_0	35	45	60	80	55	120	35	15	20	40	150
G_exp	0,4	0,4	0,4	0,4	0,4	0,4	0,4	0,4	0,4	0,4	0,4
ν	0,2	0,2	0,2	0,2	0,2	0,2	0,2	0,2	0,2	0,2	0,2
(Ir...)	350,0	225,0	150,0	100,0	34,4	63,2	350,0	75,0	50,0	50,0	93,7
k	0,0	0,0	0,0	0,0	0,0	0,0	0,0	0,0	0,0	0,0	0,0
Initial soil state											
ψ_0	-0,045	-0,022	0,000	0,004	0,019	0,017	-0,043	-0,026	-0,013	-0,001	0,022
e_0	0,56	0,56	0,55	0,53	0,51	0,50	0,57	0,55	0,54	0,52	0,52
p_0	100	200	400	800	1600	1900	100	200	400	800	1600
K_0	1,0	1,0	1,0	1,0	1,0	1,0	1,0	1,0	1,0	1,0	1,0
(σ_1...)	100	200	400	800	1600	1900	100	200	400	800	1600
OCR ("R")	2,00	1,80	1,60	1,60	1,40	1,10	2,50	1,00	1,00	1,25	1,17

Source: elaborated by the author.

Figure F.24 – NorSand calibration into NorTXL.xls (Release 2) – Trx_97_CID_100kPa.

Soil properties….

CSL parameters

Γ =	**0,8**	---
λ =	**0,041**	*on base e*

Plasticity

M_{tc} =	**1,384**	
N =	**0,0058**	*(typ 0.2 - 0.3)*
χ_{tc} =	**8,16**	*often taken as 4*
H_0 =	**160**	*> H,21*
H_ψ =	**1037**	
(H = H_0 - $H_{\psi,\psi}$...)	*206,429*	*(typ 60 - 400)*

Elasticity

G_{max} @ p_0=	**30**	MPa
G_exp =	**0,4**	*elastic exponent*
ν =	**0,20**	
(Ir ...)	*300*	---
k=	*0,0039*	---

Initial soil state…

ψ_0 =	**-0,0448**	
=> e_0 =	*0,564*	
p_0 =	**100**	***kPa***
K_0 =	**1**	---
(sig1...)	*100*	
OCR ("R") =	**2**	---

Drained or undrained… **Drained**

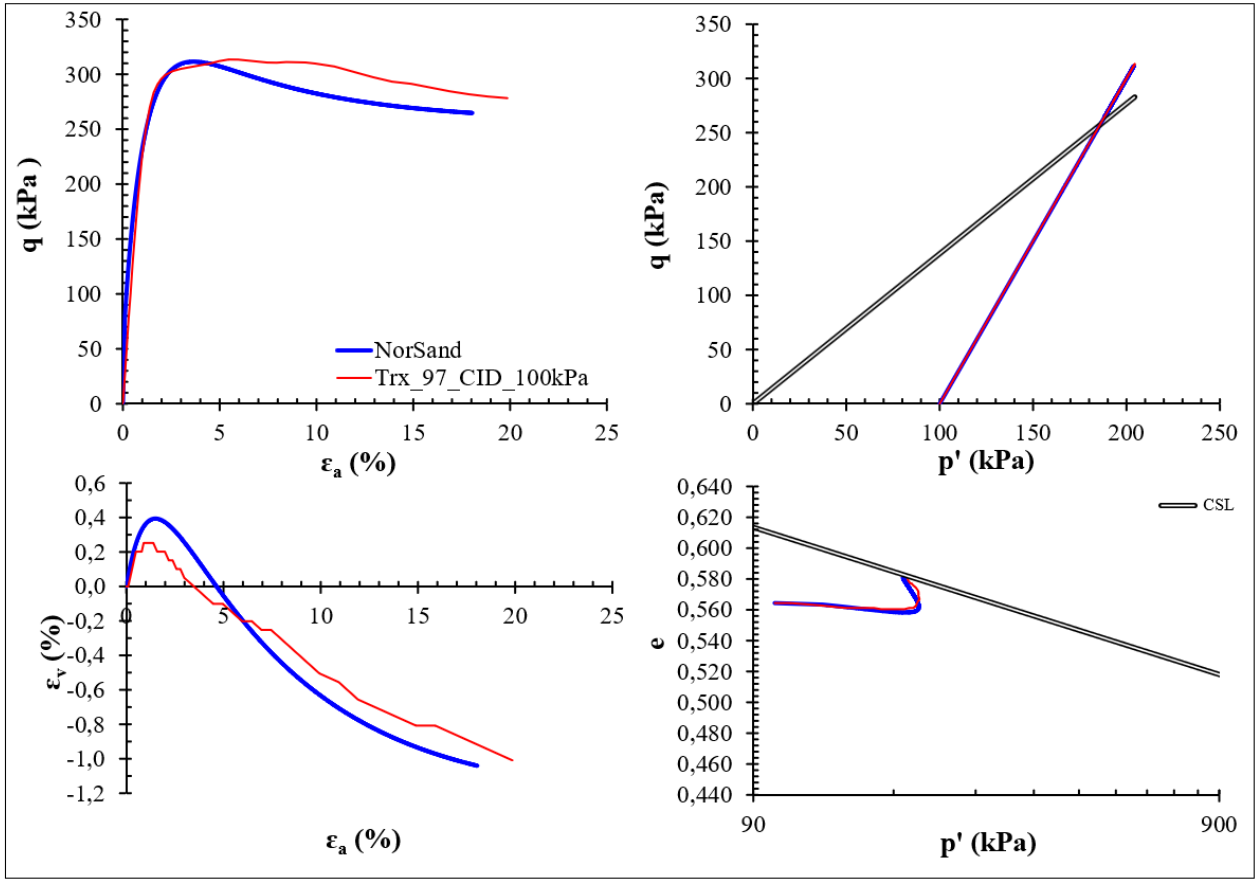

Source: elaborated by the author.

Figure F.25 – NorSand calibration into NorTXL.xls (Release 2) – Trx_97_CID_200kPa.

Soil properties….

CSL parameters

Γ =	**0,8**	---
λ =	**0,041**	*on base e*

Plasticity

M_{tc} =	**1,384**	
N =	**0,0058**	*(typ 0.2 - 0.3)*
χ_{tc} =	**8,16**	*often taken as 4*
H_0 =	**160**	*> H 21*
H_ψ =	**1037**	
(H = H_0 - H_ψ ψ...)	*183,014*	*(typ 60 - 400)*

Elasticity

G_{max} @ p_0=	**45**	MPa
G_exp =	**0,4**	*elastic exponent*
ν =	**0,20**	
(Ir ...)	*225*	---
k=	*0,0052*	---

Initial soil state…

ψ_0 =	**-0,0222**	
=> e_0 =	*0,558*	
p_0 =	**200**	***kPa***
K_0 =	**1**	---
(sig1...)	*200*	
OCR ("R") =	**1,8**	---

Drained or undrained… **Drained**

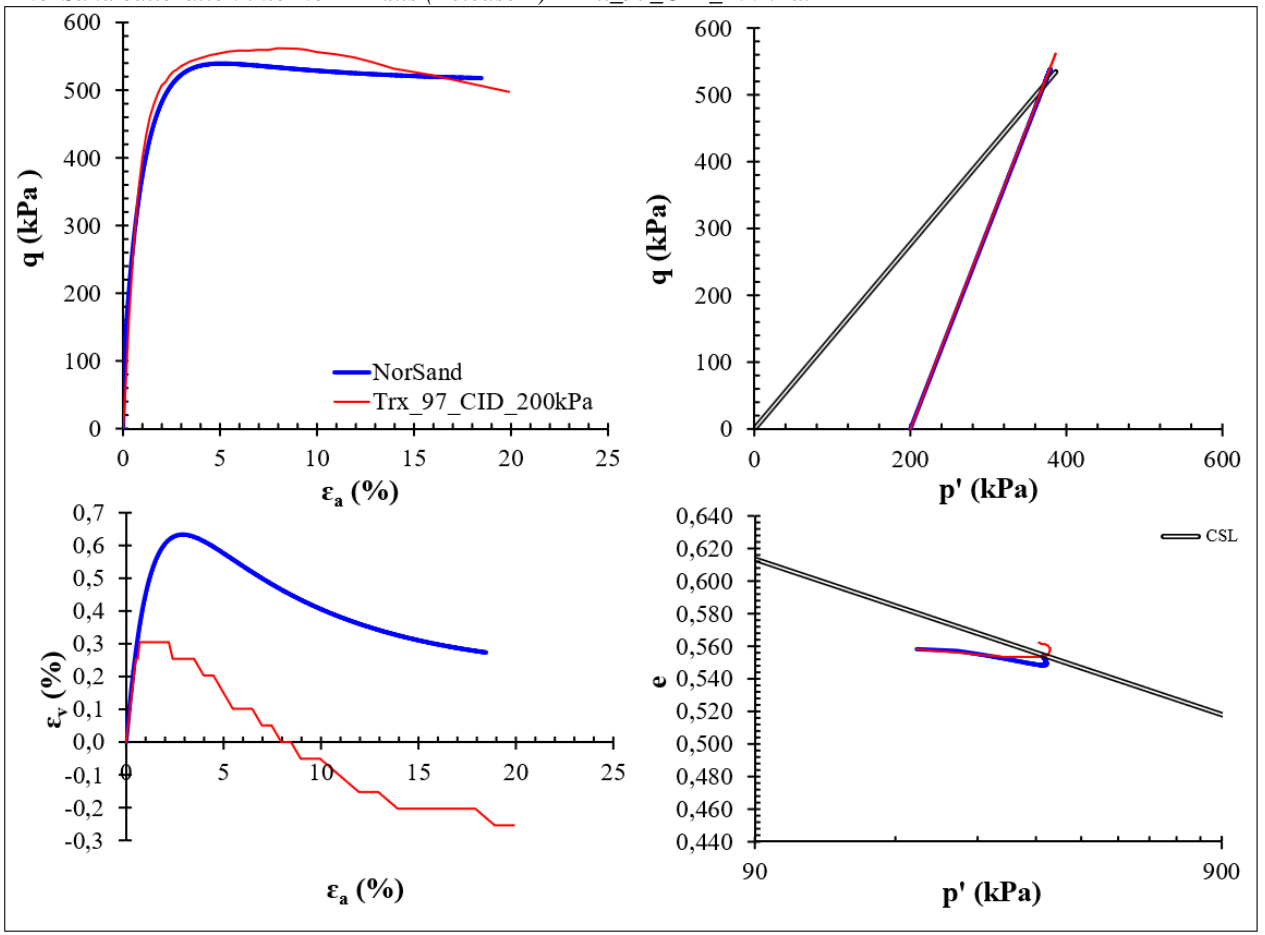

Source: elaborated by the author.

Figure F.26 – NorSand calibration into NorTXL.xls (Release 2) – Trx_97_CID_400kPa.

Soil properties….

CSL parameters

Γ =	**0,8**	---
λ =	**0,041**	*on base e*

Plasticity

M_{tc} =	**1,384**	
N =	**0,0058**	*(typ 0.2 - 0.3)*
χ_{tc} =	**8,16**	*often taken as 4*
H_0 =	**160**	*> H 23*
H_ψ =	**1037**	
($H = H_0 - H_{\psi} \psi$...)	*159,784*	*(typ 60 - 400)*

Elasticity

G_{max} @ p_0=	**60**	MPa
G_exp =	**0,4**	*elastic exponent*
ν =	**0,20**	
(Ir ...)	*150*	---
k=	*0,0078*	---

Initial soil state…

ψ_0 =	**0,0002**	
=> e_0 =	*0,552*	
p_0 =	**400**	***kPa***
K_0 =	**1**	---
(sig1...)	*400*	
OCR ("R") =	**1,6**	---

Drained or undrained… **Drained**

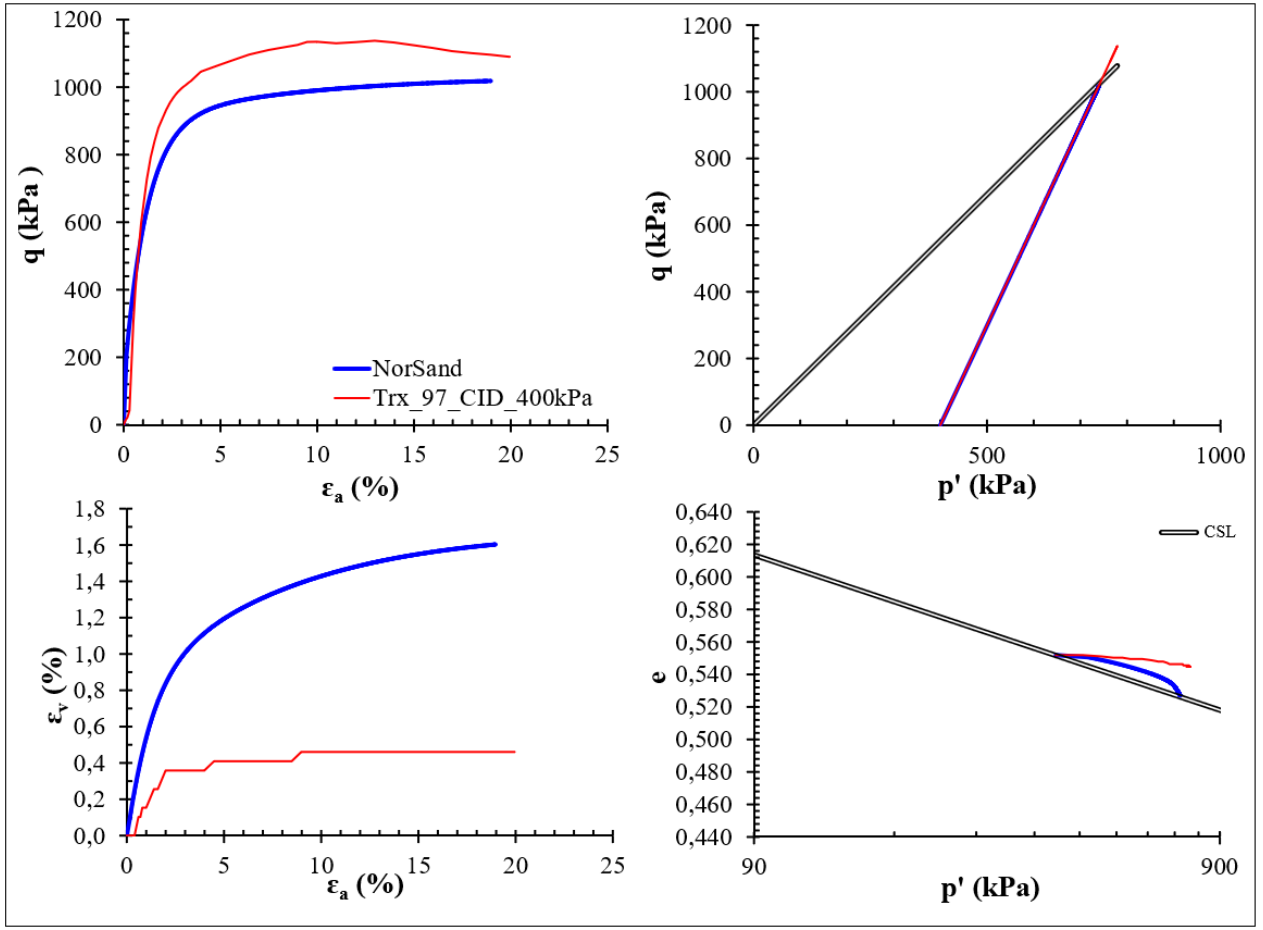

Source: elaborated by the author.

Figure F.27 – NorSand calibration into NorTXL.xls (Release 2) – Trx_97_CID_800kPa.

Soil properties….

CSL parameters

Γ =	**0,8**	---
λ =	**0,041**	*on base e*

Plasticity

M_{tc} =	**1,384**	
N =	**0,0058**	*(typ 0.2 - 0.3)*
χ_{tc} =	**8,16**	*often taken as 4*
H_0 =	**160**	*> H_25*
H_ψ =	**1037**	
(H = H_0 - H_ψ ψ...)	*155,933*	*(typ 60 - 400)*

Elasticity

G_{max} @ p_0=	**80**	MPa
G_exp =	**0,4**	*elastic exponent*
ν =	**0,20**	
(Ir ...)	*100*	---
k=	*0,0115*	---

Initial soil state…

ψ_0 =	**0,0039**	
=> e_0 =	*0,527*	
p_0 =	**800**	***kPa***
K_0 =	**1**	---
(sig1...)	*800*	
OCR ("R") =	**1,6**	---

Drained or undrained… **Drained**

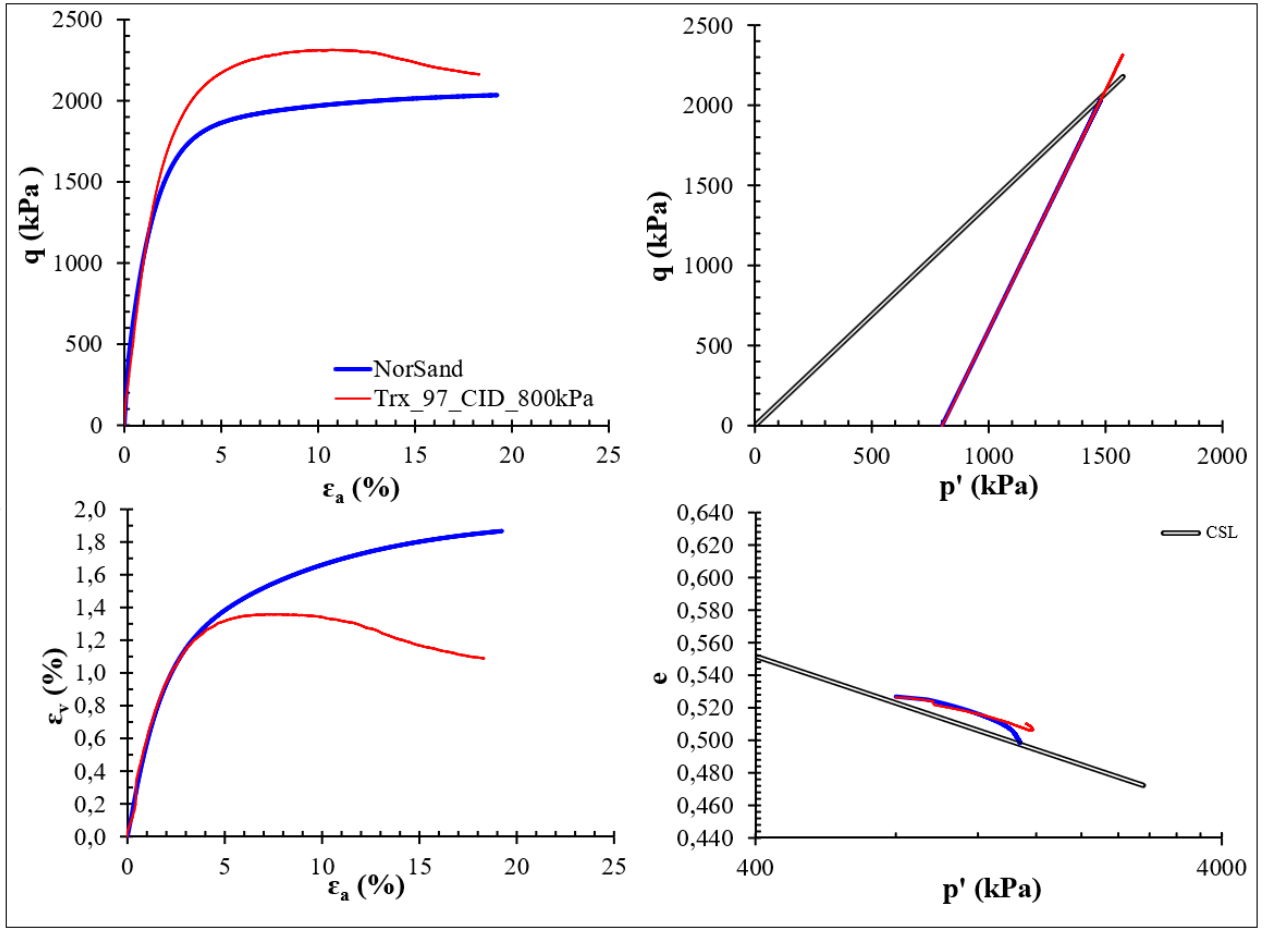

Source: elaborated by the author.

Figure F.28 – NorSand calibration into NorTXL.xls (Release 2) – Trx_97_CID_1600kPa.

Soil properties….

CSL parameters

Γ =	**0,8**	---
λ =	**0,041**	*on base e*

Plasticity

M_{tc} =	**1,384**	
N =	**0,0058**	*(typ 0.2 - 0.3)*
χ_{tc} =	**8,16**	*often taken as 4*
H_0 =	**160**	*> H_90*
H_ψ =	**1037**	
(H = H_0 - H_ψ ψ...)	*140,804*	*(typ 60 - 400)*

Elasticity

G_{max} @ p_0=	**55**	MPa
G_exp =	**0,4**	*elastic exponent*
ν =	**0,20**	
(Ir ...)	*34,375*	---
k=	*0,0330*	---

Initial soil state…

ψ_0 =	**0,0185**	
=> e_0 =	*0,513*	
p_0 =	**1600**	***kPa***
K_0 =	**1**	---
(sig1...)	*1600*	
OCR ("R") =	**1,4**	---

Drained or undrained… **Drained**

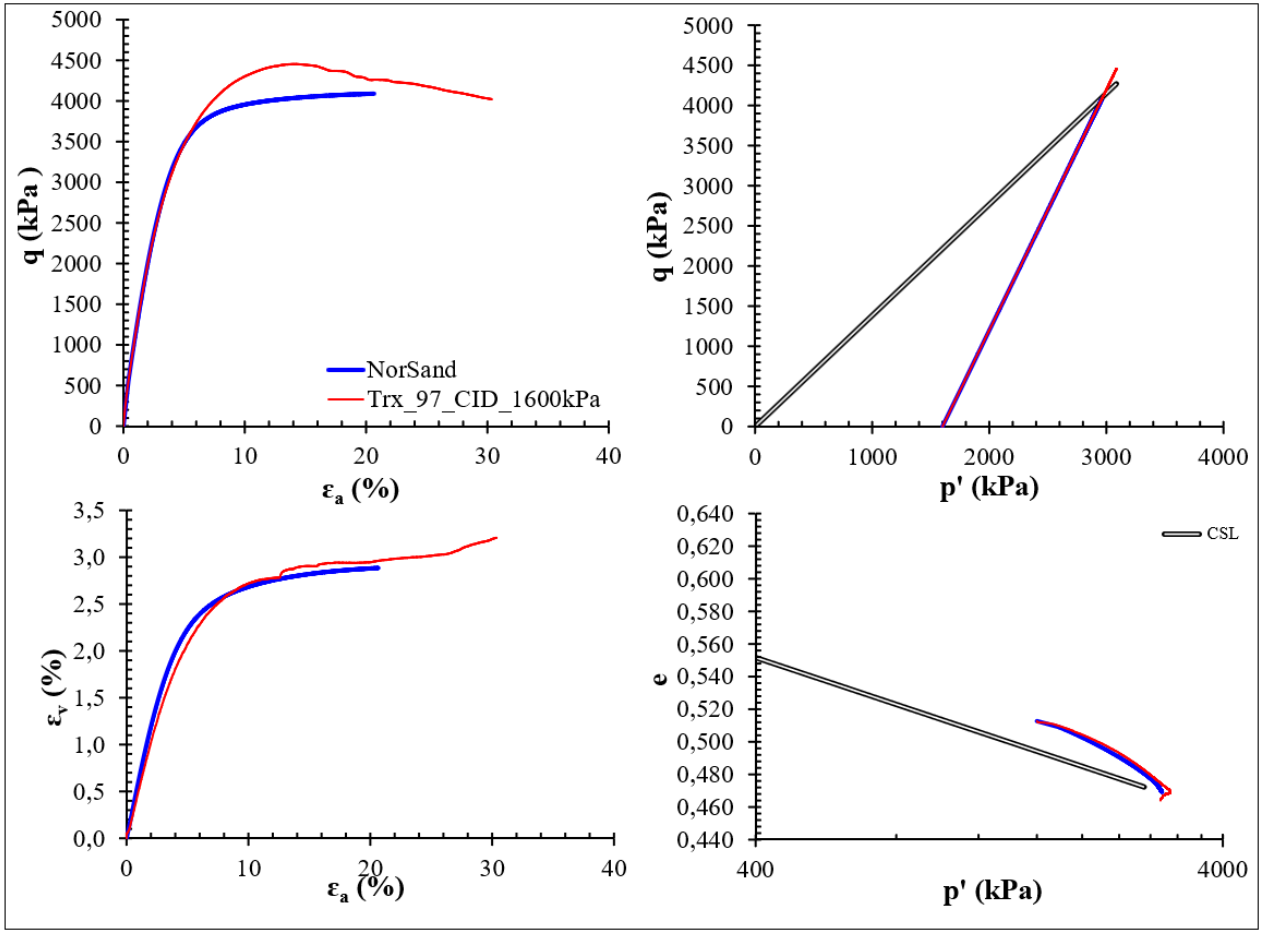

Source: elaborated by the author.

Figure F.29 – NorSand calibration into NorTXL.xls (Release 2) – Trx_97_CID_1900kPa.

Soil properties….

CSL parameters

Γ =	**0,8**	---
λ =	**0,041**	*on base e*

Plasticity

M_{tc} =	**1,384**	
N =	**0,0058**	*(typ 0.2 - 0.3)*
χ_{tc} =	**8,16**	*often taken as 4*
H_0 =	**160**	*> H .32*
H_ψ =	**1037**	
($H = H_0 - H_\psi \psi$...)	*142,348*	*(typ 60 - 400)*

Elasticity

G_{max} @ p_0=	**120**	MPa
G_exp =	**0,4**	*elastic exponent*
ν =	**0,20**	
(Ir ...)	*63,1579*	---
k=	*0,0179*	---

Initial soil state…

ψ_0 =	**0,0170**	
=> e_0 =	*0,504*	
p_0 =	**1900**	***kPa***
K_0 =	**1**	---
(sig1...)	*1900*	
OCR ("R") =	**1,1**	---

Drained or undrained… **Drained**

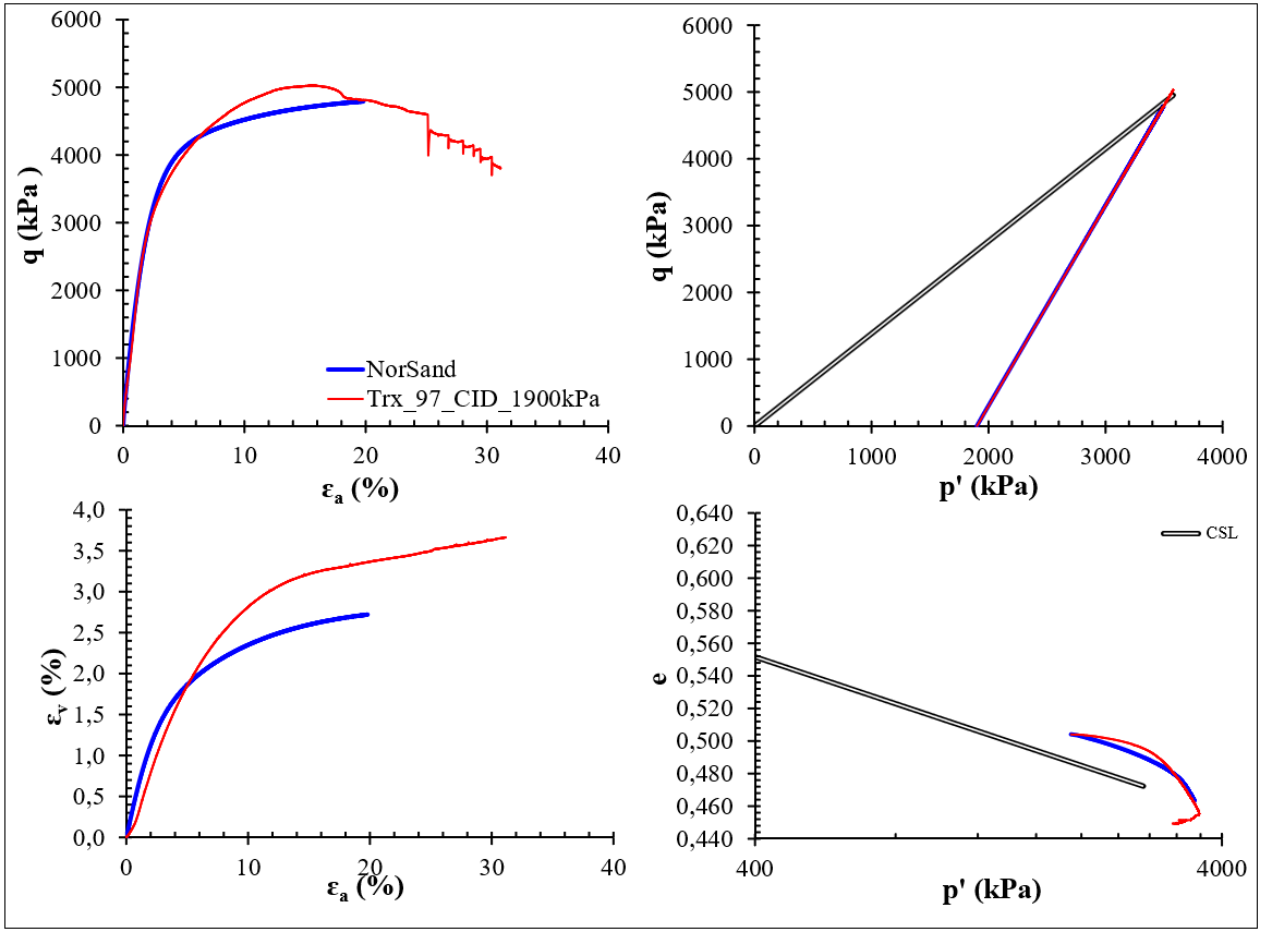

Source: elaborated by the author.

Figure F.30 – NorSand calibration into NorTXL.xls (Release 2) – Trx_97_CIU_100kPa.

Soil properties….

CSL parameters

Γ =	**0,8**	---
λ =	**0,041**	*on base e*

Plasticity

M_{tc} =	**1,384**	
N =	**0,0058**	*(typ 0.2 - 0.3)*
χ_{tc} =	**8,16**	*often taken as 4*
H_0 =	**160**	*> H_21*
H_ψ =	**1037**	
(H = H_0 - H_{ψ}ψ...)	*205,016*	*(typ 60 - 400)*

Elasticity

G_{max} @ p_0=	**35**	MPa
G_exp =	**0,4**	*elastic exponent*
ν =	**0,20**	
(Ir ...)	*350*	---
k=	*0,0034*	---

Initial soil state…

ψ_0 =	**-0,0434**	
=> e_0 =	*0,566*	
p_0 =	**100**	***kPa***
K_0 =	**1**	---
(sig1...)	*100*	
OCR ("R") =	**2,5**	---

Drained or undrained… **Undrained**

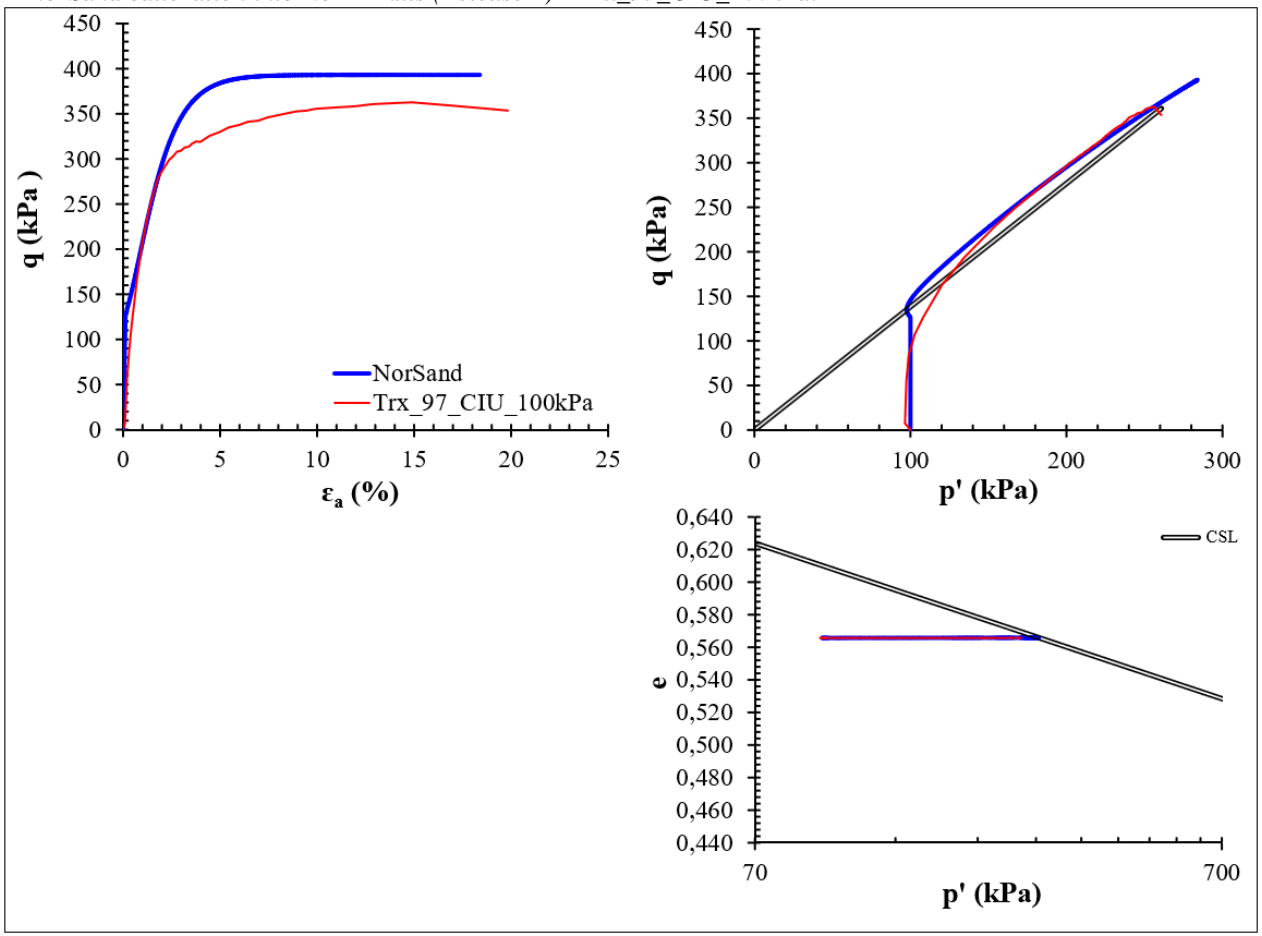

Source: elaborated by the author.

Figure F.31 – NorSand calibration into NorTXL.xls (Release 2) – Trx_97_CIU_200kPa.

Soil properties….

CSL parameters

Γ =	**0,8**	---
λ =	**0,041**	*on base e*

Plasticity

M_{tc} =	**1,384**	
N =	**0,0058**	*(typ 0.2 - 0.3)*
χ_{tc} =	**8,16**	*often taken as 4*
H_0 =	**160**	*> H .30*
H_ψ =	**1037**	
($H = H_0 - H_{\psi}\psi$...)	*186,456*	*(typ 60 - 400)*

Elasticity

G_{max} @ p_0=	**15**	MPa
G_exp =	**0,4**	*elastic exponent*
ν =	**0,20**	
(Ir ...)	*75*	---
k=	*0,0155*	---

Initial soil state…

ψ_0 =	**-0,0255**	
=> e_0 =	*0,555*	
p_0 =	**200**	***kPa***
K_0 =	**1**	---
(sig1...)	*200*	
OCR ("R") =	**1**	---

Drained or undrained… **Undrained**

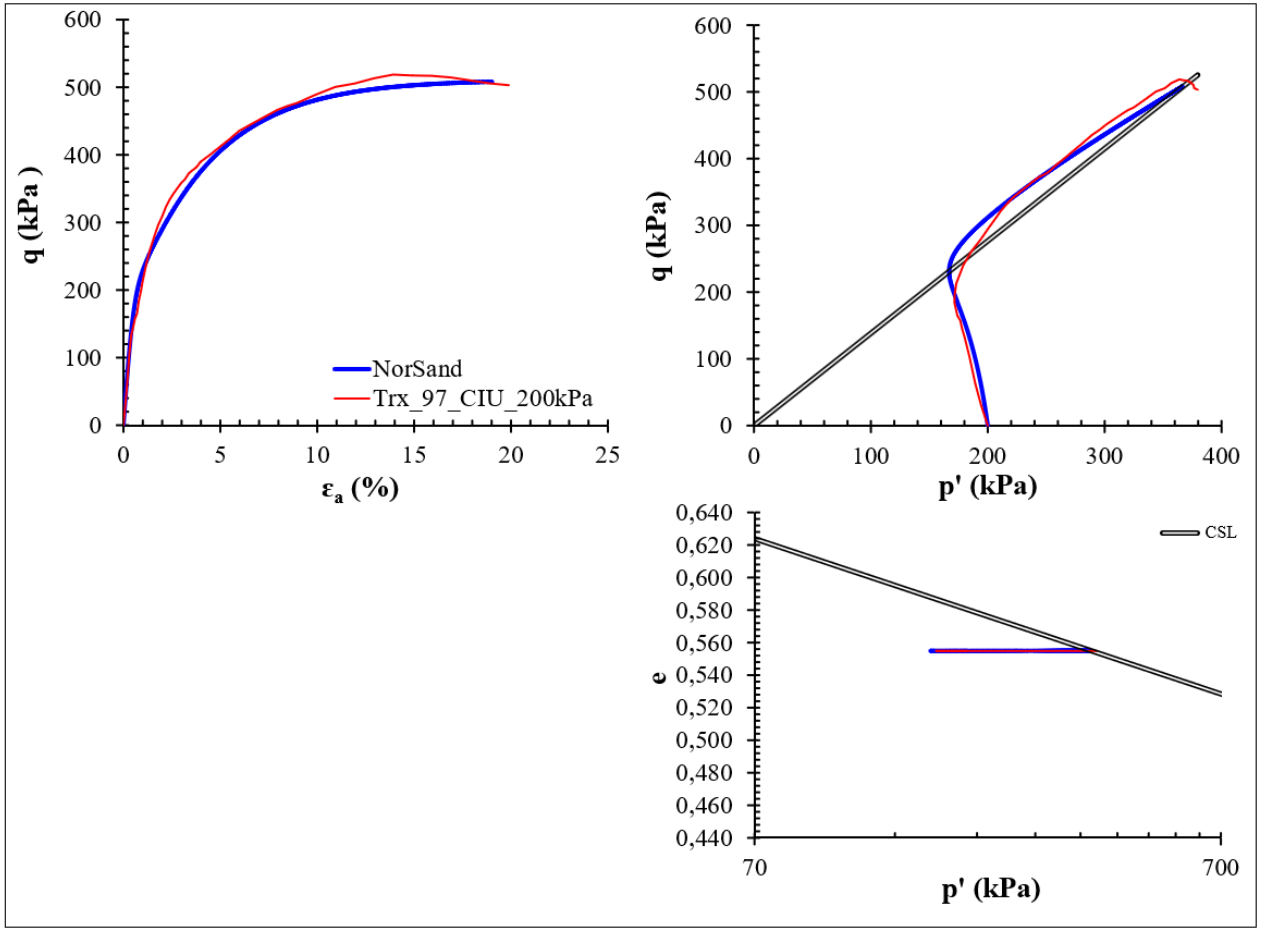

Source: elaborated by the author.

Figure F.32 – NorSand calibration into NorTXL.xls (Release 2) – Trx_97_CIU_400kPa.

Soil properties….

CSL parameters

Γ = **0,8** ---

λ = **0,041** *on base e*

Plasticity

M_{tc} = **1,384**

N = **0,0058** *(typ 0.2 - 0.3)*

χ_{tc} = **8,16** *often taken as 4*

H_0 = **160** *> H 42*

H_ψ = **1037**

(H = H_0 - H_ψ ψ...) *173,266* *(typ 60 - 400)*

Elasticity

G_{max} @ p_0 = **20** MPa

G_exp = **0,4** *elastic exponent*

ν = **0,20**

(Ir ...) *50* ---

k= *0,0231* ---

Initial soil state…

ψ_0 = **-0,0128**

=> e_0 = *0,539*

p_0 = **400** ***kPa***

K_0 = **1** ---

(sig1...) *400*

OCR ("R") = **1** ---

Drained or undrained… **Undrained**

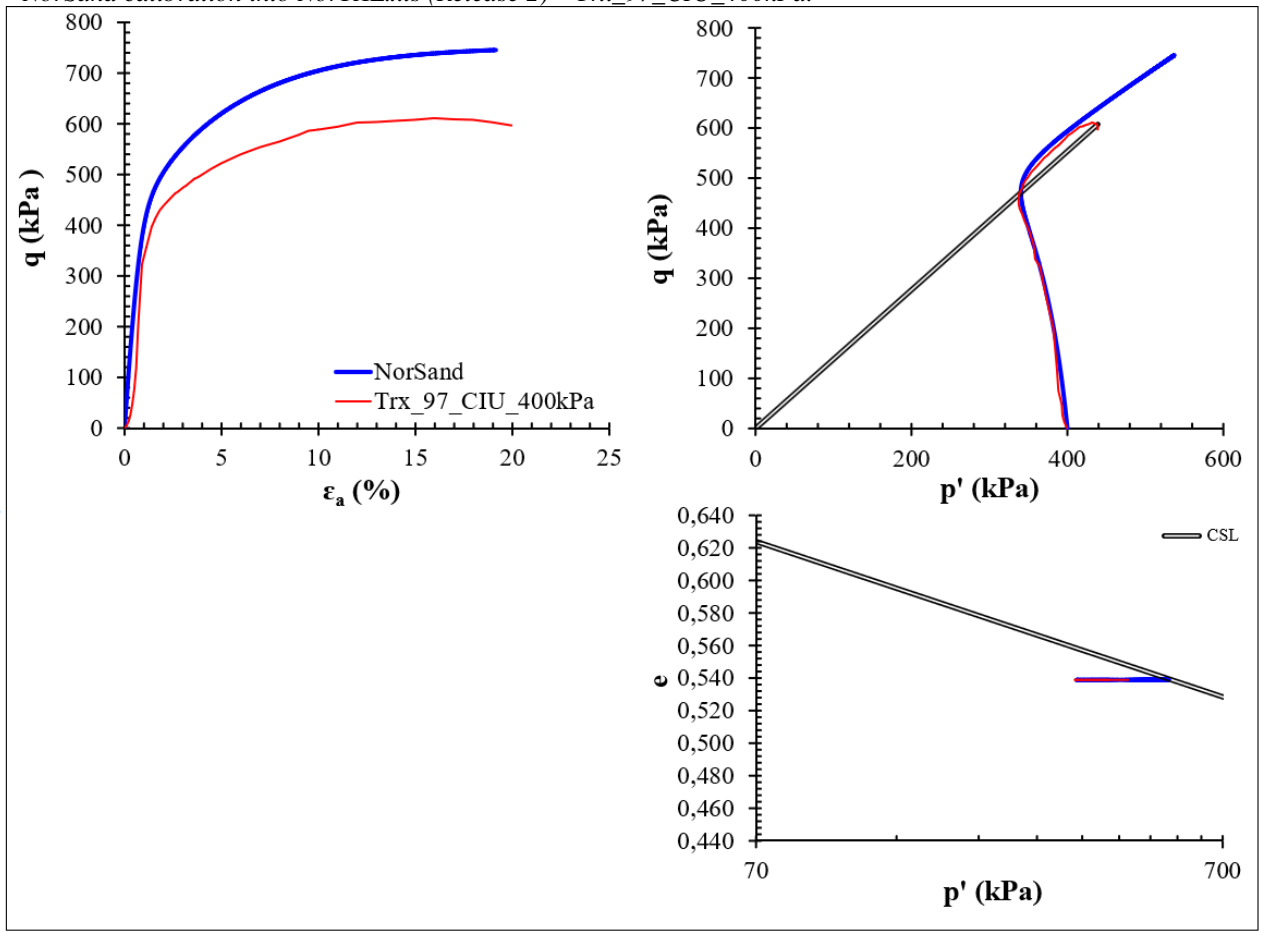

Source: elaborated by the author.

Figure F.33 – NorSand calibration into NorTXL.xls (Release 2) – Trx_97_CIU_800kPa.

Soil properties….

CSL parameters

Γ =	**0,8**	---
λ =	**0,041**	*on base e*

Plasticity

M_{tc} =	**1,384**	
N =	**0,0058**	*(typ 0.2 - 0.3)*
χ_{tc} =	**8,16**	*often taken as 4*
H_0 =	**160**	*> H 41*
H_ψ =	**1037**	
(H = H_0 - H_ψ ψ...)	*160,563*	*(typ 60 - 400)*

Elasticity

G_{max} @ p_0=	**40**	MPa
G_exp =	**0,4**	*elastic exponent*
ν =	**0,20**	
(Ir ...)	*50*	---
k=	*0,0228*	---

Initial soil state…

ψ_0 =	**-0,0005**	
=> e_0 =	*0,522*	
p_0 =	**800**	***kPa***
K_0 =	**1**	---
(sig1...)	*800*	
OCR ("R") =	**1,25**	---

Drained or undrained… **Undrained**

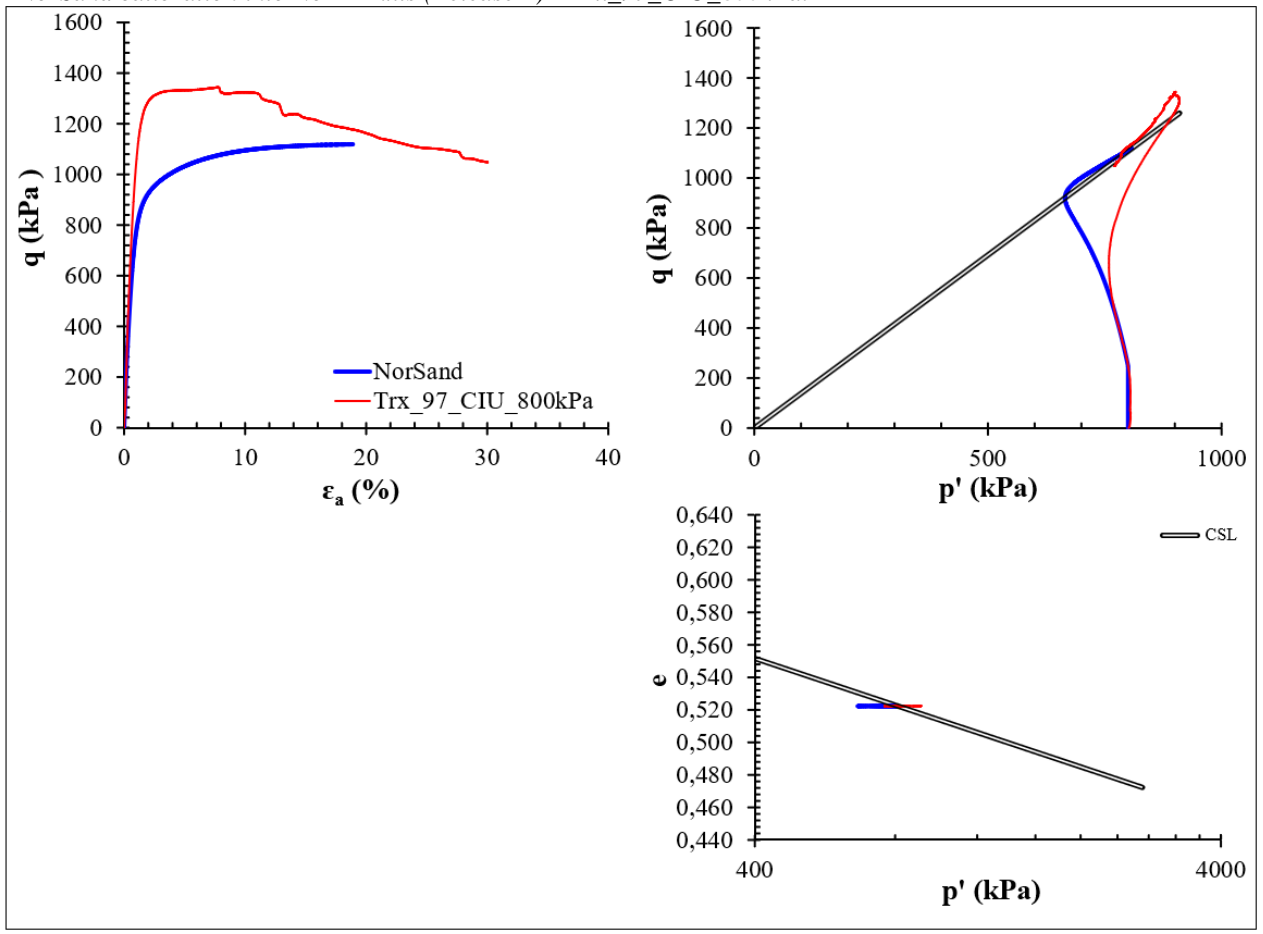

Source: elaborated by the author.

Figure F.34 – NorSand calibration into NorTXL.xls (Release 2) – Trx_97_CIU_1600kPa.

Soil properties….

CSL parameters

Γ =	**0,8**	---
λ =	**0,041**	*on base e*

Plasticity

M_{tc} =	**1,384**	
N =	**0,0058**	*(typ 0.2 - 0.3)*
χ_{tc} =	**8,16**	*often taken as 4*
H_0 =	**160**	*> H_27*
H_ψ =	**1037**	
(H = H_0 - H_ψ ψ...)	*137,603*	*(typ 60 - 400)*

Elasticity

G_{max} @ p_0=	**140**	MPa
G_exp =	**0,4**	*elastic exponent*
ν =	**0,20**	
(Ir ...)	*87,5*	---
k=	*0,0130*	---

Initial soil state…

ψ_0 =	**0,0216**	
=> e_0 =	*0,516*	
p_0 =	**1600**	***kPa***
K_0 =	**1**	---
(sig1...)	*1600*	
OCR ("R") =	**1,17**	---

Drained or undrained… **Undrained**

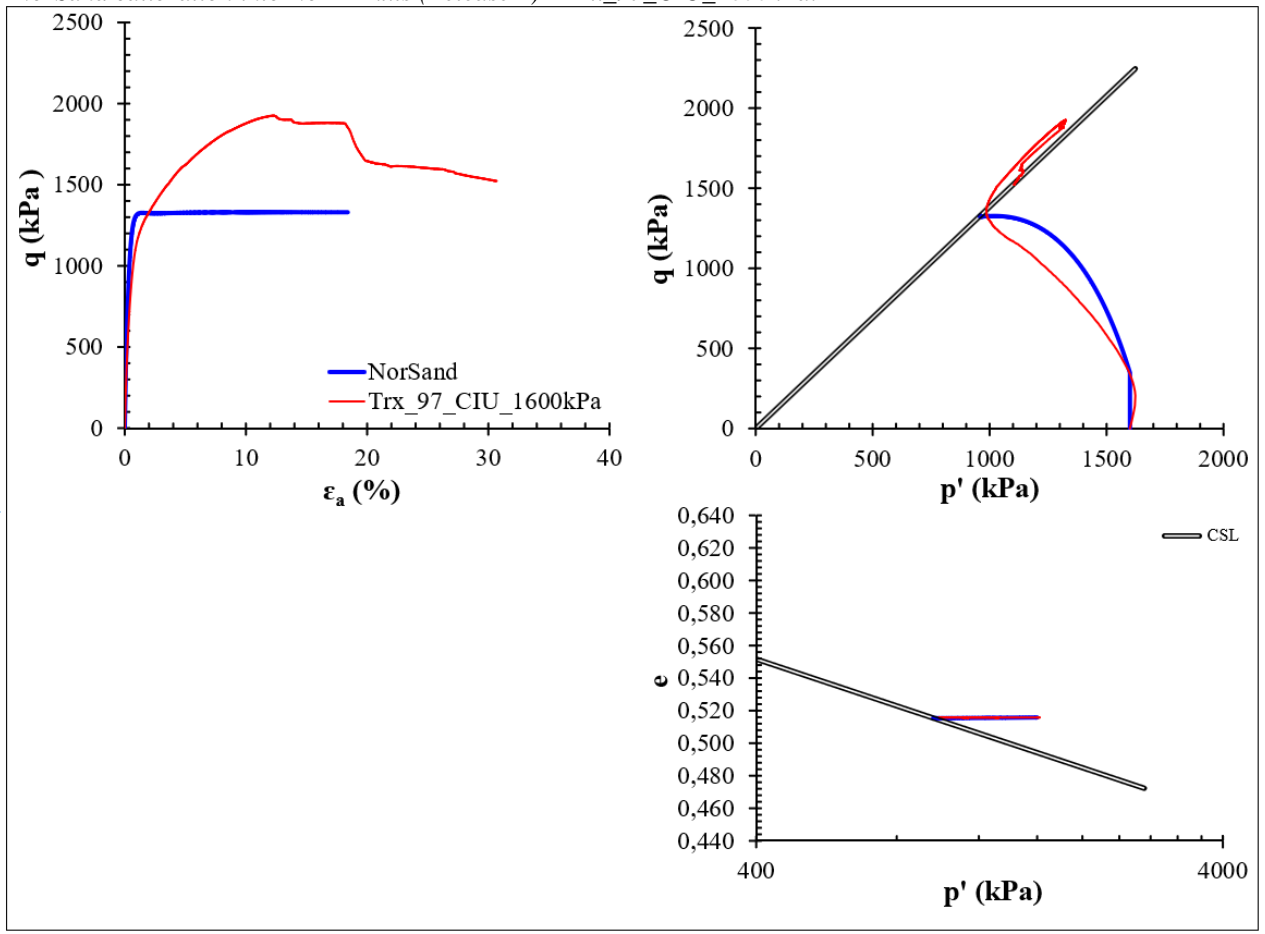

Source: elaborated by the author.

F.4 DC = 100%

Table F.4 – NorSand calibration into NorTXL.xls (Release 2) – DC = 100% – Summary.

	CID					CIU					
	100kPa	**200kPa**	**400kPa**	**800kPa**	**1600kPa**	**100kPa**	**200kPa**	**400kPa**	**800kPa**	**1600kPa**	**1900kPa**
CSL parameters											
Γ	0,8	0,8	0,8	0,8	0,8	0,8	0,8	0,8	0,8	0,8	0,8
λ	0,041	0,041	0,041	0,041	0,041	0,041	0,041	0,041	0,041	0,041	0,041
Plasticity											
M_{tc}	1,384	1,384	1,384	1,384	1,384	1,384	1,384	1,384	1,384	1,384	1,384
N	0,0058	0,0058	0,0058	0,0058	0,0058	0,0058	0,0058	0,0058	0,0058	0,0058	0,0058
χ_{tc}	8,16	8,16	8,16	8,16	8,16	8,16	8,16	8,16	8,16	8,16	8,16
H_0	160	160	160	160	160	160	160	160	160	160	160
H_ψ	1037	1037	1037	1037	1037	1037	1037	1037	1037	1037	1037
($H = H_0 - H_\psi.\psi$...)	253,3	224,5	203,5	199,1	166,9	231,4	215,9	141,2	191,8	183,1	162,6
Elasticity											
G_{max} @ p_0	50	70	95	110	105	50	50	55	65	100	95
G_exp	0,4	0,4	0,4	0,4	0,4	0,4	0,4	0,4	0,4	0,4	0,4
ν	0,2	0,2	0,2	0,2	0,2	0,2	0,2	0,2	0,2	0,2	0,2
(Ir…)	500,0	350,0	237,5	137,5	65,6	500,0	250,0	137,5	80,6	56,3	50,0
k	0,0	0,0	0,0	0,0	0,0	0,0	0,0	0,0	0,0	0,0	0,0
Initial soil state											
ψ_0	-0,090	-0,062	-0,042	-0,038	-0,007	-0,069	-0,054	0,018	-0,031	-0,022	0,0
e_0	0,52	0,52	0,51	0,49	0,49	0,54	0,53	0,57	0,49	0,47	0,5
p_0	100	200	400	800	1600	100	200	400	807	1600	1900,0
K_0	1,0	1,0	1,0	1,0	1,0	1,0	1,0	1,0	1,0	1,0	1,0
(σ_1…)	100	200	400	800	1600	100	200	400	807	1600	1900,0
OCR ("R")	3,20	3,15	3,15	3,00	2,00	3,00	2,30	1,40	1,36	1,25	2,65

Source: elaborated by the author.

Figure F.35 – NorSand calibration into NorTXL.xls (Release 2) – Trx_100_CID_100kPa.

Soil properties….

CSL parameters

Γ =	**0,8**	---
λ =	**0,041**	*on base e*

Plasticity

M_{tc} =	**1,384**	
N =	**0,0058**	*(typ 0.2 - 0.3)*
χ_{tc} =	**8,16**	*often taken as 4*
H_0 =	**160**	*> H 19*
H_ψ =	**1037**	
($H = H_0 - H_{\psi}\psi$...)	*253,252*	*(typ 60 - 400)*

Elasticity

G_{max} @ p_0=	**50**	MPa
G_exp =	**0,4**	*elastic exponent*
ν =	**0,20**	
(Ir ...)	*500*	---
k=	*0,0023*	---

Initial soil state…

ψ_0 =	**-0,0899**	
=> e_0 =	*0,519*	
p_0 =	**100**	***kPa***
K_0 =	**1**	---
(sig1...)	*100*	
OCR ("R") =	**3,2**	---

Drained or undrained… **Drained**

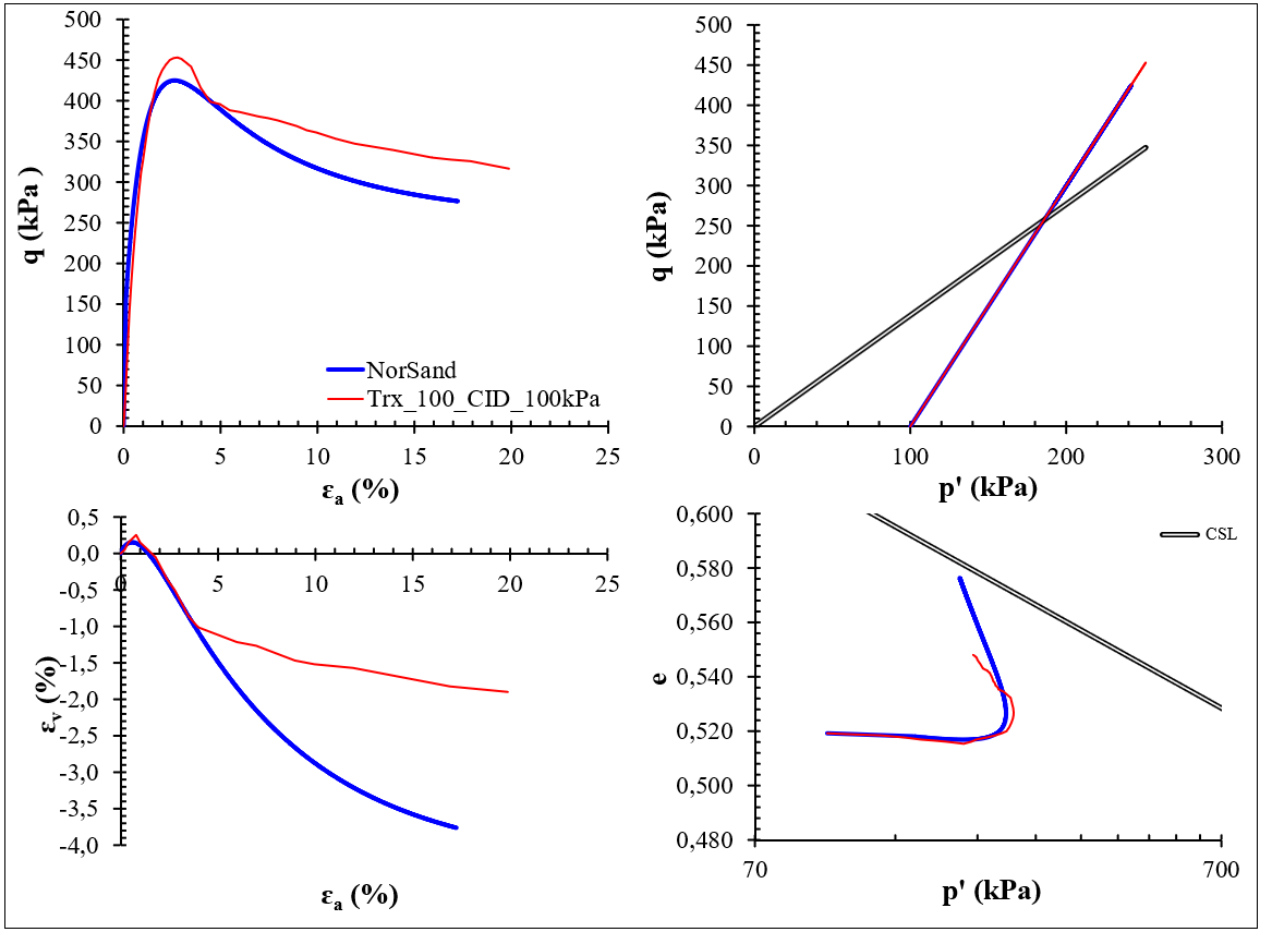

Source: elaborated by the author.

Figure F.36 – NorSand calibration into NorTXL.xls (Release 2) – Trx_100_CID_200kPa.

Soil properties….

CSL parameters

Γ = **0,8** ---

λ = **0,041** *on base e*

Plasticity

M_{tc} = **1,384**

N = **0,0058** *(typ 0.2 - 0.3)*

χ_{tc} = **8,16** *often taken as 4*

H_0 = **160** *> H_20*

H_ψ = **1037**

(H = H_0 - H_ψ...) *224,526* *(typ 60 - 400)*

Elasticity

G_{max} @ p_0= **70** MPa

G_exp = **0,4** *elastic exponent*

ν = **0,20**

(Ir ...) *350* ---

k= *0,0033* ---

Initial soil state…

ψ_0 = **-0,0622**

=> e_0 = *0,518*

p_0 = **200** ***kPa***

K_0 = **1** ---

(sig1...) *200*

OCR ("R") = **3,15** ---

Drained or undrained… **Drained**

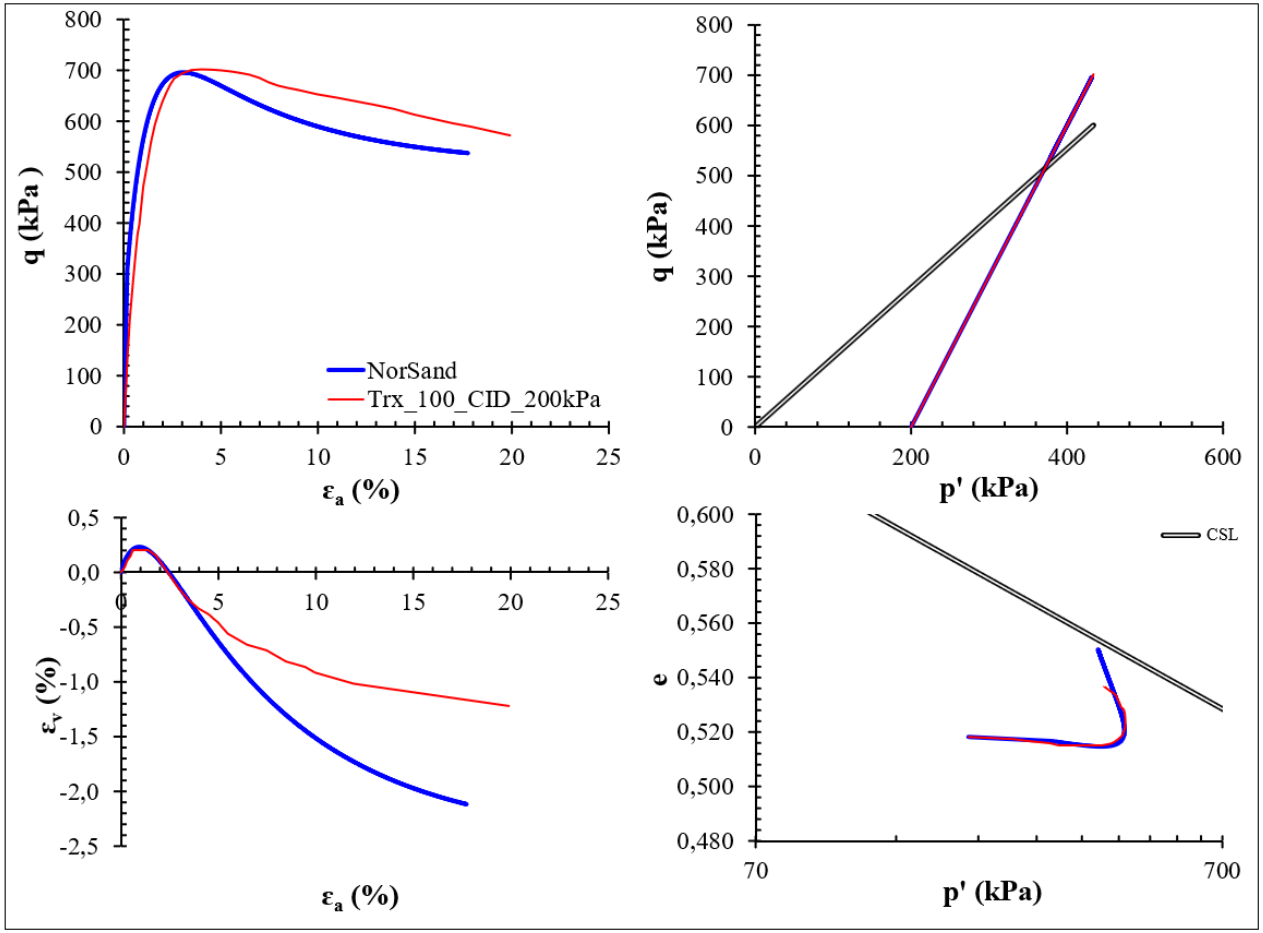

Source: elaborated by the author.

Figure F.37 – NorSand calibration into NorTXL.xls (Release 2) – Trx_100_CID_400kPa.

Soil properties….

CSL parameters

Γ =	**0,8**	---
λ =	**0,041**	*on base e*

Plasticity

M_{tc} =	**1,384**	
N =	**0,0058**	*(typ 0.2 - 0.3)*
χ_{tc} =	**8,16**	*often taken as 4*
H_0 =	**160**	*> H_21*
H_ψ =	**1037**	
(H = H_0 - H_ψ...)	*203,549*	*(typ 60 - 400)*

Elasticity

G_{max} @ p_0=	**95**	MPa
G_exp =	**0,4**	*elastic exponent*
ν =	**0,20**	
(Ir ...)	*237,5*	---
k=	*0,0048*	---

Initial soil state…

ψ_0 =	**-0,0420**	
=> e_0 =	*0,510*	
p_0 =	**400**	***kPa***
K_0 =	**1**	---
(sig1...)	*400*	
OCR ("R") =	**3,15**	---

Drained or undrained… **Drained**

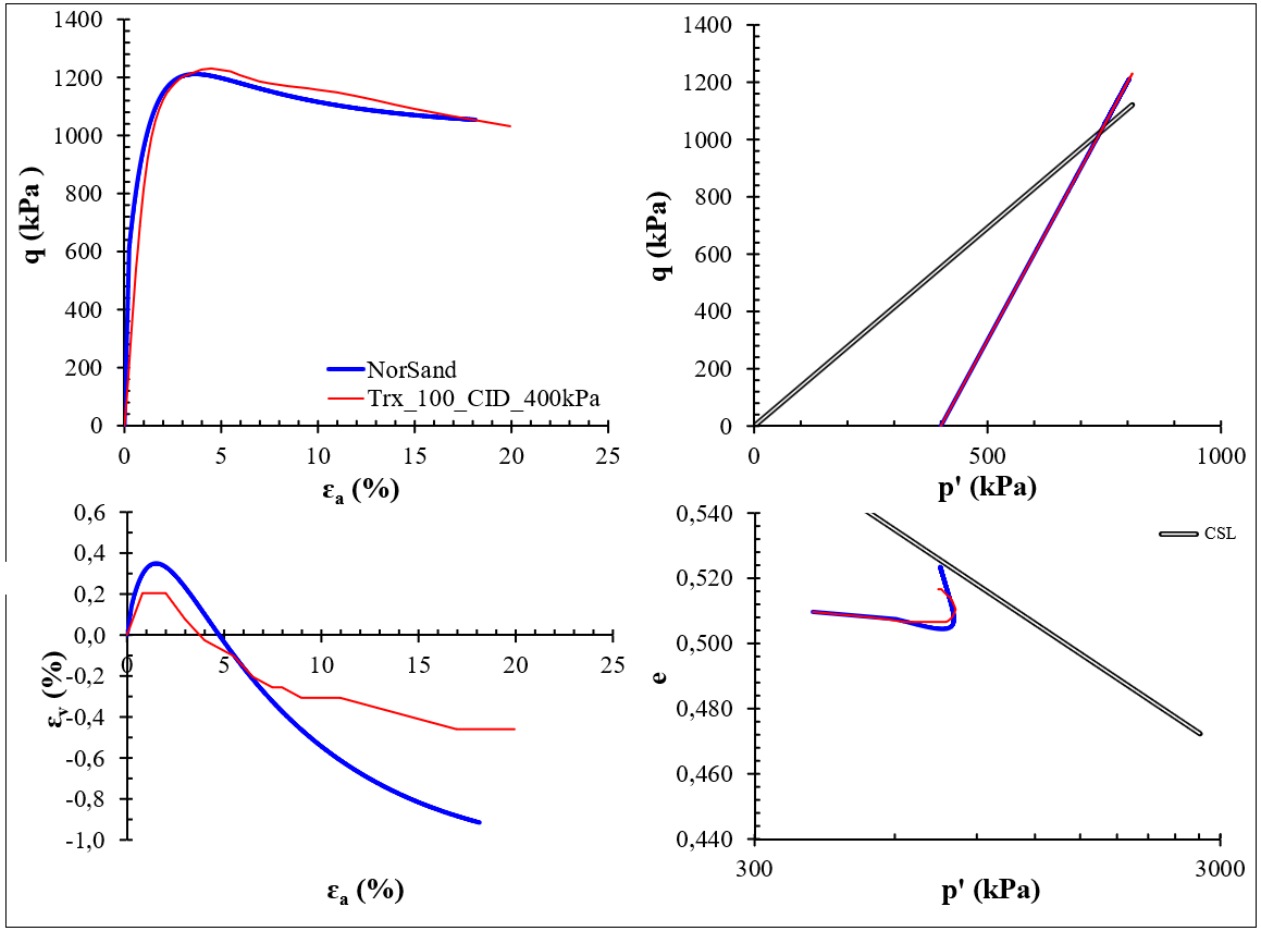

Source: elaborated by the author.

Figure F.38 – NorSand calibration into NorTXL.xls (Release 2) – Trx_100_CID_800kPa.

Soil properties….

CSL parameters

Γ =	**0,8**	**---**
λ =	**0,041**	*on base e*

Plasticity

M_{tc} =	**1,384**	
N =	**0,0058**	*(typ 0.2 - 0.3)*
χ_{tc} =	**8,16**	*often taken as 4*
H_0 =	**160**	*> H 22*
H_ψ =	**1037**	
(H = H_0 - H_ψ ψ...)	*199,088*	*(typ 60 - 400)*

Elasticity

G_{max} @ p_0=	**110**	MPa
G_exp =	**0,4**	*elastic exponent*
ν =	**0,20**	
(Ir ...)	*137,5*	**---**
k=	*0,0081*	**---**

Initial soil state…

ψ_0 =	**-0,0377**	
=> e_0 =	*0,485*	
p_0 =	**800**	***kPa***
K_0 =	**1**	**---**
(sig1...)	*800*	
OCR ("R") =	**2**	**---**

Drained or undrained… **Drained**

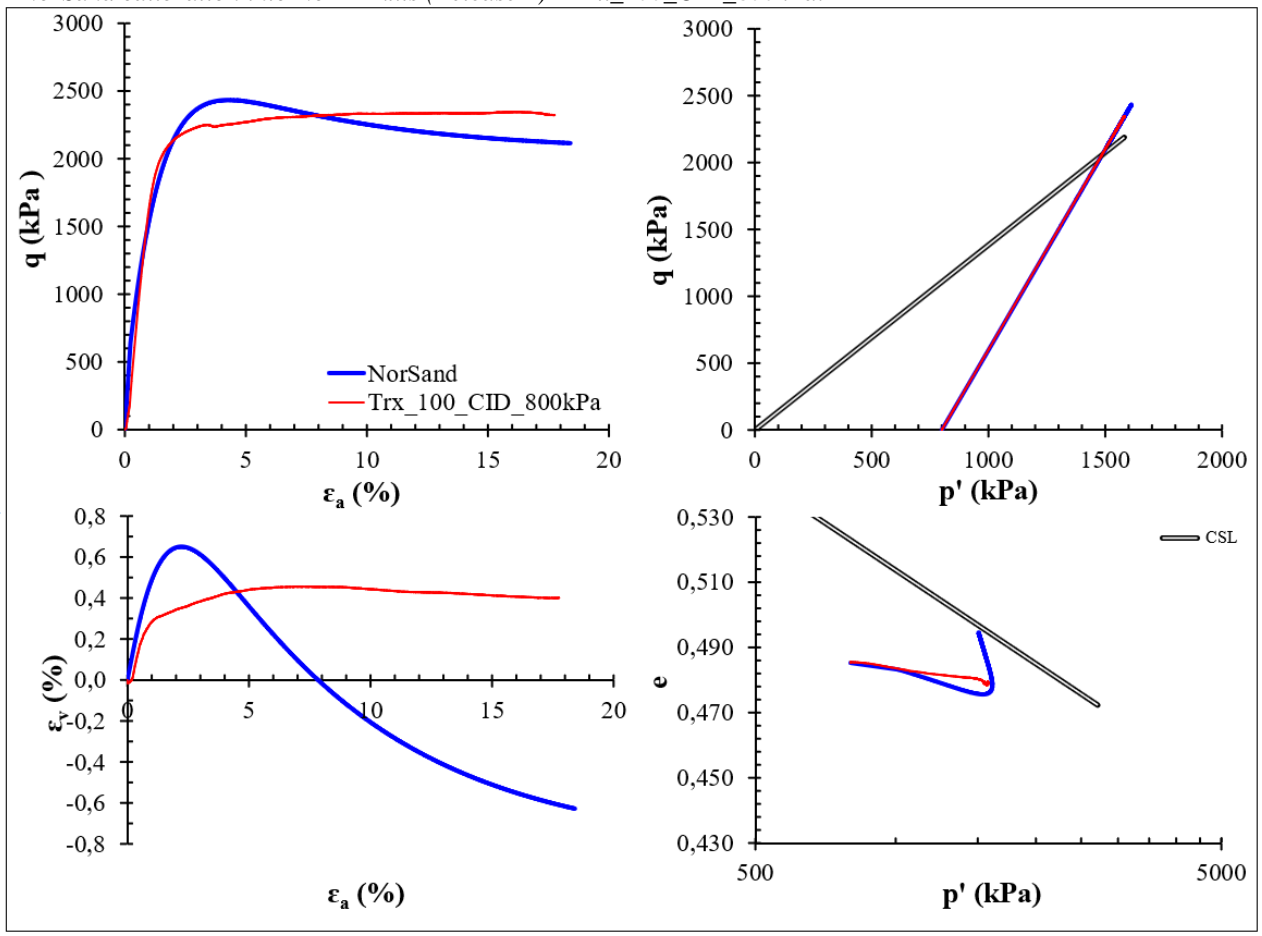

Source: elaborated by the author.

Figure F.39 – NorSand calibration into NorTXL.xls (Release 2) – Trx_100_CID_1600kPa.

Soil properties….

CSL parameters

Γ =	**0,8**	**---**
λ =	**0,041**	*on base e*

Plasticity

M_{tc} =	**1,384**	
N =	**0,0058**	*(typ 0.2 - 0.3)*
χ_{tc} =	**8,16**	*often taken as 4*
H_0 =	**160**	*> H_30*
H_ψ =	**1037**	
(H = H_0 - H_{ψ} ψ...)	*166,86*	*(typ 60 - 400)*

Elasticity

G_{max} @ p_0=	**105**	MPa
G_exp =	**0,4**	*elastic exponent*
ν =	**0,20**	
(Ir ...)	*65,625*	**---**
k=	*0,0170*	**---**

Initial soil state…

ψ_0 =	**-0,0066**	
=> e_0 =	*0,488*	
p_0 =	**1600**	***kPa***
K_0 =	**1**	**---**
(sig1 ...)	*1600*	
OCR ("R") =	**2**	**---**

Drained or undrained… **Drained**

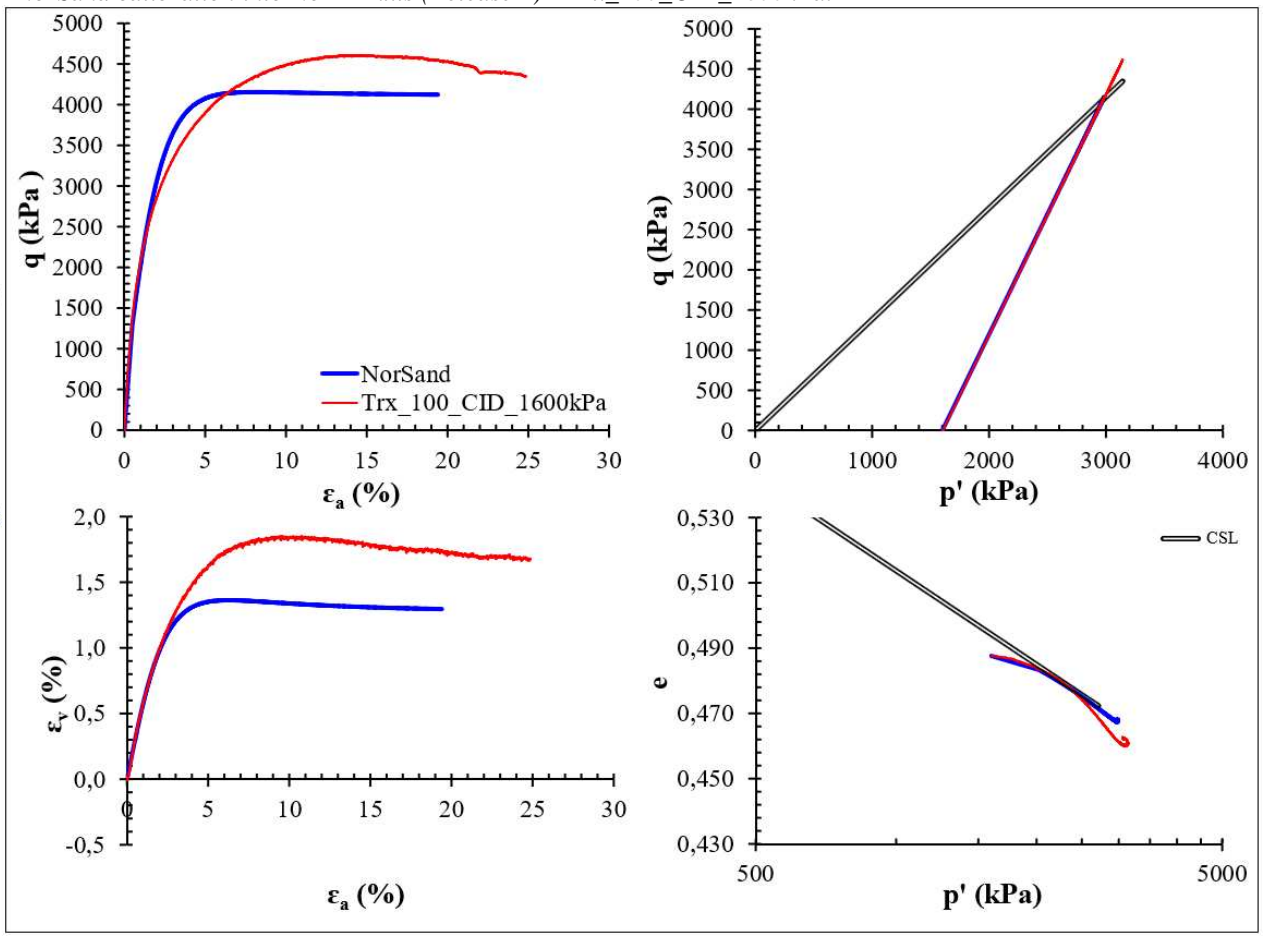

Source: elaborated by the author.

Figure F.40 – NorSand calibration into NorTXL.xls (Release 2) – Trx_100_CIU_100kPa.

Soil properties….

CSL parameters

Γ = **0,8** ---

λ = **0,041** *on base e*

Plasticity

M_{tc} = **1,384**

N = **0,0058** *(typ 0.2 - 0.3)*

χ_{tc} = **8,16** *often taken as 4*

H_0 = **160** *> H 20*

H_ψ = **1037**

(H = H_0 - H_ψ...) *231,435* *(typ 60 - 400)*

Elasticity

G_{max} @ p_0 = **50** MPa

G_exp = **0,4** *elastic exponent*

ν = **0,20**

(Ir ...) *500* ---

k= *0,0023* ---

Initial soil state…

ψ_0 = **-0,0689**

=> e_0 = *0,540*

p_0 = **100** ***kPa***

K_0 = **1** ---

(sig1...) *100*

OCR ("R") = **3** ---

Drained or undrained… **Undrained**

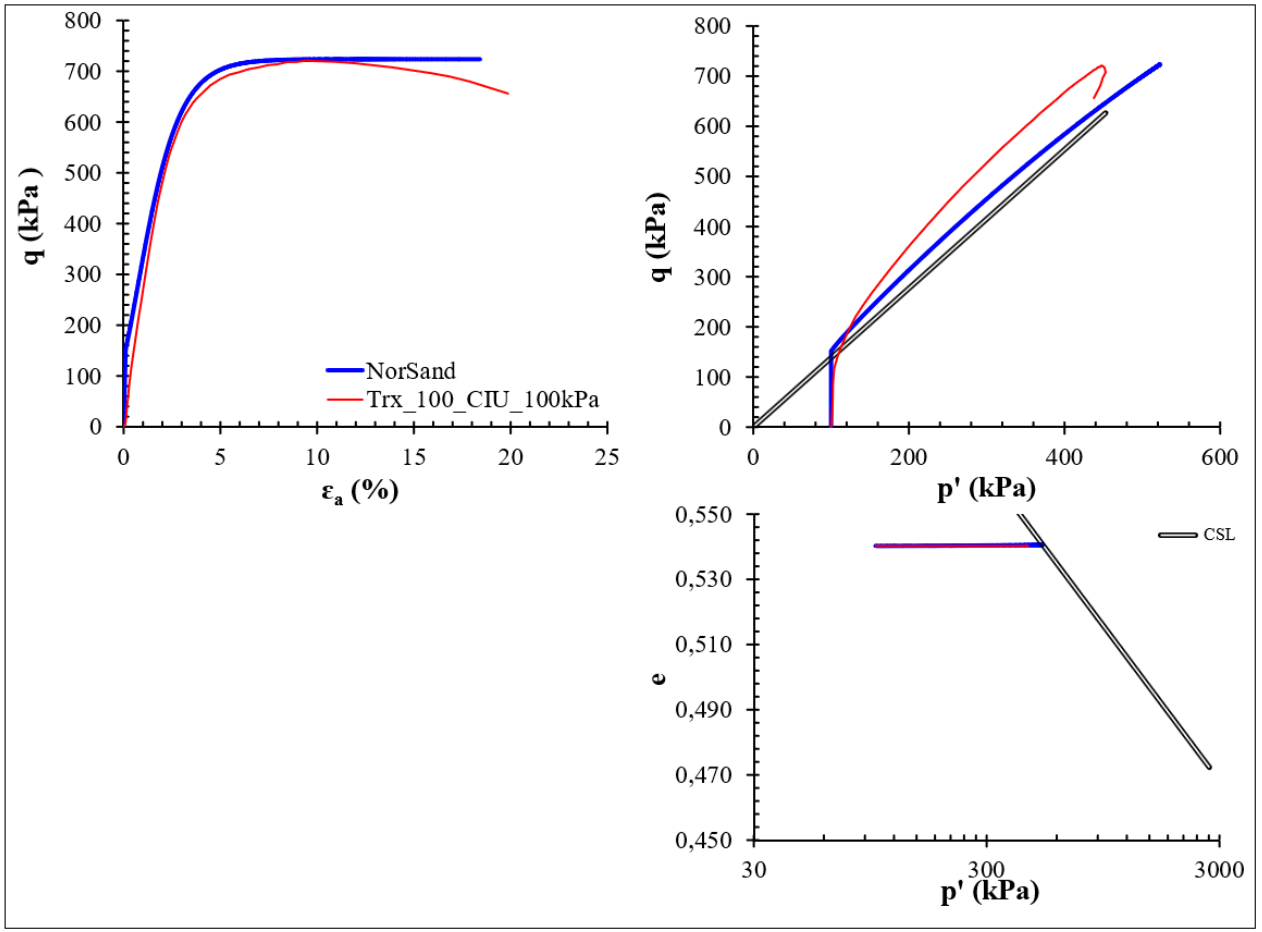

Source: elaborated by the author.

Figure F.41 – NorSand calibration into NorTXL.xls (Release 2) – Trx_100_CIU_200kPa.

Soil properties….

CSL parameters

Γ =	**0,8**	**---**
λ =	**0,041**	*on base e*

Plasticity

M_{tc} =	**1,384**	
N =	**0,0058**	*(typ 0.2 - 0.3)*
χ_{tc} =	**8,16**	*often taken as 4*
H_0 =	**160**	*> H, 21*
H_ψ =	**1037**	
(H = H_0 - H_ψ ψ...)	*215,872*	*(typ 60 - 400)*

Elasticity

G_{max} @ p_0=	**50**	MPa
G_exp =	**0,4**	*elastic exponent*
ν =	**0,20**	
(Ir ...)	*250*	**---**
k=	*0,0046*	**---**

Initial soil state…

ψ_0 =	**-0,0539**	
=> e_0 =	*0,527*	
p_0 =	**200**	***kPa***
K_0 =	**1**	**---**
(sig1...)	*200*	
OCR ("R") =	**2,3**	**---**

Drained or undrained… **Undrained**

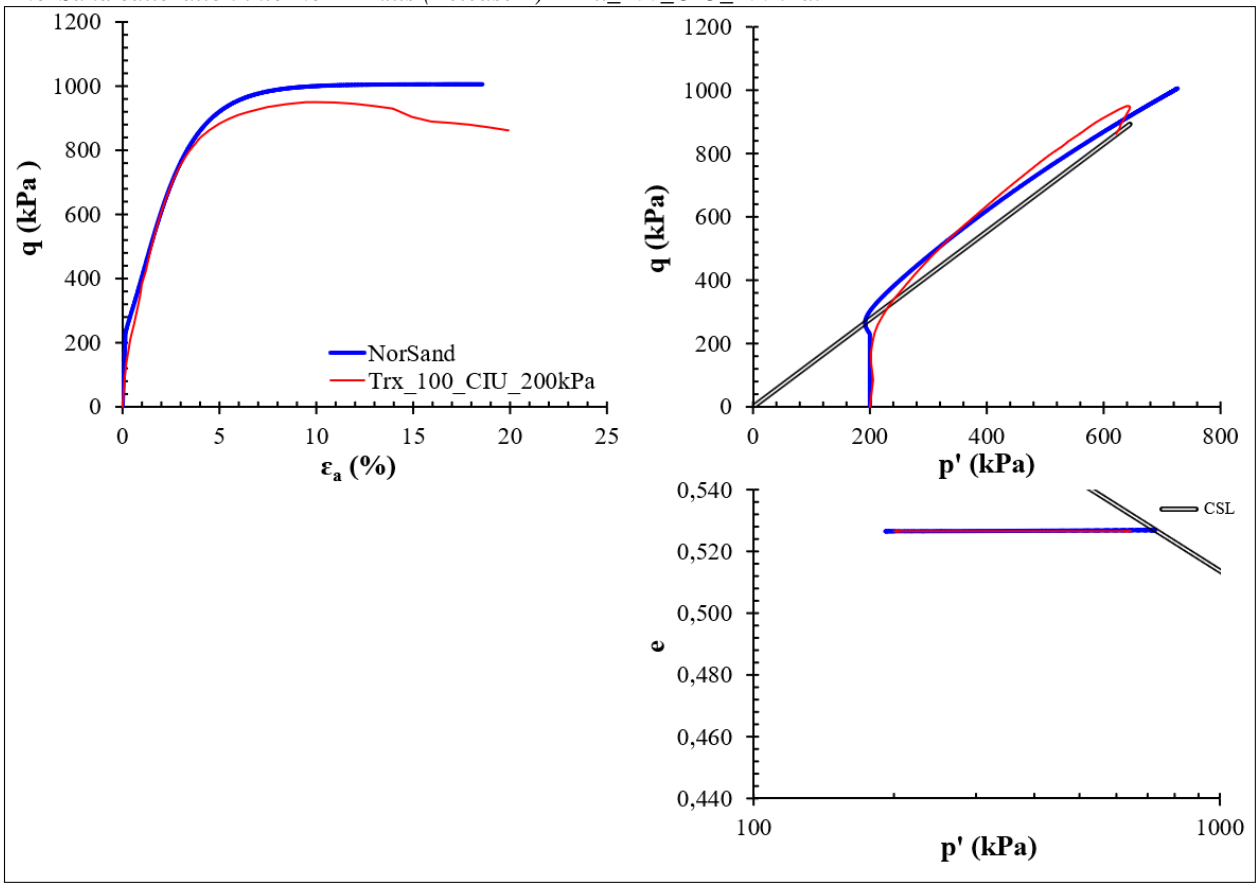

Source: elaborated by the author.

Figure F.42 – NorSand calibration into NorTXL.xls (Release 2) – Trx_100_CIU_400kPa.

Soil properties….

CSL parameters

Γ =	**0,8**	**---**
λ =	**0,041**	*on base e*

Plasticity

M_{tc} =	**1,384**	
N =	**0,0058**	*(typ 0.2 - 0.3)*
χ_{tc} =	**8,16**	*often taken as 4*
H_0 =	**160**	*> H_24*
H_ψ =	**1037**	
(H = H_0 - H_{ψ} ψ...)	*141,241*	*(typ 60 - 400)*

Elasticity

G_{max} @ p_0=	**55**	MPa
G_exp =	**0,4**	*elastic exponent*
ν =	**0,20**	
(Ir ...)	*137,5*	**---**
k=	*0,0086*	**---**

Initial soil state…

ψ_0 =	**0,0181**	
=> e_0 =	*0,570*	
p_0 =	**400**	***kPa***
K_0 =	**1**	**---**
(sig1...)	*400*	
OCR ("R") =	**1,4**	**---**

Drained or undrained… Undrained

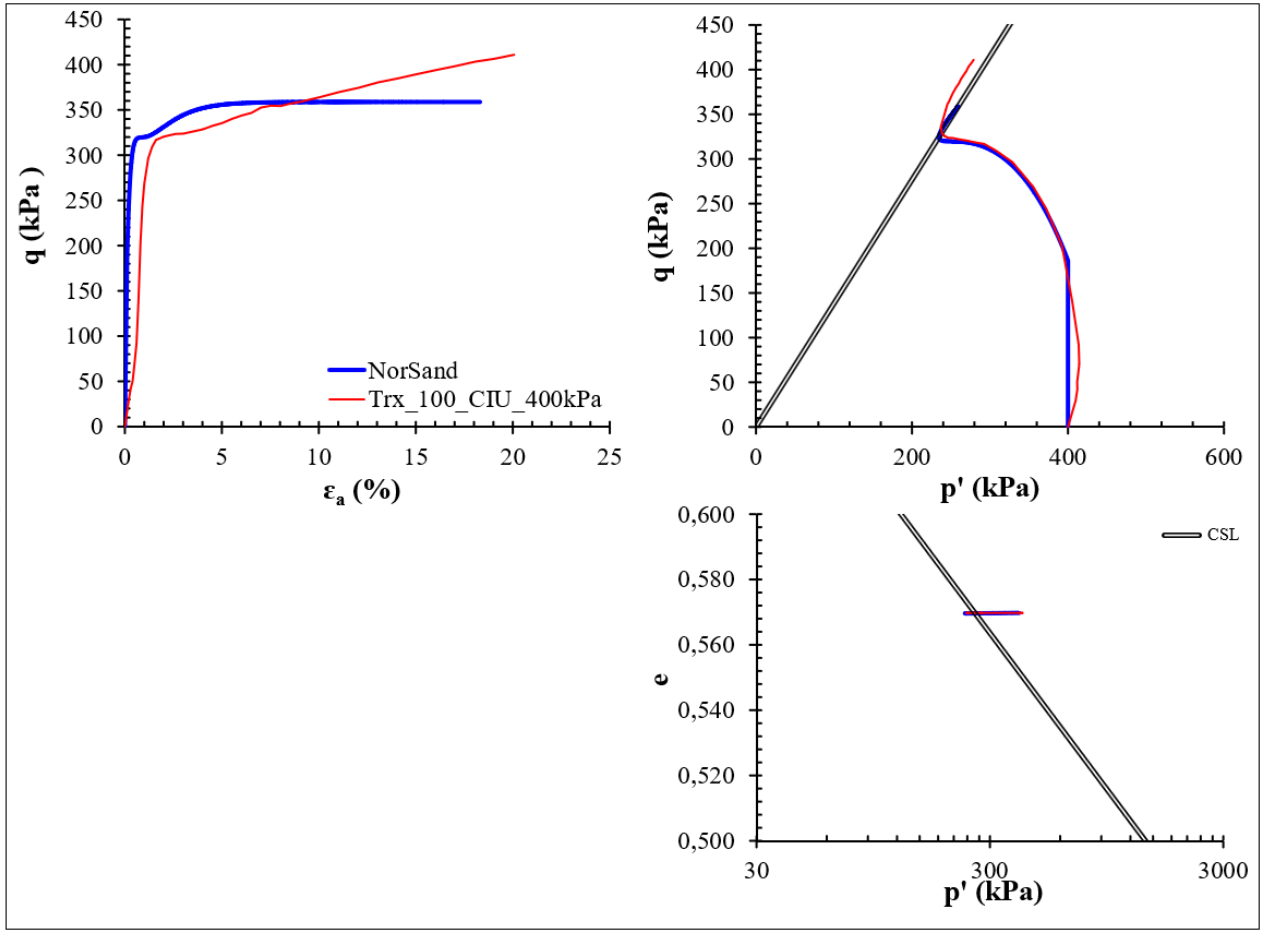

Source: elaborated by the author.

Figure F.43 – NorSand calibration into NorTXL.xls (Release 2) – Trx_100_CIU_800kPa.

Soil properties….

CSL parameters

Γ =	**0,8**	---
λ =	**0,041**	*on base e*

Plasticity

M_{tc} =	**1,384**	
N =	**0,0058**	*(typ 0.2 - 0.3)*
χ_{tc} =	**8,16**	*often taken as 4*
H_0 =	**160**	*> H ,27*
H_ψ =	**1037**	
(H = H_0 - H_{ψ} ψ...)	*191,835*	*(typ 60 - 400)*

Elasticity

G_{max} @ p_0=	**65**	MPa
G_exp =	**0,4**	*elastic exponent*
ν =	**0,20**	
(Ir ...)	*80,5752*	---
k=	*0,0139*	---

Initial soil state…

ψ_0 =	**-0,0307**	
=> e_0 =	*0,492*	
p_0 =	**806,7**	***kPa***
K_0 =	**1**	---
(sig1...)	*806,7*	
OCR ("R") =	**1,36**	---

Drained or undrained… **Undrained**

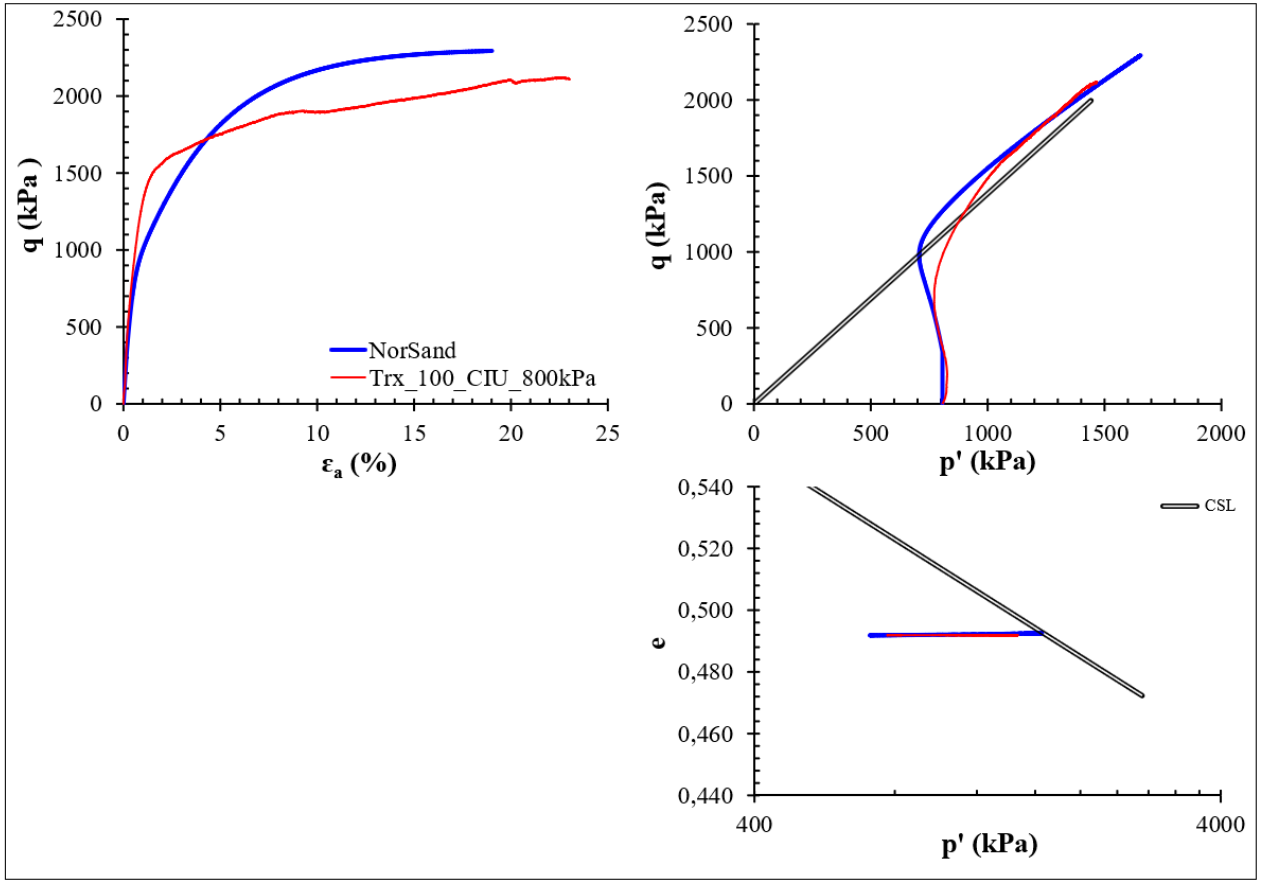

Source: elaborated by the author.

Figure F.44 – NorSand calibration into NorTXL.xls (Release 2) – Trx_100_CIU_1600kPa.

Soil properties….

CSL parameters

Γ = **0,8** ---

λ = **0,041** *on base e*

Plasticity

M_{tc} = **1,384**

N = **0,0058** *(typ 0.2 - 0.3)*

χ_{tc} = **8,16** *often taken as 4*

H_0 = **160** *> H_31*

H_ψ = **1037**

(H = H_0 - H_ψ...) *183,054* *(typ 60 - 400)*

Elasticity

G_{max} @ p_0 = **100** MPa

G_exp = **0,4** *elastic exponent*

ν = **0,20**

(Ir ...) *62,5* ---

k= *0,0177* ---

Initial soil state…

ψ_0 = **-0,0222**

=> e_0 = *0,472*

p_0 = **1600** ***kPa***

K_0 = **1** ---

(sig1...) *1600*

OCR ("R") = **1,25** ---

Drained or undrained… **Undrained**

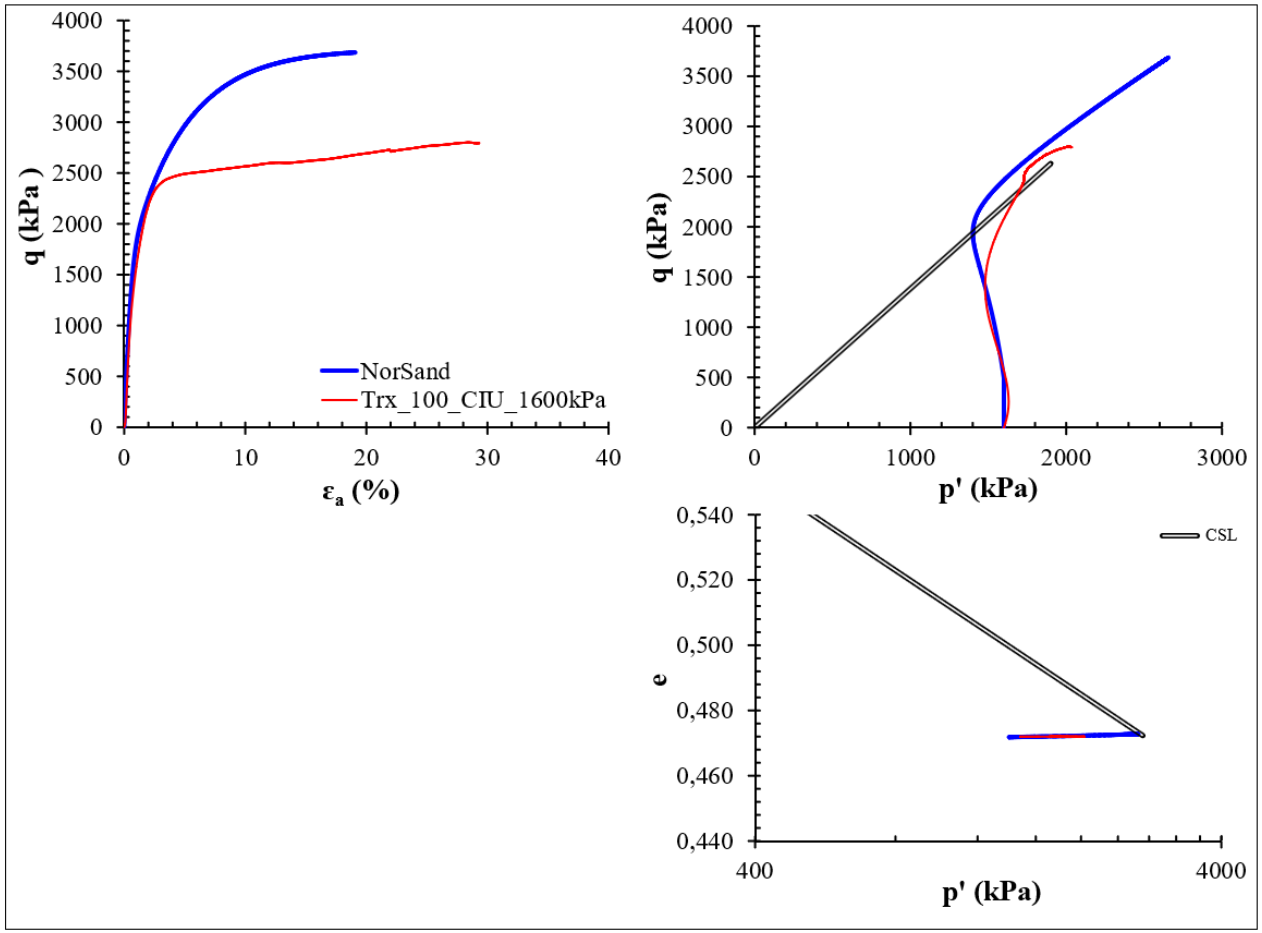

Source: elaborated by the author.

Figure F.45 – NorSand calibration into NorTXL.xls (Release 2) – Trx_100_CIU_1900kPa.

Soil properties….

CSL parameters

Γ =	**0,8**	---
λ =	**0,041**	*on base e*

Plasticity

M_{tc} =	**1,384**	
N =	**0,0058**	*(typ 0.2 - 0.3)*
χ_{tc} =	**8,16**	*often taken as 4*
H_0 =	**160**	*> H, 39*
H_ψ =	**1037**	
(H = H_0 - H_{ψ} ψ...)	*162,551*	*(typ 60 - 400)*

Elasticity

G_{max} @ p_0=	**95**	MPa
G_exp =	**0,4**	*elastic exponent*
ν =	**0,20**	
(Ir ...)	*50*	---
k=	*0,0223*	---

Initial soil state…

ψ_0 =	**-0,0025**	
=> e_0 =	*0,485*	
p_0 =	**1900**	***kPa***
K_0 =	**1**	---
(sig1...)	*1900*	
OCR ("R") =	**2,65**	---

Drained or undrained… **Undrained**

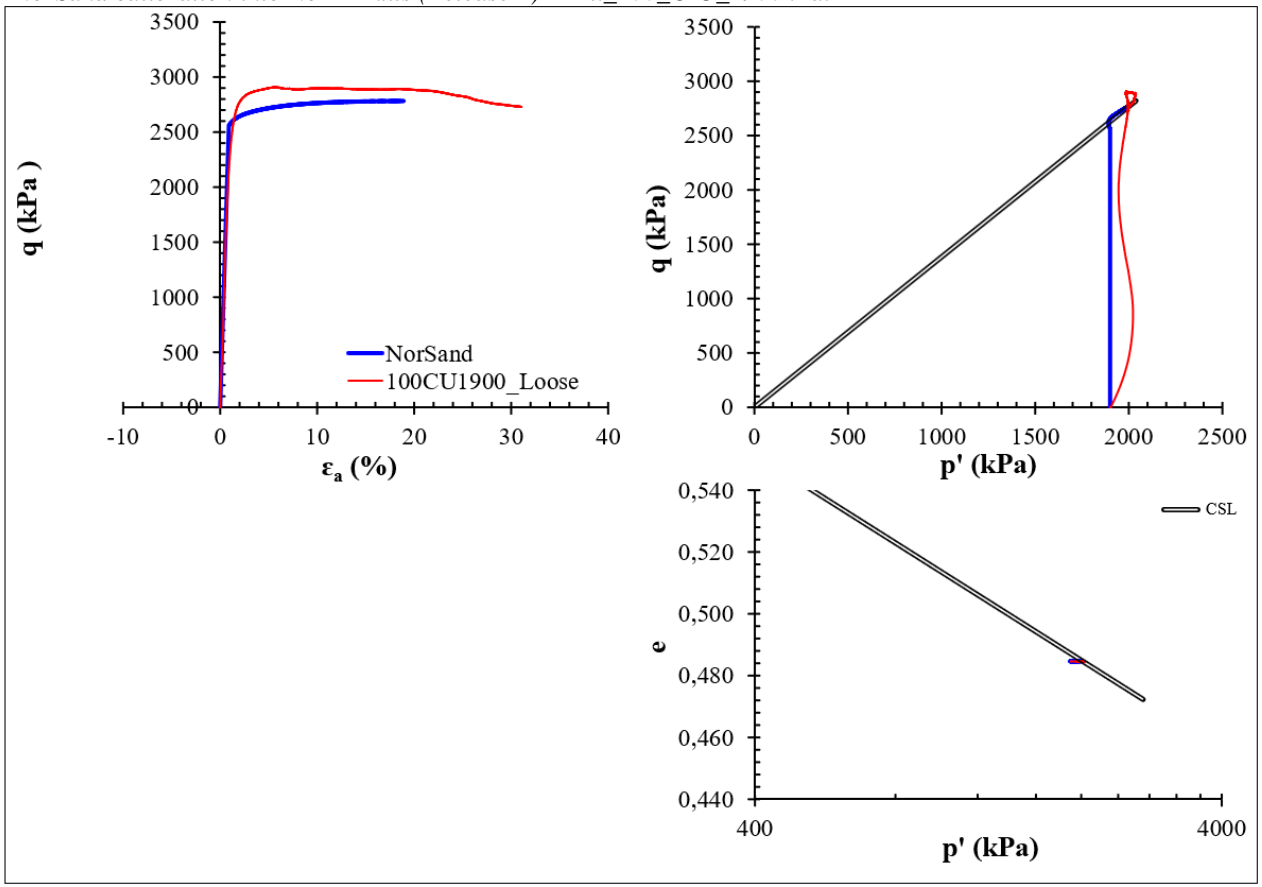

Source: elaborated by the author.

APPENDIX G – Elastic Shear Modulus

Figure G.1 – G_{max} estimated after NorSand calibration.

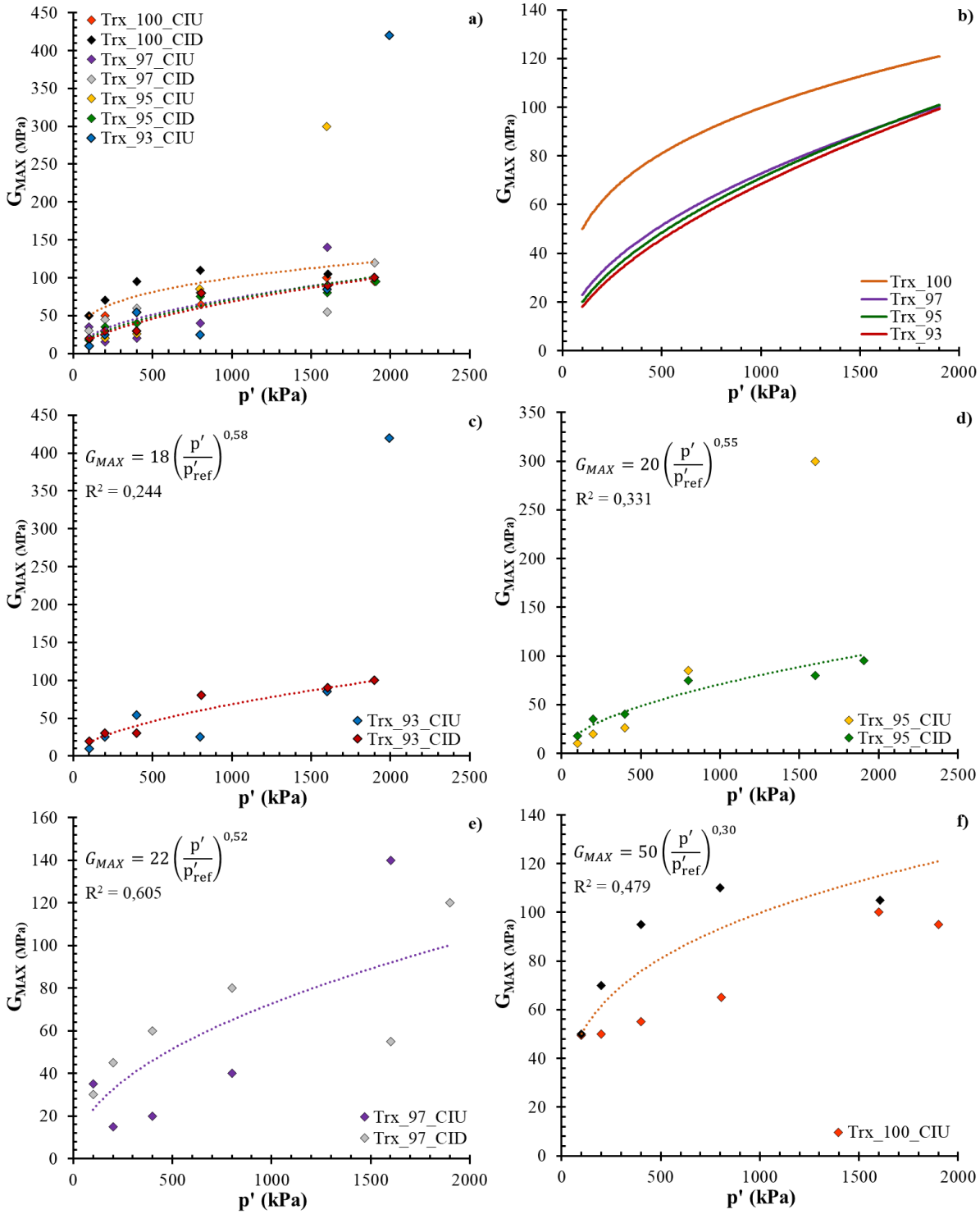

a) G_{max} estimated for each of the confining stresses of the four studied degrees of compaction; b) Trendlines determined after values of G_{max} of each degree of compaction; c) G_{max} estimated for DC = 93%; d) G_{max} estimated for DC = 95%; G_{max} estimated for DC = 97%; G_{max} estimated for DC = 100%. Source: elaborated by the author.

APPENDIX H – Elastic Secant Modulus

H.1 Drained

Figure H.1 – $E_{50,D}$ determined after triaxial tests.

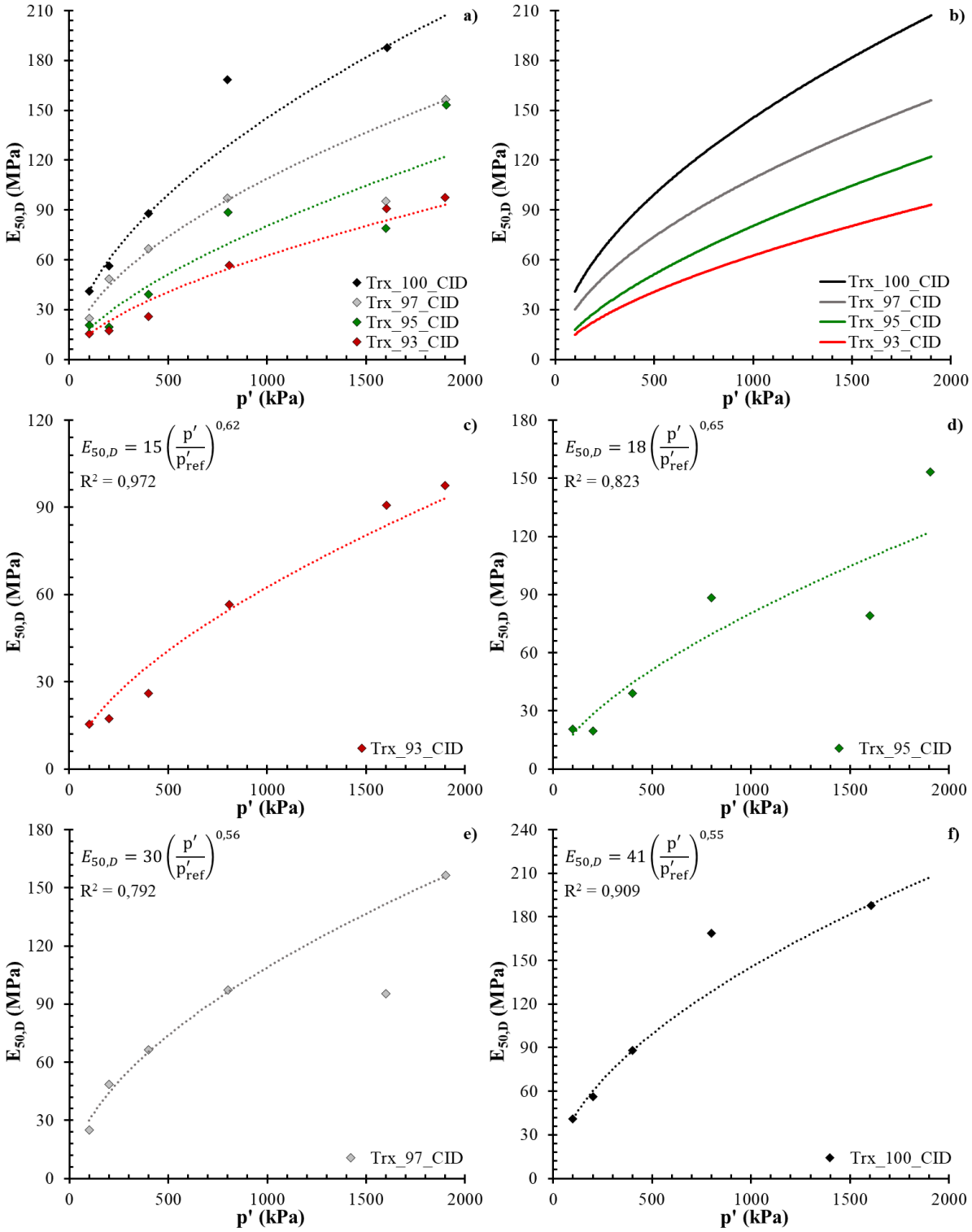

a) $E_{50,D}$ determined for each of the confining stresses of the four studied degrees of compaction; b) Trendlines determined after values of $E_{50,D}$ of each degree of compaction; c) $E_{50,D}$ determined for DC = 93%; d) $E_{50,D}$ determined for DC = 95%; $E_{50,D}$ determined for DC = 97%; $E_{50,D}$ determined for DC = 100%. Source: elaborated by the author.

H.2 Undrained

Figure H.2 – $E_{50,U}$ determined after triaxial tests.

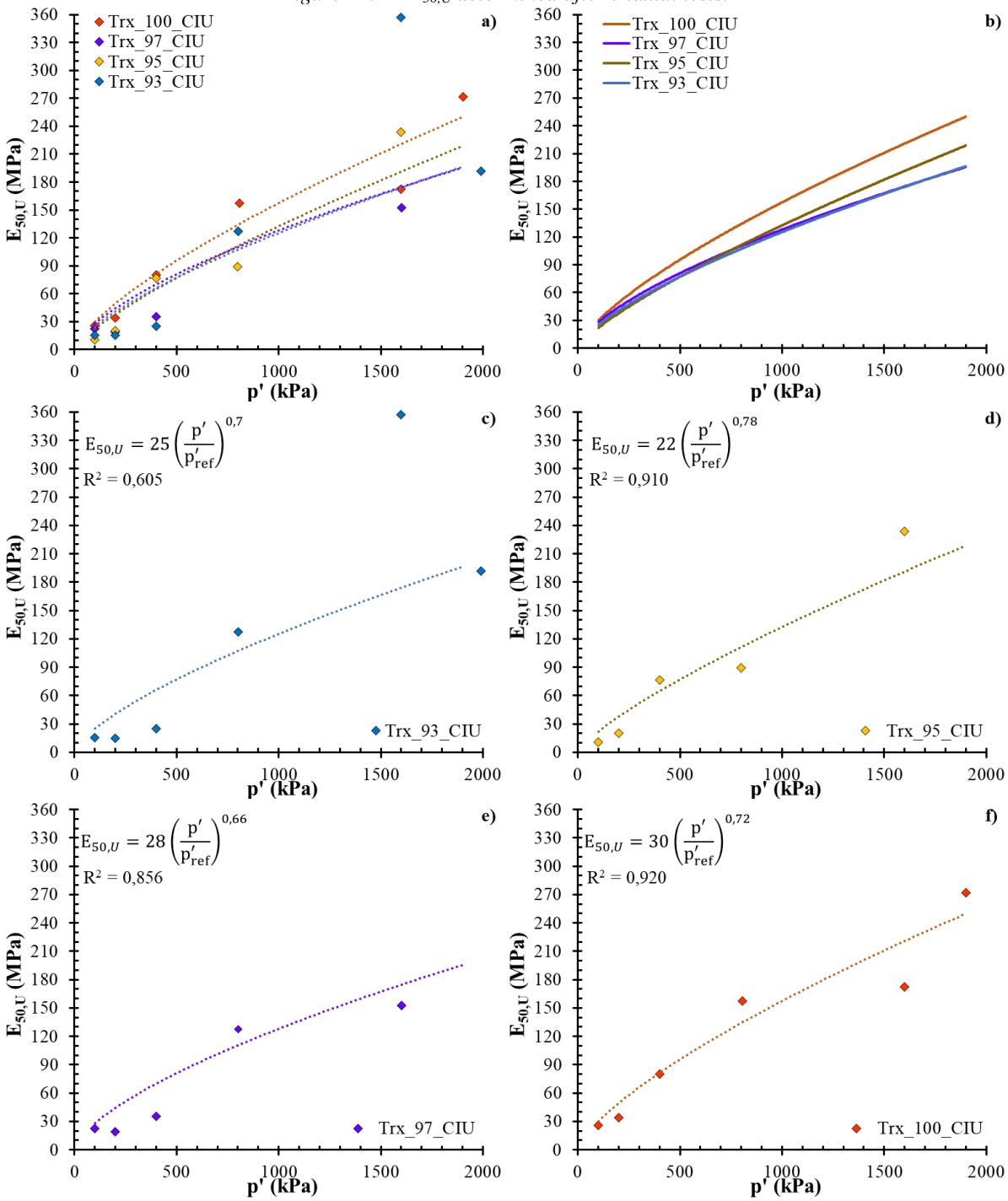

a) $E_{50,U}$ determined for each of the confining stresses of the four studied degrees of compaction; b) Trendlines determined after values of $E_{50,U}$ of each degree of compaction; c) $E_{50,U}$ determined for DC = 93%; d) $E_{50,U}$ determined for DC = 95%; $E_{50,U}$ determined for DC = 97%; $E_{50,U}$ determined for DC = 100%. Source: elaborated by the author.